UNIVERSITY OF BIRMINGHAM

STRUCTURAL AND FUNCTIONAL INTEGRITY OF ENERGY-EFFICIENT GLAZING UNITS

by

MINXI BAO

A Thesis submitted to
The University of Birmingham
For the degree of
DOCTOR OF PHILOSOPHY

School of Civil Engineering
College of Engineering and Physical Science
The University of Birmingham
March 2014

ABSTRACT

Windows are the least insulated components in the modern buildings envelopes. The energy-efficiency glazing units have been developed and used to reduce the heat loss from windows. As a type of most common glass product, insulating glass units (IGUs) have been widely adopted in the residential and commercial buildings. A type of new design of glazing units, vacuum glazing units (VGUs), has also been developed to further enhance the insulation performance. Research on the structural/durability behaviours of such new insulating glazing units is relatively limited, although the structural behaviours and safety of monolithic or laminated glass panels have been abundantly studied. This thesis intends to fill in this gap by performing thorough assessments on the structural performance of IGUs and VGUs under various environmental actions.

For double/triple IGUs, the bending deflection under coupled environmental actions is examined. Nonlinear FEM hydrostatic fluid analysis is adopted to simulate the interactions between the glass bending deflection and the volume change of the sealed air. The calculation method for the structural design of IGU, subjected to edge supports, is proposed by the draft European codes prEN 13474-2 and prEN 16612, which are examined and further developed with the aid of FEM modelling. The work is further extended to point support boundary condition, which is equally popular as the edge support. The calculation coefficients for the four point supported condition are derived and proposed. The calculation of design load share for triple glazing units under uniformly distributed

load is developed. The load share variance with different combinations of wind loads and temperature changes are analysed. The parametric studies on the edge sealant geometry layout, unit size, glass panel thickness and the air cavity width are also reported. Furthermore, a type of novel hybrid insulating glazing unit is developed by combining a VGU and an IGU with a pressure equalisation system. In the new design, the stresses in the VGU panel can be minimised.

Edge seal play a crucial role in maintaining IGUs' structural integrity and functionality. The serviceability of edge seal almost determines the life expectancy of IGUs. Therefore the mechanical behaviours of insulating secondary silicone sealants are experimentally examined in details. The nonlinear stress-strain curves in both tension and compression are recorded. A new test method, namely, the cross bonded method is employed to examine the bond behaviour of silicone sealants under different aging conditions and aging periods. The laboratory aging conditions includes high low temperature cycling, high temperature/humidity, UV exposure and salt solution immersion. The changes in the tensile bond strength, shear bond strength, Shore hardness and elongation at breakage in the aging tests are reported.

Structural safety is major challenges in the present vacuum glazing units (VGUs) technology, primarily due to the high residual stress arising during fabrication, e.g. near the supporting pillars. In this project, the mechanism and predictions of contact damage of VGUs caused by the supporting pillars is studied. The study results into the improvement suggestions of the geometry and material design of the supporting pillars. Extended finite element method is adopted to establish a Hertzian crack initiation model in order to predict the critical indentation load. Fillet pillar and spherical pillar are proposed as the substitutions to the conventional cylindrical pillar. The supporting pillars with optimised

geometry design are examined to reveal the improvement in resisting the indentation loads load. Simplified mathematical equations based on the empirical Auerbach's law are developed to calculate the critical indentation load.

KEY WORDS: Energy efficiency; glazing; IGUs; bending behaviour; FEM hydrostatic fluids analysis; interactive environmental actions; load partition, size sensitivity; edge seal system; bond behaviour; sealant aging; VGUs; contact damage; Hertzian indentation crack; XFEM; triple IGUs; hybrid IGUs; Pressure equalisation system

DEDICATION

I wish to dedicate this thesis to God, my Heavenly Father, who never gives up on me.

ACKNOWLEDGEMENT

First and foremost, I would like to express my deepest gratitude to my supervisor Prof. Jian Yang, for his expert guidance of my PhD study and research, for his caring, patience, motivation and generously providing me with an excellent academic atmosphere. I could not have imagined having a better supervisor and mentor for my PhD study.

I would like to show my great thanks to Prof. Andrew Chan and Prof. Longyuan Li, whose insight and advices were invaluable to my doctoral research life.

I am also indebted to the School of Civil Engineering, University of Birmingham, for providing me the financial, academic and technique supports. Great appreciation also goes to the staff in China Building Materials Academy, who has offered me great help in my laboratory tests. I would also thank my colleague Wenxin Zuo, for his assistance in the use of ABAQUS and MAPLE.

I would show heartfelt gratitude to John Hurman, who gave me constructive comments and warm encouragement in my academic writing.

Last but not least, special thanks go to my family. Words cannot express how grateful I am to my father and mother for all of the sacrifices that they have made on me. I could have never finished this thesis without their persistent supports. I would also like to thank all of my friends who prayed for me, and encouraged me to strive towards my goal.

TABLE OF CONTENTS

LIST OF FIGURES

LIST OF TABLES

DEFINITION OF SYMBOLS

a	shorter length of glass panel (mm)
A	the Auerbach constant (N/mm)
$\bar{a}$	radius of cylindrical supporting pillar (mm)
a^*	characteristic length
b	longer length of glass panel
C_H	0.012kPa/m, the rate of decreases of atmospheric pressure altitude,
C_T	0.34 kPa/K, the rate of increase of isochoric pressure with temperature
E	Young's modulus
E^*	effective Young's modulus (MPa)
F_d	design load (MPa)
F_T	topographical factor
h	thickness of glass panel (mm)
H	altitude of the place of use of an IGU (m)
H_A	altitude of the site (m)
H_p	altitude of production of an IGU (m)
h_{tot} i	thickness of the glass panels (m)
K	thermal conductivity of the glass (W/mK)
K_a	thermal conductivity of air (W/mK)
k_e	heat transfer coefficients of the external ambient respectively (W/m^2K)
ki	heat transfer coefficients of the internal ambient respectively (W/m^2K)
k_r	radiative heat transfer coefficient of the air layer (W/m^2K)
k_s	convective heat transfer coefficient of the air layer (W/m^2K)
n_0	initial property
n_t	new property after aging
Nu	average Nusselt number
p	applied uniform pressure, (MPa)
p^*	normalised load
p_0	initial internal pressure (MPa)
p_b	ambient pressure (MPa)
P_{cr}	critical indentation load (N)
p_e	pressure differences of outdoor ambient (MPa)

$p_{H;0}$	isochoric pressure due to altitude effects (kPa/m)
pi	pressure differences of indoor ambient (MPa)
p_p	meteorological pressure of the sealed gas at production (MPa)
R	sphere radius (mm)
s	width of air cavity (m)
S	shear force generated at edges (MPa)
SC	shading coefficient
S_T	temperature sensitivity (%/^{o}C)
T	temperature of the sealed gas in use (K)
t	aging period (h)
Tp	temperature of the sealed gas at production (K)
U	thermal transmittance (W/m^{2}K)
v	aging rate, in unit of %/h
V	initial volume of the air space
α	thermal expansion coefficient mm/^{o}C
δ	bending stiffness
Δ	integral thickness
Δp	pressure change in the cavity due to external pressure load (MPa)
Δp_0	pressure change in the cavity due to internal climatic action (MPa)
Δp_i	pressure change in the cavity (MPa)
ΔT	temperature differential (^{o}C)
ΔV	volume deformation
λ^*	pillar separation (mm)
λ	aspect ratio
σ_{max}	maximum tensile stress (MPa)
σ_{mean}	mean strength/local strength (MPa)
σ_{norm}	normalized stress
$\sigma_r (z, r)$	radical stress at an arbitrary radius r in cylindrical coordinate (MPa)
σ_z	vertical compressive stress (MPa)
υ	Poisson's ratio
ϕ	insulating unit factor

CHAPTER 1 INTRODUCTION

1.1 Background

Under the pressure of growing demand for energy and the necessity to preserve the environment, reduction in energy consumption and minimisation of carbon emission have been raised as a global concern. The Kyoto protocol, an international treaty linked to the United Nations Framework Convention on Climate Change (UNFCCC) adopted in 1997, sets binding targets for controls and cuts in greenhouse gas emissions (United Nations, 1998). The UK also aims to cut CO_2 emission by 80% by 2050 from 1990 baseline (Committee on climate change, 2008). Effective energy-saving methods and techniques are therefore in high demand in order to meet this stringent target. Buildings are deemed as the major consumer of energy thus the primary emitter of CO_2, having significant impacts on global carbon emission. As quoted by Olivier (2012), buildings are contributing to more than 40% of total primary energy consumed in the EU. A report produced by Department for Business Innovation and Skills (BIS) suggested that the amount of CO_2 emission that construction can influence and account for is up to 47% of the total emissions (BIS, 2010). Being an indispensable component of building, windows are the least insulated part and have been referred as "thermal holes". As Wilberforce (1999) stated, windows are responsible for around 40% of the total heat loss through a building. Different from opaque walls or roofs, windows allow solar radiation and sunlight to pass through due to their transparent nature. Hence their insulating capacity cannot be improved by simply increasing their thickness, let al.one the economic viability.

The concept of energy efficient glazing has emerged to resolve the "thermal holes" problem. Amongst a large variety of products from this category, two types of commercially popular components, namely, insulating glazing units (IGUs) and vacuum glazing units (VGUs) will be primarily studied in this thesis.

Double/triple insulating glazing technology is most common in the prevailing market. Vacuum glazing units sprung up in the commercial market since the late 1990s due to the increasingly stringent demand on energy conservation, and deemed as a type of novel glazing product with superior insulation performance. The increasing market demand of these energy-efficient glazing components has also raised great attention to their structural quality, service durability and life expectancy.

1.2 Research Needs

Studies on the structural and functional performances of IGUs and VGUs have been reviewed. Following knowledge gaps are summarised and the corresponding research needs are proposed.

1.2.1 Diverse environmental variables

In the existing theoretical durability assessments of IGUs, changeable ambient temperatures, non-uniform temperature distribution onto the glazing profiles or various types of boundary conditions at the edges were not fully considered in the analyses.

1.2.2 Aging performance of edge sealants under synergic environmental actions

Most pre-mature failures of IGUs are functional failures, i.e. the loss of thermal insulating property and the visual obstruction due to moisture condensation within the air space (Doll, 2005; Garvin, 1998). Edge sealant is the key factor to prevent such

types of failures and sustain excellent service quality. The aging mechanism and responses of the edge sealant should be explored, especially subjected to a synergic aging action rather than individual environmental factors.

1.2.3 Contact damage and the structural failure of VGUs.

The major failure mechanism of VGU is normally attributed to the excessive stresses generated at vulnerable locations. The contact interface between the supporting pillar and the glass surface is one of the most susceptible positions. The contact damage to the pillar indentations will evolve into larger cracks and eventually lead to the overall glass fracture. Not many research publications can be found to provide adequate precaution for structural failure induced by the contact damage.

1.2.4 Bottleneck of existing energy-efficient glazing

Drawbacks have been detected among IGUs and VGUs in spite of the dramatic improvements of the insulation performance that have been made (Collins and Simko, 1998; Fischer-Cripps et al., 1995; Koebel, et al., 2010; Liu, 2009). The immanent heat loss due to the conduction and the convection of the air layer of IGUs has created a bottleneck making further substantial progress. VGUs can produce much higher thermal resistance. However, this novel profile is still in the frontier market, and not generally adopted in the energy-efficiency glazing industry due to insufficient strength and high failure probability. New glazing profiles are expected to overcome these deficiencies in both functional and structural aspects.

1.3 Aims and Objectives

This thesis aims to investigate the structural behaviours of existing energy efficient glazing components when undergoing various environmental impacts. Based on the results and conclusions obtained, an improved design method and a novel design of the energy efficient component will be suggested.

The main objectives are presented below:

- To investigate the mechanical behaviours of IGUs/triple IGUs under different environmental loadings by means of FEM simulation
- To put forward a calculation method for the bending performance of triple IGUs on the basis of the existing analytical method of IGUs
- To explore the mechanical responses of the IGUs' edge sealant under different loading conditions, and to examine the aging behaviour of the edge sealant.
- To study the contact damage of VGUs and to propose mathematical equations to determine the minimum indentation load that triggers an indentation crack.
- To suggest and develop a novel type of energy efficient glazing component by combining the advantages of IGUs and VGUs.

1.4 Methodology and layout of the thesis

In order to achieve the above mentioned aim and objectives, a comprehensive literature review is carried out. Two main types of energy efficient glazing units, IGUs and VGUs, are studied in this thesis. The finite element method (FEM) and the extended finite element method (XFEM) were employed to simulate the structural behaviours of the glazing units under different loading conditions, which included the bending behaviours of the glass panels, the crack initiation and propagation on the glass surface, and the

sealant deformation due to the glass bending. The results of the modelling are either compared with existing code guidance or the experimental data for validation. Extended parametric studies based on the validated numerical models are carried out to further consider the structural responses of each component. Corresponding empirical mathematic methods are also proposed.

The thesis layout is as follows:

Chapter 1 presents an introduction of the background of energy-efficiency glazing units. The significance of the study, research needs, aims and objectives, and the methodology of the thesis are outlined successively.

Chapter 2 renders a state-of-the-art literature review that covers recent research on structural analysis, thermal analysis, design methods and the durability assessments of the current energy-efficiency glazing components.

Chapter 3 investigates the bending behaviour of IGUs under interactive environmental impacts. The FEM models were validated by Boyle's law for gas and the theory of plates and shells. The numerical model is then used to validate the additional coefficients for the IGU design calculation for British standards. The four point supported boundary is taken into design consideration by FEM simulation.

Chapter 4 estimates the structural performance of triple IGUs. Extended hydrostatic fluids numerical models are adopted to simulate the glass bending movements under interactive environmental actions. Linear and nonlinear mathematic equations are developed to calculate the design load share on each glass panel with different internal or external loads.

Chapter 5 presents the hyper-elastic material properties of a group of silicone sealants via the tests of dumb-bell tension, compression cycling and tension/shear bonding behaviour. A variety of aging tests were conducted with particular reference to the secondary insulating glazing sealant, so as to obtain the tensile and shear strength, hardness, elongation rate at break at different aging period. In addition, the local edge system is specified in the numerical modelling, and the structural performance is investigated with different spacer systems.

Chapter 6 provides a study on the contact damage on glass panels in VGUs due to the presence of supporting pillars. A novel finite element method branch, called as the extended finite element method (XFEM), is adopted to simulate the crack initiation and propagation. Based on the simulation results, the suggestions of design improvements of supporting pillars are proposed in both geometric and material aspects. A mathematical equation is provided to determine the critical indentation load by the given Young's modulus and the radius of spherical pillar.

Chapter 7 introduces a type of novel hybrid vacuum/triple glazing system with a pressure equalisation design has been devised and reported. In this system, a VGU is enclosed by two glass panels to form a triple glazing unit system. This new design creates an equalised air pressure on both sides of the VGU and subjects the VGU to no additional external loads apart from the inherent fabrication stress.

Chapter 8 summarises the achievements and the key findings in this work, and presents future recommendations in the design field of energy-efficiency glazing components.

CHAPTER 2 LITERATURE REVIEW

2.1 Introduction

This Chapter will present a comprehensive literature review of the research on the structural and functional performances of energy-efficient glazing components. This state-of-the-art review will cover a variety of key impact factors affecting the longevity and serviceability of IGUs and VGUs respectively during their service life.

Studies on the failure mechanisms of IGUs will be then reviewed to identify the major failure modes of IGUs in practical applications. The detailed durability/ longevity studies on IGUs will be presented, so as to introduce existing test methods and the primary concerns of researchers when assessing the IGUs' serviceability.

Based on this information, thermal performance, structural performance of IGUs and the bonding behaviour of IGU edge sealants will be specifically reviewed to obtain a better understanding of the correlation between functional and structural performances of IGUs. Likewise, thermal performances and structural behaviours of VGUs will also be reviewed in depth. Then the design deficiency and the further developments in VGUs will be discussed. The scope of this chapter is specified in the following sections with a summary of the findings at the end of the chapter:

- Background and durability development of IGUs
- Failure Mechanisms of IGUs
- Durability studies on IGUs
- Thermal performance of IGUs
- Structural analyses of IGUs

- Material features of IGU edge sealants
- Background and durability development of VGUs
- Thermal performance of VGUs
- Structural performance of VGUs
- Design concerns and further developments of VGUs

2.2 Introduction and developments of IGUs

As a type of energy-efficient component, the double/triple glazing technology has become increasingly popular as they reduce the heat transfer by a sealed cavity filled with dry air or inert gas. Insulating glass units (short for IGUs), also termed as "double glazing units", was first invented and patented by Thomas D Stetson (Stetson, 1865). The technology was then markedly improved over the century and generally emerged in United Kingdom in the early 1960 (Garvin and Marshall, 1995). A typical IGU (as shown in Figure 2-1) consists of two glass plates separated by a spacer bar which is filled with desiccant, in order to absorb the moisture condensation during its service life. The structure is sealed around the edges. The width of the inter-layer air space in the UK is typically applied with 6mm, 12mm, 16mm and 20mm. The air gap wider than 20mm will no longer contribute a better thermal insulation performance since the internal air convection will be intensified and offset the insulation effect brought by the increasing width.

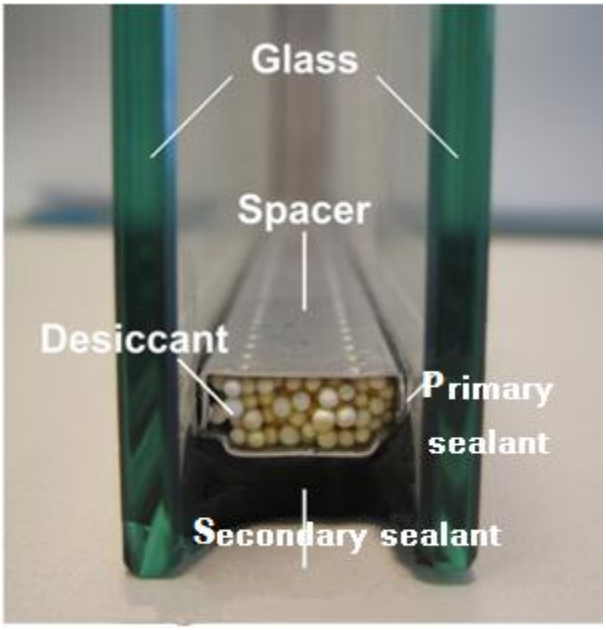

Figure 2- 1 Cross-section of an IGU

The combination of edge sealants and spacer bar is usually referred as edge-seal system. It is a crucial component in the IGUs that provides a gas and moisture barrier and to structurally bond glass panels together. A primary sealant is applied between the spacer bar and glass panel, which is to provide an additional barrier against moisture infiltration. Secondary sealant is then filled outside the bottom of the spacer bar. The common edge seal system is categorised into single-seal system and dual-seal system. Single-seal system only employs secondary sealant. Dual-edge seal system adopts both primary and secondary sealants to provide a better performance. Normally, primary sealant is made of excellent moisture-resistant material and performs as a moisture vapour barrier, while secondary sealant is required for good adhesion and outstanding elasticity to ensure the structural integrity of IGUs under various external loads. In modern IGU construction, dual-sealed system is more commonly adopted.

During years of development of IGUs, a great number of advanced technologies have also turned up to further improve the overall insulation capacity of IGUs. The inert gas

filled in the cavity between two glass panes has been developed to achieve a better insulation capacity of IGUs. The inert gas such as argon, krypton, and xenon shows excellent attributes, e.g. being stable, inert and less thermally conductive than air (Ernst, 1997).

In the meanwhile, the advancing coating technology e.g. Low-emissivity (Low-E) coatings have been also used to reduce the heat transfer through radiation. The Low-E coatings can reflect 40%- 70% of the heat that passing through the clear glass and while does not affect the light transmittance (Nadel and Amstock, 1997). The conventional soft coating Low-E coating is composed by a thin layer of silver, a transparent oxide layer and a thin metal layer between the silver and the oxide layer in order to protect the silver. The coating is normally applied to the interior side of the indoor panel of the IGU. It can be glazed on the internal side of outdoor panels in higher solar control applications, so as to provide higher visible transmission and lower reflectance.

Warm edge technology has started to thrive in recent years as a substitution of current edge-seal system, because it can effectively reduce the heat through the conventional metal spacers. The warm edge refers to the edge-seal system of lower conductivity, normally constituted by organic materials. Moreover, the flexible resilient features of the warm edge can also help alleviate the stresses in the glass near the edge when experiencing severe loading conditions (Zeuge et al., 1997).

Triple/composite glazing units (TGU) technology is developed to reduce the thermal conductivity by an additional air cavity. The working mechanism is to improve the insulation nature by an additive air cavity. Apart from monolithic glass panel, other types of glass profiles such as laminated glass panel, and vacuum glazing unit panel can also be combined.

These technologies have greatly improved the thermal efficiency of modern glazing systems. The U-value (overall thermal transmittance) of typical windows has dropped from more than 5 W/m^2K to somewhere close to 2 W/m^2K. (Collins and Simko, 1998)

Compared with single glazing, IGUs and TGUs have shown improved thermal performance with lower U-values. Garvin (2000) compared the U-values of a variety of IGUs and TGUs in Table 2- 1.

Table 2- 1. U-values for insulating glass units (BRE Digest 379)

glazing system		Degree of exposure		
		Sheltered	Normal	Severe
single		5	5.6	6.7
IGUs	Air space			
	3mm	3.6	4.0	4.4
	6mm	3.2	3.4	3.8
	12mm	2.8	3.0	3.3
	20mm	2.8	2.9	3.2
Low-E	12mm	1.7	1.8	1.9
TGUs	Each air space			
	3mm	2.8	3.0	3.3
	6mm	2.3	2.5	2.6
	12mm	2.0	2.1	2.2
	20mm	1.9	2.0	2.1

The importance and significance of the applications of energy efficient glazing in the building construction have been raised. In practice, the installed IGUs or VGUs are exposed to a variety of environmental impacts, which will severely affect their service qualities and longevity. Many countries and organizations have proposed a series of assessments on the durability of the energy efficient glazing to cover a wide range of the factors affecting both functional and structural performance. Since 1988, A.T. Wolf on behalf of Dow Corning Corporation initiated a great amount of the studies into the failure mechanisms and the life-expectancy of IGUs, particularly on the mechanical

behaviours of edge sealants (Wolf, 1988, 1992a, 1992b, 1998, 2003). As a part of the research programme at the Building Research Establishment (BRE) in UK, Garvin (1995, 1998, 2000) and his team initiated an in-situ monitor work on the installed IGUs under nature exposure. The work aimed to investigate the durability of IGUs and realise the potential longevity of the units in real installation environment. From 2002 to 2005 Aspen Research Corporation sponsored by the Department of Energy of US Government undertook a systematic research on the durability of the IGUs (2005). The project quantitatively analysed the related environmental factors and developed a comprehensive IG durability simulation tool which is to meet current and future building envelope energy performance goals. The simulation tool can be deemed as a solution to the insufficient field data and to provide constructive guidance to the IGUs from material selection, assembling, design, installation aspects and the estimation of the service life.

2.3 Failure mechanisms of IGUs

The estimated service life of IGUs is 25 to 30 years with appropriate manufacturing, assembling and installation technology (Ratcliffe, 1994). The long-term performance of IGUs depends on the edge-seal design, manufacturing, glazing system, installation and service conditions (Garvin, 1998). During the service life of IGUs, two major failure types are categorised: functional failure and structural failure. Functional failure refers to the loss of thermal insulation or the moisture fogging on the interior surfaces of the glass, which are due to the gas leak of the inter-layer space. Structural failure, such as glass breakage or de-bonding in the structural silicone glazing, often occurs under excessive ambient loads. In the following section, a variety of environmental influences

and the common failure modes of IGUs documented in published studies are summarised.

In the IGUs knowledgebase report delivered by Aspen Research Corporation (2005), the major failure modes can be concluded as follows: the fogging phenomenon; glass breakage; cohesive failure of primary and secondary sealants; adhesion loss on the glass or spacer of primary and secondary sealants; partial glass structural failure; total glass structural failure; excessive air absorption and spacer structure failure.

Similarly, Van Den Bergh et al. (2013) also outline the typical failures modes of IGUs. The failure of IGUs can be examined by the visible fogging, aesthetic degradation, increase in U-value and the loss of secondary sealant adhesion.

The failure modes of the IGUs that failed within two years since installation were investigated (Ma, 2004). It demonstrated that 63% of the IGUs failed due to the fogging phenomena, while 22% because of glass breakage and 11% for other reasons. Doll (2005) collected the cumulative failure rate of a prevailing type of IGU production at its fifth year and tenth year. Different failure modes are compared below in Figure 2- 2.

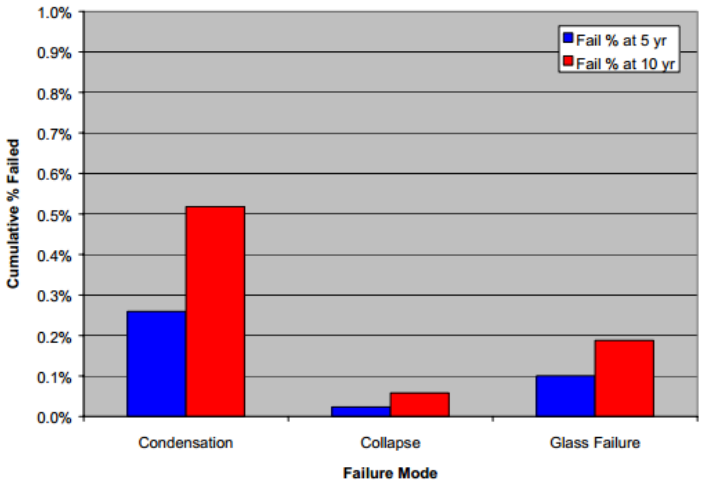

Figure 2- 2. IGU failure modes proportions (Doll, 2005)

The same failure trend was presented in BRE Digest 453 report (Garvin, 1998). The pre-mature failures of IGUs, i.e. the early failure after 5 years or less since installation were ascribed to the excessive moisture condensation within the IGUs. The water infiltration through the edge sealants generates a humid ambient that can generate mould around the unit border and lead to a progressively adverse effect on the edge sealants over time.

The following explanations were suggested in the report to account for the fogging failure. It is easily seen that the method of installation and the performance of the edge seal system to a great extent determines the life-expectancy of IGUs: insufficient quality of IGUs and poor manufacturing technology; unqualified glazing workmanship; unqualified installation of the window; adhesion loss of sealant to glass; material degradation of edge sealant by incompatible agent and sunlight ultraviolet degradation of edge sealant.

Van Den Bergh (2013) listed the following environmental factors that the installed IGU may encounter:

- Large temperature difference
- Thermal cycling
- High humidity
- Solar radiation
- Atmospheric pressure fluctuation
- Wind loads and working loads

- Relevant loading during manufacturing, transportation, installation and maintenance
- Synergetic action of water, temperature change and sunlight is reported to impose the greatest stress on the edge sealant of IGUs.

Detailed work was conducted by Wolf (1992) to explore the environmental influences on each component of IGUs. The negative effects can be divided into two types: 1) physical influence, such as the distortion and deformation of edge-sealants, or the variation of the air cavity; and 2) chemical influence, such as the deterioration of flexibility and adhesion failure of edge-sealants. Wolf outlined the environmental factors that affect the durability of IGUs as presented in Table 2- 2.

Table 2- 2. Environmental factors (Wolf, 1992)

Environmental factors	Effect types
Water /water vapour	physical/chemical
Temperature	physical/chemical
Wind/working loadings	physical
Sunlight-UV	physical/chemical
Oxygen, ozone	chemical
Aggressive atmospheric contaminants	chemical
Synergetic effects	

It can be concluded according to the existing research presented above:

1. Fogging phenomena is a primary failure criterion in the IGUs quality inspection and is found to be the most common failure type in terms of pre-mature failure of IGUs.
2. Different failure modes of IGUs are not independent of each other but highly correlated. For instance, fogging failure will also result in the degradation of

insulation function and the sealant aging due to high humidity ambient. On the other hand, the adhesion/cohesion failure of edge sealants will lead to excessive moisture ingress and the loss of insulation function because of gas leakage.

3. Simultaneous action of multiple environmental factors will contribute a synergic effect upon IGUs and exert greater stress levels than simply the cumulative effect of each single action.

With particular concern to the above mentioned conclusions, the test methods and experiments in different regions, aimed at evaluating the service life and performance of IGUs, are worthy of further review.

2.4 Durability studies on IGUs

2.4.1 National regulations and standards

A wide variety of standard methods to evaluate the durability and service life of IGUs have been published in different countries. In this section, the development and the latest version of national standards/specification in the UK, America and Canada are reviewed.

The first British standard with particular reference to IGUs is BS 5713:1979 (BSI, 1979). The standard outlines performance requirements and the six standard test methods, which include: visual examination/ initial seal test/ initial dew point test/ fogging test under UV exposure/ weather cycling test and high humidity cycling test. The specification was then superseded by the standard of UK/EU: BS EN 1279. The standard comprised of six parts as follows: BS EN 1279-1 as part 1, amended in 2004, mainly regulates the generalities, dimensional tolerances and the rules for the system (BSI, 2004). BS EN 1279-2, 3, 4 give the test methods on moisture vapour penetration, gas leakage rate, gas concentration tolerances and physical attributes of the edge seals

respectively (BSI, 2002(a), 2002(b), 2002(c)). The moisture penetration index, *I* value, was proposed to measure the amount of drying capacity consumed after standardised ageing conditions, i.e., the percentage of the desiccant capacity consumed by the moisture infiltration. BS EN 1279-5, approved in 2005, specifies the requirements, the evaluation of conformity and the factory production control of insulating glass units for use in buildings (BSI, 2010). BS EN 1279-6 provides the factory production control and periodic tests (BSI, 2002(d)). The standard is currently prevalent for the examination of IGUs' performance in UK/EU area.

The ASTM E773 "Standard Test Method for Accelerated Weathering of Sealed Insulating Glass Units" and ASTM E774 "Specification for Classification of Durability of Sealed Insulating Glass Units" was published in 1981 and adopted in following years until 2003. The harmonized test methods ASTM E2188 and E2190 were released to replace previous two (ASTM, 2002(a);2002(c)). ASTM E2189 was proposed to provide a method of examining the fogging in IGUs (ASTM, 2002(b)). The frost/dew point is determined in accordance with Test Method E546 "Standard Test Method for Frost/Dew Point of Sealed Insulating Glass Units" (ASTM, 2006).

The Canadian CAN/CGSB 12.8-97 insulating glass unit standard published in 1997 is the most recent national standard in evaluating IGUs' performance (CGSB, 1997). It is based on the acceleration of naturally occurring climatic conditions and can also be used to specify manufacturing rules. Because of close cooperation in IGUs' trade flow with America, the harmonized standards ASTM E2188, E2189 E2190 are also used by Canada, in order to make up the major discrepancies between previous standards, thus to eliminate the trade barriers in both countries.

A certain degree of similarity in the durability tests regulated in the above mentioned countries can be found. Periodical high/low temperature fluctuation, constant high temperature ambient, high humidity condition and UV exposure are all considered in the accelerated durability tests over different nations. The moisture content within the IGU specimen is a major concern with respect to estimating IGUs performance. As concluded by Burgess (1999), the basis of all IGUs durability tests is to measure the moisture quantity increase after accelerated weathering tests.

2.4.2 Short-term experiments based on national standards

Powell and Hahn (1978) conducted the tests using the dew/frost point apparatus recommended in ASTM Standard E546. They introduced the operational approach of the apparatus in detail (Powell and Hahn, 1978). In-situ dew-point measurements according to ASTM E546 were also carried out to assess the service span of IGUs (Torol et al., 2002). The relationship between the ambient air temperature, the moisture content within the IGU cavity and the dew-point temperature over the measurement period was finally outlined.

An investigation was conducted to compare the qualities of IGUs from companies with a consolidated quality system with those from companies that were not audited by a third party (Mognato et al., 2007). The laboratory tests according to BS EN 1279 were carried out to evaluate the performances from two types of IGUs producers. The test results demonstrated that efficient checking during manufacture and strict regulations would lead to a lower moisture penetration rate, lower gas leak rate, and higher performance stability during long-term aging conditions and hence significantly longer service life of IGUs.

Modified experiments based on standardized test methods have also been developed. Miguel (2005) reviewed the current predicting methods on the life expectancy of IGUs and developed a modified method to detect the fogging time hence to estimate field service time. By means of estimating the degree of saturation of the desiccant contained in the spacer, an approximate time for fogging can be inferred (Miguel, 2005).

Panait (2007) carried out the durability test of IGUs by the standardized test methods, as specified in the standard BS EN 1279-2. In addition to the measurement of the dew point and humidity penetration index I_{av}, the tests were also undertaken to measure the stresses and displacements due to the pressure applied on the edge sealants. The analysis on coupled stresses and moisture condensation effects provided a more reasonable estimation on the expectancy of IGUs.

The short-term experiments based on national standards have exhibited great time-effectiveness in evaluating the qualities of different IGU products and predicting their service life. Nevertheless, the actual service performances of IGUs installed in practice cannot be specifically accessed unless under long term in-situ monitoring. Despite data from lengthy field experiments being relatively rare in academia, field tests are unanimously deemed as the most reliable approach for assessing the durability of IGUs.

2.4.3 Long-term field experiments

In 1980, the SIGMA (Sealed Insulating Glass Manufacturing Association) initiated a field experiment of IGUs in order to establish a correlation between the actual field performance and the accelerated weather test classifications outlined in ASTM E774. Lingnell (2007) recorded the data on IGUs with visual obstruction (i.e. fogging) in the airspace or seal failures in his report on a 25-year field inspection.

The earliest field survey within the UK was conducted by Building Research Establishment (Garvin and Blois-Brooke, 1995). The study was intended to determine the actual and perceived causes of early life failure of IGUs. In one user survey lasting two years, the quality of IGUs was cited in 51% of failure cases, followed by unqualified glazing installation, poor manufacture of frames, design fault and poor frame installation. In the other survey, a total of seventeen building projects were investigated by a glazing specialist, with respect to the large-scale failure spots. A series of qualitative conclusions, such as poor sealant quality, inadequate drainage system, and unqualified glazing technique were given to account for the mechanisms of common failure mechanism.

Following the preliminary field survey, Garvin and Wilson (1998) released a group of interim data of a long-term exposure experiment from 1994 to 1996. This project was aimed at determining the potential life expectancy under the influences of actual environmental impacts, mainly by monitoring the conditions affecting installed IGUs in various types of drained and ventilated window frames. Nearly 2-year continuous monitoring allowed observations on the effects caused by seasonal alterations and the condition differences between the outdoor and indoor ambient. The three most commonly used window frame systems, i.e. aluminium, steel and timber, were chosen for comparison. By the end of the monitoring, the aluminium window system had performed the best with the lowest relative humidity inside the air space. The complete five-year field monitoring report recording from April 1994 to 1999 was then published later in 2000 (Garvin, 2000). It was found that the measured Moisture Penetration Index (I value) within IGUs of good quality is not obviously affected by the increasing moisture amount in the frames over the test period. The IGUs of good quality also

displayed consistent excellent moisture resistance, i.e. with a much lower *I* value than the maximum allowable value specified in BS EN 1279-2, regardless of the frame types.

It can be seen that both short-term laboratory tests and long-term field inspection of IGUs adopt fogging phenomena (visual obstruction) as an indication of the initial failure of IGUs. Lengthy in-situ inspection of installed IGUs demonstrated that poor quality accounts for more than half of the total IGUs failure cases (Garvin and Blois-Brooke,1995). The moisture resistance capacity of IGUs is mainly dependent on their qualities despite of the effect induced by different frame types. It can be concluded that the quality of IGUs to a great extent determines their actual service life of IGUs. However, very little specific discussion on the quality of the IGUs has been raised and the descriptive conclusions drawn from field experiments cannot substantially explain the failure mechanisms of IGUs under complicated environmental impacts.

In the following sections, environmental factors will be specifically reviewed in terms of moisture infiltration analysis, thermal analysis and structural analysis, so as to obtain an insight into the failure mechanisms.

2.5 Moisture vapour/gas diffusion of IGUs

The majority of current prevailing IGUs adopt the double-seal system to achieve better insulating performance. The primary sealant is applied between the glass panels and the spacer to provide a barrier against the permeation of liquid or gaseous substances. Polyisobutylene (PIB) sealant is almost exclusively used as the primary sealant due to its excellent moisture infiltration resistance (Bergha, 2013). In most cases, primary sealants' service time mainly depends on the water vapour resistance and the adhesion. Secondary sealants in an IGU are employed to ensure the structural integrity of the

entire glass unit. Good elastic recovery and adequate cohesive and adhesive strengths are both required so that it can resist various external loadings, as well as retain stable properties when subjected to cyclic or large deformation.

It is an intrinsic process for water vapour to permeate into the polymer edge sealants of the installed IGUs and is retained within the air cavity. The above-mentioned short-term and long-term inspections have revealed that the fogging failure occurs as a result of excessive moisture condensation beyond the incorporated desiccant capacity. The moisture diffusion mechanism within the sealant is illustrated below in Figure 2- 3 (Doll, 2005).

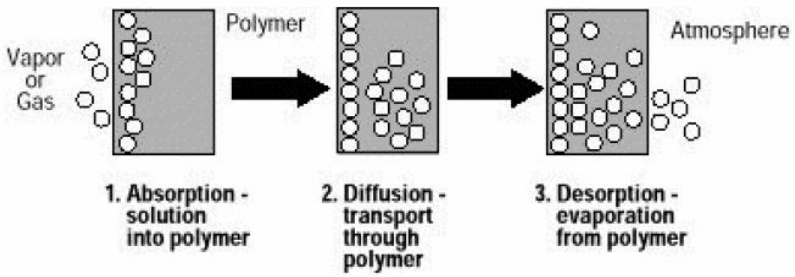

Figure 2- 3. Gas permeation through polymer (Doll, 2005)

According to the diffusion theory (Crack, 1975), high moisture-resistant edge sealants are expected to reduce the vapour diffusion rate and hence elongate the service life of IGUs. However, the theory assumes the moisture can only travel through the intact edge sealants, neglecting the possible moisture infiltration paths from the gaps between sealants and other components and/or the cracks within the sealants when going through excessive deformation. In reality, the structural integrity guaranteed by secondary sealants also helps to retain excellent moisture resistance in IGUs (Wolf 1992). It was observed in Wolf's work, that even though the silicone secondary sealant has the

highest water-vapour permeability compared to other types of secondary sealants, the combination of a silicone secondary sealant and a PIB primary sealant contributes to the lowest water pick-up within the air cavity. This is attributed to the good elastic recovery of silicone sealants, thus avoiding water ingress through the opening between sealant and glass surface due to adhesion failure. The de-bonding of the edge sealants, due to sealant aging or excessive mechanical loads, will lead to fogging failure as well. In this sense, the mechanical movements of IGUs under interactive environmental impacts should be brought to attention when addressing failure mechanisms of IGUs.

2.6 Thermal analyses of IGUs

Heat transfer mechanisms of IGUs deserve detailed reviews so as to enable a better understanding of the temperature distribution fields in them. The temperature distribution field is closely associated with the temperature-induced stress distribution and the moisture condensation risk in terms of fogging temperature (Song et al., 2008).

The heat transmission process through an IGU is complicated, as it comprises different heat transfer modes, as shown in Figure 2- 4.

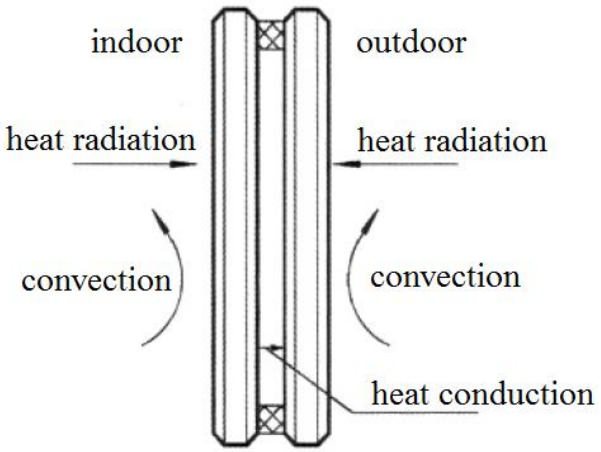

Figure 2- 4. Schematic diagram of the heat transmission process of an IGU (Song et al., 2007)

Two parameters are used in evaluating the thermal performance of IGUs: the overall heat transfer coefficient (also termed as thermal transmittance) U-value and the Shading Coefficient. The U-value of an IGU can be calculated by the equation in the following Eq.(2-1) from (Gan, 2001):

$$U = \frac{1}{\frac{1}{k_s} + \frac{1}{k_e + k_r} + \frac{h_{tot}}{K} + \frac{1}{k_i}} \qquad 2\text{-}1$$

where U is the thermal transmittance (W/m^{2}K); k_e, k_i are the heat transfer coefficients of the external and internal ambient respectively (W/m^{2}K); h_{tot} is the total thickness of the glass panels (m); K is the thermal conductivity of the glass (W/mK); and k_s is the convective heat transfer coefficient of the air layer (W/m^{2}K). In the case of a vertical air space:

$$k_S = Nu \frac{K_a}{s} \qquad 2\text{-}2$$

where Nu is the average Nusselt number; K_a is the thermal conductivity of air (W/(mK)) and s is the mean width of air cavity (m).

k_r is the radiative heat transfer coefficient of the air layer (W/m^{2}K) and is given by Eq.(2-3) (Gan, 2001):

$$k_r = \frac{4\sigma T_m^{\ 3}}{\frac{1-\varepsilon_1}{\varepsilon_1} + \frac{1-\varepsilon_2}{\varepsilon_2} + \frac{1}{F_{12}}} \qquad 2\text{-}3$$

where $\boldsymbol{\sigma}$ is the Stefan-Boltzman constant, ε_1 and ε_2 are the surface emissivity of two glass panels at the mean temperature T_m (K); F_{12} is a view factor related to the geometry of the IGUs.

The shading coefficient (SC) is defined as the ratio of solar gain from direct sunlight passing through a glass unit to the solar energy passing through a sheet of 3mm clear float glass. The SC is calculated by the following equation (Ma et al., 2009):

$$SC = \frac{\tau_s + \frac{A_s \cdot R_{out}}{R_t}}{0.87} \qquad 2\text{- }4$$

where τ_s is the ratio of direct solar radiant heat transmittance; A_s is the absorbed solar gain; R_{out} is the outside thermal resistance coefficient of glass panels ; R_t is the total thermal resistance coefficient of the whole IGU system.

Apart from analytical equations to calculate the U-value of an IGU, quite a few parametric studies on the heat transfer process of the air cavity were carried out by numerical modelling. Song et al. (2008) evaluated the thermal performances of various types of IGUs by calculating U values obtained from FEM modelling. Ma et al. (2009) also compared the SC values of different configurations of IGUs. Inert gas fill types, glass thickness and Low-E coatings are taken into account in parametric studies. Gan (2001) specified a computational fluid dynamics (CFD) method for predicting the convective heat transfer coefficient, thermal resistance and thermal transmittance for an IGU. The conductive heat transfer became significant when the width of air space is increased. Wang et al. (2009) also employed a CFD numerical simulation software FLUENT to explore the heat transfer caused by the natural convection within the air space. The natural convection was indicated to be influenced by the filled gas types, Rayleigh number, the relative thickness of the air space and the surface temperature differences. As suggested in the article, the natural convection heat transfer can be equally treated as the pure heat conduction under low relative thickness or low temperature difference.

A number of studies were also presented to discuss the heat transference and thermal performance of the edge seal-system. Hot-box measurements and numerical simulations were used to examine the glass surface temperature in the edge-glass region influenced by a variety of spacer designs (Elmahdy, 1993). The insulation improvement contributed by ten different types of warm-spacers was also studied (Elmahdy, 2006). Song et al. (2007) calculated the U values of the window centre and the total window system and the lowest temperature on the glass surface by two-dimensional steady state heat transfer is simulated. Conventional IGUs and the warm-edge IGUs were both analysed. The results show that the application of warm-edge spacer can increase the lowest temperature on the inside surface and the air humidity so as to reduce the inside surface condensation risks. Gustavsen et al. (2005) studied the total window U-values and glazing temperatures for IGUs with an aluminium conventional spacer and an insulating spacer bar. The combined impacts of climate and wall insulation on the energy benefit of IGUs adopted in façade were studied with particular regard to the UV-exposure (Mingotti et al., 2013). These studies came to similar conclusions: insulated spacers and thermally-resistant edge sealants can drastically improve the overall heat insulation quality (Van Den Bergh et al., 2013).

In general, thermal performances of IGUs are found to be closely related to the IGU geometry, gas type, glass coatings, spacers and sealant types. Uneven temperature distribution field has been found due to different thermal conductance of each component in IGUs, and the fogging phenomenon is most likely to take place in edge areas. The adoption of thermal-resistant spacer and sealants can contribute to a low probability of condensation risk. Nevertheless, very little discussion is given on the

thermal-induced stresses from thermal expansion/contraction in each component combined with the internal action generated from the sealed air.

2.7 Structural analyses of IGUs

As has been highlighted, the mechanical movements of each IGU component in IGU could have significant impacts on functional failure and the ultimate structural failure. The studies conducted on the structural responses of IGUs under various loadings will be reviewed.

2.7.1 Structural analyses of glass panels of IGUs

Vuolio (2003) explored the structural behaviour of IGU façades by numerical tools. When addressing the structural movement of IGUs, the coupling of the sealed internal air pressure change and the external environmental actions was highlighted. He developed a group of nonlinear FEM models to simulate the bending behaviour of IGUs subjected to temperature change, amplitude change and uniform wind loads. Different boundary conditions and sizes were also discussed. Experimental results were used to validate the numerical models. The calculation method in prEN 13474-2 (BSI, 2002) compared with the FEM and experimental results. It was found that the maximum stresses calculated according to the design code are relatively larger than the numerical results, as the membrane effect in the plate bending was underestimated.

Feldemeier (2003) proposed two new parameters: characteristic length "a^*" and insulating unit factor "ϕ" in a analytical method, which allowed a simplified nonlinear calculation of the maximum bending stress and deflection of glass panels for four-edge simply supported IGUs. The calculation method is also adopted in the code prEN 13474-2 to calculate the load shares on two panels of one IGU.

prEN 13474-2 provided the calculation method for the load share in IGUs when subjected to both external and internal loads. Three major concerns in IGU design work were raised (BSI, 2002):

1. The loads shares on two glass panels when subjected to one-side external loading
2. The loads acting upon two panels caused by the pressure change of the air cavity
3. The loads acting upon two panels caused by the temperature change of the air cavity

The latest published draft design guidance to determine the load capacity of glass panels is prEN 16612: "Glass in building - Determination of the load resistance of glass panes by calculation and testing" (BSI, 2013). In Annex 2 and 3, the nonlinear calculation method of maximum stress and maximum deflection were specified for IGUs and triple IGUs.

The bending behaviour of IGUs caused by uniform pressure applied to one of the glass surfaces was analysed in Ma *et al.* (2006). The maximum stress and deflection were obtained from numerical modelling and compared with the experimental results. The numerical modelling results were used for the manual iteration to eventually determine the balanced pressure.

It can be found that the existence of the air cavity makes the mechanical responses of glass panels complicated. The load share on each panel under a wind load is closely associated with the pressure generated by the deformed air cavity, due to the bending deflections of glass panels. On the other hand, the bending deflection is determined by the loads exerted on the glass panels, which is related to the pressure change within the air cavity. Furthermore, air expansion or contraction of the cavity will also act upon the glass panels when experiencing a temperature change or an altitude change. The pressure change of the air cavity caused by wind load, temperature fluctuation and

altitude should be taken into account simultaneously when evaluating the load share upon the glass panels of IGUs.

Liu et al. (2009) presented a quantitative calculation on the deflection and stress distribution of IGU glass panels under different temperature and altitude change respectively. The mathematic equations associate thin plate theory with Boyle's law, therefore the internal actions upon the glass movement can be successively calculated due to the temperature change or amplitude change (Liu, 2009). The study especially looked into the load capacity of IGUs in the case of gas leakage. It was found that the gas leakage due to sealant adhesion failure would result in an uneven load share onto two glass panels, and thus increase the breakage possibility of the glass panel under high loading level.

2.7.2 Structural analyses of the edge sealants of IGUs

The edge-seal system of an IGU is aimed to provide a gas/moisture-barrier and to structurally bond two or more panes of glass. (Wolf, 2003). The structural performance of edge sealant system has always been deemed as a crucial factor when evaluating longevity of IGUs. A number of studies have been working on the performances of the sealants under external loadings.

Panait et al. (2007) studied the effect of thermal-mechanical stresses in secondary edge sealants. A 3-D finite element analysis for six types of spacer configuration was conducted to examine the adhesive failure of secondary sealants. The hyper-elastic features of three types of secondary sealants, polyurethane, polysulfide and silicone sealant were characterised by Mooney-Rivlin models, which are implemented in the FEM package. The numerical results revealed that minor geometrical change in spacer configuration would result in considerable stresses variation, and geometry of secondary

sealants was a key determinant in the stresses undergone by both primary and secondary sealants.

In Stewart (2006), the mechanical responses of PIB edge sealant were investigated by analysing the thermal movements of spacers and glass panels. Three commercially available spacers of different materials and designs were adopted in the FEA simulations. The stainless steel spacer was found to have the least effect on the change in the cross-sectional area, while the aluminium spacer was found to impose the most substantial effect. The differential thermal movement between the spacer frame and the glass panels induces repeated shear and tension cycling, resulting in an increased leakage rate in IGUs, fatigue aging of edge sealants and a higher risk of water vapour diffusion.

The primary sealant will open up due to large deformation when the secondary sealant endures an excessive positive pressure differential between the air cavity and the environment. The tensile stresses applied on the secondary sealants and the elastic recovery was examined in laboratory (Wolf and Waters, 1993). Polysulfide sealant exhibited the highest temperature dependency in 25% tensile modulus and elastic recovery, while silicone sealant displayed the least.

The above presented studies have revealed that the fatigue aging of edge sealants due to repeated mechanical tensile and shear actions can potentially trigger various types of IGUs' failure. The structural performance of secondary sealants should be focused on, as it is responsible for maintaining overall structural integrity and air-tightness of IGUs. It has been reported that stresses generated in the secondary edge sealants are very sensitive to spacer configuration and material properties. Further studies are expected to explore the structural responses of secondary edge sealants under the combined actions

of wind loads, temperature-induced pressure in the air cavity, thermal-induced expansion of spacers, etc.

2.8 Material features and chemical composition of silicone insulating glazing sealants

The material properties of secondary edge sealant are an essential issue in assessing IGU qualities, as they determine a variety of important mechanical features i.e. tension and compression capacity, bonding function, environmental stability, elastic recovery, etc.

2.8.1 Comparison of material properties of secondary edge sealants

A variety of polymer materials have been employed as secondary sealant, such as polysulfide, polyurethane, hot melt butyl and silicone sealants (Schmidt, 1997). Wolf (1998) initiated a detailed investigation into the material properties of a variety of commercially available IGUs and the key material features are presented in Table 2- 3.

Table 2- 3. Key material features of various secondary sealants (Wolf, 1998)

Material property	**Polysulfide**	**Polyurethane**	**Silicone (alkoxy)**
Resistance of glass adhesion to sunlight	Good	Moderate	Excellent
Resistance of glass adhesion to water (Long-term exposure)	Good to moderate	Moderate	Excellent to moderate
Elastic recovery at			
23^{o}C	Moderate	Good	Excellent
60^{o}C	Poor	Moderate	Excellent
Change in Young's modulus with temperature	Very high	Moderate	Low
Water swelling	Very high	High	Low
Water-vapour permeability (3mm sheets)(g/m2d)			
at 20^{o}C	7 - 9	3 - 6	7 - 16
at 60^{o}C	40 -60	20- 30	40 - 100
Argon permeability (0.6 mm sheets) (10^{-10} cm2/(s cm Hg)	1.5 - 1.8	8 - 30	250 - 400
Water pick-up (weight %) of dual-sealed IGU	0.5 - 1.2	0.4 - 0.7	0.4 - 0.6
Gas loss (% per year) of dual-sealed IGU	0.4 -0.9	0.6 - 0.9	0.4 - 0.9

Silicone sealants are found to be superior in many aspects whereas the other two polyurethane-based secondary sealants are less satisfactory, with regard to elastic recovery especially at high temperature, water swelling, and temperature dependency of Young's modulus and the resistance of glass adhesion to sunlight and water. The only disadvantage is the high argon permeability; therefore it is not applicable to the noble gas-filled IGUs.

Around 67% of IGUs has adopted dual-seal systems globally according to the statistics in 2003, 12 % of which are sealed by silicone sealant (Wolf, 2003). Nowadays, silicone sealant occupied a higher proportion in the secondary sealant market employed in the modern IGU products (Dow Corning, 2013). The article also reviewed in particular the

chemical natures and the structural responses of silicone sealant. This literature review will focus on the chemical natures of secondary silicone sealants.

2.8.2 Chemical composition of silicone insulating glazing secondary sealant

The main constituent materials of silicone sealant include a base sealant and a cross-linking agent. The chemical backbone of silicone base sealant is a hydroxyl-ended polydimethylsiloxane (PDMS) as shown below in Figure 2- 5 (Klosowski, 1989).

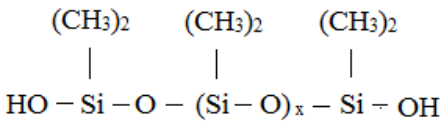

Figure 2- 5. Chemical formula of PDMS

The cross-linking agent tends to link the linear siloxane molecular chains together to create a net structure. Once the silicone sealant contacts the air, the cross-linking agent methyl triethoxysilane (MTEOS) reacts with the water in the air. The resulting product is a hydroxyl ended diethoxymethylsilane, which can react with the hydroxide siloxane and thus generate a long chain. The full cross-linking on each side of the methyl group of the backbone will eventually form a stable three-dimensional PDMA net structure. The mechanical properties of silicone, such as elastic modulus, strength, hardness and the elongation rate at the breakage point will change as the strong Si-O bonds in the cross-linking reaction are dramatically increased. The cross-linking reaction is illustrated by the following chemical formulae (Noll, 1968):

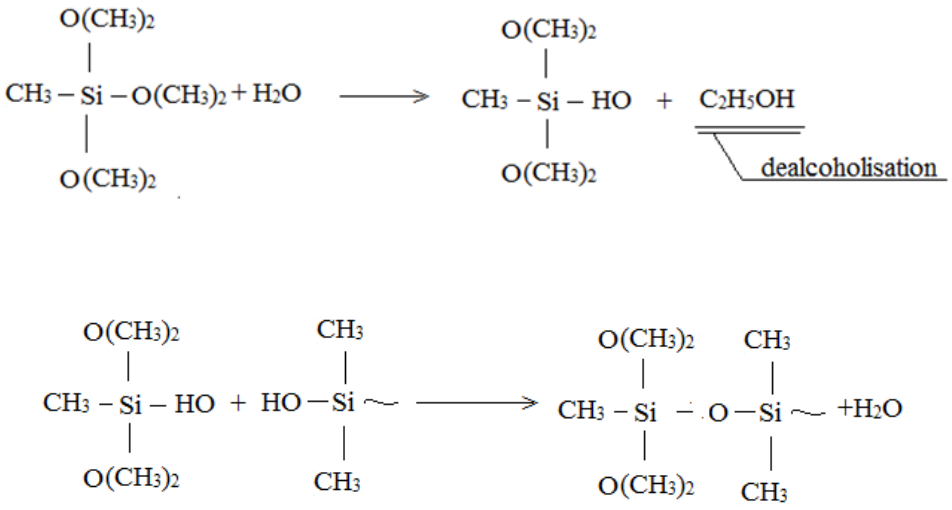

Figure 2- 6. Cross-linking reaction

In the formulation process, the release of ethanol is termed “dealcoholisation”. Silicone sealants can be classified into different types according to the side product in the cross linking reaction. The types of sealants used in this study are termed neutral silicone sealants as they do not release any aggressive products.

In the case of two-part products, atmospheric moisture is not needed to trigger the generation of cross-linking. Hydroxyl-ended polymer is contained in one component and the cross-linking agent alkoxysilane is in the other. The cross-link reaction starts as soon as two components are mixed. Catalyst and other additives are employed to help reaction to occur. For instance, the organotin can form a compound bond on the hydroxyl radical on the PDMAs, and thus reduce the electron cloud density of hydroxyl. In these conditions, the hydrogen ion in the hydroxyl radical will become very active and be more inclined to cross link. The catalytic process is illustrated below in Figure 2-7:

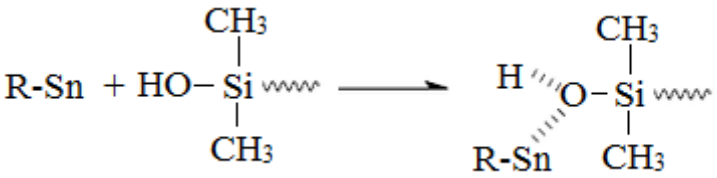

Figure 2- 7. Catalytic process

Compared to other types of secondary sealants, such as polysulfide sealant, silicone sealant performs with excellent elasticity and prior resistance against severe environmental attacks such as UV exposure or high temperature/ relative humidity (Garvin, 1995; Lawrence, 2007). These favourable features can be attributed to the molecular bonds that are different from the other adhesives. There is no unsaturated or weak bond found in the backbone of helical conformation of PDMAs. The bond energy of Si-O bond in PDMS is 425kJ/mol, which is much higher than S-S bond 264kJ/mol and C-S bond (289kJ/mol) in the polysulfide sealant (Wolf and Waters, 1993). When subjected to severe environmental actions, the Si-O bond is the least to break due to its higher bond energy and therefore provides a superior weather-proof feature. In addition, the methyl group on the Si-O bond can freely rotate, and hence leads to high flexibility of the silicone sealant in the macro-perspective (Clarson, 1993).

As a type of organic polymer material, silicone sealant adopted in IGUs is of typical hyper-elastic response, and therefore does not have a constant Young's modulus, as is revealed in the test. It is also observed that the stress-strain curve in the tensile test is different from compressive test (Wolf, 2004). Both tension and compressive test results are required in FEM modelling to describe the mechanical properties of the sealants. In order to better assess the mechanical performance of double glazing in the FEA modelling, sufficient physical attributes of the sealants should be measured in the laboratory.

2.8.3 Bonding mechanism

The key function provided by secondary silicone sealants is to hold together the IGUs' components, i.e., glass panels and the spacer bar. It is generally accepted the bonding action comprises two effects: adhesion and the cohesion, as illustrated in Figure 2- 8 (Adhesive and sealant Council, 2013).

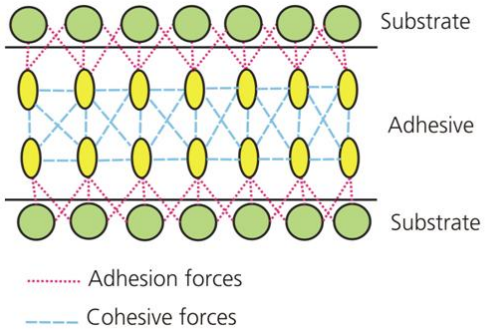

Figure 2- 8. Illustrative diagram of bonding interface (Adhesive and Sealant Council, 2013)

Regarding interfacial adhesion, a number of theories have been given to account for the adhesion phenomenon. Nevertheless, there is no generalised theory, since adhesion behaviour is found to exist between a large diversity of material combinations. In practice, the interfacial adhesion phenomenon is more likely to be a synergetic action of multiple driving forces introduced below.

Adsorption theory interprets adhesive forces by the Van der Waal's forces. The chemisorbed and physic-sorbed atomic and molecular groups are moving in the phase interface and the polar molecules/groups can be oriented in an ordered way.

In diffusion theory (Voyutski, 1963), the chemical chains in polymer sealants are characterised by considerable flexibility and are able to fully diffuse onto the interface

driven by Brownian movement. The theory emphasizes the entanglement of chemical chains due to mutual inter-diffusion phenomenon, as shown in Figure 2- 9.

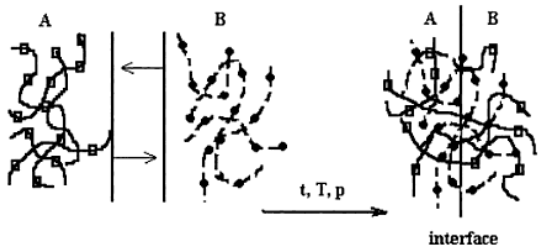

Figure 2- 9. Illustrative diagram of interfacial adhesion through diffusion (Kulshreshtha and Vasile, 2002)

Chemical bond theory indicates that the formation of chemical bonds on the interface can considerably enhance adhesion between two materials (Ahagon and Gent, 1975). However, it is not commonly observed in many substrate/adhesive bonding interfaces. The reported substrate/adhesive combinations with interfacial chemical bonds are silicone and glass, polyurethane and glass, epoxy resin and aluminium (Adhesive and Sealant Council, 2013) and zinc-copper alloy and vulcanized rubber (Kulshreshtha and Vasile, 2002).

Bond energy and length of chemical bonds and intermolecular interactions are listed and compared in Table 2- 4. It can be found that the bond energy of chemical covalent bond is distinctively higher than the other forces. Therefore the chemical bonds are deemed as the key force to guarantee the adhesion performance.

Table 2- 4. Bond length and energy comparison between bonding forces (Adhesive and sealant Council, 2013)

Type	bond length (nm)	bond energy (kJ/mol)
chemical covalent bonds	0.1-0.2	150-950

Van der Waal Forces	0.4-0.5	2-15
Hydrogen bonds	0.2	20-30

Cohesion refers to the internal cohesive forces of the sealant itself. Cohesion action is determined by: chemical bonds from cross-linking of polymer sealants; intermolecular forces between the molecules within the sealants; and the physical adhesion between the molecules within the sealants (Adhesive and sealant Council, 2013).

These findings suggest that the adhesion/cohesion behaviour of secondary edge sealants is a consequence of the molecular structures of polymer sealant, i.e. corresponding chemical covalent bonds. The chemical bonds within polymer sealants will rupture if subjected to higher energy than its own bond energy. The higher energies come most likely from external ambient actions, like high temperature, high humidity or UV exposure. Adhesion and cohesion performances should be examined in the laboratory by conducting various aging tests.

2.9 Introduction and developments of vacuum glazing units (VGUs)

A new emergent glazing technology, the vacuum glazing unit (VGU), is believed to provide a possible solution to further reduce the U-values of windows. By utilising the same mechanism as a thermos flask, an almost vacuum cavity of a very low pressure typically below 10^{-6} of atmosphere pressure (Collins and Simko, 1998), is realized to minimise the heat transfer through conduction and convection. The first idea of a VGU was proposed by Zoller in 1913 and documented in his patent in 1924 (Zoller, 1924). However, no significant progress was made to commercialise this type of novel glazing until 1990s. In early 1990s, a batch of solder-glass-sealed vacuum glazing samples of 200mm × 250mm were successfully fabricated in the laboratory of Sydney University

by Collins and his research group. The basic manufacturing process was specified in detail (Garrison and Collins, 1995).

Nowadays, a typical vacuum glazing unit (shown in Figure 2- 10) consists of two glass panels, separated by a narrow evacuated gap. An array of small high strength metal or ceramic support pillars are placed between two glass plates to maintain their separation under the barometric pressure. The internal space between the glass panels is evacuated through a small pump-out tube, and the internal outgas process is conducted by heating to temperatures up to 200^{o}C. A small piece of degasser is placed in the tube in order to absorb the inner gas generated during service life. Water vapour within the cavity of a VGU will occur when experiencing thermal cycling (Lenzen et al., 2003), and CO/CO_2 will be generated when it is subjected to external excitation (Minaai et al., 2005). The structure is completely sealed by melting the end of the pumping tube and the solder glass powder at the edges with heating the entire structure to a temperature of about 450 ^{o}C (Collins and Simko, 1998).

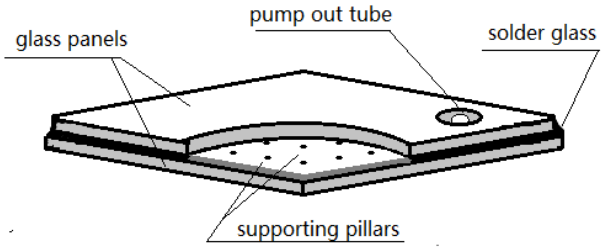

Figure 2- 10.Schematic graph of vacuum glazing

A great number of commercial VGUs have sprung up rapidly across the world. One Japanese company, Nippon Sheet Glass (NSG), firstly industrialised VGU in 1997 and

successively established two assemble lines with an annual output of 100,000m^2 and 500000m^2. The brand Pilkington Spacia, Spacia II and Laminated Spacia developed by NSG are currently commercially available (NSG, 2011). The USA Guardian Industry Corporation has started its market on VGU, by taking advantage of an outstanding Low-E coating technique and translucent ceramic pillars (Guardian, 2009). The Chinese company Synergy, founded in 1998, has commercialised VGUs and composite VGU i.e. vacuum glazing incorporated in a double glazing up to a total of 500,000 m^2 annually. The products can guarantee half-tempered VGU products with a U-value of 0.3 to 0.6$Wm^{-2}K^{-1}$ (Tang, 2011).

2.10 Serviceability and durability performance of VGUs.

Vacuum glazing technology is generally deemed as one of the alternative solutions of conventional IGUs (Van Den Bergh, et al., 2013). However, VGUs have not been generally accepted as a type of commercially available security glazing profile, as the bulk strength is much lower than other conventional glazing profiles. The University of Sydney, acting as a pioneer, published a series of research on the thermal resistance and the structural challenges of VGUs in early 1990s. They subsequently initiated a series of comprehensive studies on the design optimisation and performance degradation (Collins, 1991, 1992, 1998; Garrison, 1998). The failure mechanisms were discussed and the design criteria of VGUs were established based on thermal transmittance requirements and the maximum allowable stresses occurring in different parts of VGUs. The work is partly associated with the University of California sponsored by the US Government. Ulster University and Warwick University are keenly investigating the thermal performance of VGUs (Fang and Eames, 2006; Fang et al., 2006; Fang et al., 2009; Manz, 2008), and have developed the first VGU fabricated by low temperature metal-

sealing technology (Griffiths et al., 1998; Hyde et al., 2000; Wang et al., 2007). Manz et al. in the Swiss Federal Laboratories for Materials Testing and Research (EMPA) have also conducted a number of analyses on the heat transfer through VGUs and triple VGUs and on the temperature-induced stresses by means of numerical tools.

In this section, a diversity of studies on the thermal insulation performance, structural responses, and the design methods are reviewed, in order to obtain a comprehensive understanding of the functional and structural limits of VGUs.

2.10.1 Thermal analyses

Theoretical analysis

The University of Sydney proposed theoretical equations to calculate the thermal conductance of VGUs (Collins and Simko, 1998). The centre-of-glazing heat conductance of VGUs designed by the University of Sydney can be reduced to as low as 0.85 to 1$Wm^{-2}K^{-1}$ with low-E coatings (Garrison and Collins, 1995). The overall heat transfer process was analysed in terms of radiative heat transfer, conduction through low pressure gases, conduction through the pillars and heat conduction at the edges. The well-established theory of heat transfer can be employed to calculate the thermal conductance of each part (Holman, 1981):

The conductance due to radiative heat transfer between two glass panels can be written in (Collins and Robinson, 1991)

$$C_{rad} = 4\sigma T^3(\varepsilon_1^{-1} + \varepsilon_2^{-1} - 1)^{-1} \qquad 2\text{-}5$$

where σ is the Stefan-Boltzmann constant; T is the average temperature between two glass panels; ε_1 and ε_2 are the emitting coefficients of two glass panels.

The conductance of conductive heat transfer through low pressure gases in the vacuum cavity can be expressed as (Collins et al., 1992):

$$C_{rad} = \alpha\left[\frac{\gamma+1}{r-1}\right]\left[\frac{R}{8\pi MT}\right]^{0.5} P \qquad 2\text{- }6$$

where α is a combined accommodation coefficient of the gas molecules on two glass surfaces (Collins, 1992); γ is the specific heat ratio of the gas, P is the gas pressure; M is the molar weight of the gas; R is the molar gas constant.

The heat conduction of a pillar array can be derived from the sum of all individual pillars. The conductance can be written in

$$C_{pillar} \approx \frac{2Ka}{\lambda^2(1+2h/\pi a)} \qquad 2\text{- }7$$

where K is the thermal conductivity of the pillar; a and h is the radius and the height of the pillar. Collins and Simko (1998) draw the conclusion that a uniform slab of material with a proper thermal conductance is a good approximation of the array of discrete pillars in general thermal analysis.

Numerical analysis

Manz (2008) also quantified the heat transfer process through VGUs and presented the possibilities and limitations of reducing total heat transfer based on both theoretical and numerical approaches. In order to further improve the thermal insulation, Manz and his group set out to explore the theoretical heat conductance in a triple VGU. An innovative design of triple vacuum glazing is patented by Wuethrich (2005) by using thin wires in the evacuated cavity to support the glass panels. The heat loss via supporting pillars can be hence reduced to the least. Ulster University (Fang and Eames, 2006; Fang et al., 2006; Fang et al., 2009; Manz, 2008) published a series of papers on the thermal

performance of VGUs in respect of numerical modelling. Two-dimensional and three-dimensional thermal modelling was compared and a less than 3% difference was found achievable (Fang et al., 2009). The thermal performance of low-E coated triple VGUs were estimated by FEM modelling (Fang and Eames, 2006). The U-value measured at the centre of this triple VGU profile can be reduced to less than 0.2 $Wm^{-2}K^{-1}$.

Experimental analysis

To further assess the thermal performance of VGUs, laboratory work was also carried out. Fang et al. (2009) undertook extreme thermal cycling tests of vacuum glazing, so as to analyse the thermal degradation of VGUs. Ng et al. (2006) investigated the relation between sunlight radiation and the inner pressure. It was observed that the samples' pressure increased when exposed to the sunlight. Furthermore, the major gas released inside was identified to be CO_2 and CO rather than water vapour. A high temperature outgassing technique is suggested to improve the stability of thermal insulation. Lenzen and Collins (1997) published a group of one-year long term field experimental data, in order to explore the practical viability of VGUs as an application to thermal-insulation window. The VGUs were exposed to the sunlight, water vapour and periodic temperature change. The in-situ results indicated an extreme temperature differential of 60K that VGUs may experience in practical application. It is also observed that the U-value degradation of VGUs was caused by the increased inner pressure, and was strongly dependent on environmental variations. Under severe temperature variation, water vapour in the evacuated cavity would be generated and lead to pressure increase.

The heat transport processes through different paths in VGUs was quantified. Heat transfer by convection and gaseous conduction becomes negligible where the cavity has

been evacuated to a very low level (Manz, 2008). Therefore the supporting pillars and the edges are the predominant heat transfer paths.

The above studies suggest a number of solutions to improve the thermal performance of VGUs:

1. Application of low-E coatings on glass surfaces so as to minimise heat radiation
2. Adoption of triple VGUs by providing an additional evacuated cavity
3. Adoption of an effective outgassing technique so that the pressure level within the evacuated cavity remains low
4. Reduction in the amount and dimension of supporting pillars in order to cut down the heat conduction through the pillars

Therefore more studies on the design of pillar array incorporated in VGUs are necessary, as the pillar array not only influences the thermal performance, but more substantially, contributes to the overall structural integrity of VGUs. The employment of a high number of pillars within VGUs can effectively reduce the stress concentration in VGUs adjacent to the pillars, whereas undermine the thermal insulation effect because of greater heat transport through the pillars. A trade-off between the thermal insulation performance and structural safety concern should be considered in the design of supporting pillars.

2.10.2 Structural analyses

Compared with conventional IGUs, VGUs are more susceptible to environmental actions like wind load or temperature-induced loads during the service life. Severe stresses induced in the VGU because of the evacuated cavity are a pressing challenge in terms of the durability of VGUs. As the tests carried out in a previous study (Liu, 2009) indicated, the bending strength of vacuum glazing units is only 40% or 50% of that of

normal monolithic glass panel. The low strength of VGUs has become a hindrance factor from replacing conventional glazing with VGUs.

Stresses induced by atmospheric pressure/pressure change

Atmospheric pressure can even impose intensive loads onto VGUs. This is because the interlayer cavity is in almost vacuum state, i.e. below 10^{-6} of atmospheric pressure (Collins and Robinson, 1991; Collins et al., 1992; Collins and Simko, 1998). VGUs will undergo severe stresses under atmospheric pressure. Collins et al. (1995) summarised four parts in VGUs that experience large stresses due to atmospheric pressure that lead to their mechanical failures as shown in Figure 2- 11. Tensile stresses are found adjacent to the pillars and outside above the pillars and near the edge seals. Compressive stresses are observed in the supporting pillars.

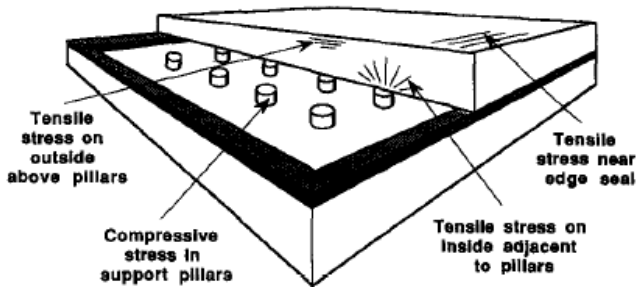

Figure 2- 11. Schematic diagram of a VGU showing regions of stresses under atmospheric pressure (Collins and Simko, 1998)

The tensile stresses on the external surface of the glass panel above the supporting pillar are due to the glass bending inward over the pillars, which is caused by the atmospheric pressure. The stress was studied by Fischer-Cripps et al. (1995) by employing the finite element method. An analytical solution (Collins and Fischer-Cripps, 1991) was used to provide good validation to the FEM modelling. The analytical method assumed a unit of

pillar/glass area of VGUs to be a typical Timoshenko thick plate model with built-in boundary condition and subjected to a central force. The results demonstrated that the maximum tensile stress on the outside pressured surfaces is a function of thickness of glass and the distance of pillar separation, whereas independent of the pillar radius. Eq. (2- 8)

$$\sigma_{\max} = \pi q \lambda^{*2}(1+v)\{0.485\ln(\lambda / 2h) + 0.52\} / 4h^2 \qquad 2\text{- }8$$

where σ_{max} is the maximum tensile stress (MPa), v is the Poisson ratio; h is the thickness of glass panel (mm), λ^* is the pillar separation (mm).

When subjected to atmospheric pressure, the supporting pillars will be pressed into the glass surface. Inner stresses induced by the pillar indentation can be well described by Hertz theory (1896). This type of mechanical action will lead to the formation of a conical crack near the contact zone. The critical indentation load that triggers the first conical crack can be explored via Auerbach's empirical equation, which indicates a linear relation between the critical indentation load and the radius of spherical indenter (Auerbach, 1891). Collins and Fischer-Cripps (1991) provided an alternative derivation of Auerbach's equation which can be applied to the conventional cylindrical pillars. By combining the experimental data presented by Langitan and Lawn (1969) and Mouginot and Maugis (1954), a quantitative relation between the pillar radius and the pillar separation was hence determined in Eq. (2-9).

$$\lambda^* = 155\bar{a}^{3/4} \qquad 2\text{- }9$$

where $\bar{a}$ is the radius of cylindrical supporting pillar.

The stresses near the edge seal were normally studied in association with the compressive stresses in supporting pillars (Collins and Simko, 1998). It was observed that a number of manufactured VGUs failed due to the delayed propagation of cracks

near the edge seal (Collins et al., 1995). The fracture is attributed to excessive glass bending near the edge seal, which is caused by the non-recoverable deformation of the supporting pillar when undergoing the first evacuation process. Therefore supporting pillars with sufficient strength are required.

Stresses induced by bending behaviour (Temperature differential/ wind load)

The bending stresses and deflections in the glass will take place at the sealed edges when experiencing a temperature differential between two glass panels. It was indicated that the external side of the hot panel was in tension and the internal side is in compression. Stresses of the opposite sense were in the cold glass panel (Collins and Simko, 1998). In the latter, the position most likely to fracture due to excessive bending stress was stated to be the external surface of hot glass panel. A simple model was proposed to analyse the unconstrained VGU model with uniform temperature distribution in each glass panel (Collins et al., 1995). Collins and Robinson (1991) developed an analytical model to describe the bending stresses on VGU due to temperature difference accompanied by the bending effect caused by atmospheric pressure and internal localised reaction forces.

Shear forces generated at the edges were particularly calculated.

$$S / t = \alpha E \Delta T / 2(4 - 3\nu^2) \qquad 2\text{- }10$$

where S is shear force generated at edges; ΔT is the temperature differential; α is thermal expansion coefficient. E and ν are the Young's modulus and Poission ratio of glass respectively.

Simko et al. (1998) summarised various temperature-induced stresses and particularly analysed the mechanical constraints of the bonded edge seal and the influences from the

frame design. A complicated non-uniform temperature field was implemented in the numerical simulation with experimental good validation. It was found that window frames can effectively reduce the bending stresses near the edge seal, however the stresses at the corners were increased. Wullschleger (2009) conducted static non-linear finite element analyses to investigate the temperature-induced deflection of vacuum glazing. The parametric studies on the transverse stiffness of pillar array were further carried out to study the pillars' impacts on the physical behaviour of VGUs.

Researchers have examined the stresses caused on the seal edges, pillars and the corners of VGUs when subjected to the external loads by means of theoretical equations and numerical tools. The existence of supporting pillars and soldered glass edges causes most of high-stress parts in VGUs.

2.10.3 Design concerns and developments of VGUs

The load capacity of VGUs can be enhanced in two perspectives: to improve the glass strength adopted in VGUs, and so to reduce the possibility of fracture failure when experiencing severe stress concentrations. The other perspective is to optimise the distribution of supporting pillars, so that it can both provide adequate structural loading resistance and satisfy thermal requirement. Studies will be reviewed in terms of two aspects.

Low temperature sealing technique

It was reported that the sealing temperature at high temperature contributed to a more stable glazing performance than a lower temperature, when subjected to accelerate testing (Ng, 2006). However, a high sealing temperature would undermine the strength of glass sheets, as fully tempered glass would deteriorate above 575 ^{o}C (Eames, 2008).

Furthermore, soft low-E coatings cannot be employed in the VGUs unless the fabrication temperature is reduced to less than 200^{o}C due to coating degradation (Griffiths et al., 1998; Hyde et al., 2000; Wang et al., 2007). The University of Ulster devoted great efforts to develop low temperature edge seals that avoid temper loss and the restrictions of soft coatings. Indium and indium alloy were introduced, acting as a glass bond, combined with a resin seal to ensure moisture tightness (Griffiths et al., 1998). This type of edge seal was found to enable the VGU production at a temperature less than 160^{o}C and the removal of the pump-out tube. A research group in the University of Warwick launched an experimental and theoretical study on the durability of the VGUs produced at low temperatures. Temperature-induced stresses and deflections were particularly addressed by means of detailed FEA models and weather cycling tests. The VGU fabricated with an indium-based edge seal was reported to have good resistance under severe winter conditions (Manz et al., 2006).

Pillar design constraints

There is no generalised international/EU standard for the design of VGUs. The University of Sydney did a trade-off between the maximum allowable stresses and acceptable thermal conductance by proposing four design criteria for the pillar design of VGUs (Collins, et al., 1992; Collins and Robinson, 1991; Collins and Simko, 1998; Collins, et al.,1995; Fischer-Cripps et al., 1995). The optimal design range can be determined by combining these design constraints as illustrated in Figure 2- 12. An acceptable pillar separation and pillar radius can be obtained satisfying all these design constraints. This design method was successively applied by Manz et al. (2006) in his design work on triple VGUs.

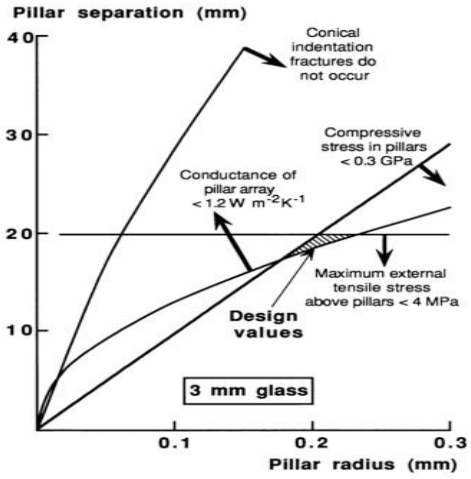

Figure 2- 12. Design range (hatched zone) of pillar array obtained by combining four concerns (Collins and Simko, 1998)

The design range will vary in terms of different VGUs construction. It is noted that the conical indentation fracture criteria was based on a specific group of experimental results (Fischer-Cripps, 2007), regardless of the variations caused by different glass surfaces, indenter geometry and its material properties. Further investigations would help to better understand the relationship between various designs of supporting pillars and conical crack failure.

2.11 Summary

An extensive literature review of two types of energy-efficiency glazing profiles: IGUs and VGUs have been presented. The main findings and needs through this chapter are summarised as follows:

The service life and failure mechanisms of IGUs have been studied by both long term in-situ monitoring and short-term accelerated tests aligned to national standards. A great number of studies have pointed out that the pre-mature failure of IGUs is predominately caused by the functional failures, i.e. the fogging

phenomenon due to the excessive moisture infiltration and the consequent U-value degradation. Existing regulations/standards adopt accelerated high temperature/relative humidity cycling tests to assess IGU quality by calculating the fogging probability, but it does not provide an insight into the fogging failure mechanisms. Among the lengthy durability assessments presented in previous studies, there is a close correlation between different failure modes: the loss of the bonding function of edge sealants could result in excessive moisture ingress, U-value degradation, gas leakage and even glass breakage failure. Therefore the performance of edge sealant to a great extent determines the quality of IGUs, and should be underlined in this thesis.

Edge sealants have to undergo both physical actions and chemical attacks induced by environmental impacts. In terms of mechanical actions exerted on IGUs, temperature differential and uniform external loading such as wind load are the two most frequent environmental impacts that installed IGUs may encounter. The combined environmental actions impose a synergic action upon IGUs. Also, the mechanical behaviour of each component of IGUs will exert an interactive effect on overall structural responses. A number of analytical methods have proposed the mathematic equations to describe load transferring from one glass panel to both the deformed air and the other glass. However, there is a lack of thorough coupling investigations by means of numerical simulation. FEM simulation should be developed in order to give a full account of various boundary conditions and the local edge sealant, which cannot be achieved by analytical methods.

The physical attributes and corresponding mechanical behaviours of edge sealants are found to be drastically affected by environmental conditions in manner of chemical reactions. A number of prevailing bonding theories are reviewed to explain the bond mechanism between the edge sealants and the glass surface. The chemical and physical properties of a variety of secondary sealants have been compared. Silicone sealant has exhibited excellent physical attributes comparing with various commercial popular secondary insulating sealants, i.e. high stability, lowest dependency on environmental actions and superior elastic recovery. These beneficial features are attributed to the high bond energy of Si-O bonds. It was reported (Wolf, 1992) that the combined effects would contribute to a much higher loading level on the edge seal rather than simply cumulative effects of each single action. Therefore it is worthy further laboratory investigation on the material properties and aging behaviours of silicone sealants.

The research scope of the IGU analysis in this thesis is highlighted in Figure 2-13.

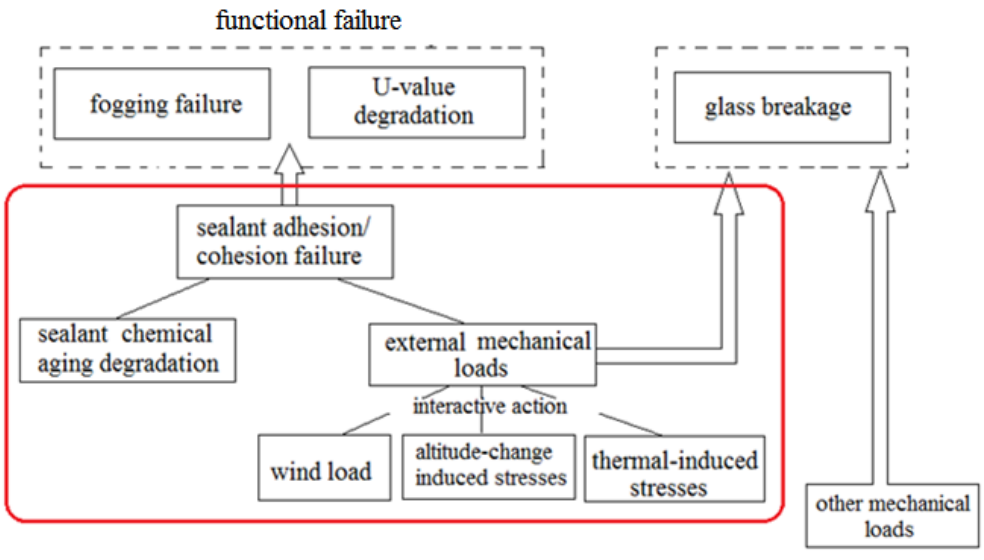

Figure 2- 13. Correlation between external environmental impacts and failure modes

With respect to VGUs, extensive studies have been carried out in both thermal and structural aspects. The U-value of VGUs can be effectively reduced to a much lower level than IGUs because of the evacuated cavity. In terms of structural performance, the interaction between the glass panels and the interlayer air does not exist since the cavity is in nearly vacuum state. However, VGUs have to encounter with greater stresses compared to the IGUs exposed to the same loading level of atmospheric pressure, temperature differential or wind load. To date there is no generalised standard/specification in Britain for the design of VGUs. The University of Sydney proposed a design restriction to determine the appropriate pillar radius and pillar separation by making a trade-off between major stress concentrations caused in the VGUs and the acceptable heat conductance of the pillar array. Nevertheless, the contact damage due to pillar indentation is underestimated in this design approach, and the criterion of conical crack was derived from only one group of spherical indentation test. Further exploration on the indentation contact damage with various supporting pillars is imperative.

Low strength has impeded VGUs' commercialization in the current energy-efficiency glazing market. To improve the load capacity of VGUs is a major concern in future designs. New technique such as low-temperature sealing method has been verified to allow tempered glass panels in VGU manufacturing and hence considerably improve the overall strength. Nevertheless, the high cost of low-temperature sealing technique may hinder its development in practical application. Therefore economical and effective methods to enhance the structural performance of VGUs are expected.

CHAPTER 3. STRUCTURAL PERFORMANCE OF INSULATING GLAZING UNITS (IGUS) UNDER INTERACTIVE ENVIRONMENTAL ACTIONS

3.1 Introduction

During the service life, IGUs will endure a multitude of actions caused by a large diversity of environmental factors, which impose great threats to their durability. Dramatic changes in temperature and barometric pressure due to changing environmental conditions and wind loads are deemed as the most common environmental actions on IGUs.

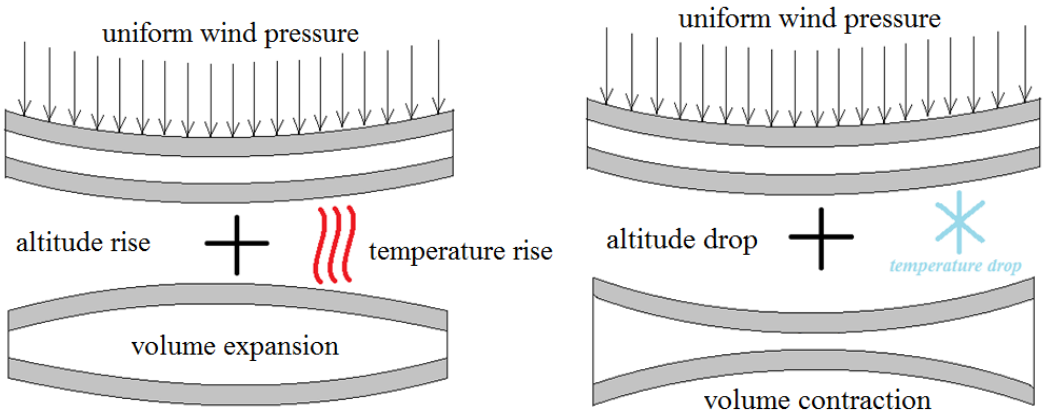

Figure 3- 1. Schematic diagram of the combination of thermal effect and wind load

The combination of thermal/barometric-wind load can be illustrated in Figure 3- 1. When the ambient temperature increases, the enclosed air will expand and glass panels will bend outward. The deflection of the glass panels will further result in a change in the air volume and then a pressure change inside the air space. Moreover, the change in altitude also results in an internal pressure change of IGUs.

In engineering practice, it is common to consider that a wind load applies to the glass panel at the outdoor side, and the pressure load is transferred to the indoor side via the

change of the pressure within the air cavity. When the wind load is applied together with the abovementioned actions due to temperature/altitude change, the effect becomes coupled. The external actions combined with induced internal actions will cause undesirable bending stresses and deflections in IGUs.

In this chapter, the interactive actions of the change in temperature and pressure differences and wind load will be studied. Commercial FEA package ABAQUS 6.12 is employed to carry out a series of numerical simulations. The numerical models will be validated by: 1. Boyle's law for gas 2. Nonlinear analytical equations for the bending behaviours of monolithic glass panels. The validated numerical models will be used to examine the additional parameters proposed in the draft European standards prEN 13474-2 and prEN 16612 that are used to calculate the load shares in IGUs. Four point supported boundary condition will be considered, and the nonlinearity intensity will be discussed in details.

The layout of this chapter is given below:

Section 3.2 introduces the current European standards for the design guidance of IGUs. Section 3.3 gives a detailed description of the FEM numerical method. Section 3.4 discusses the size sensitivity of IGUs under different combinations of thermal-mechanical loads. Section 3.5 proposed new design parameters for four point supported boundary condition.

3.2 Guidance code for glass design

prEN 13474-2 (2002) is the draft European standard, providing an evaluation method of the environmental influences acting upon flat glass panels. The recent published draft standard prEN 16612 (2013) updated the coefficients in the calculation for the

maximum stresses and deflections of rectangular IGUs. When establishing the design loads, the self-weight, wind load, snow loads and the internal pressure caused by temperature change, altitude change and other external loads are considered. There are two limit states that need to be examined for conventional flat glass panels, i.e. ultimate limit state (ULS) and serviceability limit state (SLS). ULS refers to the severe states that may endanger the safety of users, like glass breakage due to external actions. SLS accounts for the damage to IGUs due to internal actions and excessive deformations or deflections that affect the appearance or effective use of the glazing.

3.2.1 Determination of loads due to environmental actions

Wind load

Wind load is deemed as a uniformly distributed pressure applied on the glass surface. In this section it is considered as a static load. According to BS 6262, a minimum wind loading of 600Pa should be at least considered in any location. A simplified method to obtain the design wind loading for the site is provided for the glazing installed building lower than 15m in overall height.

$$F_A = (1 + \frac{H_A \cdot F_T}{1000})^2 \qquad 3\text{- }1$$

where H_A is the altitude of the site in metres; F_T is the topographical factor. If the result loading is less than 600Pa, then a value of 600Pa is used. When the site condition does not satisfy the limit of the abbreviated method, full considerations should be taken. The design wind load is classified by three parameters: the site terrain conditions, wind speed and the height of the building in BS 6262. However, there is no mathematic equation that estimates multiple environmental actions quantitatively.

Pressure caused by altitude change

The draft standard prEN 13474 (2002) gives a simple method to calculate the cavity pressure increase due to the altitude change.

$$p_{H;0} = C_H (H - H_p) \qquad 3\text{- }2$$

where $p_{H;0}$ is the isochoric pressure due to altitude effects (kPa/m), C_H = 0.012kPa/m, is the rate of decreases of atmospheric pressure altitude, H is the altitude of the place of use of an IGU; H_p is the altitude of production of an IGU.

Pressure caused by thermal expansion/contraction

$$p_{C;0} = C_{\mathrm{T}}(T - T_p) - (p - p_P) \qquad 3\text{- }3$$

where C_T = 0.34 kPa/K, is the rate of increase of isochoric pressure with temperature, p and T are the meteorological pressure and temperature of the sealed gas in use, p_p and T_p are the meteorological pressure and temperature of the sealed gas at production.

The steady cavity temperature T_c can be calculated by following equations (BSI, 2013):

$$T_c = \frac{T_{g;ext} + T_{g;\mathrm{int}}}{2} \qquad 3\text{- }4$$

where, $T_{g;ext}$ is the external temperature of glass, $T_{g;int}$ is the internal temperature of glass. The two coefficients can be expressed as follows:

$$T_{g;ext} = \frac{\varphi_{\mathrm{e}}\alpha_{e1}(k_i + k_S) + \varphi_{\mathrm{e}}\alpha_{e2}k_S + k_e(k_i + k_S)T_{ext} + k_i k_s T_{\mathrm{int}}}{k_e k_i + k_e k_s + k_i k_s} \qquad 3\text{- }5$$

$$T_{g;\mathrm{int}} = \frac{\varphi_{\mathrm{e}}\alpha_{e1}k_S + \varphi_{\mathrm{e}}\alpha_{e2}(k_i + k_S) + k_i k_s T_{ext} + k_e(k_i + k_S)T_{\mathrm{int}}}{k_e k_i + k_e k_s + k_i k_s} \qquad 3\text{- }6$$

where k_e is the external heat transfer coefficient; k_i is the internal heat transfer coefficient, k_s is the thermal conductance of the gas spaces; The definitions of these

coefficients are presented in BS EN 673 (2011). α_{e1} and α_{e2} are the solar direct absorptance of two panels, determined in BS EN 410 (2011). The calculation equations are only applicable for the IGUs without blind or backup (BSI, 2013).

A simplified evaluation method is provided in prEN 13474-2 (2002) as reference, in case the values for the temperature-induced loads or the altitude-induced loads cannot be specified.

Table 3- 1 Simplified values of internal loads for summer and winter conditions

Condition	Isochoric pressure (kPa)		
	Climatic action $p_{C,0}$	Altitude action $p_{H,0}$	
		For use up to 400m altitude	For use up to 700m altitude
Summer	12.0	3.6	8.4
Winter	-15.0	-3.6	-8.4

The combination of the environmental actions

The combined design load is obtained by combing the effects of each environmental action by using following rules (BSI, 2002):

$$F_d = \sum_{j\geq 1} \gamma_{G,j} G_{K,j} + \gamma_{Q,1} Q_{K,1} + \sum_{i>1} \gamma_{G,i} \psi_{0,i} Q_{K,i} \qquad 3\text{- }7$$

$G_{K,j}$ is the characteristic value of the permanent action,; $Q_{K,1}$ is the characteristic value of one of the variable actions; $Q_{K,i}$ is characteristic value of the other variable actions; $\gamma_{G,j}$, $\gamma_{Q,1}$, $\gamma_{Q,i}$ are the partial factors for permanent actions, one of the variable and the other variables respectively; $\psi_{0,i}$ is the combination factor.

For IGUs, the interaction of the panels should be considered in the design load equation. One additional parameter "insulating unit factor" ϕ is introduced:

$$\phi = \frac{1}{1+\left(\frac{a}{a*}\right)^4} \qquad 3\text{- }8$$

where a is taken as the shorter dimension of an IGU; a* is the characteristic length of the unit as defined in Eq.(3-9):

$$a* = 28.9\left(\frac{s h_1^3 h_2^3}{\left(h_1^3 + h_2^3\right) k_5}\right)^{0.25} \qquad 3\text{- }9$$

where h_1, h_2 are the thicknesses of the outer-panel and inter-panel; s is the width of the air cavity; k_5 is a dimension parameter, which will be introduced in the next section.

3.2.2 Design of load bearing capacity

The load share on each glass panel when subjected to a uniform external pressure load is outlined in Table 3- 2.

Table 3- 2. Load share for external loads (prEN 16612, 2013)

Load	Share of load carried by panel 1	Share of load carried by panel 2
External load F_d acting on panel 1	$F_{d;1} = (\delta_1 + \phi\delta_2)F_d$	$F_{d;2} = (1-\phi)\delta_2 F_d$
External load F_d acting on panel 2	$F_{d;1} = (1-\phi)\delta_1 F_d$	$F_{d;2} = (\phi\delta_1 + \delta_2)F_d$

For ease of reference, the load receiving panel is denoted as panel 1 and the other panel is named panel 2 in the following discussions.

$$\delta_1 = \frac{h_1^3}{h_1^3 + h_2^3}, \qquad \delta_2 = \frac{h_2^3}{h_1^3 + h_2^3} \qquad 3\text{- }10$$

Where, h_1 and h_2 are the thicknesses of panel1 and panel 2 respectively.

For the four-edge supported rectangular glass panels, following equations are given to determine the maximum stress σ_{max}, maximum deflection ω_{max} and the change in volume V:

$$\sigma_{\max} = k_1 \frac{a^2}{h^2} F_d \qquad 3\text{- }11$$

$$\omega_{\max} = k_4 \frac{a^4}{h^3} \frac{F_d}{E} \qquad 3\text{- }12$$

$$V = k_5 \frac{a^4}{h^3} \frac{F_d}{E} ab \qquad 3\text{- }13$$

The dimensionless coefficients k_1, k_2, k_4, and k_5 are specified in prEN 13474-2 for different aspect ratio λ and varying normalised load p^*, which is defined as below:

$$p^* = \frac{a^4}{h^4} \frac{F_d}{E} \qquad 3\text{- }14$$

It is observed that p^* is a function of the design load F_d. For small deflections bending, namely linear analysis, the value p^* is taken as 0. Therefore the dimensionless geometric coefficients are not dependent on the design load F_d. For large deflection cases, the normalised load-dependent geometric coefficients contribute to the nonlinearity in the equations.

3.3 FEM hydrostatic fluids analysis

Considering the hermetic air cavity of IGUs, hydrostatic fluid analysis is employed to simulate the interaction between glass bending and the deformation of sealed air.

3.3.1 Hydrostatic Fluid Analysis

Hydrostatic fluid analysis provided in the FEA software ABAQUS is to predict the mechanical response of a fluid filled or gas filled structure. Yuan (2009) employed this method to successfully analyse a vehicle air spring. In this study, the air sealed in the IGU can be deemed as the ideal gas, and modelled with pneumatic fluid elements by satisfying Boyle's law for gas, described by Eq (3- 15) (Hibbitt et al., 2007):

$$\frac{\tilde{p}V}{\theta - \theta^{z}} = nR \qquad 3\text{- }15$$

where $\tilde{p}$ is the total fluid pressure; V is the air volume; θ is the temperature; θ^{z} is the absolute zero on the temperature scale being used; n is amount of substance and R is the ideal gas constant.

Since the air is sealed in the cavity and the air mass is considered fixed, the air volume can be taken as a function of the pressure and the temperature shown in Eq.(3 -16):

$$V_c = \overline{V}(p,\theta) = \frac{m}{\rho(p,\theta)} \qquad 3\text{- }16$$

where V_c is the actual volume of air cavity, $\overline{V}$ is the calculated air volume, p is the air pressure, θ is the air temperature, m is the total mass of air, ρ is the air density. The density of the air in the cavity can be calculated as Eq. (3- 17):

$$\rho(p,\theta) = \rho_R \frac{(\theta_R - \theta^Z)(p + p_A)}{(\theta - \theta^Z)(p_R + p_A)} \qquad 3\text{- }17$$

where θ_R and p_R are the reference temperature and pressure, ρ_R is the reference density, θ^Z is the temperature at absolute zero, and p_A is the ambient pressure.

Thus the corresponding volume-pressure compliance is obtained in Eq.(3- 18):

$$\frac{d\overline{V}}{dp} = -\frac{m \cdot d\rho}{\rho^2 \cdot dp} = -\frac{m}{\rho_R} \frac{(\theta - \theta^Z)(p_R + p_A)}{(\theta_R - \theta^Z)(p + p_A)^2} \qquad 3\text{- }18$$

In the modelling, the reference temperature, pressure and density are required to be supplied a priori. A reference node is set in the middle of the air cavity, used to calculate the overall volume change. In using this model, a uniform temperature is assumed in the air cavity.

3.3.2 Geometry of numerical model

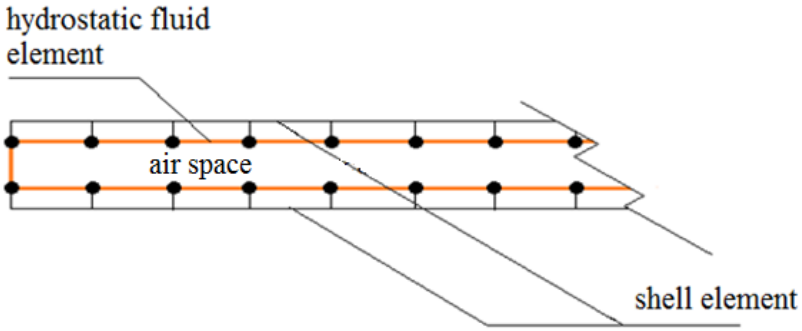

Figure 3- 2. Schematic diagram of the simplified model

Hydrostatic fluid analysis only allows for the models to be fully hermetic fluid-filled cavities. However, to precisely simulate the complicated seal system in the full model requires expensive computation resources even in elastic linear analysis. In this section, a simplified model as shown in Figure 3-2 is proposed to particularly investigate the mechanical behaviour of glass panel. In order to facilitate the computation load, the details of seal system are not simulated but replaced with normal shell elements. In this study, IGUs are square-shape with the length from 500mm to 2500mm. the cavity width is 12mm. The thickness of the glass is 6mm.

3.3.3 Material property

The material properties of glass panels are given: Young's modulus E = 72000MPa, Poisson ratio $\nu = 0.22$. As introduced above, the edge seal system is not considered in the model so the material properties of sealants, aluminium spacer and desiccant will be not applied to the edges.

3.3.4. Element type

Glass panel

The glass panel can be deemed as a discrete Kirchhoff thin shell, as the thickness to width ratio is far less than 0.1. In the numerical modelling, shell elements S4 are adopted to simulate the glass panels, which feature fully integrated, finite-membrane-strain shell elements (shown in Figure 3-3). It has three translational and three rotational DOFs (degree of freedom). S4 element is not sensitive to element distortion, and effectively avoids parasitic shear locking that often takes place in first-order fully integrated solid elements when the panel experiences bending (Hibbitt et al., 2007). S4 element is suitable for the nonlinear large-deflection analysis, as the finite membrane strain is taken into account, which will have predominant role in the non-linear behaviour. Besides, this type of element also allows the change in thickness with loading, which is caused by Poisson's effect. Compared with reduced-integrated element S4R, S4 can yield more accurate results to in-plane bending issues (Vuolio, 2003).

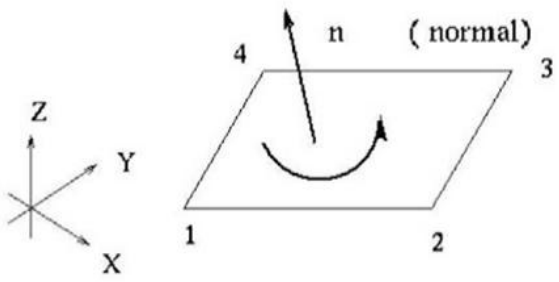

Figure 3- 3. General-purpose shell element S4 (Hibbitt et al., 2007)

Enclosed air

The hydrostatic fluid elements share the same nodes with the adjacent glass surfaces. The 4-node, three dimensional hydrostatic fluid elements "F3D4" are used to define the properties of the enclosed air (see Figure 3- 2). Although they appear as surface elements, they are volume elements by connecting all nodes to the reference one, in order to calculate the volume change and internal pressure change. As depicted in Figure 3- 4(b) the dashed lines demonstrate that the element is actually pyramidal in shape.

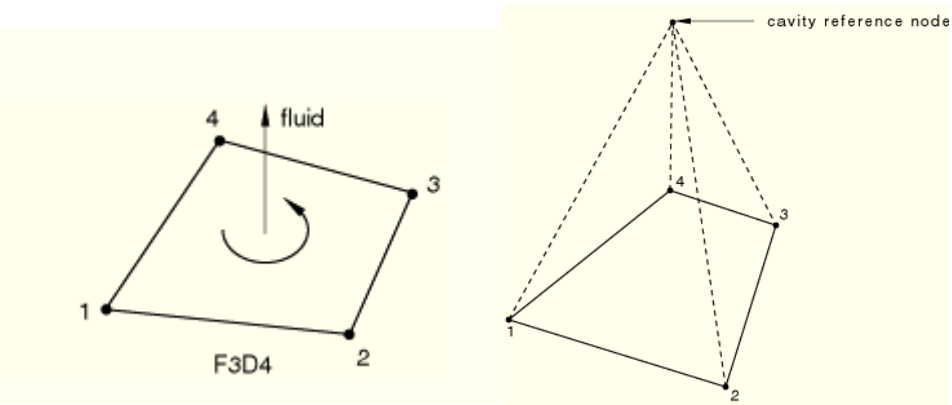

(a) Element F3D4 (b) Volume element "F3D4"

Figure 3- 4. Element type F3D4 (Hibbitt et al., 2007)

3.3.5. Boundary conditions

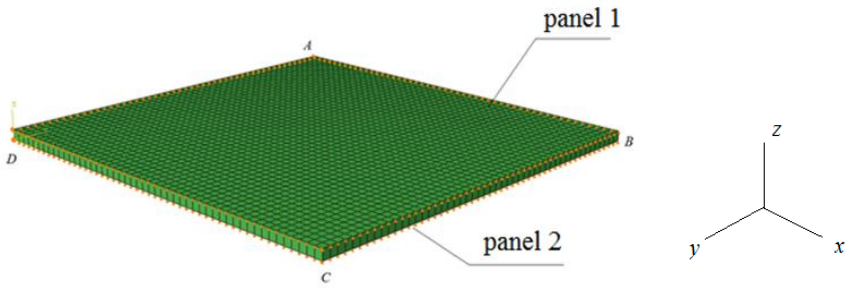

Figure 3-5. An IGU numerical model of 1000mm×1000mm

The models are simply supported in the simulations. As shown in Figure 3-5, the displacements of the nodes at edges are restrained in *z* direction.

3.3.6 The meshing scheme

The simulation results are to a great extent sensitive to the meshing scheme. In order to improve the computing accuracy meanwhile reduce the computational workload, a group of meshing types are tried to determine the optimal scheme. The total CPU running time, calculated deflection and maximum principal stress are compared below in Table 2 and 3 for two loading levels. The glass bending behaviour can be described by linear analysis under small loading p = 0.6kPa, and by nonlinear analysis with higher load p = 6kPa. Mesh size 200×200 is taken as the reference group, since very few differences can be detected in modelling results with this mesh density and above. It can be found that the mesh schemes adopted have achieved relatively accurate results but the total CPU time for the modelling differs a lot. By plotting the relation between total CPU time and mesh size in Figure 3- 6, it is observed that the CPU time decreases significantly with coarse meshing and levels off when the seed number per edge becomes less than 50. In the present work, the seed density 50×50 is chosen as it provides both good accuracy (less than 0.2%) and effective computational work. It is noted that the CPU time presented below in Table 3-3 and 3-4 is for the calculation of single-layer panels. The magnitudes would be increased in terms of more complicated numerical models

Table 3- 3 Mesh scheme for linear analysis p = 0.6kPa

Mesh size	Total CPU time (s)	ω_{max} (mm)	σ_{max} (MPa)	Error (Ref./)
200×200	37.1	1.768	4.627	Ref.
150×150	19.2	1.767	4.626	0.022%

100×100	7.7	1.766	4.624	0.065%
50×50	1.7	1.764	4.618	0.195%
40×40	1.2	1.763	4.616	0.238%
30×30	0.6	1.762	4.611	0.346%

Table 3- 4. Mesh scheme for nonlinear analysis p = 6kPa

Mesh size	Total CPU Time (s)	ω_{max} (mm)	σ_{max} (MPa)	Error (Ref./)
200×200	97.6	11.18	31.21	Ref.
150×150	50.9	11.17	31.2	0.032%
100×100	21.1	11.17	31.3	-0.288%
50×50	4.9	11.17	31.17	0.128%
40×40	3.1	11.16	31.14	0.224%
30×30	1.8	11.16	31.14	0.224%

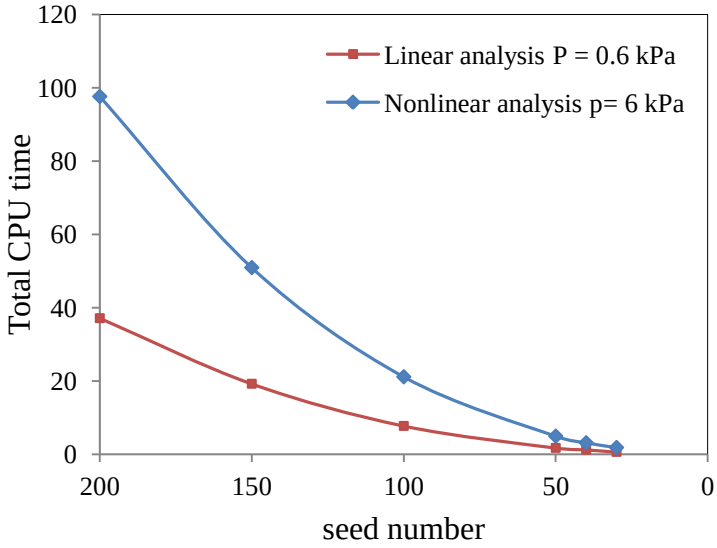

Figure 3- 6. Relation between mesh size and total CPU computational time

3.3.7 Geometric nonlinearity

A linear method ignores the membrane action that is developed at large deflection. So the linear results are reliable for the case that the maximum deflection of the plate is less than the plate thickness (Chien and Yeh, 1957). When the deflection increases at higher loading level, the linear analysis will yield much higher value than the real deflection.

The membrane theory (Hess 1896) points out that the large bending deflection is induced by both membrane stresses and bending stresses in nonlinear stage. Therefore membrane stresses have to be taken into account in nonlinear analysis. A number of studies have presented the applications of the membrane theory in various shell movements (Ventsel and Krauthammer, 2001).

Von-Karman (1910) delivered a group of governing differential equations for the large deflections of thin plates. However, to solve these coupled nonlinear partial differential equations requires laborious iterative numerical procedures. Various approximate geometrically nonlinear bending theories were proposed for simplified solutions on the basis of Von-Karman equations. (Chien, 1947; Fares et al., 2000; Koiter, 1966; Palmerio, 1990; Pietraszkiewicz, 1989; Reddy, 1982, 1990; Reddy and Chandrashekhara, 1985; Schmidt and Reddy, 1988; Sing et al., 1994). In this study, the nonlinear FEM numerical analysis will be employed.

In the numerical modelling, the linear and nonlinear results are both presented below to illustrate the differences caused by the membrane stresses. In Figure 3- 7(a), the bending behaviour is governed by pure bending stresses, and the peak value of the maximum principal stress is located at the centre of the panel. When the maximum deflection increases, the membrane action due to panel stretching stiffens the plate and meanwhile increases the tensile normal stresses at corners. As shown in Figure 3- 7(c), the peak values of the maximum principal stresses are found at corners rather than centre position.

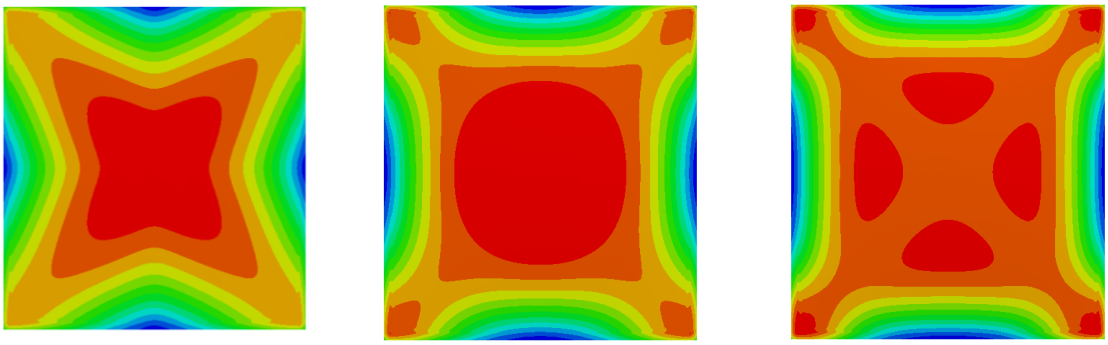

(a) Deflection=2.051mm (b) Deflection=8.206mm (c) Deflection =12.9mm

Figure 3- 7. Stress distribution from nonlinear bending analysis for a glass panel 1000mm×1000mm×6mm

The accuracy of geometry nonlinearity is found to be closely associated with the dimension of glass panels. Three square models of the length a = 2500mm, 1500mm and 500mm are created to explore the size sensitivity to the geometry nonlinearity. The thickness of all three models are equal, h = 6mm. A uniform pressure of 5kPa is applied on the panel surface. The maximum deflections obtained by the both linear and nonlinear analyses are presented. The results differ significantly with increasing loading pressure in Figure 3- 8(a). However, sample a = 500mm has close linear and nonlinear results, as shown in Figure 3- 8(c). It can be found that under the same loading condition, the nonlinear and linear analyses present greater discrepancy in the plate that the deflection to thickness ratio is greater. When the size is restricted to a relatively small range, as shown in the model 500mm×500mm, the deflection to thickness ratio is much lower, and the linear analysis is applicable, as it is time-efficient and easier to converge. Given that the large deflection may occur frequently in the following modelling work, the numerical geometric nonlinear analysis is adopted, in order to ensure the calculation accuracy.

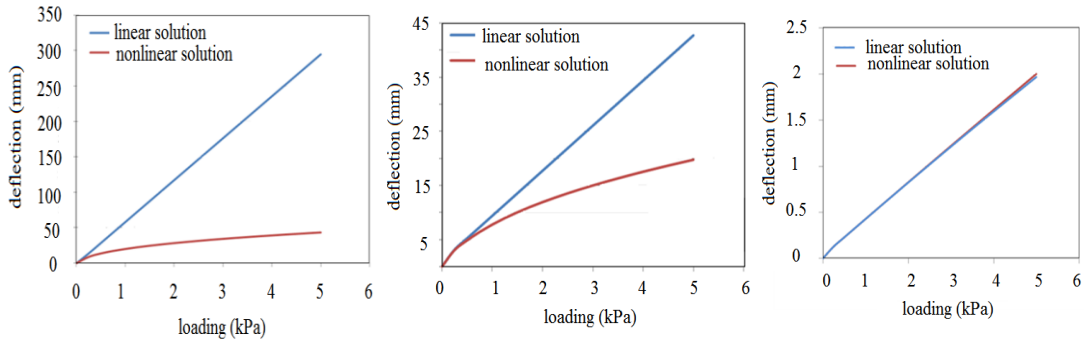

(a) 2500mm×2500mm (b)1500mm×1500mm (c)500mm×500mm

Figure 3- 8. Nonlinear and linear analysis comparison in different sizes of glass panel

3.3.8 Validation of FEM hydrostatic fluid model

Boyle's law for gas and Eq. (3-12) in prEN 13474-2 are used to validate the hydrostatic fluid model in two aspects. Boyle's law for gas is employed to examine the air tightness of the sealed air cavity. The bending behaviour of each glass panel obtained from FEM simulation will be compared with the values calculated by the nonlinear equations.

The size of numerical model is 1000mm × 1000mm, and the other geometric parameters are the same as in section 3.3.2. The following scenario is adopted in both the analytical calculation and numerical simulation. Assuming the IGU model is vertically installed, self-weight is not considered. The magnitude of wind load is steadily increasing from 1kPa to 8kPa. In this case, no climatic action is added. For a sealed air cavity, Boyle's law for gas is applicable to describe the relation between the cavity pressure and the corresponding cavity volume change. The product of pressure and cavity volume in Eq. (3-19) should be a constant, which can be expressed as:

$$PV = nR(\theta - \theta^{z}) = constant \qquad 3\text{- }19$$

The cavity pressure and cavity volume are calculated on each loading step. As shown in Table 3- 5, the product of the two variables remains constant at different loading level. So the cavity is proved to be completely sealed and the pressure and the volume of the cavity gas are validated to follow Boyle's law for gas.

Table 3- 5.Cavity volume and pressure change with increasing uniform loading

Load(MPa)	Cavity volume V (mm^3)	Cavity pressure P (MPa)	$P*V(\times 10^6)$
0	1.200×10^7	0.1010	1.212
0.001	1.194×10^7	0.1015	1.212
0.002	1.189×10^7	0.1019	1.212
0.003	1.183×10^7	0.1024	1.212
0.004	1.178×10^7	0.1029	1.212
0.005	1.173×10^7	0.1033	1.212
0.006	1.168×10^7	0.1038	1.212
0.007	1.163×10^7	0.1042	1.212
0.008	1.158×10^7	0.1047	1.212

The combined action of the wind load and the pressure difference Δp determines the load share of each glass panel in an IGU. As illustrated in Figure 3- 9, the load distributed in the panel 1 equals to p-Δp, while the load in panel 2 is Δp. So the deflection of two panels can be calculated by substituting the applied load into Eq. (3-12). The geometry parameter k_4 is provided in prEN 13474-2.

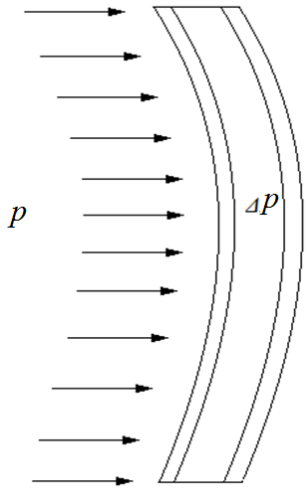

Figure 3- 9. Schematic diagram of an IGU subjected to a uniform wind load *p*

The calculated deflection/stress and the numerical outputs are presented below in Figure 3- 10 and Figure 3- 11 to make a comparison.

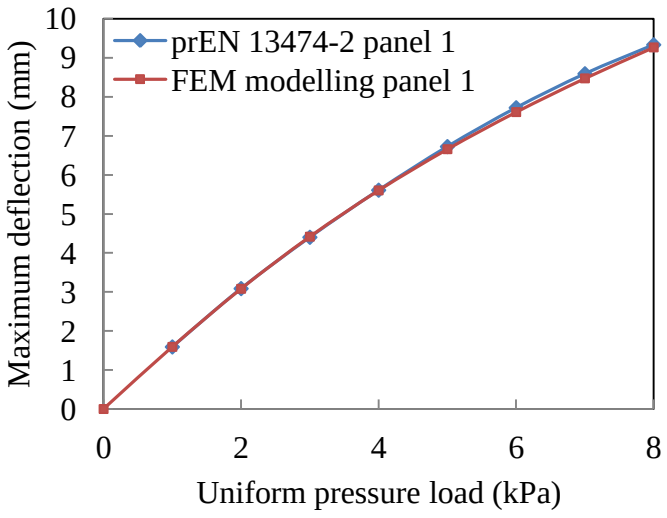

(a). panel 1

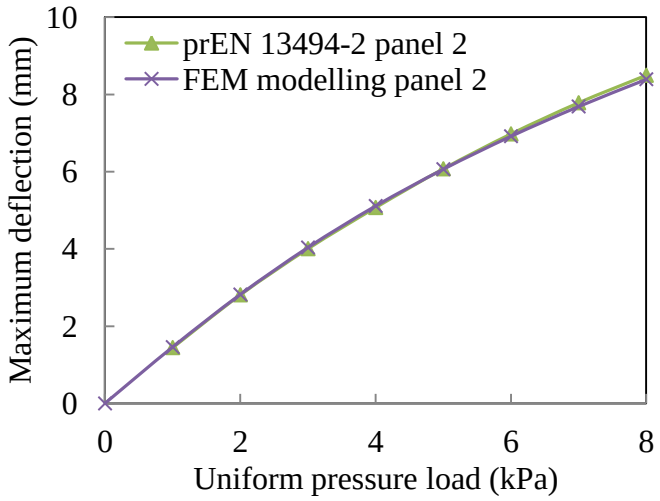

(b). panel 2

Figure 3- 10. Maximum deflection comparison between FEM and prEN 13474-2

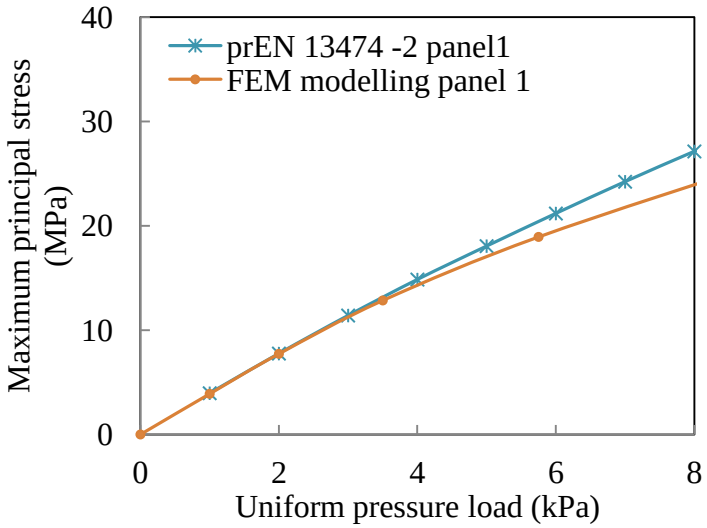

(a). panel 1

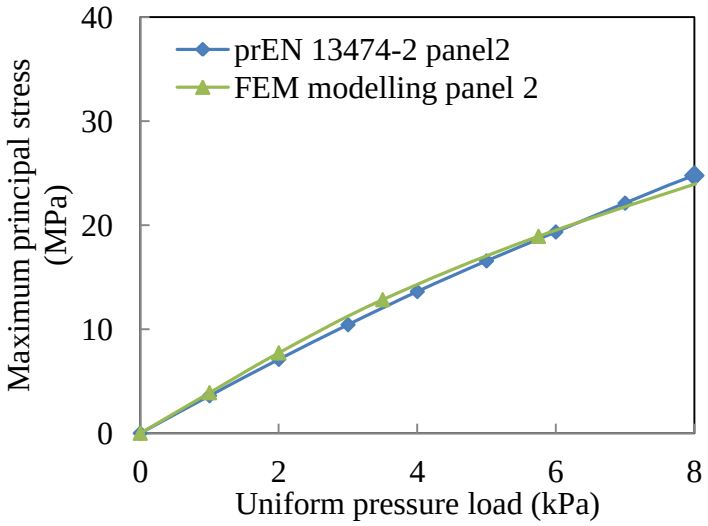

(b). panel 2

Figure 3- 11. Maximum principal stress comparison between FEM and prEN 13474-2

It can be observed that the deflection curves are in excellent agreement with an only 0.12% maximum difference, which successfully validates the numerical model. But a certain degree of discrepancy in the maximum stresses is found at higher loading levels. FEM exhibits stronger nonlinearity as a consequence of the membrane stresses acting in the panels. The deviation grows with increasing loading level. The maximum stresses obtained in the FEM modelling is 10.3% smaller than the design code for panel 1, and 9.1% for panel 2, at the highest loading level p = 8kPa. The results suggest that the maximum principal stresses calculated by Eq. (3-11) are overestimated, and the design code provides a more conservative evaluation. Higher maximum bending stresses obtained by the design code were also reported by Vuolio (2003).

Deflection ratio and stress ratio between two panels in the IGU under an increasing wind load are presented. It can be seen in Figure 3- 12 that the stress ratio and deflection ratio remains consistent under varying pressure load. It can be therefore concluded that

the stress ratio and deflection ratio on two panels are independent on the magnitude of uniformly applied wind load. As shown the average ratio calculated by two approaches presented in Table 3- 6, the maximum principal stresses generated in panel 1 is 8.2% larger than that in panel 2 according to the numerical prediction, while 5.2% in the design code prEN 13474-2. The maximum deflection of panel 1 is roughly 10.5% greater than that of panel 2 given in the numerical modelling, 9.3% in the calculation of design code.

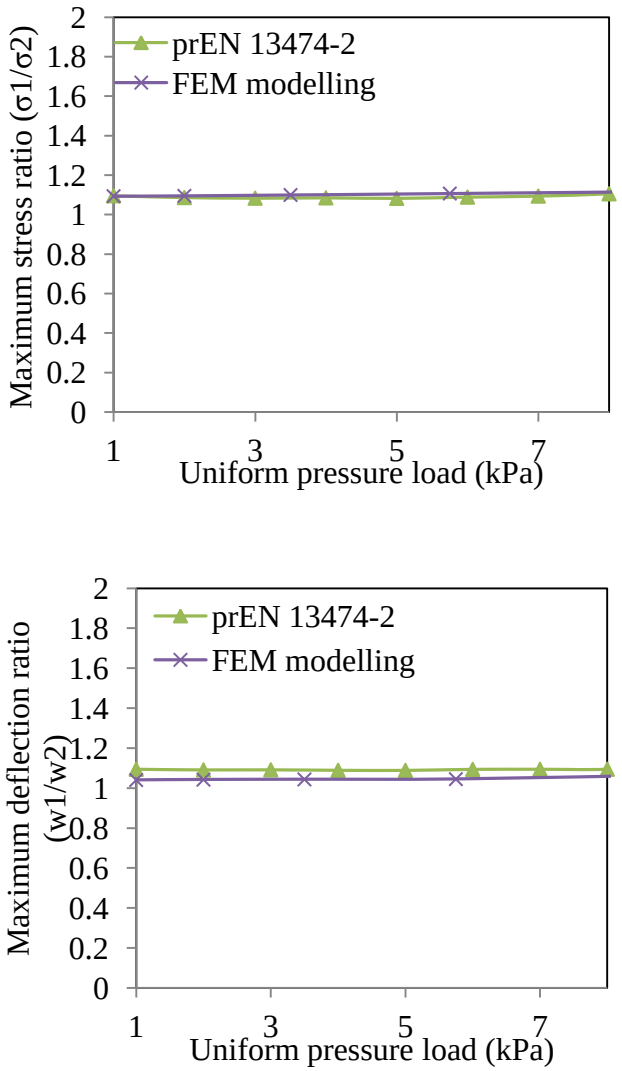

Figure 3- 12. Maximum principal stress and deflection ratio comparison

Table 3- 6. Average stress and deflection ratio comparison

	Average σ1/σ2	Average ω1/ω2
FEM	1.082	1.105
prEN 13474-2	1.052	1.093

3.3.9 Validation of the additional calculation parameter for IGUs in the code

As introduced in section 3.3.2, an additional parameter "insulating unit factor" ϕ has been proposed in prEN 13474-2 to directly calculate the design load share on each glass panel. By combining Eq. (3-8) and (3-9), the insulating unit factor can be expressed as a function of dimensionless parameter k_5 given in Eq. (3-20).

$$\phi = \frac{1}{1 + \frac{a^4}{28.9^4 \left(\frac{s h_1^3 h_2^3}{\left(h_1^3 + h_2^3\right) k_5} \right)}} \qquad 3\text{- }20$$

It is noted that k_5 introduced in prEN 13474 is not a constant in nonlinear analysis, but relies on the normalised load p^*, which is a function of the design load F_d. Therefore, iteration method is employed to determine k_5 that should satisfy both normalised load p^* and the load share on the panel. The iteration algorithm chart is shown as below in Figure 3- 13:

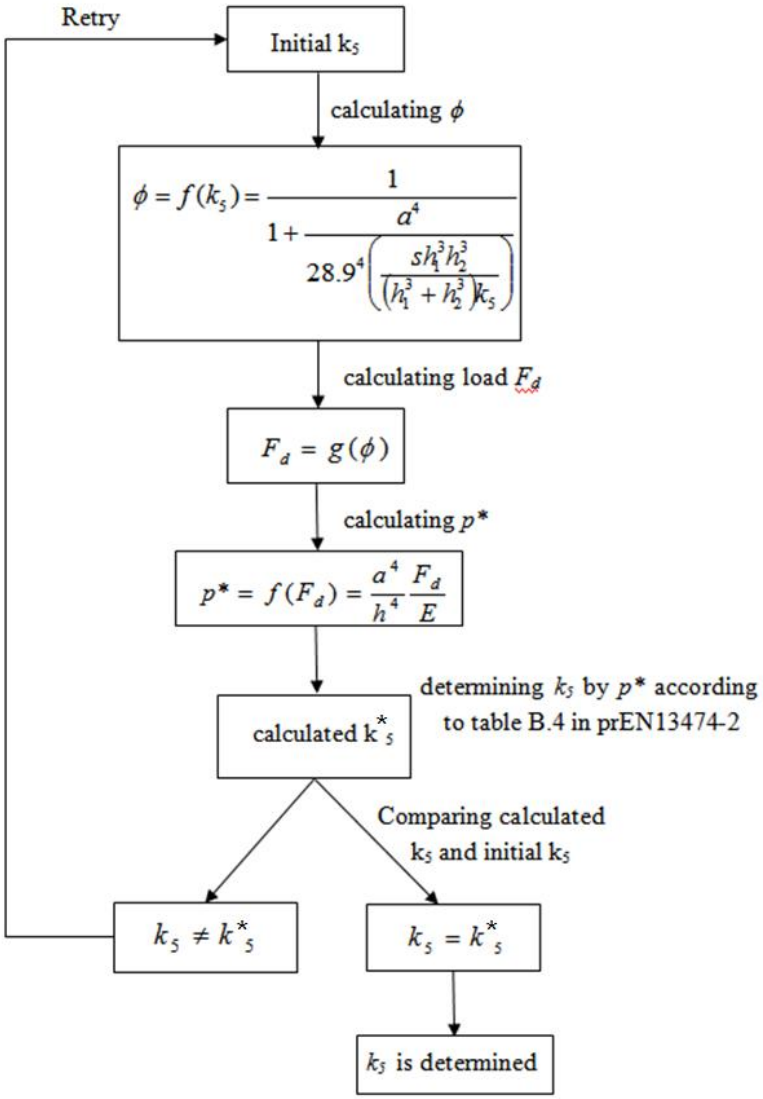

Figure 3- 13. Flow chart of the determination of k_5

In the validation model, the IGU is assumed to be subjected to a wind load only. The wind load is increasing from 0 to 8kPa. The equations to calculate the design loads are presented in Table 3- 2:

$$F_{panel1} = (\delta_1 + \phi_1 \delta_2) P \qquad 3\text{- }21$$

$$F_{panel2} = (1 - \phi_2) \delta_2 P \qquad 3\text{- }22$$

where, ϕ_1 and ϕ_2 are the insulating factor for panel 1 and 2 respectively.

Once k_5 is found, the insulating unit factor can be determined and the applied load share can be calculated according to Eq. (3-21) and (3-22). Another k_5-dependent variable: deformed cavity volume V_d also can be calculated.

The volume change in panel 1 and panel 2 are given below:

$$V_1 = k_5 \frac{a^4}{h^3} \frac{F_{panel1}}{E} ab \qquad 3\text{- }23$$

$$V_2 = k_5' \frac{a^4}{h^3} \frac{F_{panel2}}{E} ab \qquad 3\text{- }24$$

where k_5 and k_5' are respectively for panel 1 and 2. The deformed volume is written as:

$$V_d = V_0 - (V_1 - V_2) \qquad 3\text{- }25$$

where V_0 is the initial cavity volume of the IGU model.

The validated hydrostatic fluid model is now employed to examine the applicability of the insulating unit factor ϕ. The load share and the deformed cavity volume obtained from the formulas and numerical analysis are presented to make a comparison.

The load share on each panel from code method and numerical results are plotted in Figure 3- 14, which reveals the linear relation between the distributed loads on each panel and the increasing applied wind load. The results from the theoretical formulae and the numerical modelling are in good agreement.

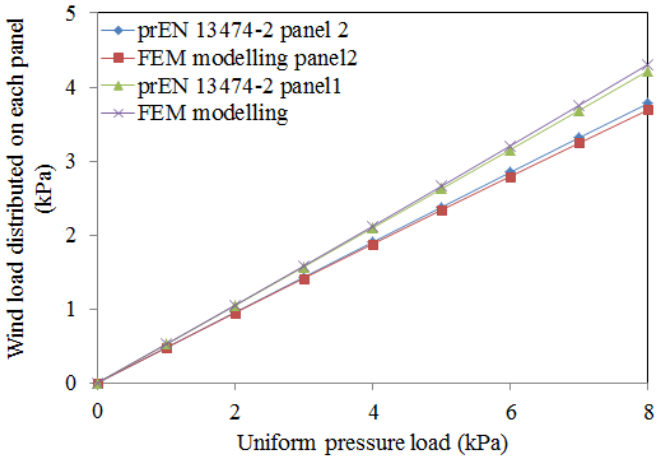

Figure 3- 14. Comparison of the load share on each panel

The deformed volume of the air cavity calculated by Eq. (3-25) and the FEM modelling are compared in Figure 3- 15. The volume calculated by the code is slightly higher than modelling under increasing loading level, but only with a 0.7% maximum difference. Therefore it can be concluded that the FEM modelling results coincide well with the mathematical calculation results.

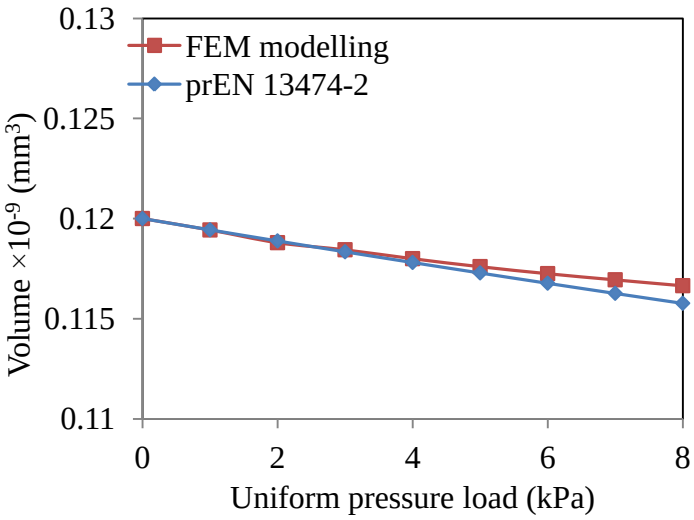

Figure 3- 15. Volume variation of the air cavity of IGUs with increasing uniform load

In summary, the FEM numerical model has been successfully validated by Boyle's law and the nonlinear bending formulae for thin plates. An empirical method that introduces "insulating unit factor" ϕ is validated by the FEM models. The load share in each panel and the total deformed volume change are compared. It has been observed that the results are in good agreement.

Now the climatic action provided in the design code is considered in the FEM modelling. In the first step, the climatic action is modelled individually to validate the temperature load given in the European product standard. In prEN 13474-2, two seasonal scenarios are given to demonstrate winter and summer conditions. A group of simplified values are presented below according to Table 3- 7.

Table 3- 7. Two seasonal scenarios (BIS, 2002)

Condition	Climatic action $p_{C;0}$	Temperature in use	Meteorological pressure in use	Temperature for production	Meteorological pressure for production
Summer	12kPa	45°C	100.5 kPa	18°C	103kPa
Winter	15kPa	3°C	104 kPa	30°C	98kPa

In the hand calculation, the formula of the design loads for the climatic action only can be put in the form:

$$F_{panel1} = \phi p_{C;0} \qquad 3\text{- }26$$

$$F_{panel2} = -\phi p_{C;0} \qquad 3\text{- }27$$

As seen in Eq. (3- 26) and (3- 27), the climatic action calculated in the codes depends on the insulating unit factor ϕ, which is a combination of IGU geometric parameters.

The accuracy of the equivalent load of the climatic actions given in Table 3- 7 will be examined in FEM simulation. The maximum deflections of IGUs obtained from two methods are presented to compare the results.

In the design code, the deflection is calculated by substituting the equivalent climatic actions (shown in Table 3- 7) into Eq. (3- 26) to obtain the design load on the panel, and then substituting design load *F* into Eq. (3- 12). In the FEM modelling, the temperature differential and the meteorological pressure changes are both applied to the model in terms of two pre-defined fields. Different IGU sizes and air cavity widths are considered in the modelling, in order to make a close comparison. The maximum deflection variation along the IGU length and cavity widths in both summer and winter conditions are presented below.

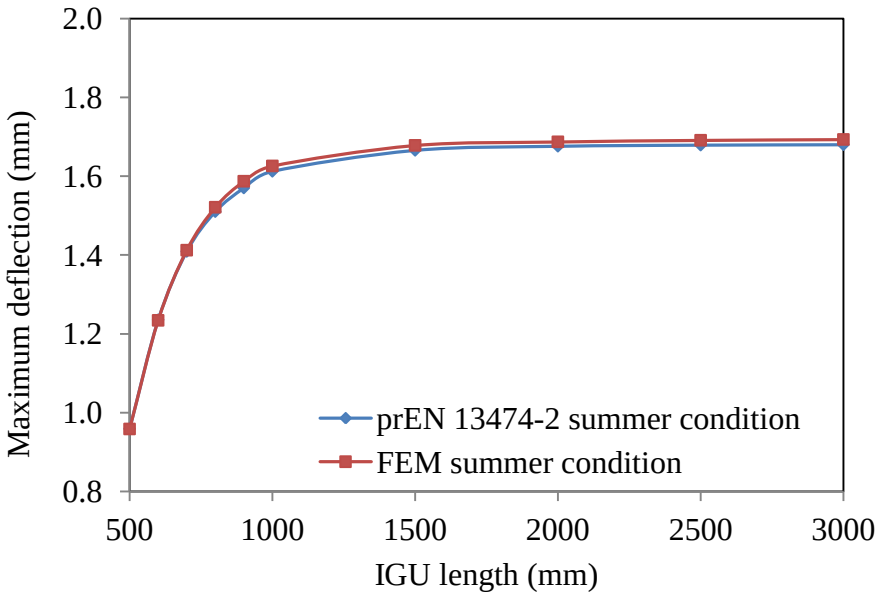

Figure 3- 16. Maximum deflection variation of a square IGU for the summer season with increased IGU length

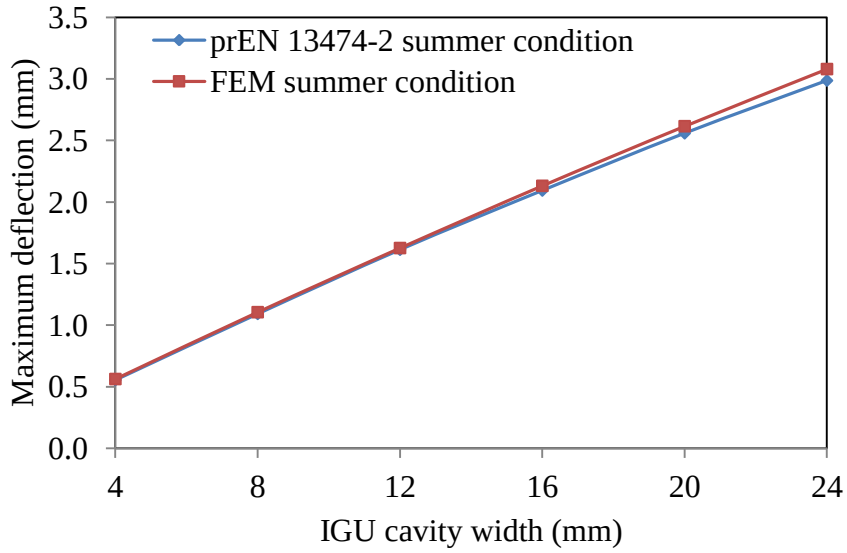

Figure 3- 17. Maximum deflection variation of a 1000×1000mm square IGU with increased cavity width in the summer season

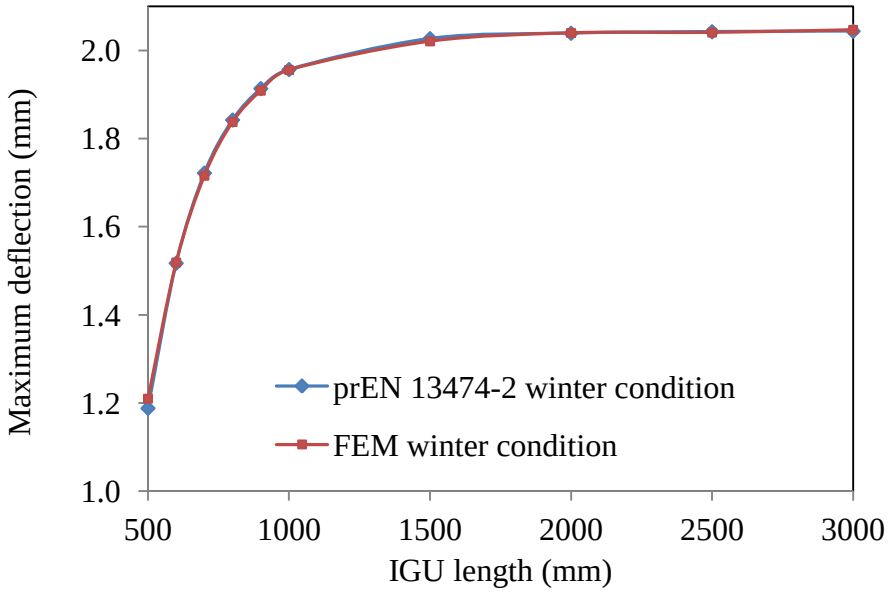

Figure 3- 18. Maximum deflection variation of a square IGU for the winter season with increased IGU length

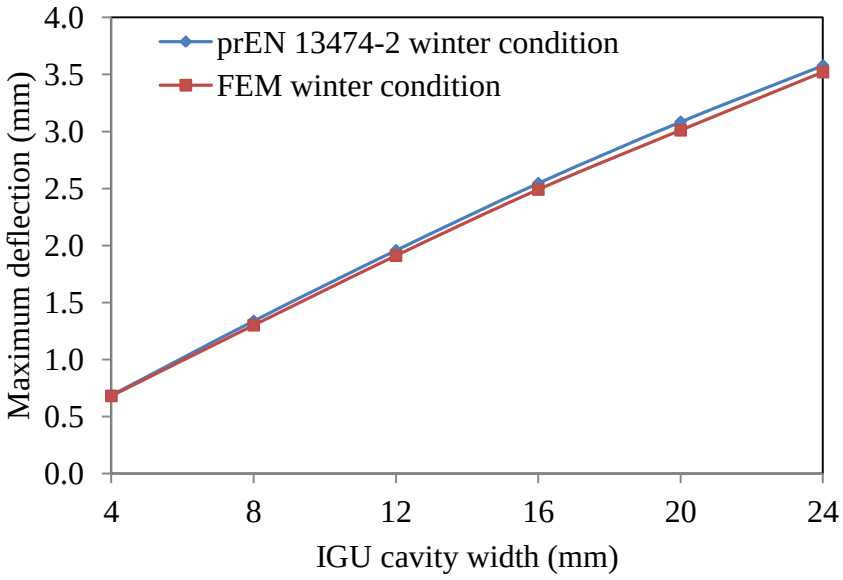

Figure 3- 19. Maximum deflection variation of a 1000×1000mm square IGU with increased cavity width in the winter season

The results confirmed that the equivalent climatic pressure loads given in the numerical models coincide well with the design code. The simplified climatic parameters are validated to accurately reflect the corresponding extreme weather influences. It is also observed that under a consistent uniform loading, the increasing cavity width results in a linear rise in the maximum deflection of IGUs. In contrast, the increasing length of square IGUs leads to a nonlinear increase of the maximum deflection. There is a sharp increase in the maximum deflection induced by climatic action onto IGUs when the glazing length rises from 500mm to 1000mm, and then tends to flatten off with greater length, and finally remains constant. The ultimate maximum deflection caused by the climatic action in the summer season is 1.68~1.69mm, and 2.044~2.047mm in the winter season.

3.3.10 Validation of the interactive environmental actions

In the European product design, the external and internal loads acting upon IGUs are calculated separately. Then the overall impacts on IGUs are obtained by simply adding two parts of evaluation results together. In reality, there is an interaction between the external wind load and the internal action due to temperature changes. The numerical modelling has taken this interactive effect into consideration by simultaneously applying a wind load and a temperature differential field to the IGU model. In this section, the FEM modelling is used to examine the significance of the interaction and the applicability of the simple superposition

i. Assuming an IGU is vertically installed, and subjected to a wind load and summer climate exposure. The magnitude of wind load is steadily increasing from 0kPa to 8kPa. According to Table 3- 1, a simplified value for the internal loads under the summer condition is 12kPa.

ii. Assuming an IGU is vertically installed, subjected to a wind load and winter climate. The wind load increases gradually from 0 to 8kPa. The ambient condition is assumed to be winter season and the internal action used in the calculation is -15kPa.

The maximum deflection and the peak value of maximum principal stress from FEM modelling and the draft European code prEN 13474-2 are presented in Figure 3- 20 and Figure 3- 21. Inward bending and deflection is deemed to be positive and vice versa.

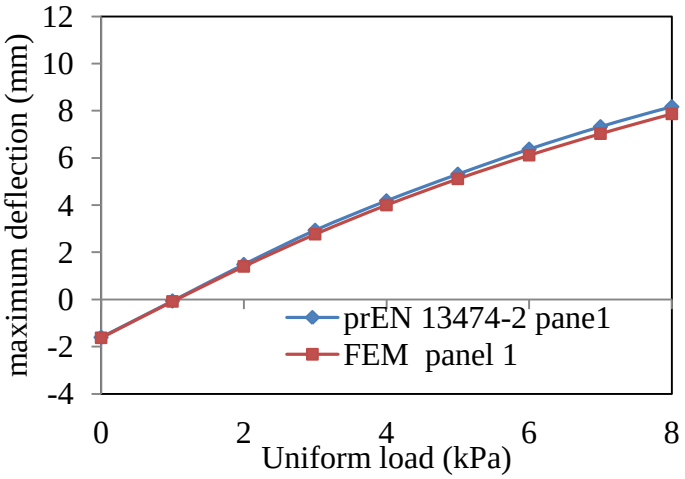

(a). Panel 1

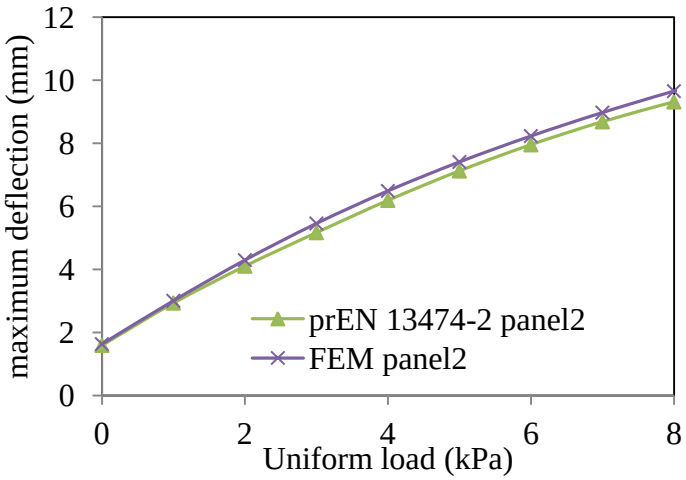

(b). Panel 2

Figure 3- 20. Maximum deflection comparison between the FEM modelling and the design code

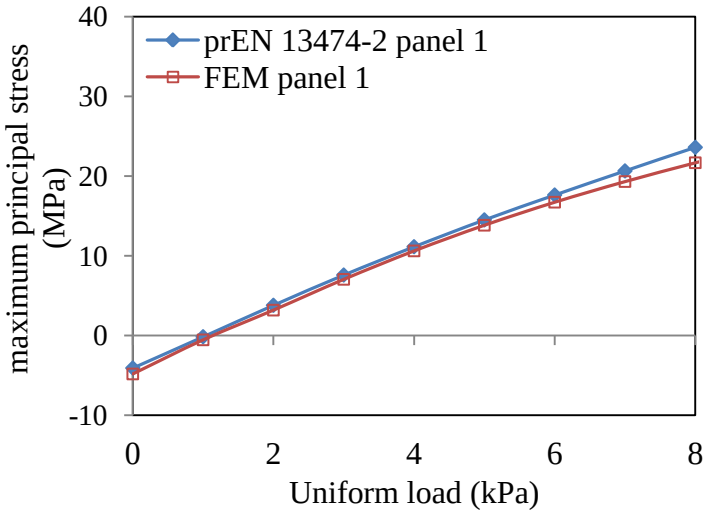

(a). Panel 1

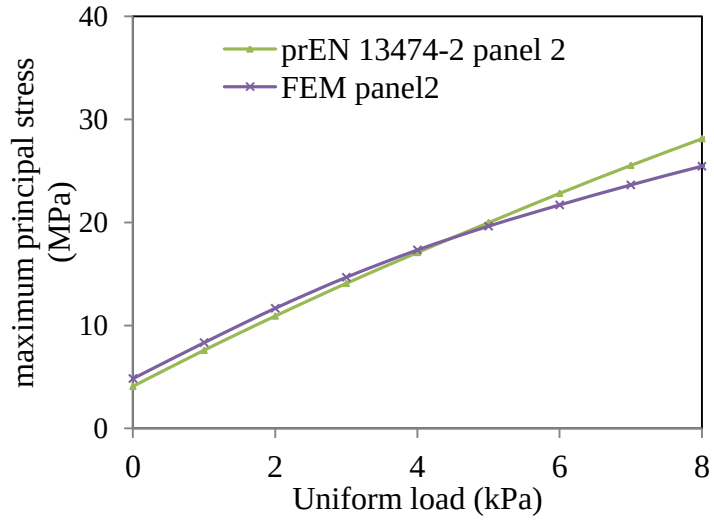

(b). Panel 2

Figure 3- 21. Maximum principal stress comparison between the FEM modelling and the design code

As shown in Figure 3- 20, the deflections of both panel 1 and panel 2 obtained from two approaches reach good agreements. In the FEM modelling, the maximum deflection is on average 5.3% lower than the design code results in panel 1, whereas averagely 3.57% higher than the code results in panel 2. In other words, the loads on panel 1 and panel 2 are more evenly distributed in the FEM modelling than that in the design code.

Slight deviation is observed in the maximum principal stress plotted in Figure 3- 21. The FEM curves exhibit relatively lower results compared with the code, especially in nonlinear stage. Similar to the results in section 3.3.9, the maximum principal stresses of the FEM models are lower than the mathematical results in higher loading levels. The discrepancy in the maximum stresses can be observed with the load greater than 5kPa. It is also found that higher loading level will amplify the discrepancy.

In terms of scenario ii, the maximum deflection and stresses comparisons are displayed below in Figure 3-22 and Figure 3- 23:

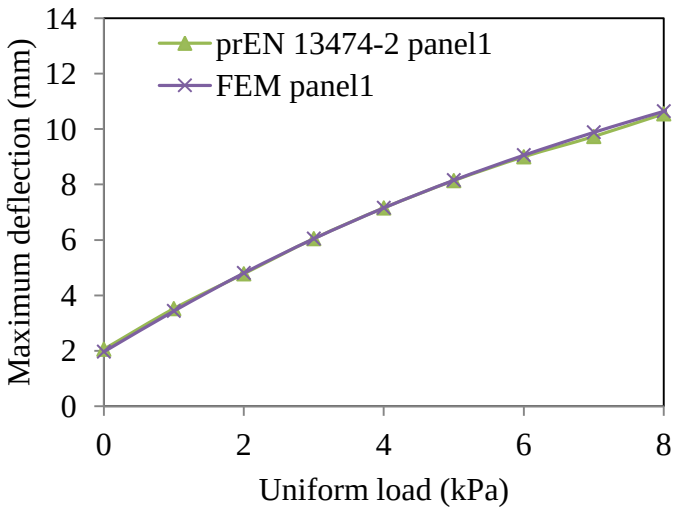

(a). Panel 1

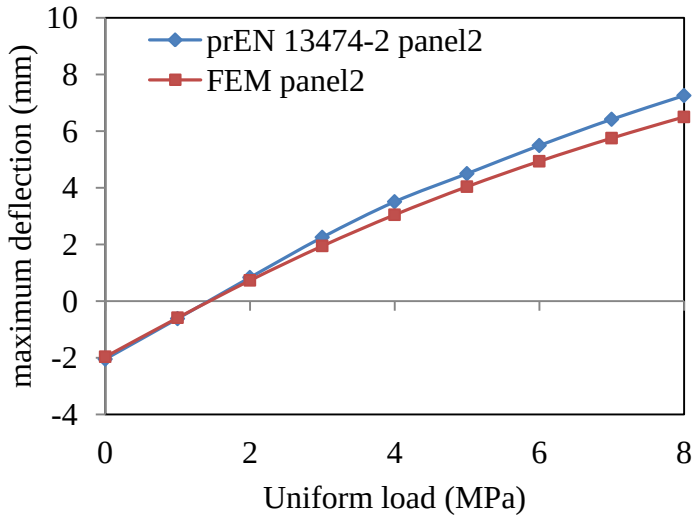

(b) Panel 2

Figure 3-22. Maximum deflection comparison between FEM and prEN 13474-2

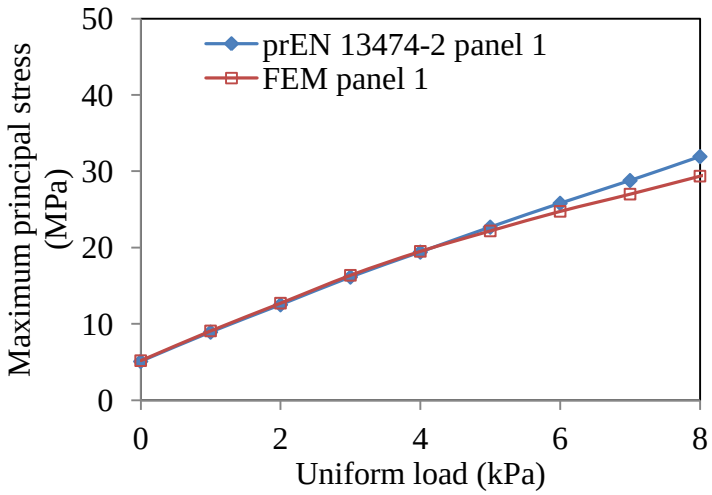

(a). Panel 1

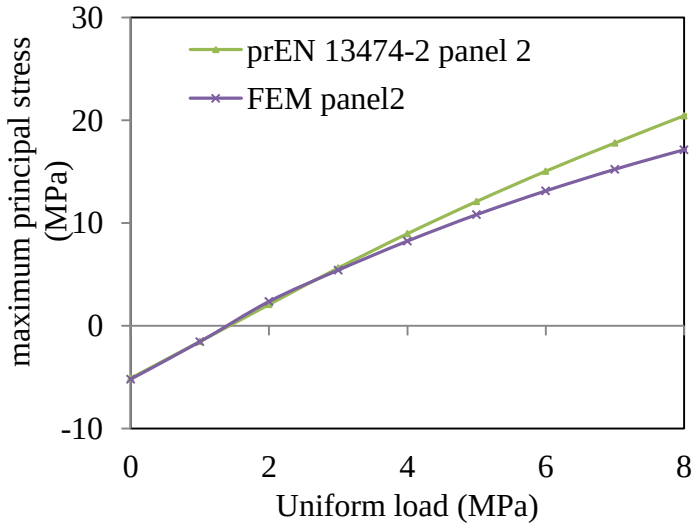

(b) Panel 2

Figure 3- 23. Maximum principal stress comparison between FEM and prEN 13474-2

The maximum deflections calculated by the FEM modelling and prEN 13474-2 are in general good agreement. However, greater deviations are found in the results of the winter condition, in contrast to the summer condition. The design code yielded averagely 11.4% greater deflections in panel 2 than the numerical results, and 13.48% greater bending stresses in terms of higher loading levels (from 4kPa to 8kPa).

In the previous section, the bending deflection has been examined for wind load and the thermal load separately. The numerical modelling and the product design code are in good agreement. However, a certain degree of disagreement is observed in terms of combined actions. It is believed that the interactive effect between the wind load and internal loads are not considered in the simple superposition given by the product design code. On the other hand, simultaneous applied pre-defined fields in the numerical modelling allow for a full interaction between different environmental actions.

3.4 Size effect of IGUs under thermal-wind loading

In the following section, the interactive influences of wind loads and climatic actions upon different sizes of IGUs are discussed. The numerical model is assumed to be installed vertically so that the self-weight will not influence the overall loading. A uniform pressure from 0 to 8kPa is applied on panel 1 step by step, representing lateral wind load. The initial temperature and pressure of the inner air is set to be 20^{o}C and 0.1013MPa. The installation temperature in the air space relies on seasonal conditions, sunlight UV intensity and the local climate fluctuation. Different from the code, a group of more severe temperatures are considered. The characteristic ambient temperature is taken to be 60^{o}C for the extreme scenario in summer time, and -30^{o}C in winter.

3.4.1 FEM modelling results

The square IGU models with a = 2500mm, 2000mm, 1500mm, 1000mm and 500mm and thickness h = 6mm are created respectively, in order to explore the size effect to the glass bending. The maximum deflections of panel 1 and 2 of three sizes of models that experience 60^{o}C, 20^{o}C and -30^{o}C are plotted in Figure 3- 24 to Figure 3- 28.

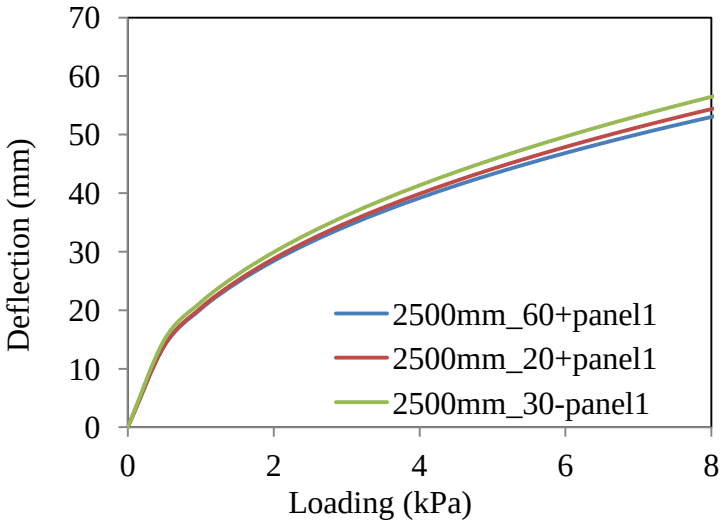

(a). Panel 1

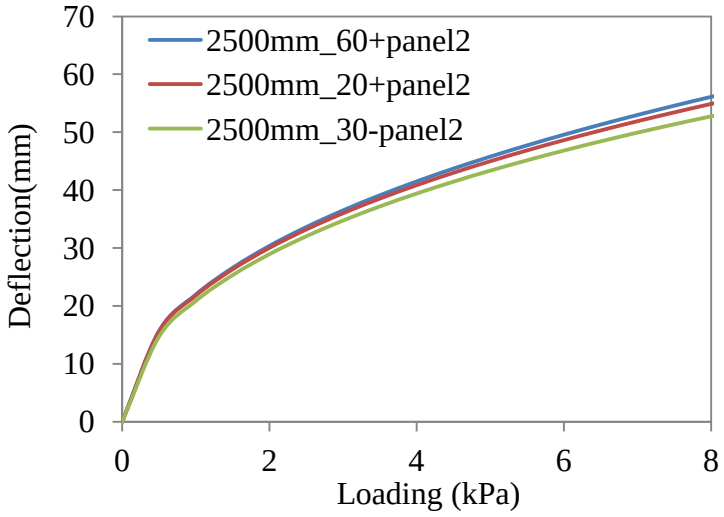

(b). Panel 2

Figure 3- 24. Temperature dependent deflection curves with *a* = 2500mm

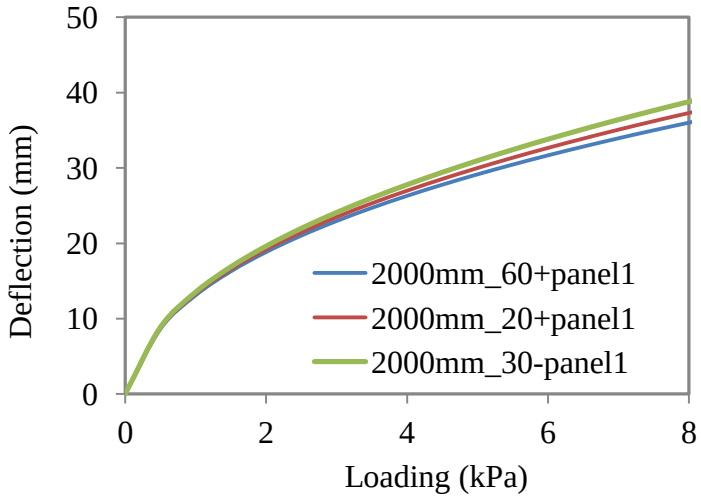

(a). Panel 1

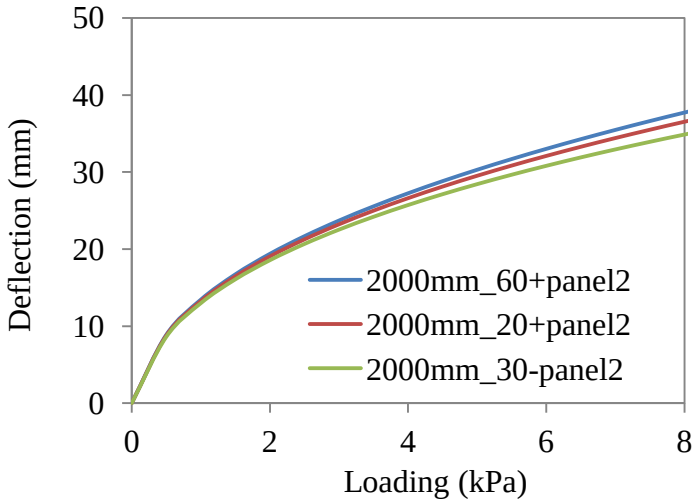

(b). Panel 2

Figure 3- 25. Temperature dependent deflection curves with *a* = 2000mm

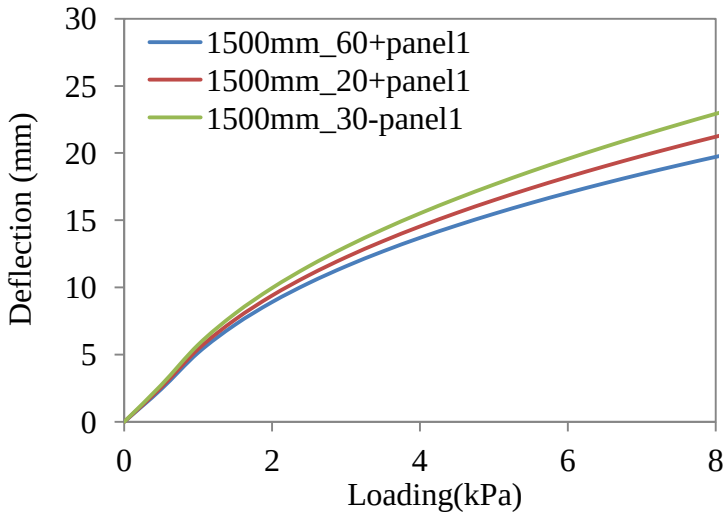

(a). Panel 1

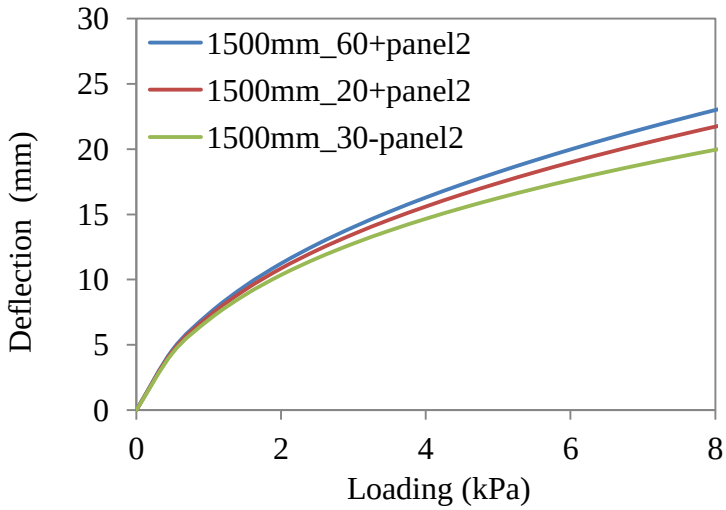

(b). Panel 2

Figure 3- 26. Temperature dependent deflection curves with *a* = 1500mm

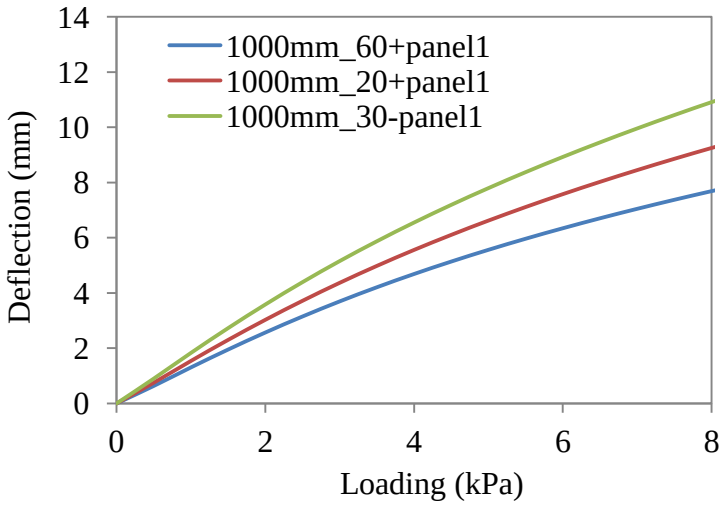

(a). Panel 1

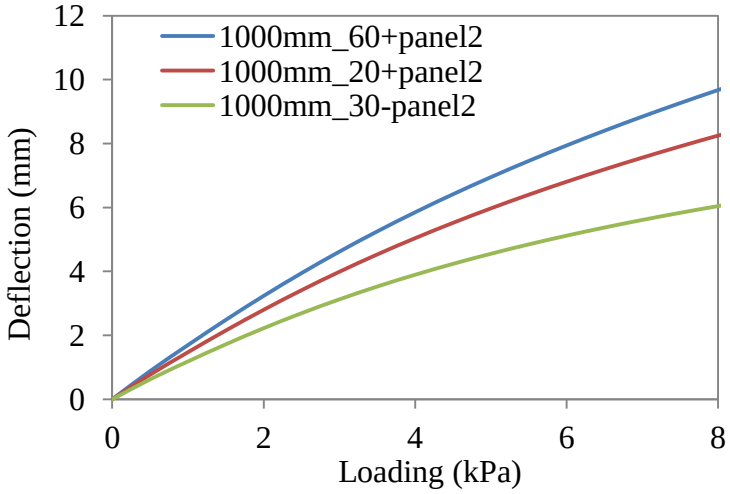

(b). Panel 2

Figure 3- 27. Temperature dependent deflection curves with *a* = 1000mm

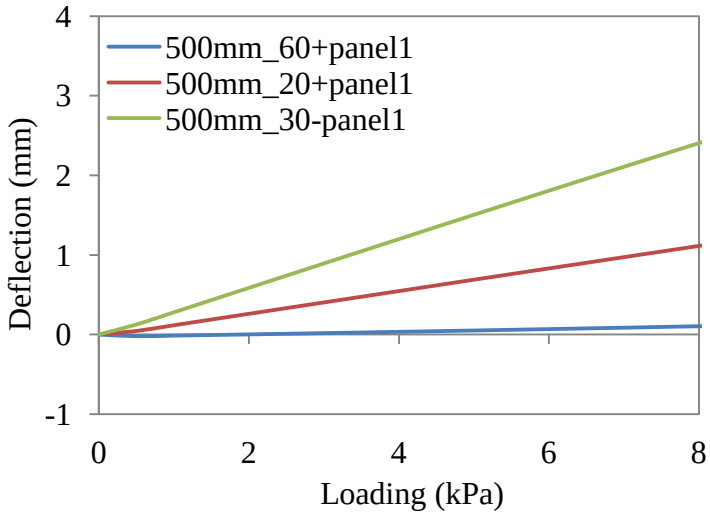

(a). Panel 1

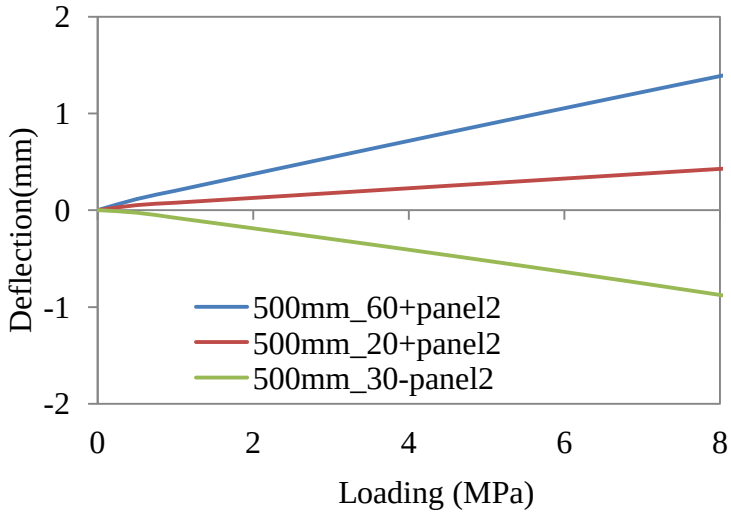

(b). Panel 2

Figure 3- 28. Temperature dependent deflection curves with *a* = 500mm

3.4.2 Discussions

With regard to panel 1, the temperature rise compensates the inward bending caused by the wind load. The thermal expansion of the inner air pushes panel 1 outward to balance off the inward wind pressure and therefore reduce the deflection. On the other hand, the temperature drop reinforces the bending. The thermal contraction due to the temperature drop pulls the panel from inside, further increasing the deflection of panel 1 combined with the external wind load. It is directly opposite to panel 2, that the higher temperature has a synergic action with the wind load, while the temperature drop will offset the wind load. It is noted that in the case of a = 500mm, rather than a reduction of the deflection by compensating the wind load, the thermal contraction leads to a larger deflection in the opposite direction, as shown in Figure 3- 28 (b). This is because the thermal contraction has become the predominant impact, much greater than the opposite wind pressure.

From Figure 3- 24 to Figure 3- 26, it can be found that that the temperature change does obviously influence the maximum deflection in the models with a =1500mm or above. The deflection differences due to the temperature change become obvious when the sample size reduces shown in Figure 3- 27 and Figure 3- 28. In the sample a =500mm (see Figure 3- 28), the thermal action has acted as a predominant factor to determine the glass deflection. Table 3- 8 demonstrates clearly that the impact of thermal action grows stronger along with the decreasing glazing size.

Table 3- 8. Maximum deflection in two panels of IGU with different size, at temperature of 60 °C, 20 °C and -30 °C

2500mm				
Temp. °C	Panel1		Panel2	
	Deflection (mm)	Ratio	Deflection (mm)	Ratio
20	59.834	ref.	60.2069	ref.
60	52.9925	0.972773	61.6919	1.024665
-30	62.28	1.070013	57.7194	0.958684
2000mm				
Temp. °C	Panel1		Panel2	
	Deflection (mm)	Ratio	Deflection (mm)	Ratio
20	41.248	ref.	40.3047	ref.
60	39.6759	0.961887	41.781	1.036628
-30	43.0864	1.044569	38.2713	0.949549
1500mm				
Temp. °C	Panel1		Panel2	
	Deflection (mm)	Ratio	Deflection (mm)	Ratio
20	24.45	ref.	23.41	ref.
60	22.81	0.932924	24.94	1.065357
-30	26.35	1.07771	21.28	0.909013
1000mm				
Temp. °C	Panel1		Panel2	
	Deflection (mm)	Ratio	Deflection (mm)	Ratio
20	10.6918	ref.	9.47021	ref.
60	8.82606	0.825498	11.16	1.178432
-30	12.63	1.181279	6.789	0.71688
500mm				
Temp. °C	Panel1		Panel2	
	Deflection (mm)	Ratio	Deflection (mm)	Ratio
20	1.39103	ref.	0.526955	ref.
60	0.142051	0.102119	1.71345	3.251606
-30	2.98857	2.148458	-1.12466	-2.13426

It is observed that the change of the deflection ratio is the greatest when the size *a* =1000 comes down to *a* = 500mm. Therefore the deflections of the size in between, i.e.

a = 600, 700, 800, and 900mm are further modelled. The relations between the deflection ratio and the model size are depicted in Figure 3- 29 and Figure 3- 30.

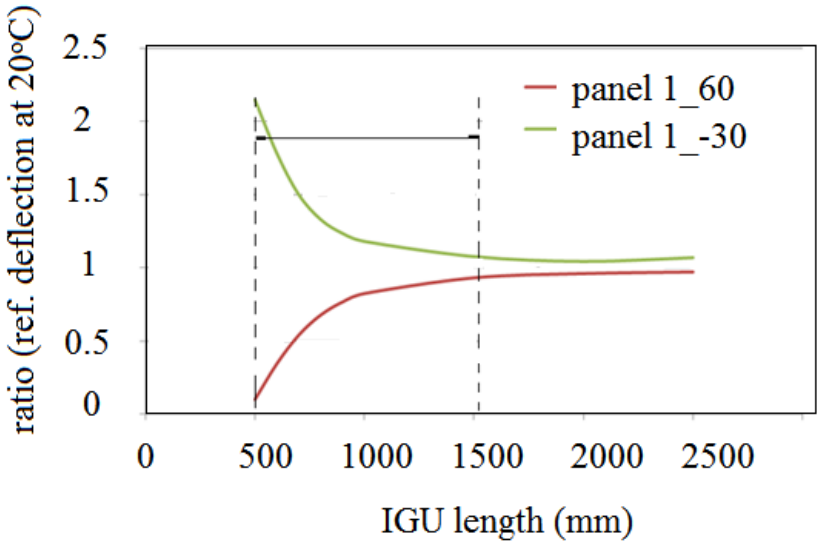

Figure 3- 29. Deflection ratio curves vs. glass length for panel 1

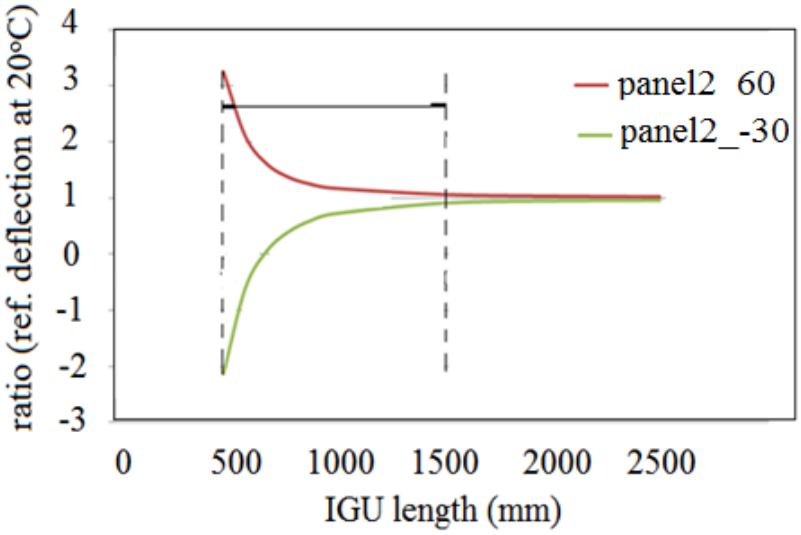

Figure 3- 30. Deflection ratio curves vs. glass length for panel 2

In Figure 3- 29 and Figure 3- 30, a size range i.e. the glass length 500mm to 1500mm is highlighted. Within the range the thermal actions make significant differences on the glass bending deflection. The thermal actions can be negligible when the length *a* is

above 2000mm. The absolute values of deflection ratios are the highest in the beginning but quickly converge to 1 with increasing size. With regards to panel 2 at temperature -30^{o}C, when a≥700mm, thermal contraction can offset the wind load and reduce the deflection; When a≤700mm, the thermal contraction will exceed the wind load and result in a growing deflection in the opposite direction.

The absolute value of the deflection ratio versus IGU size is plotted below in Figure 3-31. It can be seen that when the IGU length is within the range 500mm to 1500mm, the absolute values of the deflection ratio in panel 2 vary significantly. It can be concluded that panel2 is more susceptible to the interacting loads.

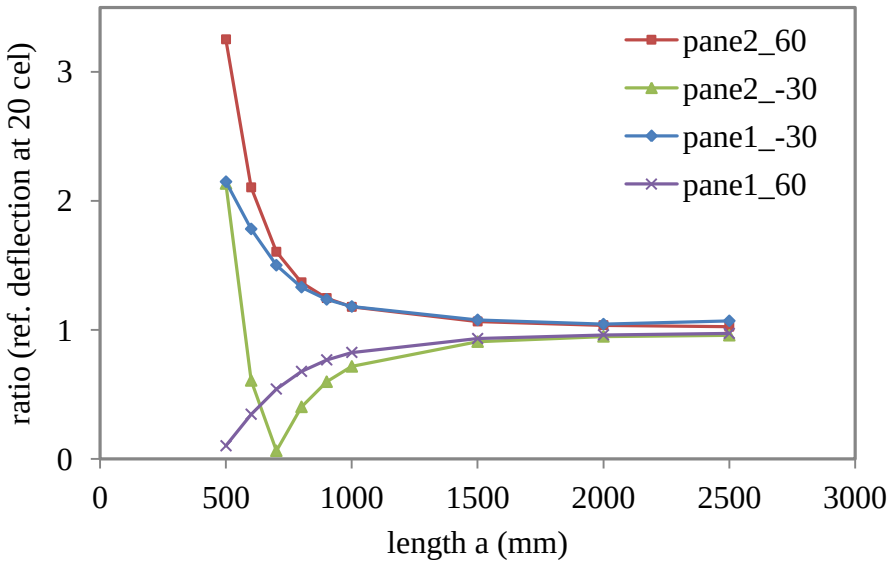

Figure 3- 31 Absolute value of deflection ratio versus IGU length

The phenomenon can be explained by Figure 3- 32, which shows the deflection ratio of panel 1 to panel 2 subjected to wind load only. We can find that the deflection share on panel 1 is 2.7 times of that on panel 2 in the beginning. The deflection ratio drops rapidly to 1 when IGU length is increased from 500mm to 1500mm. In the early stage,

the wind load mainly carried by panel 1 rather than panel 2. In this situation the internal thermal action becomes predominant to panel 2 that contribute to the bending. Therefore panel 2 is more sensitive to the internal thermal expansion or contraction.

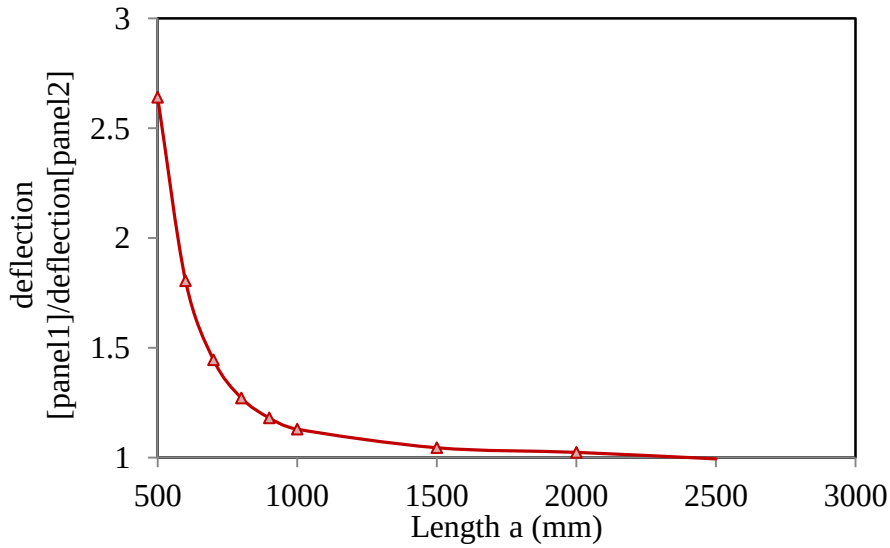

Figure 3- 32. Deflection ratio of panel 1 and panel 2 vs. IGU size

3.5. Four point supported boundary condition

In the given formulae, the glass panels are assumed to be with continuously simply supported edges, which conform to the definitions given in prEN 13474-2. The edges are free to rotate and free to move in the panel plane. The code also covers the approximate equations for the stress and deflection calculation in cases of three-edge supported and two-edge supported panels. In this section, four-point support will be discussed by means of FEM numerical modelling. A simplified four-point support model is built as illustrated in Figure 3- 33. The point supports are assumed to be located at the corners and act as clamped supports, which apply the constraints in all 6 degree of freedoms.

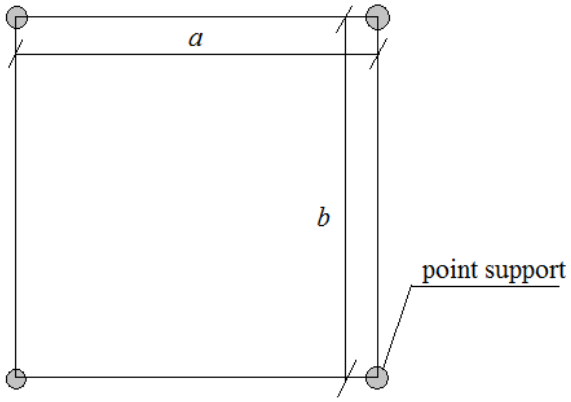

Figure 3- 33. Schematic diagram of the numerical point supported glass panel model

The new geometry coefficients k_4 and k_5 in term of four-point supported condition will be determined by means of FEM modelling for the generic design consideration. It is noted that k_1 is not taken into account in the discussion. This is because that the maximum stresses in the four-point supported glass panel always take place in the vicinity of the bolts due to severe stress concentrations. The magnitudes of the stresses are closely associated to the size, material properties, geometry structure of the bolts and the isolation materials. Therefore the general theoretical method derived from FEM modelling would be difficult to give an accurate evaluation.

3.5.1 Determination of coefficient k_4

The coefficient k_4 can be determined by simulating the nonlinear bending behaviour of a piece of monolithic glass panel. The maximum deflection ω_{max} and the corresponding applied uniform pressure p can be obtained in the numerical simulation. By substituting the results into Eq. (3- 12) and the new parameter k_4 can be inversely derived. The substitution of Eq. (3- 12) into Eq. (3-14) leads to a relation of k_4 and the normalised p^*:

$$p^* = \frac{\omega_{\max}}{k_4 \cdot h} \qquad 3\text{- }28$$

The aspect ratios from 1 to 0.5 are considered in the modelling and the results are plotted in Figure 3- 34 and the values of k_4 for calculation of the maximum deflection are given in Table 3- 9. It can be found that k_4 with different aspect ratio differ a lot when the normalised load is small, i.e. a smaller aspect ratio contributes to a higher k_4. The curves rapidly decline and converge with increasing normalised load.

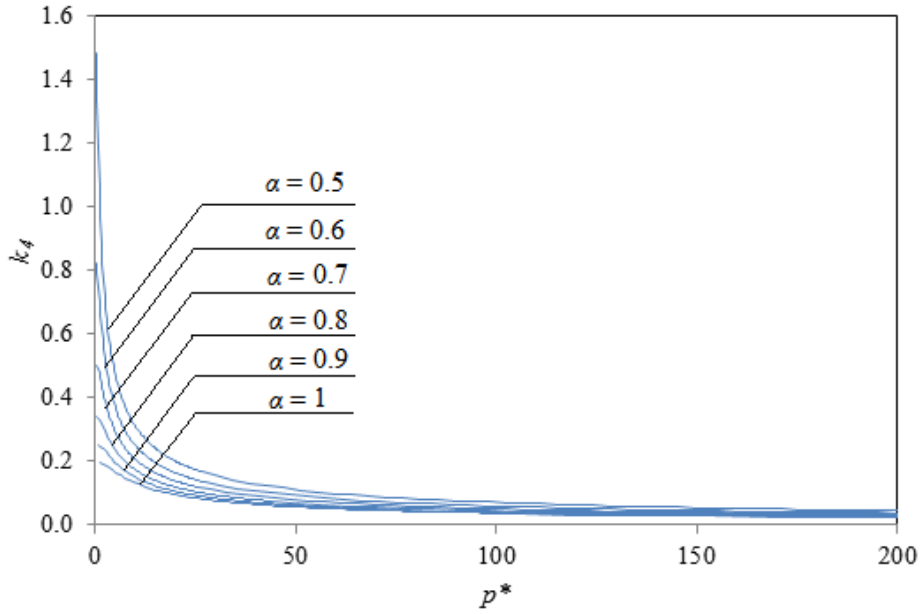

Figure 3- 34. Relations between k_4 and p^* with different aspect ratios α

Table 3- 9. Coefficient k_4 for calculation of the maximum deflection

	aspect ratio α					
p^*	**1**	**0.9**	**0.8**	**0.7**	**0.6**	**0.5**
1	0.1978	0.2480	0.3394	0.4780	0.7007	1.0590
2	0.1924	0.2377	0.3050	0.4158	0.5822	0.7648
3	0.1860	0.2226	0.2814	0.3629	0.4774	0.6442
4	0.1750	0.2074	0.2601	0.3224	0.4089	0.5402
5	0.1643	0.1980	0.2335	0.2911	0.3712	0.4701
6	0.1582	0.1853	0.2188	0.2720	0.3324	0.4248
7	0.1474	0.1741	0.2062	0.2507	0.3093	0.3890
8	0.1401	0.1640	0.1951	0.2332	0.2839	0.3562
9	0.1350	0.1557	0.1809	0.2184	0.2633	0.3296

10	0.1300	0.1480	0.1728	0.2058	0.2500	0.3074
20	0.0936	0.1037	0.1182	0.1375	0.1636	0.1995
30	0.0756	0.0829	0.0930	0.1066	0.1247	0.1551
40	0.0644	0.0702	0.0786	0.0889	0.1062	0.1274
50	0.0559	0.0609	0.0697	0.0793	0.0908	0.1092
60	0.0503	0.0546	0.0596	0.0688	0.0819	0.0987
70	0.0459	0.0497	0.0557	0.0635	0.0733	0.0887
80	0.0421	0.0467	0.0516	0.0581	0.0679	0.0808
90	0.0392	0.0430	0.0472	0.0538	0.0624	0.0756
100	0.0368	0.0399	0.0450	0.0502	0.0587	0.0702
200	0.0227	0.0257	0.0282	0.0320	0.0372	0.0444
300	0.0180	0.0198	0.0218	0.0246	0.0284	0.0341
400	0.0152	0.0144	0.0182	0.0204	0.0236	0.0282

3.5.2 Determination of coefficient k_5

As has been emphasized, k_5 is a nonlinear parameter in prEN 13474-2, i.e., it is varying with different normalized load p^* which nevertheless relies on the load share in the corresponding glass panel. Therefore, the determination of k_5 requires a series of trial and error. However, in the draft code prEN 16612 (2013), k_5 is modified to be a parameter which is only dominated by the aspect ratio λ. In the case of $\lambda = 1$, k_5 is a constant, equal to 0.0194. According to Eq. (3- 21) and (3- 22), the load share ratio can be expressed as λ:

$$\lambda = \frac{F_{panel1}}{F_{panel2}} = \frac{\delta_1 + \phi_1 \delta_2}{1 - \phi_2 \delta_2} \qquad 3\text{- }29$$

As given in Eq. (3- 29), the load share ratio is dependent on the insulating unit factor and the bending stiffness of the glass panels. According to Eq. (3- 20), the constant k_5 will contribute to a constant insulating unit factor and hence lead to an unchanged load share ratio (F_{d1}/F_{d2}) in an IGU, regardless of the influences by the increasing external loads.

The load share ratio calculated with p*-dependent k_5 used in prEN 13474-2 and p*-independent k_5 are compared below in Table 3- 10.

Table 3- 10. Comparison of the load share ratio λ calculated by prEN 13474-2 and prEN 16612

Applied load (kPa)	varying k_5'	consistent k_5	Error (k_5'/k_5)
1	1.095	1.095	0.02%
2	1.096	1.095	0.05%
3	1.098	1.095	0.30%
4	1.101	1.095	0.57%
5	1.104	1.095	0.86%
6	1.108	1.095	1.16%
7	1.111	1.095	1.49%
8	1.117	1.095	2.00%

The load share ratio calculated in prEN 13474-2 is rising slightly with increasing applied wind load. However the deviation from the corresponding results obtained from prEN 16612 is nearly negligible. The maximum error is 2%, which is within the error tolerance (≤ 5%). The maximum deflection and stresses on each glass panel calculated by both codes are presented below.

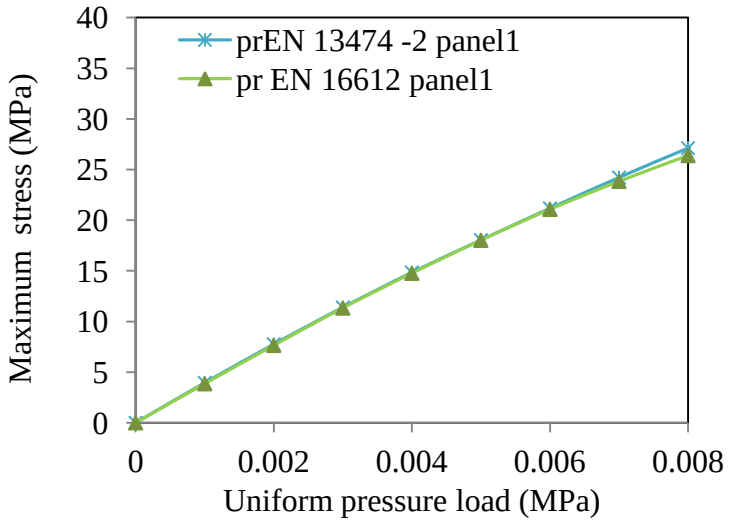

(a) Panel1

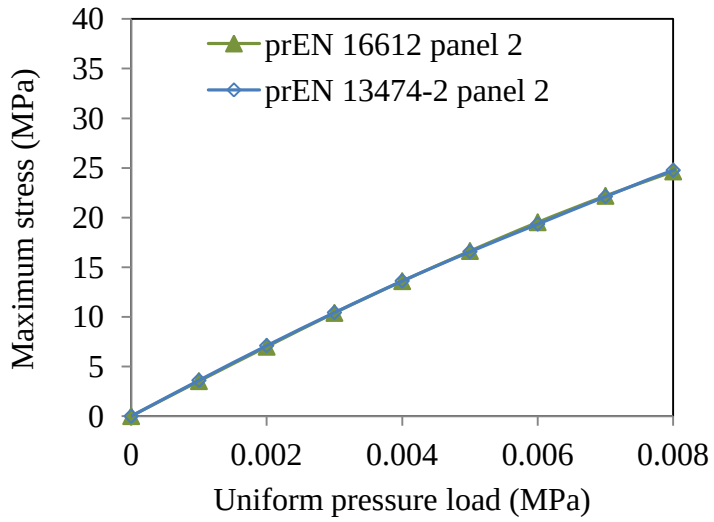

(b) Panel 2

Figure 3- 35. Maximum stresses in panel 1 and panel 2 for a 1000mm×1000mm IGU (6+12+6)

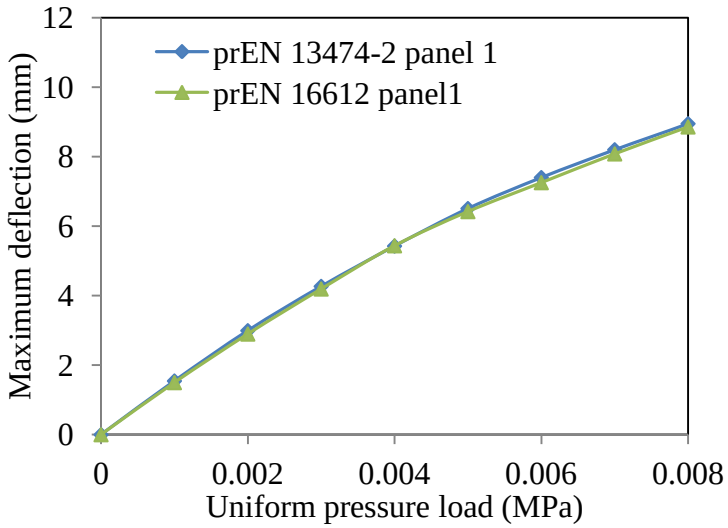

(a) Panel1

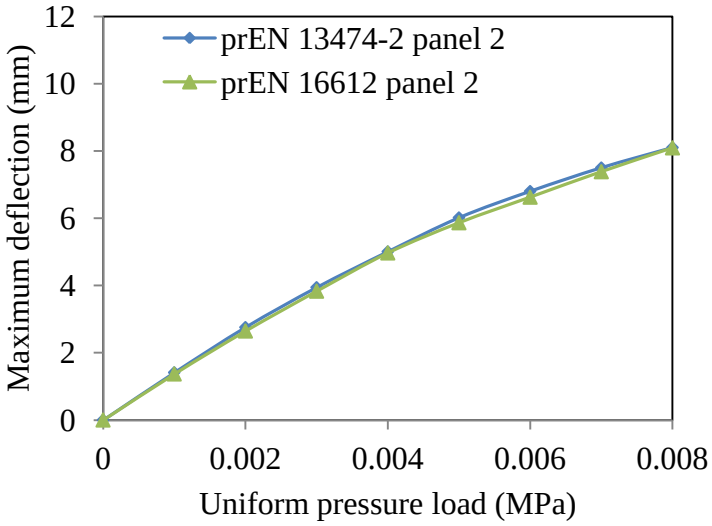

(b) Panel 2

Figure 3- 36. Maximum stresses in panel 1 and panel 2 for a 1000mm×1000mm IGU (6+12+6)

The results shown in Figure 3- 35 and Figure 3- 36 respectively, are in good agreement. Therefore the simplification of the parameter k_5 in prEN 16612 is acceptable to achieve the calculation accuracy. More importantly, it can effectively relieve computation loads by avoiding tedious iteration process.

The hydrostatic fluid model is employed to simulate the volume change and so as to determine the parameter of k_5. As has been verified, k_5 can be deemed as a parameter that is independent of the normalised load p^*. There is only a variable i.e. the aspect ratio α that affects the values of k_5. In the bending movement of an IGU, the total volume change ΔV can be calculated as follows:

$$\Delta V = V - (\Delta V_1 - \Delta V_2) \qquad 3\text{- }30$$

where V is the initial air cavity volume, ΔV_1 and ΔV_2 are the volume changes generated by the bending of panel 1 and panel 2, which are mathematically expressed by Eq (3-

13). Substituting Eq (3- 13) into Eq (3- 30), it can be put in the form of an expression of k_5.

$$k_5 = \frac{(V - \Delta V)h^3}{a^4(A/E)(p - 2\Delta p)} \qquad 3\text{- }31$$

where p is the external uniform pressure load, applied on the panel 1. A is the glass area, E is the Young's modulus, Δp is the pressure change of the deformed air cavity due to glass bending; a is the shorter dimension of the glass panel; h is the glass thickness.

Therefore, a group of IGU hydrostatic fluid models of different aspect ratios are established. The results are displayed in Figure 3- 37 and listed in Table 3- 11.

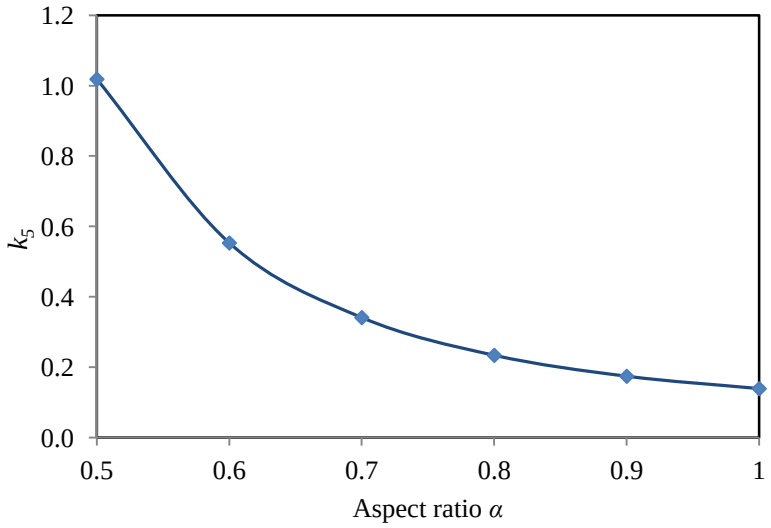

Figure 3- 37. Relation between k_5 and the aspect ratio of an IGU

Table 3- 11. Coefficient k_5 for calculation of the volume change

aspect ratio	1	0.9	0.8	0.7	0.6	0.5
k_5	0.139	0.174	0.234	0.341	0.553	1.018

Table 3- 9 and Table 3- 11 can be used for the calculation of maximum deflection, volume change, and the insulating unit factor in four point supported IGUs with thickness h = 6 mm.

3.6 Summary

In this chapter, hydrostatic fluids analysis implemented in the FEM package ABAQUS is adopted to simulate the structural responses of IGUs under interactive environmental impacts, which include: wind load, temperature-induced and altitude-induced pressure differential. Boyle's law for gas and the nonlinear mathematical equations to calculate the maximum stress and deflection of a monolithic glass panel are adopted to successfully validate the applicability of FEM models.

The validated IGU numerical models are then used to examine the IGU calculation parts in two draft European standards: prEN 13474-2 and prEN 16612. The insulating unit factor "ϕ" introduced in prEN 13474-2 is validated, as the numerical results and analytical results according to the draft code are found in good agreement. Then the modified coefficient k_5 proposed in prEN 16612 is investigated by means of FEM modelling. The value of the coefficient k_5 is confirmed to be independent on the normalized p*. Therefore the arduous iteration method for the determination of k_5 can be avoided, hence effectively relieves the computation load.

Size sensitivity of IGUs is considered in the coupling simulation. When subjected to same interactive environmental actions, the glass panels of different dimensions responded differently. In the sample with a = 500mm, thermal load induced by the temperature differential has acted as a predominant factor to determine the glass deflection, whereas the temperature change does not result in obvious influence in terms

of the maximum deflection in the sample with a =1500mm or above. It is found that the thermal actions can be negligible when the length a is above 2000mm. Compared with panel1, the deflection of panel 2 is observed to be more sensitive to the combined environmental loads. The size of IGUs also makes great difference on the load shares on panel 1 and 2. Panel 1 will be able to endure most of external loads when the IGU length is small, and the loads distributed onto two panels will be gradually equal with increasing IGU length.

Four-point corner supported condition is considered by FEM modelling. In order to conform to the existing code for the design calculation of continuously simply supported condition, new coefficients k_4 and k_5 are determined for the calculation of maximum deflection and volume change. The value of k_4 is dependent on the normalised load p^* and the aspect ratio of glass panel. Coefficient k_5 is found only to be different under varying aspect ratio, insensitive to the normalised load p^*. The tabular data of k_4 and k_5 with corresponding p^* and aspect ratio are provided for the design guidance of four-point supported boundary condition.

CHAPTER 4. STRUCTURAL ANALYSIS OF TRIPLE INSULATING GLAZING UNITS

4.1 Introduction

In addition to double IGUs, triple IGUs (TGUs) have emerged and been rapidly growing in the commercial market to achieve higher insulation performances (Reed, 2012). PPG Industry co. reported a 38.01% average reduction in the U-value of TGUs compared to the IGUs with the same specifications (PPG, 2010). However, very limited studies to date were found to examine the structural behaviour of these glazing products.

In this chapter, the structural behaviour of TGUs subjected to a uniform pressure load will be investigated numerically as a first step. FEM numerical models of TGU based on the validated IGU numerical models as introduced in Chapter 3 are established to examine the load sharing conditions of each glass panel in TGUs. Different loading combinations including differential temperature change and wind loads are investigated.

It is then followed by theoretical analysis to estimate the bending behaviours of TGUs. A linear analytical method is developed according to the thin plate theory and the Boyle's law for gas. The pressure changes in two air cavities Δp_1 and Δp_2 can be solved by a set of simultaneous quadratic equations. The results will be compared with FEM modelling. This linear solution is then extended to the nonlinear bending behaviour by using a group of empirical equations derived based on the design formula for IGUs proposed in prEN 13474-2. The external pressure, internal pressure caused by climatic/altitude changes are considered in the analytical equations. The mathematical derivation will be validated by FEM modelling as well. By means of validated

analytical method, the size sensitivity analysis of the load shares in each glass panel will be carried out in a parametric study.

4.2 FEM numerical modelling of conventional TGUs

In contrast to IGUs, TGUs encompass a more complicated interaction between three glass panels and two air cavities. In Chapter 3, FEM hydrostatic analysis has exhibited outstanding computation efficiency that allows for the consideration of different combination of environmental actions, different boundary conditions and the non-linear performance. Therefore, hydrostatic TGU models will be further developed in this chapter by extending the hydrostatic IGU models, which have been previously validated.

4.2.1 Model description

A TGU specimen is created as shown Figure 4-1. As the glass thickness is far less than its length, it can be deemed as a thin shell. Shell element S4 is therefore applied to simulate the glass panels. To reduce computational demand, the detailed edge configurations are simplified into uniform layers, which can also be modelled with shell elements. The TGU model is considered to consist of three monolithic glass panels of the same thickness 6mm. The unit size is 1000mm×1000mm.

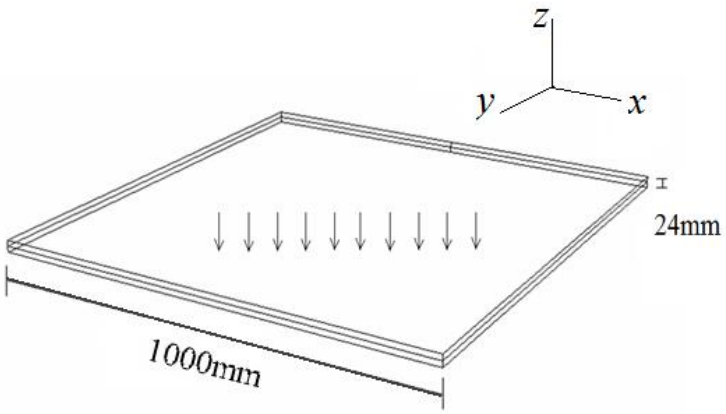

Figure 4- 1. Numerical model of a TGU

Two air cavities are considered in a TGU. Two air cavities will interact with each other via the inter-panel's bending deflection and the consequent cavity deformation. In ABAQUS CAE, fluid cavity can be defined in the module "Interaction" to simulate more than one fluid-filled or gas-filled structures based on Boyle's law for gas. Similar to the hydrostatic fluid analysis, the cavity surface boundaries and the associated reference nodes for two respective cavities need to be specified. Ambient pressure is set to be atmospheric pressure 0.1013MPa, and fluid cavity property is defined to be "pneumatic". The molecular weight of the sealed air is assumed to be 29 g/mol (Jacob, 1999). As shown in Figure 4- 2, the lower cavity is established, and the cavity boundary is highlighted in pink colour. It is noted that the ambient pressure is automatically predefined only within the cavities, not including the external surface of the TGU. An ambient pressure with the same magnitude should be manually imposed outside the TGU to balance the inner ambient pressure. The TGU model is simply supported on four edges, by fixing the displacement in *z* axis.

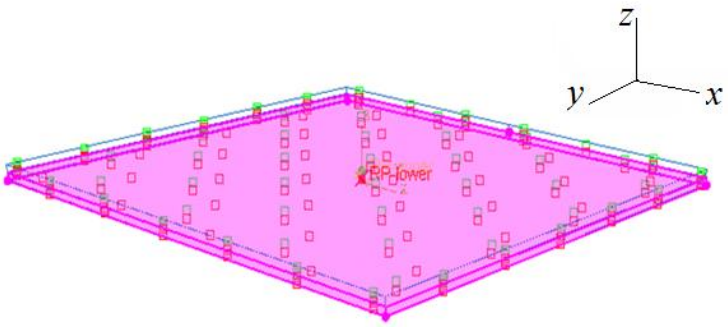

Figure 4- 2. Pneumatic fluid cavities defined in ABAQUS CAE

4.2.2 Thermal-mechanical coupling simulation

In this section, the thermal-mechanical coupling action will be investigated by nonlinear numerical modelling. Three actions are considered:

- Thermal expansion of glass panels
- Thermal expansion or contraction in two air cavities
- Uniform wind load

The assembling temperature T_a is assumed to be 18^{o}C, which represents the initial cavity temperature. The linear thermal expansion coefficient of glass panel is $9\times10^{-6}K^{-1}$. Due to the thermal insulation feature TGUs possess, the ambient temperatures on two sides of the TGU can differ substantially. Four seasonal scenarios are used in the modelling as illustrated in Figure 4- 3:

1. T_{upper}= -30^{o}C, T_{lower}= 30^{o}C, T_a=18^{o}C

2. T_{upper}= -30^{o}C, T_{lower}= 0^{o}C, T_a=18^{o}C

3. T_{upper}= 50^{o}C, T_{lower}= 20^{o}C, T_a=18^{o}C

4. T_{upper}=40^{o}C, T_{lower}= 10^{o}C, T_a=18^{o}C

where T_{upper} denotes the outdoor temperature, T_{lower} stands for indoor temperature and T_a is the ambient temperature of manufacturing.

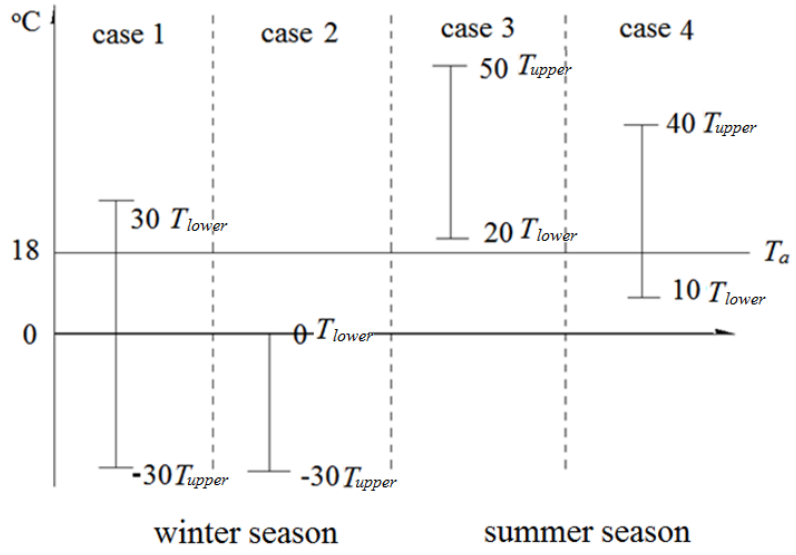

Figure 4- 3. Illustrative diagram of four temperature-wind coupling scenarios

The temperature of the upper cavity is assumed to be equal to the outdoor temperature and the same approximation is made to the lower cavity. A group of uniform load from zero up to 8kPa represents different wind levels. The modelling is conducted in three steps. In the initial step, the manually applied exterior pressure and the interior predefined pressure contribute to the equilibrium of the whole system. In the second step, the bending movement caused by the temperature change is simulated, and the wind load is applied in the third step.

The deflection contours of TGUs and the deflections of each glass panel under increased wind loads are presented below in Figure 4- 4 to 4-7. We define that the deflection in the same direction of the applied wind load is possitive.

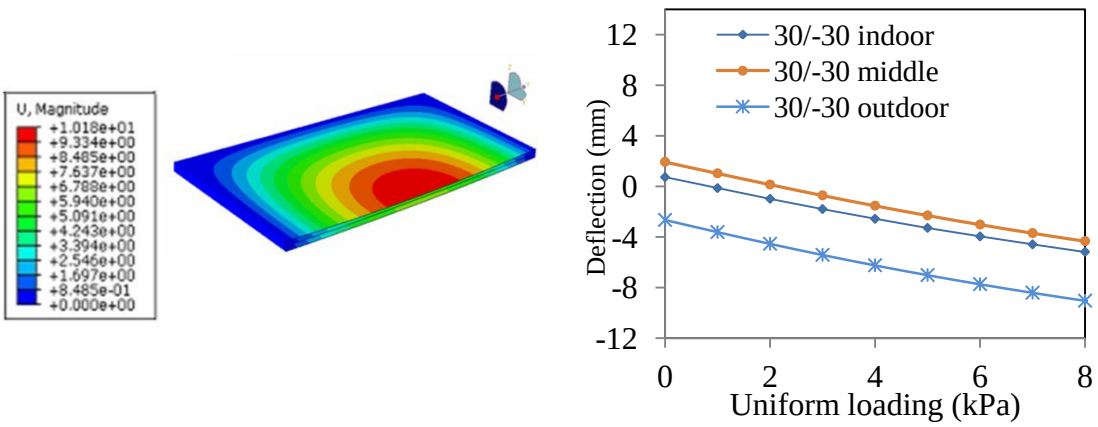

(a) Deflection contour of the TGU model (b) Deflections with increasing loading

Figure 4- 4. Glass panel deflections under increased wind load, with a temperature differential -30°C to 30°C

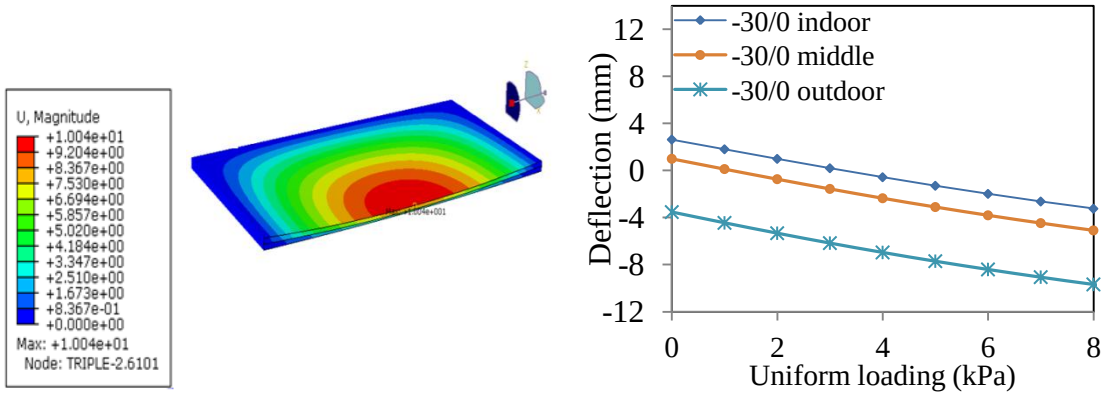

(a) Deflection contour of the TGU model (b) Deflections with increasing loading

Figure 4- 5. Glass panel deflections under increased wind load, with a temperature differential 0°C to 30°C

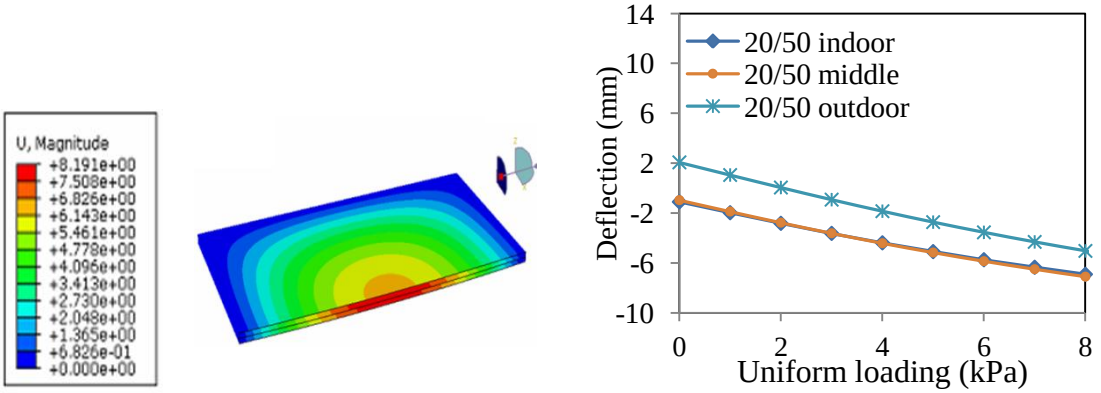

(a) Deflection contour of the TGU model (b) Deflections with increasing loading

Figure 4- 6. Glass panel deflections under increased wind load, with a temperature differential 20°C to 50°C

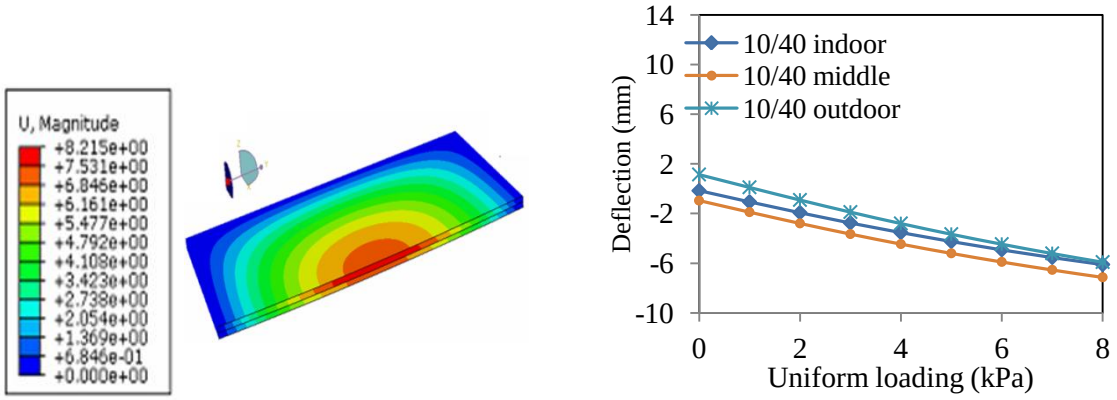

(a) Deflection contour of the TGU model (b) Deflections with increasing loading

Figure 4- 7 Glass panel deflections under increased wind load, with a ttemperature differential $10^{o}C$ - $40^{o}C$

In general, various coupling actions of wind load and seasonal temperature change will result in different mechanical responses of the glass panels. The bending deflection trend can be precisely estimated by FEM simulation. The outside panel will endure the greatest deflection in winter season, as the air contraction and wind load have a synergistic effect to increase the glass bending. In terms of summer season, wind load will counteract the outward bending of the outside panel because of the air expansion with increased temperature. So the maximum deflection takes place in the inter-panel.

4.3 Linear analytical calculation method

An analytical method is proposed to calculate the internal pressure changes in two air spaces in TGUs, which combined the Boyle's law for gas and the small deflection theory of rectangle plates (Timoshenko, 1940). Figure 4- 8 depicts the mechanical response of the test specimen due to the negative uniform pressure. Δp_1, Δp_2 is the pressure change in two air cavities. ω_1, ω_2 and ω_3 are the deflections of the lower, middle and upper panel respectively. Table 4- 1 provides the parameters and the corresponding denotations and values in the calculation.

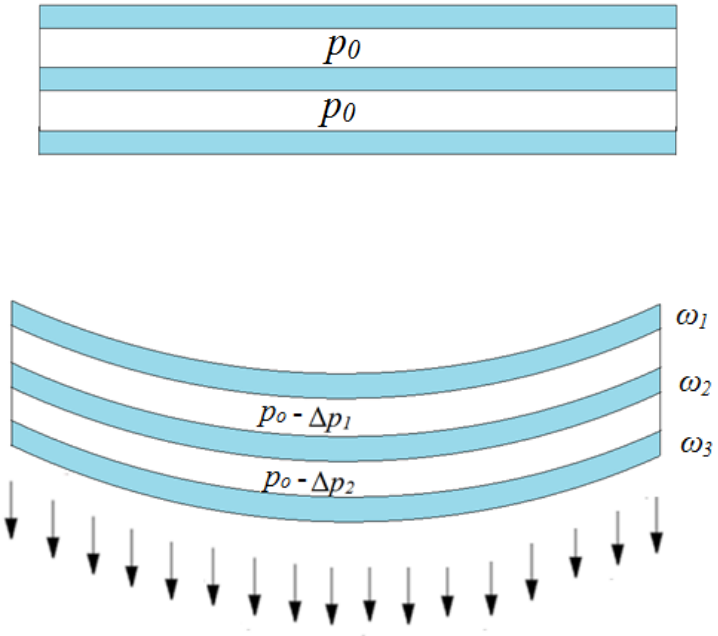

Figure 4- 8. Schematic diagram of the mechanical response of a TGU when subjected to uniform pressure

Table 4- 1. Required parameters in the analytical equations

Symbol	Denotation	Value
E	Young's modulus	72000MPa
υ	Poisson's ratio	0.22
a	shorter length of glass panel	1000mm
b	longer length of glass panel	1000mm
h	thickness of toughened glass panel	6mm
s	cavity thickness	12mm
V	initial volume of the air space	$1.2\times10^{7}mm^{3}$
p_0	initial internal pressure (atmospheric pressure)	0.1013MPa

Since the upper and lower panels are bonded with polymer sealants, they are deemed as simply supported. The spacer width is 20 mm for both cavities, which is only 1/50 of

the glass length. It is hence assumed that the edge sealants can provide a free rotation for the middle panel, i.e., a simply supported.

4.3.1 Mathematical derivation of linear analytical equations

According to the Theory of Plates and Shells (Timoshenko, 1940), for a simply supported model, the deflection at the location (*x*, *y*) on the glass (as shown in Figure 4-9) can be expressed as a function of the corresponding applied uniform pressure p_0 in Eq. (4-1):

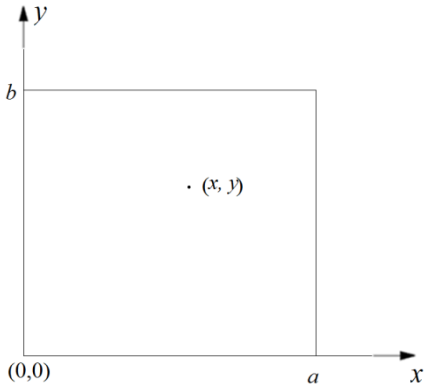

Figure 4- 9. Diagram of the location (x, y) in a Cartesian coordinate system

$$\omega(x,y)=\frac{16p_0}{\pi^6\delta}\sum_{m=1,3,5,\ldots}^{\infty}\sum_{n=1,3,5,\ldots}^{\infty}\frac{\sin\frac{m\pi x}{a}\sin\frac{n\pi y}{b}}{mn(\frac{m^2}{a^2}+\frac{m^2}{b^2})^2} \qquad 4\text{-}1$$

where, the formula converges quickly, hence *m* and *n* are deemed to be 1. Integrating the displacement over the whole plate,

$$\int_0^a\int_0^b \omega dxdy=\frac{16p_0}{\pi^6\delta}\int_0^a\int_0^b\frac{\sin\frac{\pi x}{a}\sin\frac{\pi y}{b}}{(\frac{1}{a^2}+\frac{1}{b^2})^2}dxdy \qquad 4\text{-}2$$
$$=\frac{64a^5b^5}{\pi^8(a^2+b^2)^2\delta}p_0=\frac{B}{\delta}p_0$$

where we define a geometric constant $B = \frac{64a^5b^5}{\pi^8(a^2+b^2)^2}$ 4- 3

The total volume changes of two air cavities can be calculated

$$\Delta V_1 = \left|\iint (w_2 - w_1)dxdy\right| = \left|\frac{B(p_0 - 2\Delta p_1 + \Delta p_2)}{\delta}\right| \quad 4\text{- }4$$

$$\Delta V_2 = \left|\iint (w_3 - w_2)dxdy\right| = \left|\frac{B(\Delta p_1 - 2\Delta p_2)}{\delta}\right| \quad 4\text{- }5$$

where, p_0 is the applied uniform pressure, Δp_1 and Δp_2 are the pressure change exerted by the deformed air cavities. δ is the bending stiffness of the glass panels. $\omega_1, \omega_2, \omega_3$ are the deflections of each panel, as illustrated in Figure 4- 8.

By substituting the volume change ΔV into the Boyle's law for gas as given,

$$p_0 V = (p_0 + \Delta p)(V - \Delta V) \quad 4\text{- }6$$

A set of simultaneous quadratic equations in terms of Δp_1 and Δp_2 can be established in Eqs. (4-7) and (4-8).

$$\begin{cases} p_0 V = (p_0 - \Delta p_1)\left(V + \frac{B}{\delta}(p_0 - 2\Delta p_1 + \Delta p_2)\right) & 4\text{- }7 \\ p_0 V = (p - \Delta p_2)\left(V + \frac{B}{\delta}(\Delta p_1 - 2\Delta p_2)\right) & 4\text{- }8 \end{cases}$$

In this method, the analytical solutions of the simultaneous equations are very complicated. Therefore Δp_1 and Δp_2 are directly solved numerically. A uniform pressure p_0 from 0 to 8kPa is applied in this method. The results are presented in Table 4- 2.

Table 4- 2. Numerical solutions of the simultaneous quartic equations

p_0 (kPa)	Δp_1 (kPa)	Δp_2 (kPa)
1	0.617	0.295
2	1.234	0.589
3	1.851	0.883
4	2.464	1.176
5	3.083	1.47
6	3.70	1.763
7	4.312	2.055
8	4.926	2.345

By substituting the results in Eq (4-7) and (4-8) given in Roarks' Formula (Young and Budynas, 2002), we obtain the stresses and deflections on each panel of the composite glazing unit.

$$\sigma_{upper} = \frac{\beta b^2 (p - \Delta p_1)}{h^2},\ \sigma_{mid} = \frac{\beta b^2 (\Delta p_1 - \Delta p_2)}{h^2},\ \sigma_{lower} = \frac{\beta b^2 \Delta p_2}{h^2} \qquad 4\text{- }9$$

$$\omega_{upper} = \frac{\alpha b^4 (\Delta p - \Delta p_1)}{E h^3},\ \omega_{mid} = \frac{\alpha b^4 (\Delta p_1 - \Delta p_2)}{E h^3},\ \omega_{lower} = \frac{\alpha b^4 \Delta p_2}{E h^3} \qquad 4\text{- }10$$

where α and β are the numerical constants that are related to the aspect ratio and material properties. When the aspect ratio of the plate equals to 1, $\alpha = 0.0463$, and $\beta = 0.2874$ for v = 0.22.

4.3.2 Validation of linear analytical equations

The calculated maximum bending stress and deflections are plotted below in Figure 4-10, Figure 4- 11 and Figure 4- 12, compared with FEM nonlinear modelling.

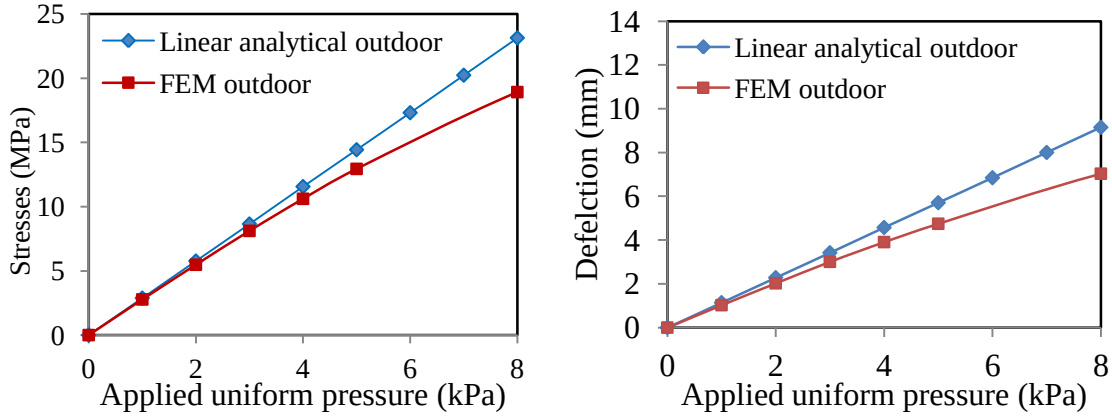

Figure 4- 10. Comparison of the maximum principal stresses and the maximum deflection in the outdoor panel

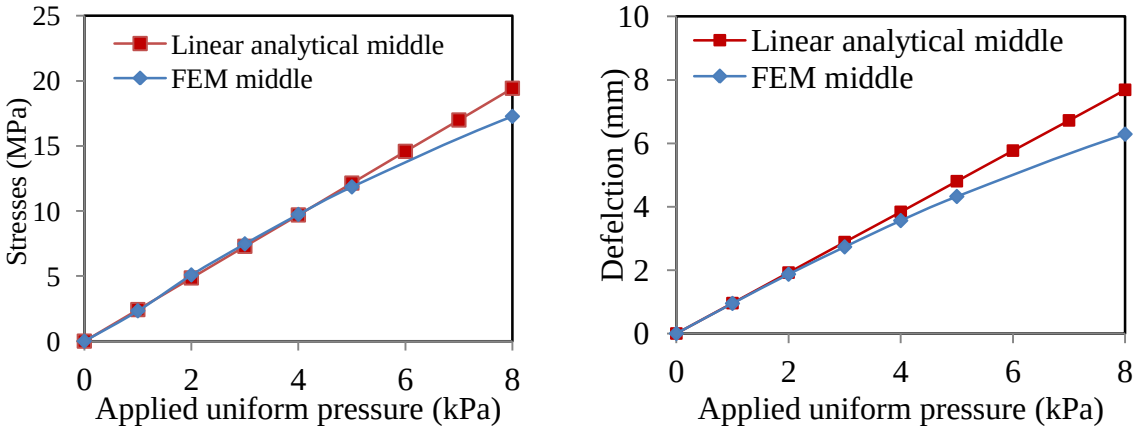

Figure 4- 11. Comparison of the maximum principal stresses and the maximum deflection in the inter-panel

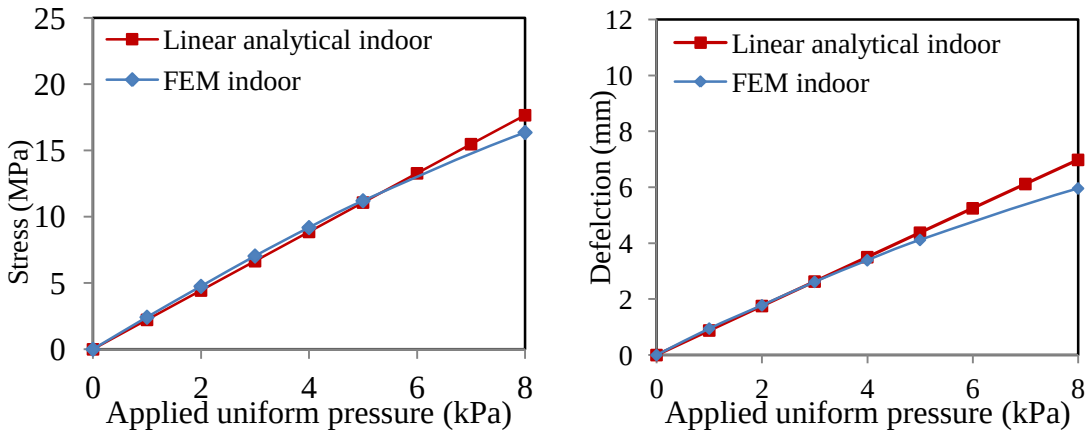

Figure 4- 12. Comparison of the maximum principal stresses and the maximum deflection in the indoor panel

It can be found that the results from the linear analytical method fit well with FEM

modelling for the loading level below 3kPa. Disagreements between two methods in the higher loading levels are observed, i.e. the linear analytical solution provides higher values than the FEM modelling. The discrepancy in the upper panel is the most significant. Therefore, the nonlinear analytical solution is expected to better depict the large bending deformation of glass panels.

4.4 Nonlinear analytical calculation method

4.4.1 Theoretical evaluation method for IGUs adopted in prEN 13474-2

prEN 13474-2 has provided a detailed estimation method to calculate the maximum bending stress and the deflection in IGUs with large deformation. In this section, a similar method is proposed on the basis of prEN 13474-2, in order to calculate the load share on each glass panel in a TGU. The analytical results will be compared with the validated numerical models, so as to check the applicability of the equations.

As introduced in Chapter 3, a new parameter is defined in prEN 13474-2: insulating factor ϕ. The definition of ϕ is first introduced by Feldmeier (2003). Feldmeier gave an approximation expression of the pressure difference of the cavity Δp in IGUs by using the insulating factor ϕ.

The schematic diagram is presented in Figure 4- 13.

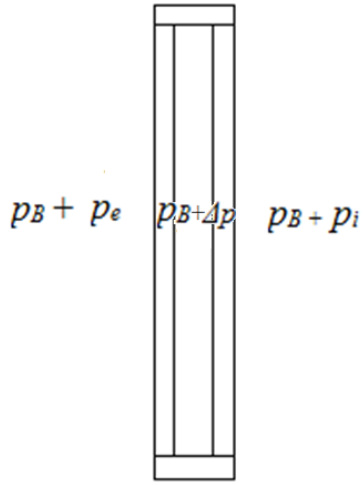

Figure 4- 13. Schematic figure of IGU subjected to a pressure differential

And the pressure difference is expressed in Eq. (4-11):

$$\Delta p = (1-\phi)\cdot(\delta_i \cdot p_e + \delta_e p_i) + \phi \cdot \Delta p_0 \qquad 4\text{- }11$$

where, p_b is the ambient pressure; δ_i and δ_e are the stiffness of external and internal panel, p_e and p_i denote the pressure differences of outdoor and indoor ambient. Δp_0 refers to the pressure change in the cavity due to internal climatic action. ϕ is the insulating unit factor, given as Eq.(4-12) (Feldmeier, 2003).

$$\phi = \frac{1}{1+(v_e+v_i)p_B/V_P} \qquad 4\text{- }12$$

where v_e and v_i are defined as the volume per load for panel 1 and panel 2; p_B is the ambient pressure; V_p is the cavity volume at the production time.

4.4.2 Empirical formula derivation for TGUs

In the case of triple glazing unit, Eq. (4- 11) can be also adopted to calculate the pressure differences in both air cavities, by treating TGU as two IGUs. The calculation model is illustrated in Figure 4- 14

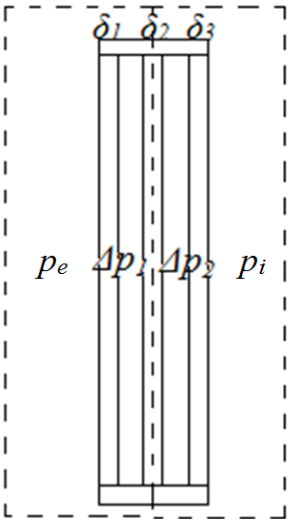

Figure 4- 14. TGU analysis model

From the left two glass panels and the air cavity in between, we have

$$\Delta p_1 = (1-\phi_1)\cdot(\delta_2 \cdot p_e + \delta_1 \cdot \Delta p_2) \qquad 4\text{- }13$$

Similarly, from the right two panels and the air cavity in between, we have,

$$\Delta p_2 = (1-\phi_2)\cdot(\delta_3 \cdot \Delta p_1 + \delta_2 \cdot p_i) \qquad 4\text{- }14$$

where ϕ_1 and ϕ_2 are the insulating unit factors of the left and right air cavities respectively; δ_1 , δ_2, and δ_3 are the bending stiffness of each panel.

By substituting Eq. (4-14) to Eq.(4-13), Δp_1 can be expressed as following:

$$\Delta p_1 = \frac{\delta_2(1-\phi_1)\cdot[p_e + (1-\phi_2)\cdot\delta_1 p_i]}{\Delta} \qquad 4\text{- }15$$

By substituting Eq.(4-13) into (4-14) and Δp_2 can be obtained:

$$\Delta p_2 = \frac{\delta_2(1-\phi_2)[(1-\phi_1)\cdot\delta_3 \cdot p_e + p_i]}{\Delta} \qquad 4\text{- }16$$

where,

$$\delta_1 = \frac{h_1^3}{h_1^3 + h_2^3} \qquad 4\text{- }17$$

$$\delta_2 = \frac{h_2^3}{h_1^3 + h_2^3} \quad \text{4- 18}$$

$$\delta_3 = \frac{h_3^3}{h_2^3 + h_3^3} \quad \text{4- 19}$$

$$\phi_1 = \frac{1}{1 + (v_1 + v_2)\, p_B / V_P} \quad \text{4- 20}$$

$$\phi_2 = \frac{1}{1 + (v_2 + v_3)\, p_B / V_P} \quad \text{4- 21}$$

$$\Delta = 1 - \delta_1 \delta_3 (1 - \phi_1)(1 - \phi_2) \quad \text{4- 22}$$

According to prEN 13474-2, the air volume can be expressed in terms of unit load as:

$$v = k_5 \frac{a^5 b}{h^3 E} \quad \text{4- 23}$$

Therefore, the load share acting on each glass panel $F_{d;i}$ can be expressed as:

$$F_{d;1} = p_e - \Delta p_1 = \frac{[\Delta - (1 - \phi_2) \cdot \delta_2]\, p_e - (1 - \phi_1)(1 - \phi_2)\delta_1 \delta_2\, p_i}{\Delta} \quad \text{4- 24}$$

$$F_{d;2} = \Delta p_1 - \Delta p_2 = \frac{(1 - \phi_1)[1 - (1 - \phi_2)\delta_3]\delta_2\, p_e - (1 - \phi_2)(1 - \delta_1)\delta_2\, p_i}{\Delta} \quad \text{4- 25}$$

$$F_{d;3} = \Delta p_2 = \frac{\delta_2 (1 - \phi_2)[(1 - \phi_1) \cdot \delta_3 \cdot p_e + p_i]}{\Delta} \quad \text{4- 26}$$

4.4.3 Validation using FEM modelling

Again, the nonlinear FEM models are adopted to validate the derived equations. A group of uniform pressure p_0 from 1kPa to 8kPa is applied. The maximum principal stresses and maximum deflection are examined for both mathematic equations and FEA models. The linear analytical results are also presented for comparison.

In the nonlinear analytical solution, the maximum deflections and maximum tensile bending stresses can be calculated by following the equations given in prEN 16612 (2013)

$$\sigma_{max} = k_1 \frac{a^2}{h^2} F_d \qquad 4\text{- }27$$

$$\omega_{max} = k_4 \frac{a^4}{h^3} \frac{F_d}{E} \qquad 4\text{- }28$$

The varying nonlinear geometry coefficients k_1, k_4 and k_5 are given in the code.

The analytical results and FEM modelling are presented and compared below in Figure 4- 15 to Figure 4- 20.

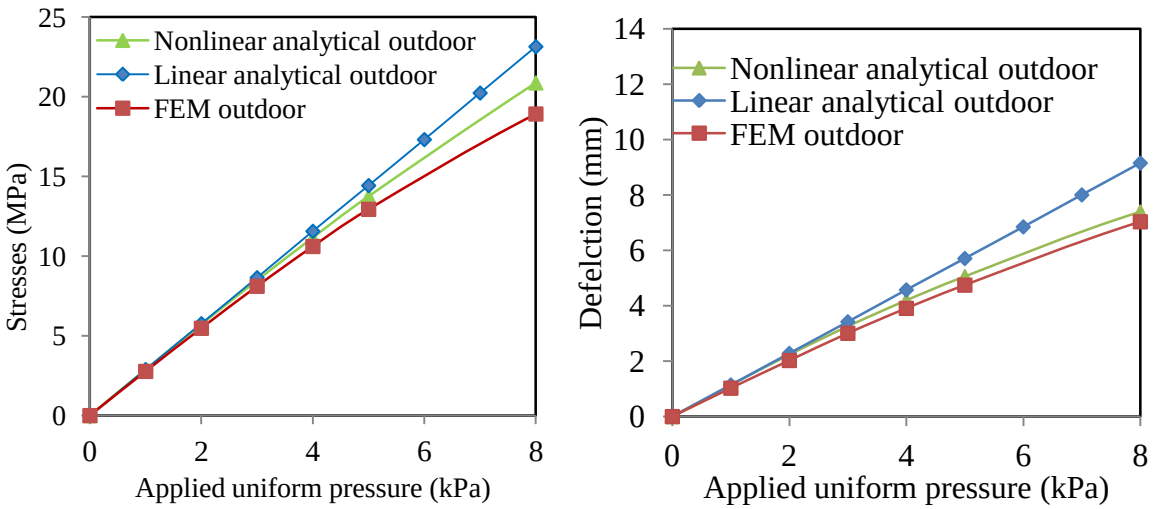

Figure 4- 15. Comparison of the maximum deflection and maximum principal stresses in the outdoor panel

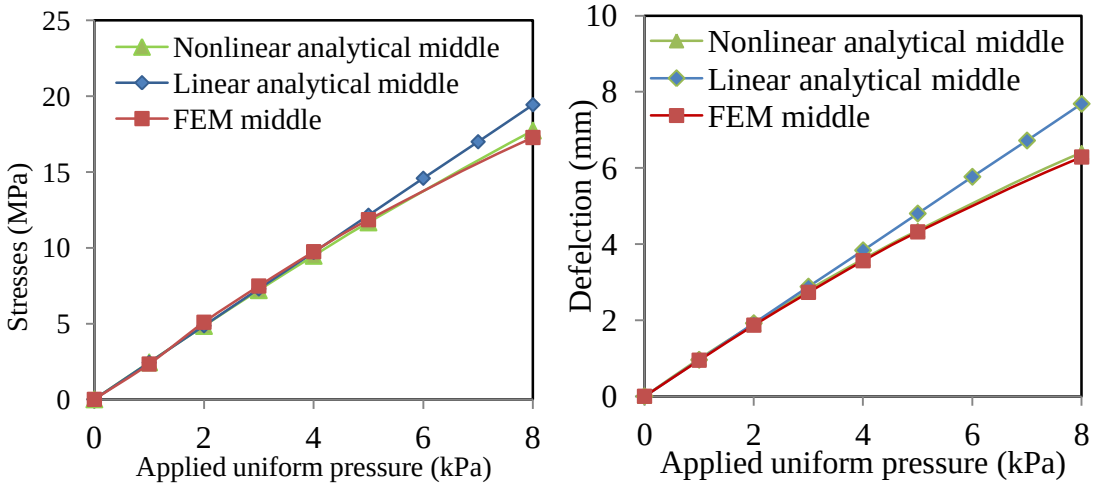

Figure 4- 16. Comparison of the maximum deflection and maximum principal stresses in the inter-panel

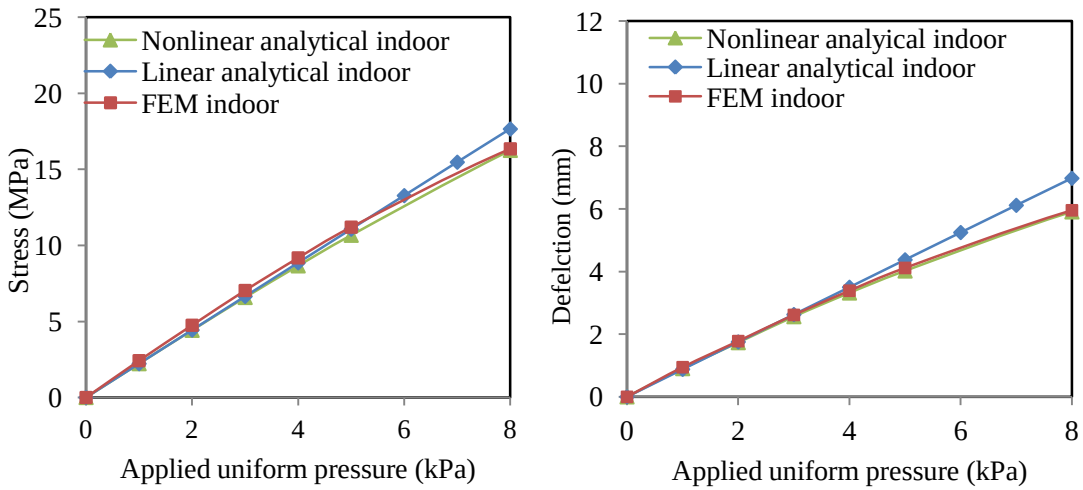

Figure 4- 17. Comparison of the maximum deflection and maximum principal stresses in the indoor panel

By observing Figure 4- 15 to Figure 4- 17, it can be found that the nonlinear analytical results are in good accordance with FEM modelling, which address the problem arising from linear analysis. Higher loading conditions are further considered to explore the theoretical applicability range of the derived mathematic equations. A group of uniform pressure loads from 0 to 20kPa is applied.

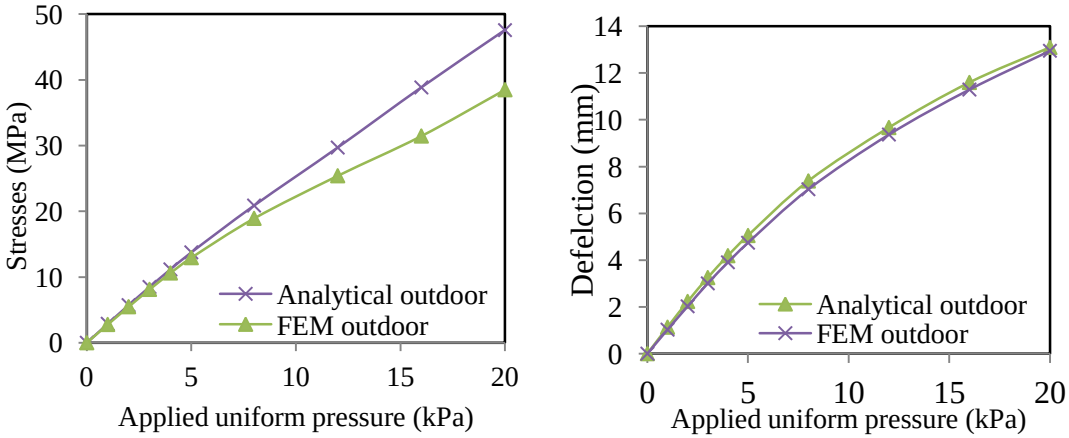

Figure 4- 18. Comparison of the maximum deflection and maximum principal stresses in the outdoor panel

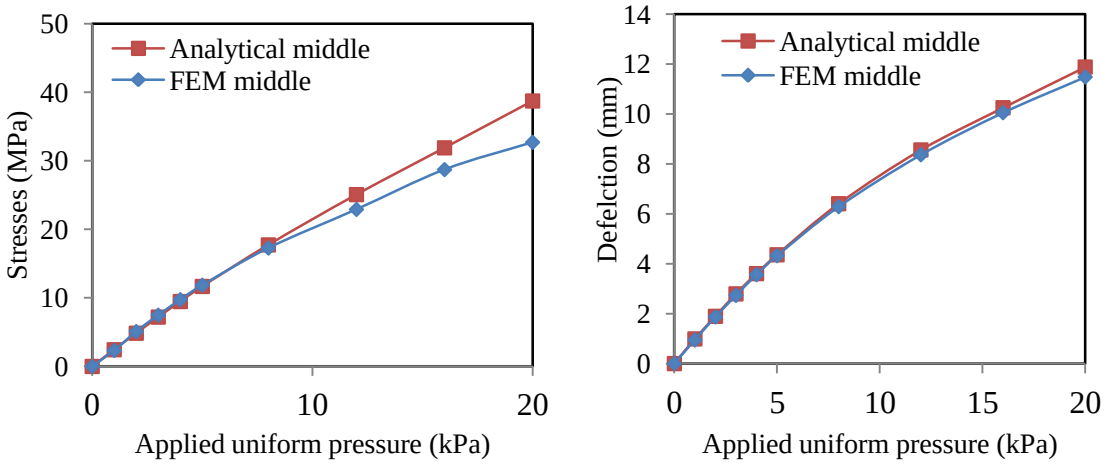

Figure 4- 19. Comparison of the maximum deflection and maximum principal stresses in the inter-panel

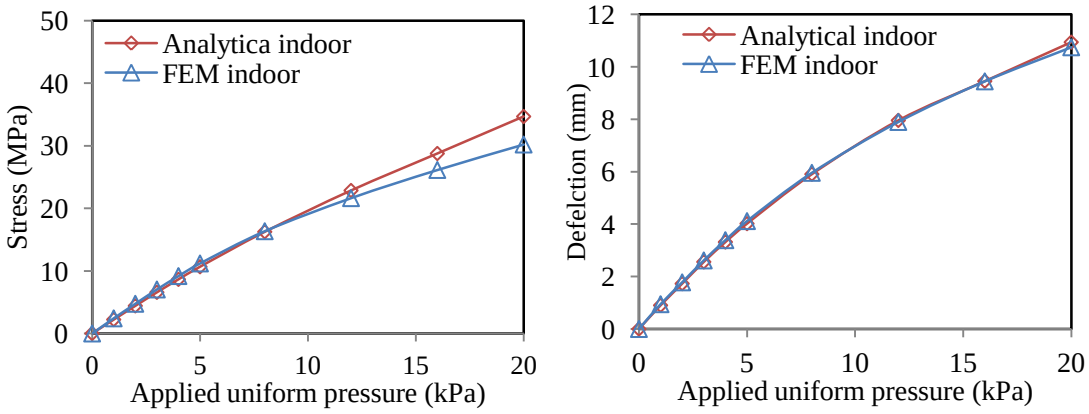

Figure 4- 20. Comparison of the maximum deflection and maximum principal stresses in the indoor panel

In Figure 4- 18 to Figure 4- 20, it is observed that considerable discrepancies take place in the maximum bending stresses at higher loading condition, whereas the maximum deflections obtained from two approaches concur well. It is the membrane effect in the nonlinear FEM modelling that offsets a certain amount of bending stresses. Detailed

discussion of membrane stresses and bending stresses is referred to section 3.3.7 in Chapter 3. As Vuolio (2003) stated, the product design code on the other hand underestimated the membrane effect and provided relatively conservative stress results. It is noted that the glass panels are very likely to have fractured before the pressure loads reach this high level in reality. Therefore the deviations between FEM results and analytical equations at high loading level have little influence on the accuracy of the theoretical calculation in terms of practical scenarios.

The load shares in each glass panel calculated from the linear and the nonlinear analytical method are compared in Figure 4- 21

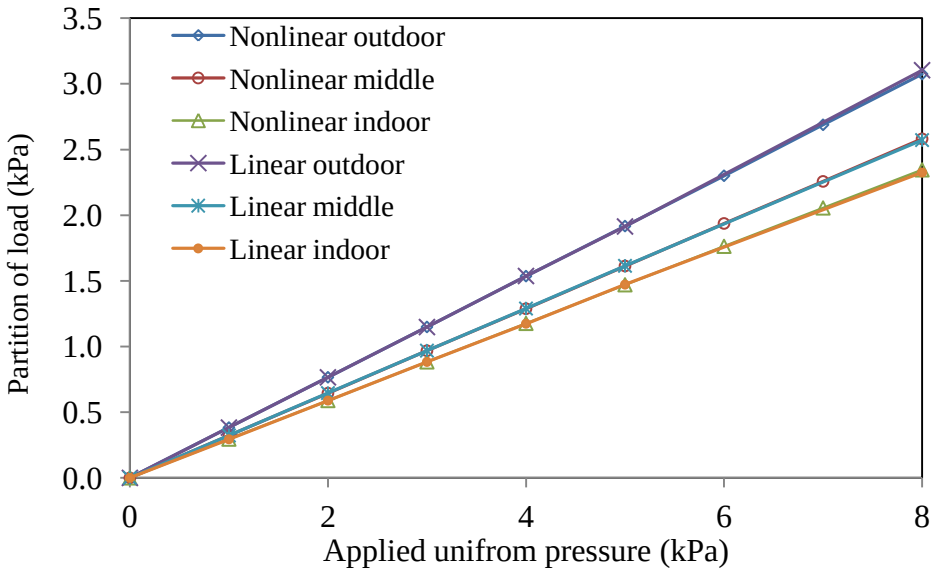

Figure 4- 21. Load share on each glass panel calculated by linear and nonlinear methods

It is surprising to find that the shares of load carried by each glass panel in the two methods are remarkably consistent. However, the maximum stresses/deflection demonstrates significant distinction between linear and nonlinear results. Therefore it can be concluded that the nonlinearity features in the TGUs bending calculation mainly affect the values of the maximum bending stresses and deflection, but are irrelevant to the load share on each glass panel.

4.4.4 Theoretical equations for climatic/altitude actions and the coupling actions

With the analytical equations in terms of uniform pressure load being validated, the same mathematical derivation can also be adopted to calculate other types of loading conditions. In the case of climatic or altitude differential induced actions only, the glass panels in a TGU will undergo the internal pressure changes Δp_{int} induced in two air cavities. Eq. (4-11) can be expressed as follows:

$$\Delta p_{\text{int};1} = (1-\phi_1)\delta_1 \Delta p_{\text{int};2} + \phi_1 p_{p;1} \quad \text{4- 29}$$

$$\Delta p_{\text{int};2} = (1-\phi_2)\delta_3 \Delta p_{\text{int};1} + \phi_2 p_{p;2} \quad \text{4- 30}$$

where $p_{p,1}$ and $p_{p,2}$ are the isochoric pressure change caused by climatic or altitude differential in the upper air cavity and lower air cavity respectively.

Combining Eq. (4- 29) and (4- 30), the internal pressure changes of the upper and lower air cavities are obtained:

$$\Delta p_{\text{int};1} = \frac{(1-\phi_1)\delta_1\phi_2}{\Delta} p_{p;2} + \frac{\phi_1}{\Delta} p_{p;1} \quad \text{4- 31}$$

$$\Delta p_{\text{int};2} = \frac{(1-\phi_2)\delta_3\phi_1}{\Delta} p_{p;1} + \frac{\phi_2}{\Delta} p_{p;2} \quad \text{4- 32}$$

The load share on each glass panel is given :

$$F_{d;1} = p_e - \Delta p_{\text{int};1} = p_e - \frac{(1-\phi_1)\delta_1\phi_2}{\Delta} p_{p;2} - \frac{\phi_1}{\Delta} p_{p;1} \quad \text{4- 33}$$

$$F_{d;2} = \Delta p_{\text{int};1} - \Delta p_{\text{int};2}$$
$$= \frac{[(1-\phi_1)\delta_1 - 1]\phi_2 p_{p;2} + [1-(1-\phi_2)\delta_3]\phi_1 p_{p;1}}{\Delta} \quad \text{4- 34}$$

$$F_{d;3} = \Delta p_{\text{int};2} = \frac{(1-\phi_2)\delta_3\phi_1}{\Delta} p_{p;1} + \frac{\phi_2}{\Delta} p_{p;2} \quad \text{4- 35}$$

In the case of combined actions of wind load and the isochoric pressure changes, we have :

$$\Delta p_{tot;1} = (1-\phi_1)(\delta_2 p_e + \delta_1 \Delta p_{tot;2}) + \phi_1 p_{p;1} \quad \text{4- 36}$$

$$\Delta p_{tot;2} = (1-\phi_2)(\delta_3 \Delta p_{tot;1} + \delta_2 p_i) + \phi_2 p_{p;2} \quad \text{4- 37}$$

In the same manner, the substitution of Eq. (4-36) into Eq.(4-37) leads to

$$\Delta p_{\text{tot;1}} = \frac{\delta_2(1-\varphi_1)\cdot[p_e + (1-\varphi_2)\cdot\delta_1 p_i] + (1-\phi_1)\delta_1\phi_2 p_{p;2} + \phi_1 p_{p;1}}{\Delta} = \Delta p_1 + \Delta p_{\text{int;1}} \quad \text{4- 38}$$

$$\Delta p_{\text{tot;2}} = \frac{\delta_2(1-\varphi_2)[(1-\varphi_1)\cdot\delta_3\cdot p_e + p_i] + (1-\phi_2)\delta_3\phi_1 p_{p;1} + \phi_2 p_{p;2}}{\Delta} = \Delta p_2 + \Delta p_{\text{int;2}} \quad \text{4- 39}$$

It is found that the pressure change in two cavities under combined loading can be expressed as a simply superposition of the pressure change caused by the individual actions.

4.4.5 Parametric study of the TGU size and spacer width

In order to investigate the size sensitivity of the TGU, a group of square TGUs with the length from 500mm to 3000mm are taken into consideration. Each glass panel is of the thickness 6mm. As mentioned above, a unit uniform pressure load p_e is applied on the upper panel. The calculated load share ratio under unit pressure is showed in Figure 4-22

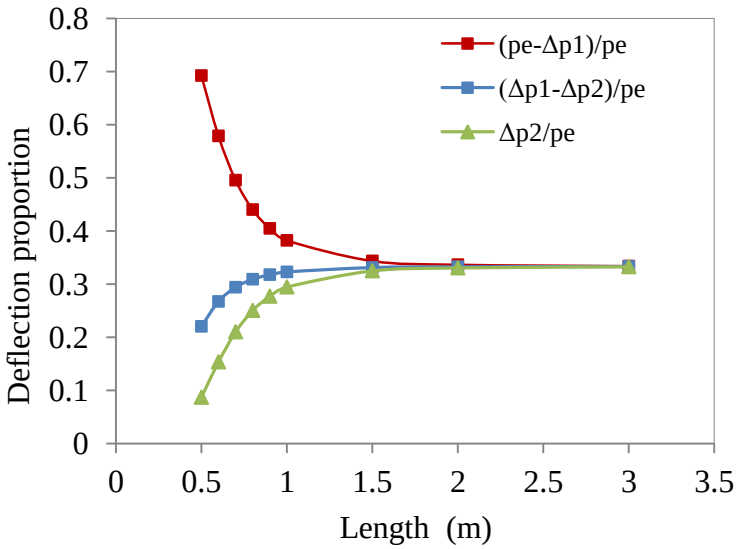

Figure 4- 22. Load share ratio versus glazing size under unit pressure load

The load share ratio is found to be very sensitive to the size. When the length is 500mm, the upper panel carries 69.24% of the total applied pressure, while the inter-panel and the lower panel endure 22% and 8% respectively. The great divergence converges rapidly with increasing size. When the length of the glazing is more than 2000mm, the loads in each panel are evenly allocated for 6 mm monolithic glass panel. Each panel carries 33.33% of the total load and the proportion remains unchanged with larger size. The results indicate that the upper panel carries most proportion of the applied pressure in the case of small size models.

The thickness of the air cavities *s* is taken into account in the parametric study. The results are plotted in Figure 4- 23.

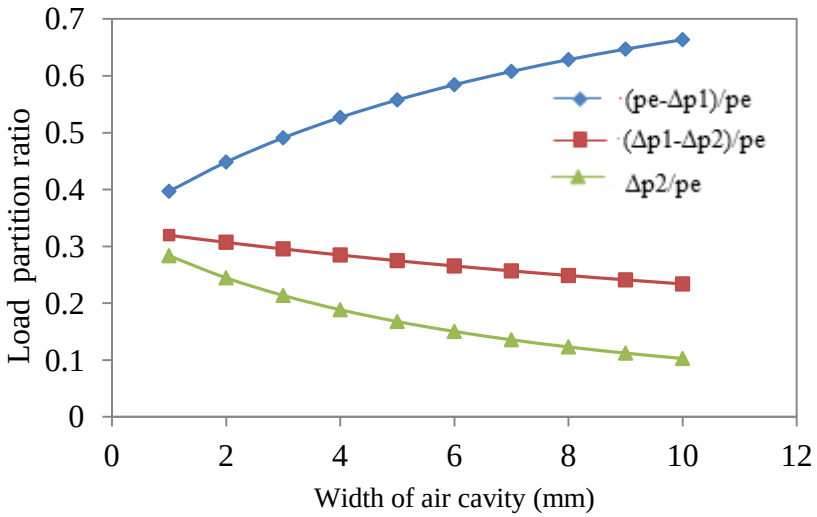

Figure 4- 23. Load share ratio versus the width of air cavity under unit pressure load

It can be seen that the load share ratio is very sensitive to the width of air cavity. The load share ratio diverges with increasing width, which indicates that the upper panel will carry more loads with larger width of the air cavity. When the width of air cavity is reduced to 1mm, the applied loads are nearly averagely imposed on each panel. However, the thin air cavities will result in inevitable degraded thermal insulation. The insulation function can be eliminated by using a VGU as the inter-panel. Observing Figure 4- 22 and Figure 4- 23, the larger the glazing size or the smaller the cavity width is, the more average three load share ratios are. Therefore it can be inferred that the ratio of the glazing size and the width of air cavity *a/s* is larger, the load share ratio is more average, vice versa.

4.4.6 Parametric study of the thickness of the inter-panels in TGUs

In this section we will focus on the thickness of the inter-panel and the consequent structural influences to the whole glazing construction. The thickness of the inter-panel is considered from 1mm to 8mm with an interval of 1mm. Two terms “normalised stress”

and “normalised deflection” are proposed, so only one variable, “thickness of the inter-panel” will be taken into analysis.

$$\begin{cases} \sigma_{NORM.\text{outdoor}} = \dfrac{k_1 b^2 (p_e - \Delta p_1)}{1000 h_1^{\,2} p_e} \\ \sigma_{NORM.\text{middle}} = \dfrac{k_1 b^2 (\Delta p_1 - \Delta p_2)}{1000 h_2^{\,2} p_e} \\ \sigma_{NORM.\text{indoor}} = \dfrac{k_1 b^2 \Delta p_2}{1000 h_3^{\,2} p_e} \end{cases} \qquad 4\text{- }40$$

$$\begin{cases} \omega_{NORM.\text{outdoor}} = \dfrac{k_4 b^4 (p_e - \Delta p_1)}{1000 E h_1^{\,3} p_e} \\ \omega_{NORM.\text{middle}} = \dfrac{k_4 b^4 (\Delta p_1 - \Delta p_2)}{1000 E h_2^{\,3} p_e} \\ \omega_{NORM.\text{indoor}} = \dfrac{k_4 b^4 \Delta p_2}{1000 E h_3^{\,3} p_e} \end{cases} \qquad 4\text{- }41$$

The normalised stress distribution and deflection distribution along with different inter-panel thickness are plotted in Figure 4- 24.

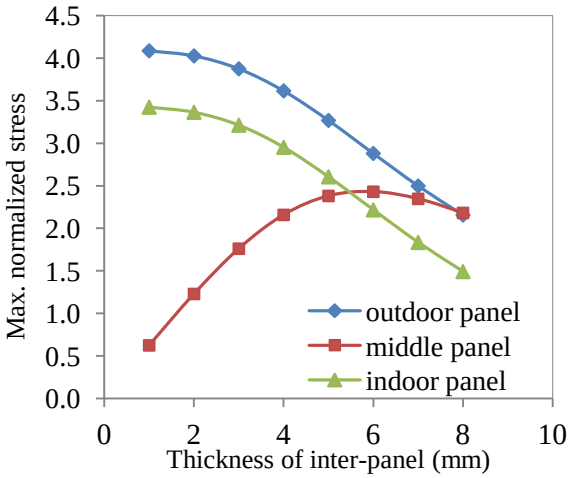

(a). Normalized maximum stress

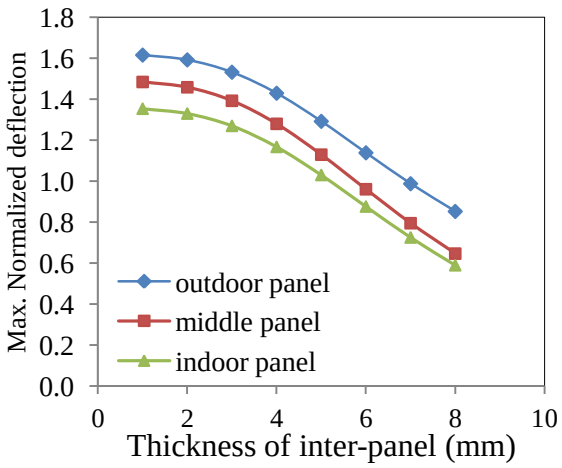

(b). Normalised maximum deflection

Figure 4- 24. Normalised stress and deflection on each panel with increasing loads

It Figure 4- 24(a), the proportionate declines of the normalised stresses in the upper and lower panel are observed with increased inter-panel thickness. On the contrary, the maximum principal stress in the inter-panel increases rapidly in the low thickness range and then drops slightly since the thickness of inter-panel exceeds the other two panels. The maximum normalised stress in the inter-panel reaches peak value when the thicknesses of three panels are equal. As shown in Figure 4- 24 (b), the increase in the inter-panel thickness will consistently reduce the deflections of all three panels in the TGU, namely increase the overall bending stiffness of the TGU.

Figure 4- 25 presents the deflection proportions of three panels. The increasing thickness of the inter-panel will result in higher deflection proportion of the receiving panel (upper panel), whereas slightly reduce the deflection proportions of the inter-panel and lower panel. This is because higher stiffness leads to a lower deflection in the inter-panel, and successively hinders the bending behaviour of the lower panel, by reducing the volume change of the second air cavity.

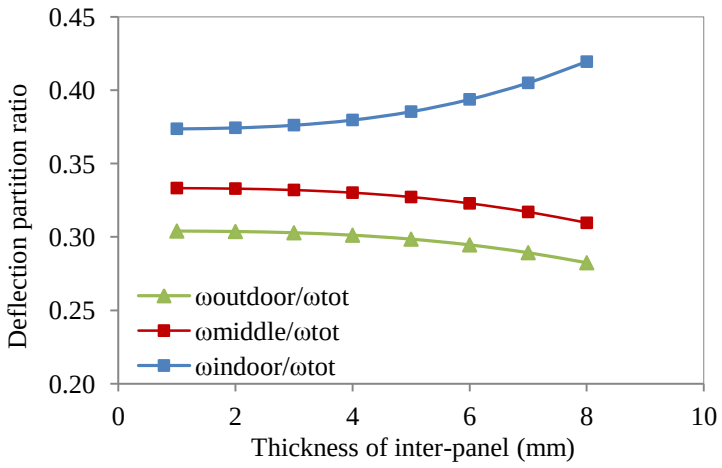

Figure 4- 25. Deflection proportion of three panels with increasing inter-panel thickness

The load share ratios varying with increasing thickness of the inter-panel are plotted in Figure 4- 26. The uniform load applied on the inter-panel is found to be reduced to nearly zero when its thickness reaches 1mm. The loads are carried by the lower and upper panel. The load proportion then can be estimated by ignoring the inter-panel. The TGU can be then equivalent to an IGU with double-sized cavity from the view of structural performance. The thin glass panel is only acting as an insulation layer, without actual mechanical support.

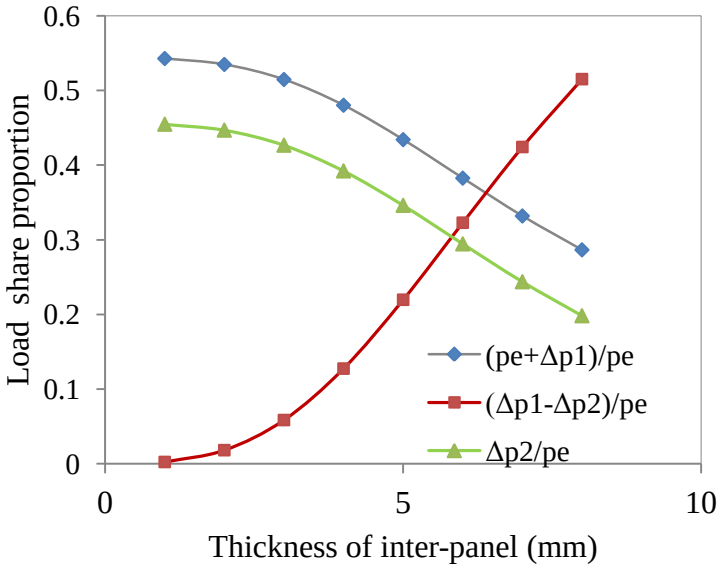

Figure 4- 26. Load share ratio on each panel with increasing thickness

4.5 Summary

In this chapter, the bending behaviour of triple glazing units is thoroughly analysed. FEM nonlinear hydrostatic TGU models are developed based on the validated IGU models. The interactive action of temperature change and wind load is studied. The mechanical responses of each glass panel in winter and summer extreme scenarios are considered in the FE simulation. It is found that the maximum deflection of the whole unit occurs in the outside panel for winter and in the inter-panel for summer.

A type of linear analytical method is proposed, which combines the small deflection theory of rectangular plate and Boyle's law for gas. When subjected to a wind load, the load share and the exact solutions of corresponding maximum stress/deflection of each glass panel can be calculated by solving a set of simultaneous quadric equations. By comparing with FEM results, the calculated stresses and deflections fit well in linear phase, but start to perform obvious deviations at higher loading level, where the nonlinear bending behaviour becomes dominant.

Therefore an approximate nonlinear analytical solution for the load design of TGUs is taken into consideration. The mathematic equations are derived from the calculation method of IGUs provided by Feldmeier (2003). An empirical method is adopted to derive the calculation equations for TGUs and derivation is validated by the FEM modelling. The equations for wind load, temperature/altitude change and the coupling actions are all developed. In addition, the nonlinearity feature is studied during the whole loading stage. It is found that the load share process still behaves in linear fashion. The nonlinearity is mainly reflected in the values of maximum stresses and deflections.

The size sensitivity of load share ratio is discussed. The TGU size and the width of the air cavity are taken into parametric study. The changes of these parameters are found to be influential to the load share on each glass panel. When the length is 500mm, the upper panel carries 69.24% of the total applied pressure, while the inter-panel and the lower panel endure 22% and 8% respectively. The great divergence converges rapidly with increasing size. When the length of the glazing is more than 2000mm, the loads in each panel are evenly allocated. The opposite tendency is observed for the increased width of the air cavity. The load share ratio starts to disperse with large air cavity width.

It can be concluded that when the ratio of the glass size and cavity width *a/w* is greater, the external load onto each glass panel is more averaged.

The thickness of the inter-panel is also discussed in the parametric study. The normalised maximum stress and deflection are proposed in the discussion. The increased inter-panel thickness leads to a proportionate decline in the maximum normalised stresses of the lower and upper panels. The maximum normalised stress in the inter-panel is on the other hand, is increasing until the thickness of the inter-panel exceeds the other two panels. The stress in the inter-panel reaches a maximum when the thicknesses of the three panels are equal. The increase in the thickness of the inter-panel causes a consistent drop of the maximum normalised deflections in all three panels. The deflection proportion of the outdoor panel is getting higher whereas the proportions in the inter-panel and the indoor panel are reduced. When the thickness of the inter-panel is 1mm, the uniform pressure allocated on it is deemed negligible. The load carrying condition can be equivalently calculated as an IGU. The thin glass panel planted in between only acts as a functional insulation layer.

CHAPTER 5. EXPERIMENTAL/FEM STUDIES OF MECHANICAL PROPERITES AND AGING PERFORMANCE OF SECONDARY SILICONE SEALANTS FOR IGUs

5.1 Introduction

An in-depth examination on the physical properties of the constituent components of IGUs is needed in order to carry out the assessment on the structural performance during the IGUs' service life using FEA. As was introduced in Chapter 2, the mechanical performance of the secondary sealant significantly influences the IGUs' longevity (Wolf, 1992). Since most organic polymer materials are sensitive to environment actions, the long-term environmental exposure of IGUs will inevitably result in the sealant deterioration in the mechanical properties and consequently lead to the functional failure. It is reported that the loss of the adhesion in the secondary sealant is the primary cause of pre-mature failure in IGUs (Feldmeier, 1984). An in-depth examination on the mechanical properties of edge sealant is crucial to further evaluate the durability and service life of IGUs.

Silicone secondary sealant has exhibited more desirable material properties than polysulfide or polyurethane sealants and been used as the most popular secondary sealant in the prevailing IGUs market (Wolf, 1998). The mechanical properties of silicone sealant, such as strength, resilience, elasticity, hardness, etc., are strongly dependent on environmental conditions. Aging tests are required to simulate the practical environmental conditions that installed IGUs may experience, and since to obtain the sealant behaviours in different aging conditions.

In this chapter, the mechanical properties of insulating glazing silicone sealant will be examined in the laboratory, through which, the following objectives can be achieved:

1. To obtain the stress-strain curves for sealants under both tension and compression
2. To measure the tensile and shear bond strength at the sealant/glass interface
3. To investigate the failure mechanisms of the silicone sealant adopted in IGUs
4. To study the mechanical properties of the silicone sealants subjected to various synergetic aging conditions

The tensile and compressive stress-strain curves of the insulating glazing silicone sealants are then incorporated in the FEM analysis. Specific edge seal systems will be examined by using the FEM hydrostatic fluids IGU models to investigate the structural responses of the secondary sealants with different geometry configurations.

5.2 Test specimens and preparations

The tests carried out in this work include dumb-bell nss, compression cycling tests, cross-bonded tensile tests, cross-bonded shear tests and cross-bonded aging tests.

5.2.1. Sealant type

Three types of commercially popular silicone sealants are considered in the tests for comparison, which are labelled as A，B and C (shown in Table 5- 1). Both types A and B are one-part sealant, and C is two-part sealant.

As the mechanical properties of sealants depend on both the material composition and the test method (loading rate, temperature, humidity, specimen geometry, etc.), specimen comparisons are made under the same testing conditions.

Table 5- 1**.** Sealant materials

Sealant	Sealant label	Sealant feature
Silicone structural sealant	A	One-part
Silicone insulating glazing sealant	B	One-part
Silicone structural sealant	C	Two-part

5.2.2 Curing condition

The one-part sealant specimens were placed in the curing room for 28 days, with the relative humidity 50% and a constant temperature 25±1^{o}C for a full cure. This is because one-part sealant develops cross-links at ambient moisture. The curing of one-part sealant demands strict control of the ambient condition. Less relative humidity (lower than 40%) or lower temperature (below 15.6^{o}C) will extend the curing period and undermine the ultimate sealant strength (Amstock, 1997). Two-part sealant does not depend on atmospheric moisture during the cross-linking forming process, and considerably shortens the curing time because of the use of catalyst. The test pieces made with two-part sealant in this study were cured for two weeks.

5.2.3 Laboratory condition

According to BS ISO 23529:2010 (BSI, 2010), the standard laboratory temperature is 25±2^{o}C, and the preferred relative humidity is 50±10%.

5.2.4. Loading mode

The loading mode in the following tests is displacement control. The loading rate for each test should comply with corresponding standard specification (BSI, 2011(a); BSI, 2011(b); ISO/TC 206, 2011).

5.3 Tensile test

Tensile test is carried out to obtain the tension stress-strain curve, as well as the tensile strength. The test is carried out in accordance with BS ISO 037 (BSI, 2011).

5.3.1 Preparation of test specimens

In this test, a thin sealant specimen piece of required thickness 2mm is made. After fully cured, the sealant piece is cut into the specified specimen shape with the cutter. The specimen size is illustrated as below in Figure 5- 1. Geometry of dumb-bell test piece (BSI, 2011)

and listed in Table 5- 2:

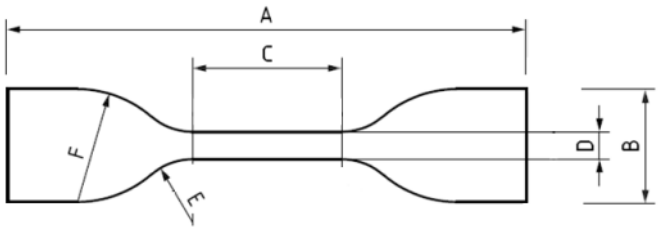

Figure 5- 1. Geometry of dumb-bell test piece (BSI, 2011)

Table 5- 2. Geometry details of the specimen (mm)

A Overall length	B Width of ends	C Length of Narrow portion	D Width of Narrow portion	E Outside Transition	F Inside Transition
100	25	21	5(±0.1)	11(±1)	25(±2)

The specimen cutter and the specimens ready to use are shown in Figure 5- 2.

(a) The cutters (b) The dumb-bell shaped test pieces

Figure 5- 2. Specimen cutters and the dumb-bell test pieces

Each group of test should contain at least three valid specimen pieces. In order to guarantee the quality of the specimens and the repeatability of the test results, ten specimens of each sealant are cut into the size specified in the design code and tested.

5.3.2 Test procedures and data acquisition

1. The dumb-bell test pieces are marked with two reference lines to specify the gauge length. The original gauge length is 20mm.
2. The test specimen is fixed on the tensile test machine by clamping two ends. The end tabs were gripped symmetrically to ensure the uniformly distributed tension, as shown in Figure 5- 3 (a). A MTS C4 series Universal testing machine is employed to carry out the tensile test.

3. To fully engage the test specimen, a small tension stress 0.1MPa is applied to the specimen in advance.
4. During the loading, the nominal rate of the moving grip is 500mm/min. The deformations are recorded by a digital-image-capture device (shown in Figure 5-3(b)) until the test specimen breaks.

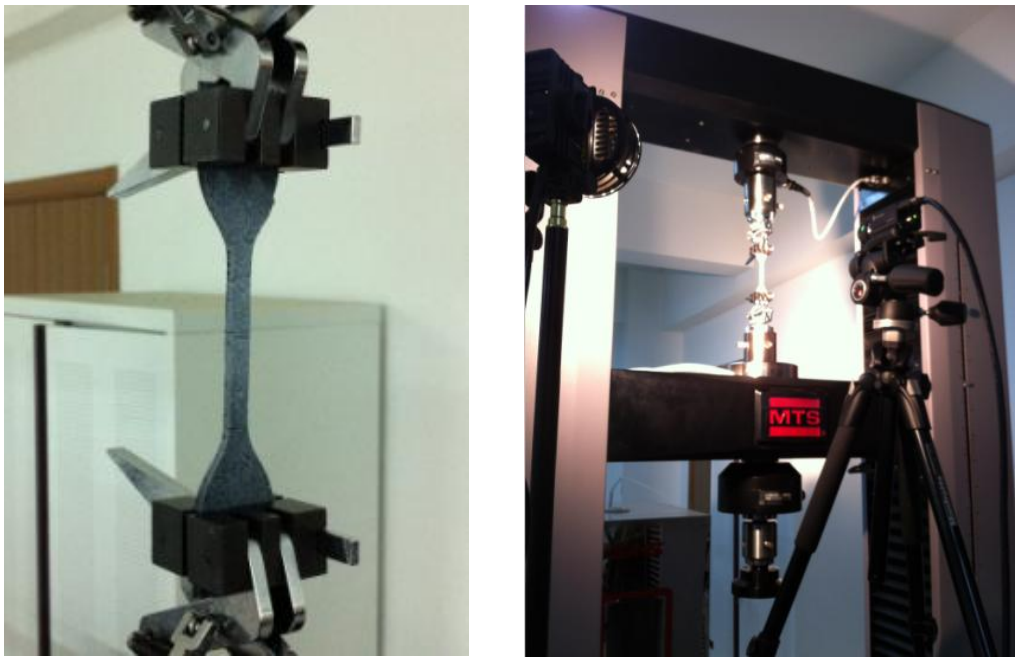

(a). Tension sample (b).Non-contact strain measuring device

Figure 5- 3 .Non-contact strain measuring device

The stress-strain relation is recorded by manually synchronizing the stress-time curve and strain-time curve. The loading-time curve can be obtained from the data-logger of the universal test machine. Then the stress-time curve is determined by dividing the original cross section area of the test range. The non-contact strain measuring device consists of a digital camera, a spot light, a data logger and a post-processing programme installed in a laptop. Before the test commences, the camera should be mounted right in front of the specimen, and the focus should be set, so as to ensure the images transferred

to the data logger are of high quality. The spot light should be turned on during the whole test process to highlight the test specimen. The camera records length variation of the gauged region as marked in Figure 5- 3 with a frequency of $5mm^{-1}$. The images shot by the camera are instantaneously transferred to the data logger. After the test, the images are imported into the post-processing software to collect the strain-time data.

The stresses (σ) and strains (ε) described in the curves are termed "nominal stress" and "nominal strain", which are calculated by (BSI, 2011)

$$\sigma = F / A \qquad 5\text{- }1$$

where F is the loading (N), A is the original cross-section area

$$\varepsilon = (l_F - l_0) / l_0 \qquad 5\text{- }2$$

where l_F is loading length, l_o is original length

The tensile test is recorded in Figure 5- 4. It is noted that if the test piece breaks outside the gauged region or yields outside the same region, it should be discarded and replaced with a new specimen and repeat the test.

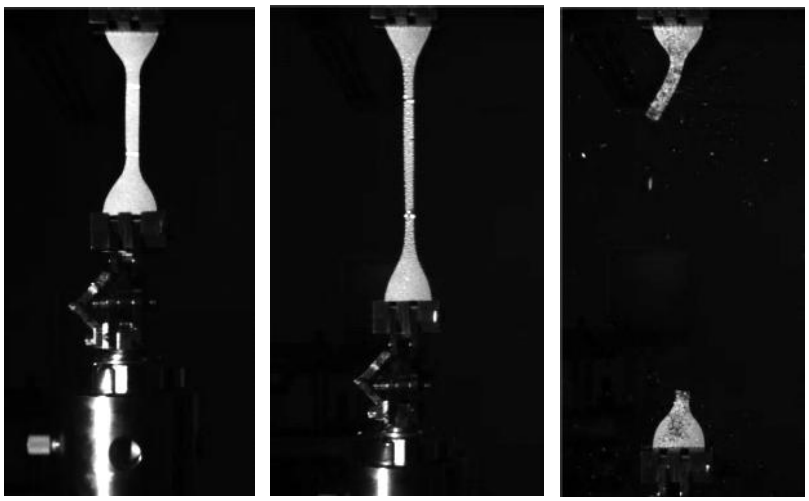

(a) Initial state (b) under the tension (c) breakge
Figure 5- 4. Tensile test recorded by digital camera

5.3.3 Results and discussion

On inspecting the fractured specimens, the specimens containing internal defects, e.g. bubble voids, or those break outside the gauge range are discarded. For each type of sealant, three valid specimens are considered. The average results are presented in Table 5- 3.

Table 5- 3. Average strength and standard deviance

Uniaxial tensile test	sealant type		
	A	B	C
Mean strength (MPa)	2.317	2.357	1.726
S.D.	0.160	0.071	0.095

It is found that sealant C has the lowest strength, which is 34.2% lower than sealant A, and 36.56% lower than sealant B. The lower strength of two-part silicone can be explained by the chemical composition and formulation of sealant. Silicone sealants are compounds of a hydroxyl-ended polydimethysiloxane (PDMA) matrix and a variety of additives. Ingredient types have great influence upon the sealant mechanical properties (Dow Corning, 1993). For instance, the catalyst organotin salt commonly used in the two-part silicone sealant is found to limit the stability of the elastomer in high temperature (Buyl, 2001); vinyl trimethoxysilane used as cross-linking agent will result in less strength and elastic modulus than methyl triethoxysilane (Chen, 2013). Even though the detailed ingredient formula of the commercial silicone sealants adopted in these tests are confidential and not available to public, it can be implied that the selection of additives of two-part silicone sealant is account for the lower strength.

Apart from the silicone polymer PDMS, silicone sealant also consists of a cross-linking agent, a coupling agent, a reinforcing agent, etc. The strength of the sealant is predominant by the net-linking structure of PDMS. However, the additives contained in the sealant are oligomers that are not bonded as a part of net-structure. Therefore the increase of additives will reduce the proportion of the cross-linking structure of PDMS in the silicone sealant, and hence reduce the overall strength. In conventional two-part silicone sealants, organotin salt is added as a catalyst. Other accelerating additive like butylamine is also employed to facilitate cross-linking reaction. The mixture of these additives does not contribute to the overall strength, but dilutes the cross-linking density in the silicone sealants. Therefore in this tensile test, the two-part sealant C performed the lowest strength.

The stress-strain curves of each sealant type are plotted in Figure 5- 5.

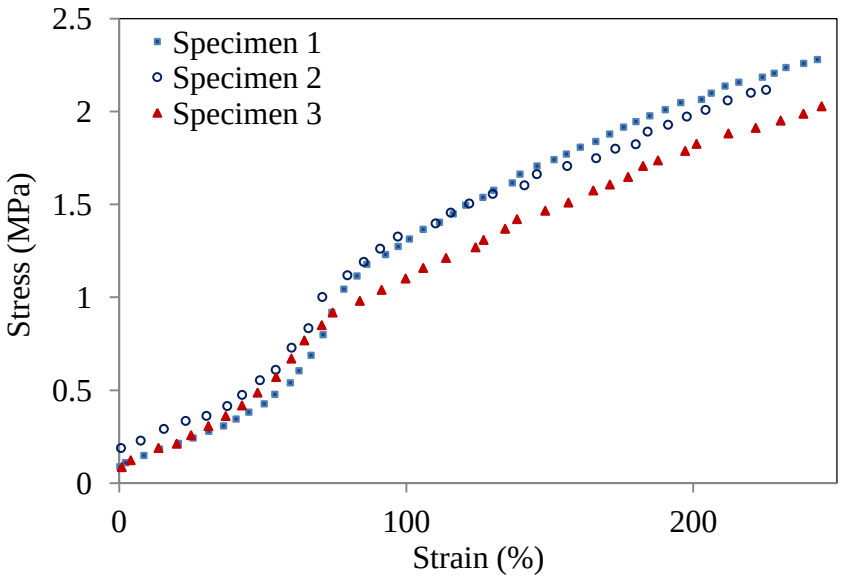

(a). Sealant A

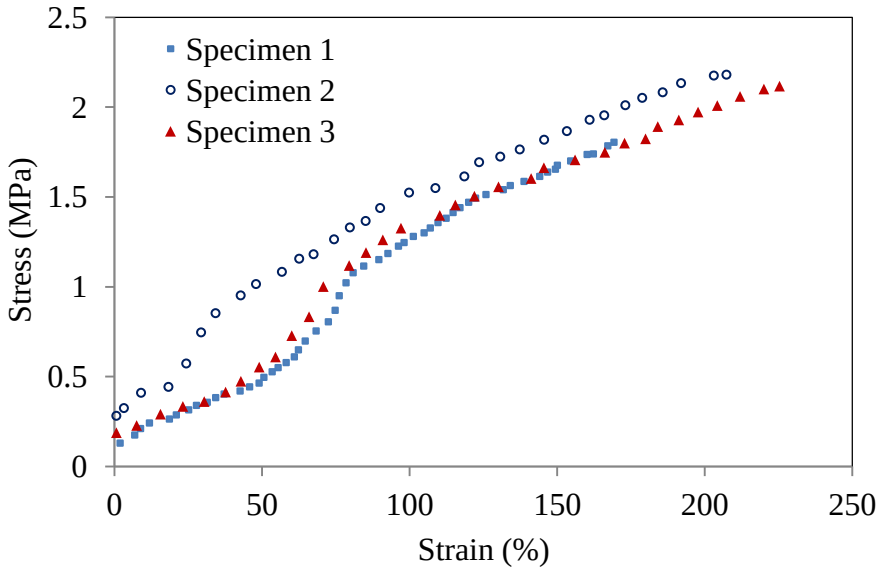

(b). Sealant B

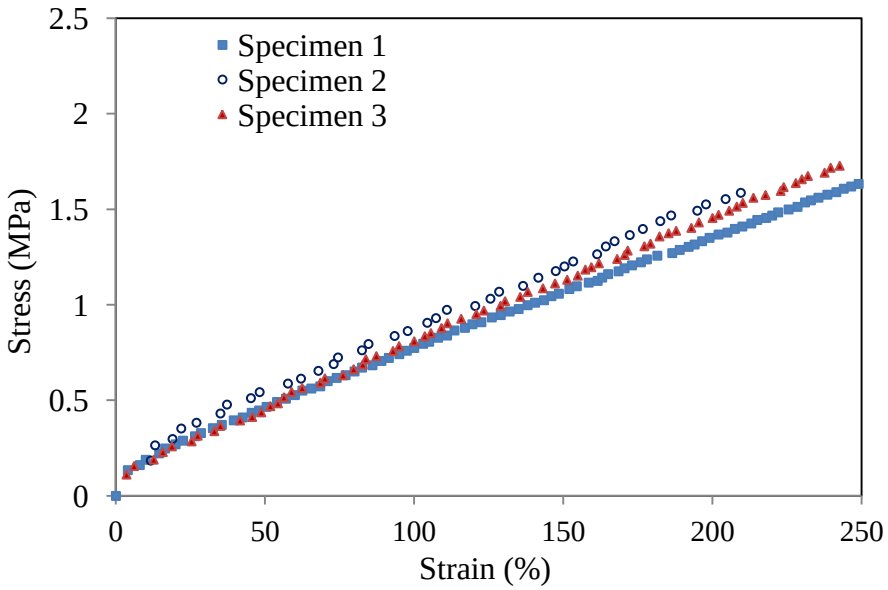

(c). Sealant C

Figure 5- 5. Stress-strain curves in tensile test

According to the stress-strain curves, all the three sealants show nonlinear stress-strain trend. The curves for sealants A and B also show hardening behaviour which is

reflected an increase in gradient in the curves shown in Figure 5- 5; whereas sealant C does not show such trend. The tensile secant moduli at 20%, 50%, 80%, 100% and 200% strain levels are listed and compared.

Table 5- 4. Tensile secant modulus at different strain levels

Sealant	10%	20%	50%	80%	100%	150%	200%
A	1.802	1.359	0.980	1.142	1.080	0.953	0.859
B	2.404	1.865	1.192	1.308	1.231	1.080	0.938
C	2.457	1.624	1.090	0.954	0.896	0.829	0.793

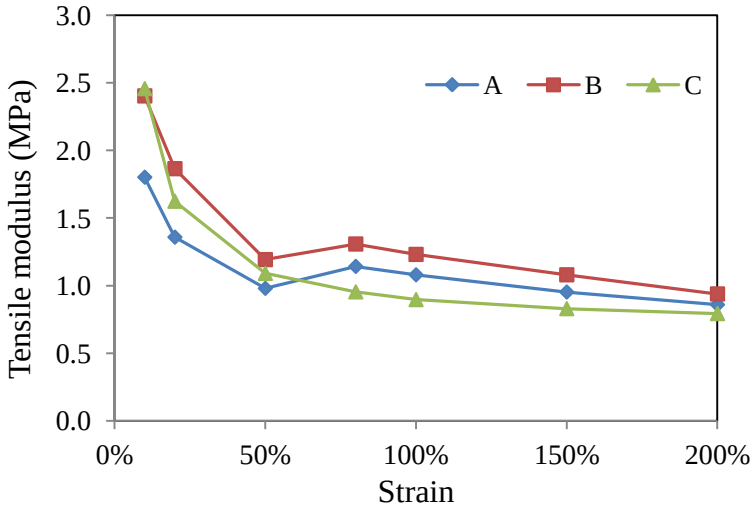

Figure 5- 6. Tensile modulus vs. strain of three types of sealants

In Figure 5- 6, it is found that the tensile moduli of all three sealants are not constant, but strongly dependent on the strain level. The modulus –strain relationship of sealant C has a monotonously decreasing trend. In contrast, the tensile moduli of both A and B drop to the minimal level at around 50% strain level, and then rise before undergoing a mild decline following strain exceeding 80%. This agrees with the hardening phenomenon observed in the stress-strain curves.

The differences in the stress-strain curves and moduli curves of one-part and two-part sealants can be explained by the orientation of polymer molecular chains. The orientation is a unique phenomenon in polymers. When subjected to a uniaxial force, the backbones of polymer molecular chains will be aligned in a certain direction. The strength and modulus of polymer are improved in this direction because of strong covalent bonds along the chain axis. Orientation is a process that the molecular chains move from disordered state to aligned state. The process is time-dependent as the molecular movement within the polymer has to overcome viscous resistance. The orientation hysteresis renders the hardening behaviour in the stress-strain curves. The orientation does not take effect if the chain-intrinsic properties are isotropic. (Gedde, 1995)

In the chemical backbone of silicone sealant PDMS, the bond energy of side group Si-C is 318.2kJ/mol, C-C 345kJ/mol and C-O 351kJ/mol (Wolf, 1993), which are lower than that of the saturated Si-O bond, 425kJ/mol. When the molecular chains are oriented in the loading direction, the directional strength will be augmented due to high dissociation energy of Si-O bond whereas in other directions the strength will be weakened. On the other hand, if the cross-link reaction fully takes place, most PDMS chains will be transformed to be a three dimensional net structure of Si-O bonds and tends to be isotropic. In this case, the orientation will not be obviously detected. As a result, the orientation phenomenon is dependent on the degree of cross-linking reaction. In contrast to the one-part silicone sealants that cross-link spontaneously with sufficient moisture, the cross-linking reaction in the two-part sealant is induced by catalyst and accelerators. So the three-dimensional cross-linking structure in the two-part sealant is more common

than that in the one-part sealants, which explains that the hardening phase is not observed in stress-strain curve of sealant C.

5.4 Compression cyclic tests

Compressive tests were carried out in compliance with BS ISO 7743:2011 (BSI, 2011), in order to obtain the compressive stress-strain relation. Method C introduced in the standard is chosen for the tests.

5.4.1 Preparation of test specimens

The standard test specimen for method C is a cylinder of a diameter 17.8±0.15mm and a height 25±0.25mm. The test specimens are moulded in the shape as shown in Figure 5-7. For each type of sealant, at least three test specimens that were carefully prepared.

Sealant A Sealant B Sealant C

Figure 5- 7. Test specimen used in compressive test

5.4.2 Test procedure:

1. With the standard laboratory room condition, i.e. temperature 25±2^{o}C, and the preferred relative humidity is 50±10%, place the test specimen at the central location of the loading plates of the compression machine and operate the

loading machine at a speed of 10mm/min until a strain of 25% is reached. The compressive test machine and the setting up of the test piece are shown in Figure 5- 8. Even though there is no specific requirement for the contact surface from the standard, the interfaces between the sealant specimen and the loading plates of the test machine are lubricated by Vaseline to minimise any boundary effect caused by the interfacial friction. To ensure the loading plate is fully contacted with the specimen surface, a small fraction pre-loading is applied in the beginning.

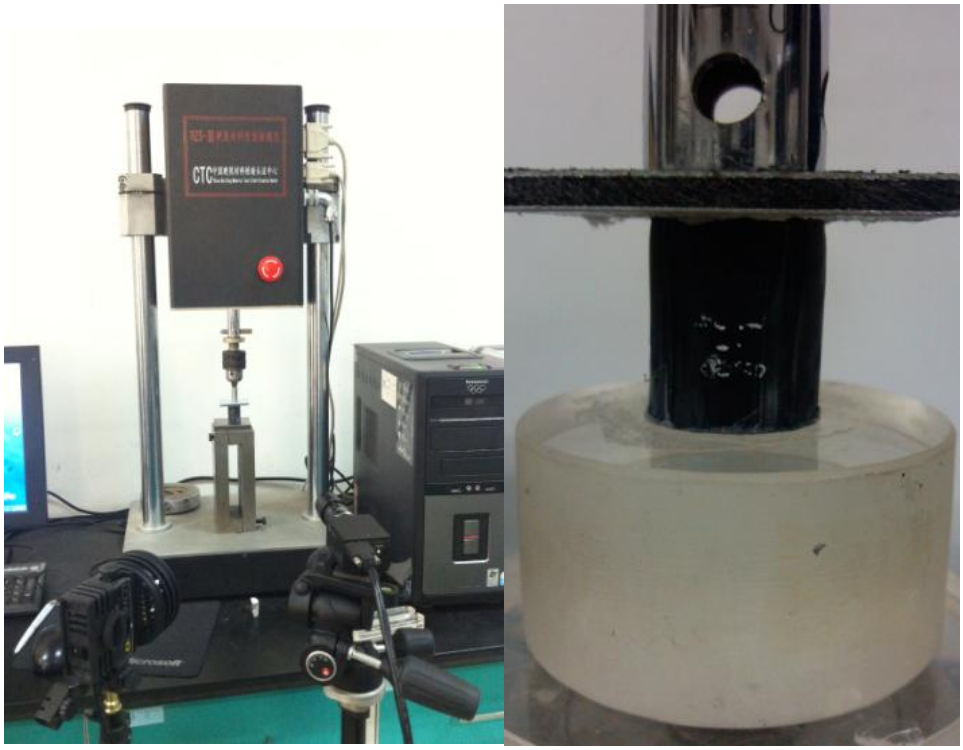

(a). Compressive test machine (b) Setting-up of test specimen

Figure 5- 8. Setting-up of the compressive test

2. Unload the specimens at the same speed of 10mm/min until the loading plate reaches the initial location, i.e. zero strain and repeating the compressive loading

and unloading cycles three more times. Four compression cycles forms an uninterrupted sequence.

3. Record the force-strain curves. The average results of the compressive modulus of three specimens at the 10% and 20% strain are reported. The strain can be calculated by shifting the coordinate origin to the starting point of the fourth loading cycle as illustrated in Figure 5- 9.

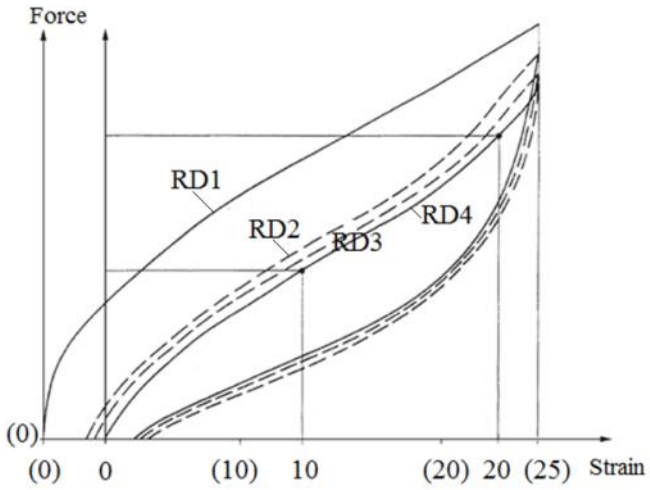

Figure 5- 9. Schematic diagram of force– strain curve of the compressive test (BSI, 2011)

5.4.3. Results and discussions

In accordance with the BS ISO 7743: 2011, the force - strain curves of each test specimen of three sealant types are plotted below in Figure 5- 10 to Figure 5- 12.

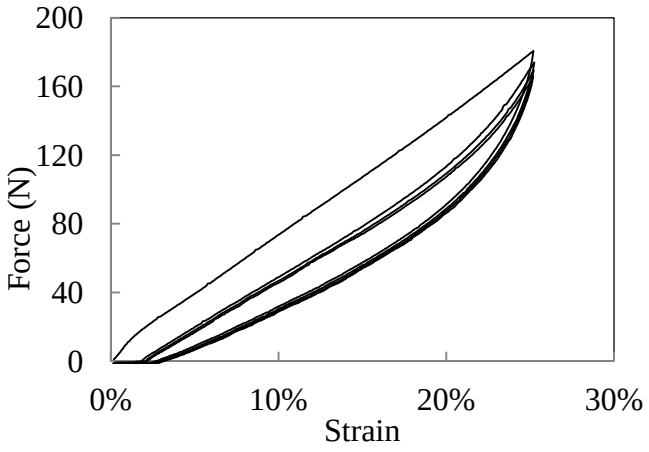

(a). Sealant A-1

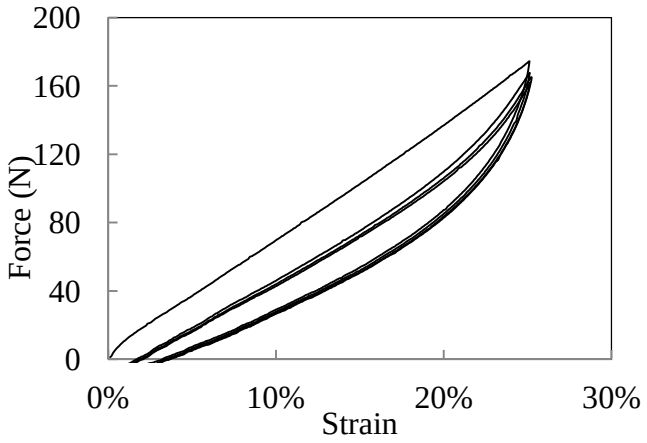

(b). Sealant A-2

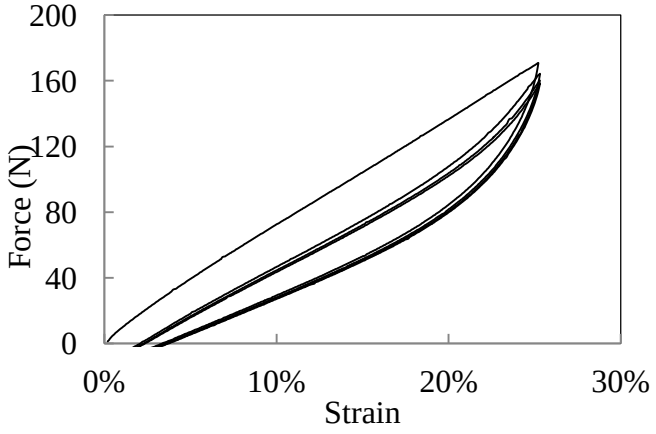

(c).Sealant A-3

Figure 5- 10. Force-strain relationship of sealant A

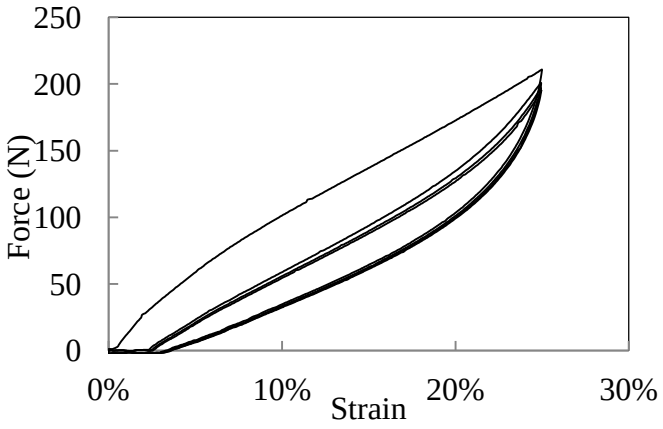

(a). Sealant B-1

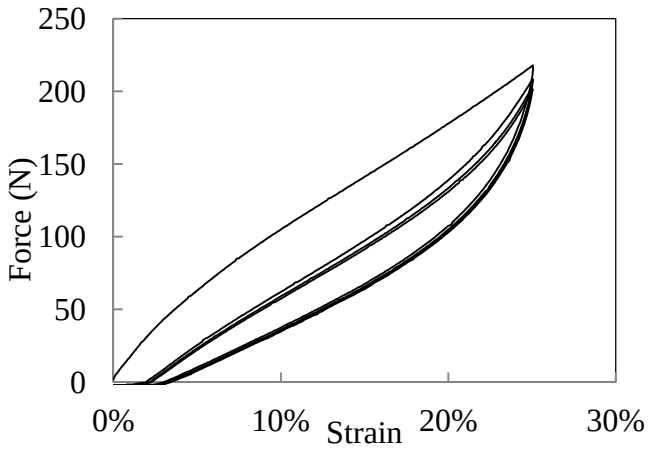

(b). Sealant B-2

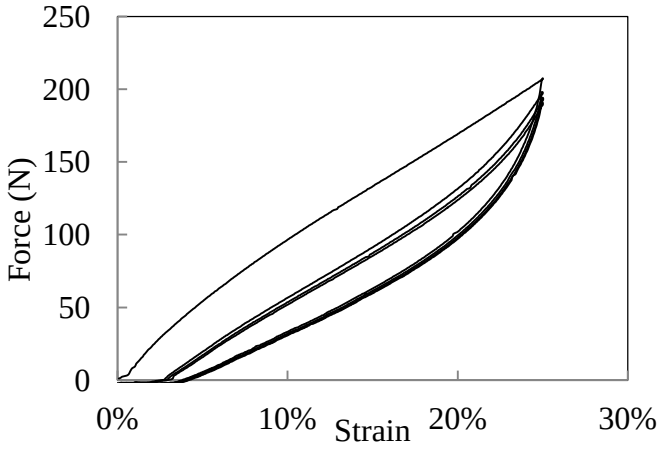

(c). Sealant B-3

Figure 5- 11. Force-strain relationship of sealant B

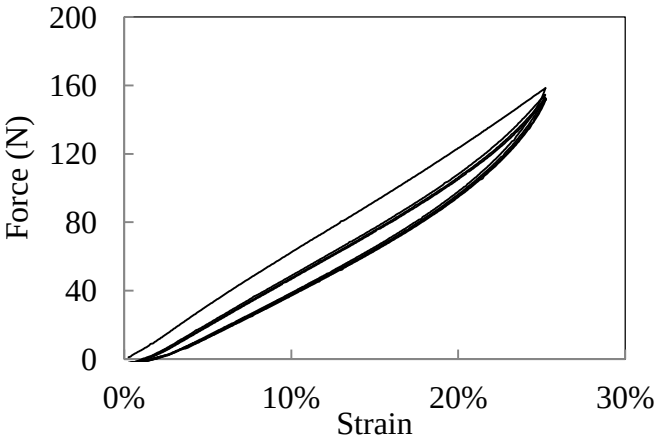

(a). Sealant C-1

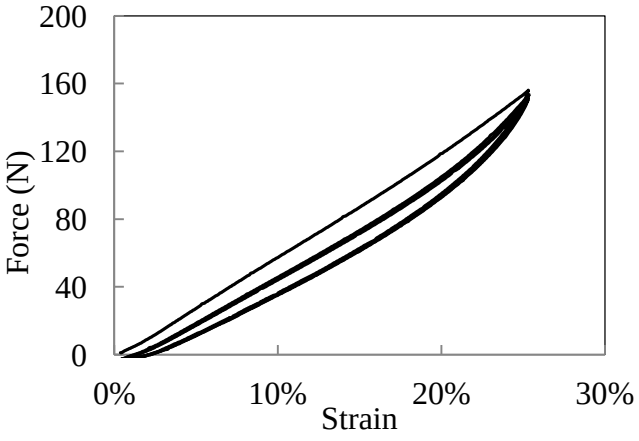

(b). Sealant C-2

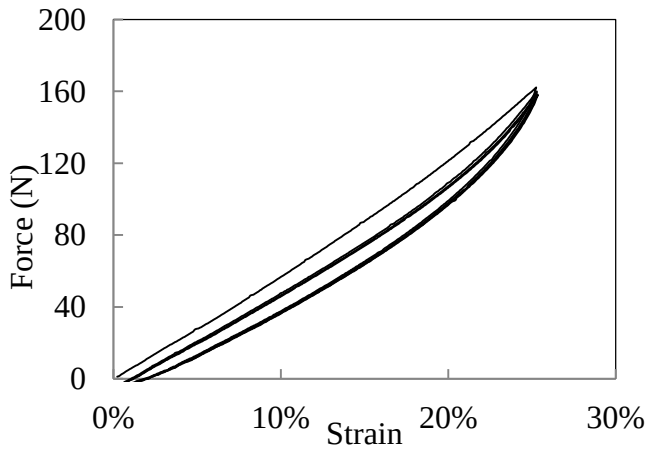

(c). Sealant C-3

Figure 5- 12. Force-strain relationship of sealant C

From Figure 5- 10 to Figure 5- 12, it can be easily observed that for all three sealants, there is a residual deformation between the consecutive loading and unloading cycles, which is attributed to the visco-elastic-plastic performance of sealants. The residual deformation consists of non-recoverable and recoverable parts, as indicated as RD 1 and RD2 in Figure 5- 9. The gap between RD1 and RD2 represents non-recoverable sealant deformation due to the relaxation of the specimens. In this compressive test, four compression cyclic loading-unloading regimes are adopted in order to eliminate the non-recoverable residual deformation, which happens in the first cycle. As is revealed from Figure 5- 10 to Figure 5- 12, the first cycle loading curve differs significantly from the other three; whereas the latter three curves agree rather well. This suggested that most of non-recovered residual deformation has occurred during the first loading cycle. It is reasonable to infer that the stress-strain curve in the fourth loading cycle is sufficiently accurate to dictate the sealant deformation properties during the practical service duration.

The comparison of the non-recoverable deformation in the first loading cycle as shown in Figure 5- 10 with Figure 5- 12 suggests that the largest amount occurs in sealant B, and smallest in sealant C.

The compressive secant moduli at 10% and 20% strain levels are presented below in Table 5- 5 to Table 5- 7:

Table 5- 5. Compressive secant moduli of sealant A

Load (N) Specimen A.	Strain10%	Strain20%	Diameter (mm)	Area (mm^2)	10% Compressive modulus	20% Compressive modulus
1	38.2	105.6	21.9	376.68	1.01	1.4
2	36	102.4	21.58	365.76	0.98	1.4
3	37.6	101.2	20.87	342.09	1.1	1.48
Average value					1.03	1.43
S.D.					0.06	0.05

Table 5- 6. Compressive secant moduli of sealant B

Load (N) Specimen B	Strain10%	Strain20%	Diameter (mm)	Area (mm^2)	10% Compressive modulus	20% Compressive modulus
1	46	149.4	21.7	369.84	1.24	2.02
2	48	130.2	21.4	359.68	1.33	1.81
3	45.8	130.2	21.5	363.05	1.26	1.79
Average value					1.28	1.87
S.D.					0.05	0.13

Table 5- 7. Compressive secant moduli of sealant C

Load (N) Specimen C.	Strain10%	Strain20%	Diameter (mm)	Area (mm^2)	10% Compressive modulus	20% Compressive modulus
1	38.2	95.6	21.82	373.94	1.02	1.28
2	43.4	94.8	22.04	381.52	1.14	1.24
4	43.1	116.2	21.92	377.37	1.14	1.54
Average value					1.1	1.35
S.D.					0.07	0.16

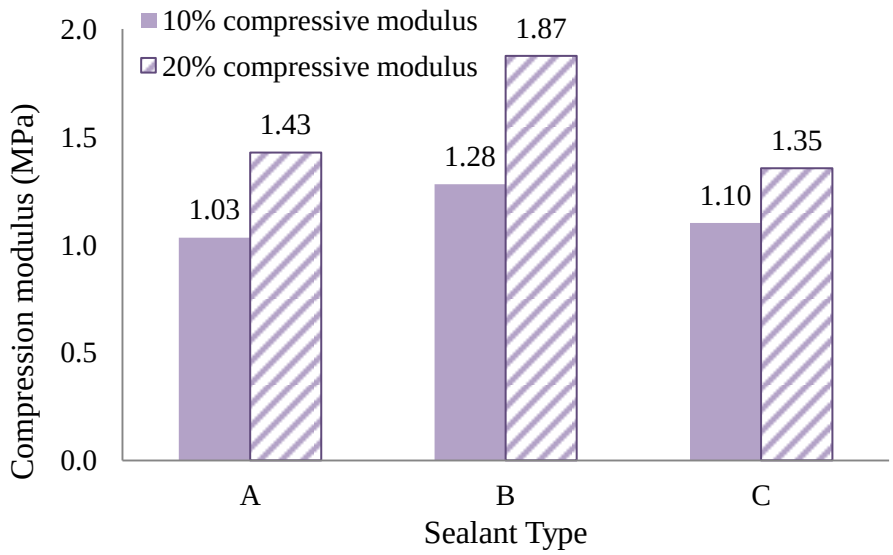

Figure 5- 13. Compressive secant modulus at 10% and 20% strain levels

Similar to the tensile tests, sealant B also has the highest compression modulus at both 10% and 20% strain levels as shown in Figure 5- 13. Sealant A and C have similar compressive moduli. By observing the trend of force-strain curves, the compressive modulus appears to be monotonously increasing with increasing strain levels. When the strain rises from 10% to 20%, the compressive modules increase by 38.14%, 46.4% and 23% for sealant A, B and C, respectively. So it can be concluded that the compressive modulus of sealant B is most sensitive to the strain, and sealant C least.

In these two tests, tensile and compressive stress-strain properties are obtained. The data can be used in the FEM modelling to further investigate the mechanical response of silicone sealants in the edge seal system under different environmental actions. In the next section, the tensile and shear bond behaviour of the secondary silicone sealant will be investigated and discussed.

5.5 Tensile and shear bond strength test

Sealant failure in IGUs can fall into two main categories: adhesion and cohesion failure (BSI, 2002). Adhesion failure is also termed as de-bonding failure, which is due to the insufficient interfacial strength between the sealant and other components. Cohesion failure is the fracture within the sealant because of degraded elasticity or excessive mechanical actions. Both failure modes could be caused by severe environmental attacks or repeating mechanical actions acting upon the IGUs, such as slam, wind load, snow load and the sealed air movement due to climatic change. During the service life, the major mechanical actions upon the sealants in IGUs are tensile loading and shear loading. Therefore the tensile bond strength and shear bond strength of the sealant will be primarily studied in this work.

Two objectives will be achieved through this test series as follows:

1. To measure the tensile and shear bond strength of three types of silicone sealants;
2. To study the influence of pre-loading process to the loading-displacement path.

5.5.1 Bond mechanism

The bond of the silicone sealants is achieved by a combined action of sealant adhesion and cohesion. Adhesion refers to the bond between the silicone sealant and the substrate surface. There is no unified theory to account for the interfacial adhesion so far. It is generally accepted that the interfacial adhesion is attributed to a combination of chemical bonds, adsorption, electrostatic attraction and diffusion (Rowland, 1998). The details of a variety of adhesion mechanisms can be referred to Chapter 2 the Literature Review. The chemical bonds are deemed as the key force to guarantee the adhesion performance (Adhesive and sealant Council, 2013). The sealant cohesion is the internal

strength of sealant itself, formed by a series of chemical bonds and inter-molecular interactions.

In terms of the silicone sealant and the glass surface, three types of interactions exist at the bond interface to maintain the adhesion: covalent Si-O bond, Van der Waal forces and hydrogen bonds. Within the sealant, the Si-O bonds resulting from cross-linking reaction plays a predominant part in sustaining the cohesion strength.

5.5.2 Preparation of test specimens and test procedures

EN 1279-4 provides a detailed test method to measure the physical attributes of edge sealants. The glass-sealant-glass joints are prepared as shown below in Figure 5- 14:

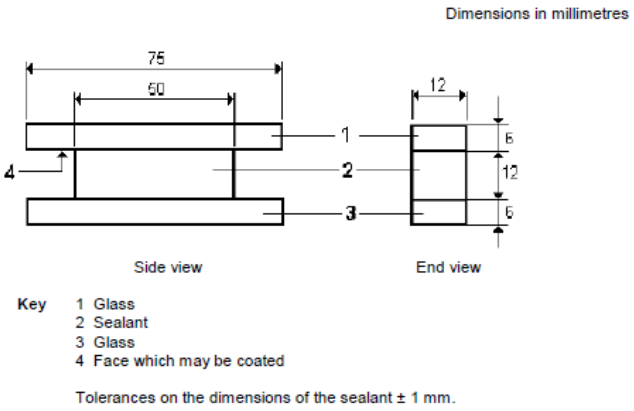

Figure 5- 14. Schematic figure of cross-bonded specimen (BSI, 2002)

In this test, the sealant is glued to a pair of glass bars, and the glass bars were clamped in the test machine. However, the glass bars tend to break before the sealant fails during the tensile test. When the joint is mounted onto the test machine, the tensile load is applied on two ends of each glass bar while the structure is joined by the sealant in the middle. It is easy to fracture the glass bar near the bond edge between the glass and the sealant due to the large moments induced by the tensile loading. Moreover, the joint

specimens are not appropriate to examine the shear behaviour of the bonded joint. As two bars are parallel, it is difficult to fix the specimen to the machine, and is very likely to cause unsymmetrical stresses during the test. To address these challenges, a new shape of joint specimen is proposed inspired by a test method introduced by ISO 13124 (ISO/TC 206, 2011). The test method is to determine the interfacial bond strength of ceramic materials. The geometry of test specimens has been improved in a way that the silicone sealant bonds two glass bars which are perpendicular placed as shown in Figure 5- 15 . The joint specimen will be denoted as “cross-bonded specimen” in the following analysis.

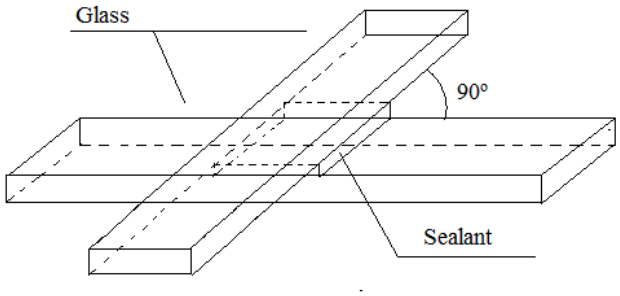

Figure 5- 15 Schematic diagram of cross-bonded specimens

As the sealant is employed to seal the glass panels at edges, the substrate of the cross-bonded specimen is soda-lime glass bar. The size of the glass bar is 75×12×6mm, and the bonded area is 24(±1) × 24 (±1) mm. The thickness of sealant is 5 (±1) mm.

A group of cross-test, each containing three specimens, are prepared and carried out. The preparation of specimens is introduced below (ISO/TC 206, 2011):

1. The glass surfaces should be cleaned by acetone solution before sealing, in order to achieve best bonding effect.
2. The glass bars are placed perpendicular to each other. Four spacer blocks coated by polyethylene films are employed to surround the glass bar, thus to retain the sealant in the designed bonding area. Polyethylene film is favourable for de-mounding because silicone sealant is not clinging to polyethylene material.
3. The test specimens are placed in a standard curing cabinet. After initial cure (24 hours), the spacer blocks can be removed and stand by for a full cure. The fully-cured specimens are trimmed, which means the excessive parts outside the test region will be removed. The sealant parts are eventually of the same size: 24mm×24mm×5mm. The specimens' preparation is shown in Figure 5- 16.

(a) Glass bars

(b) Mounding kit

(c). Glued test pieces

(d) Curing cabinet

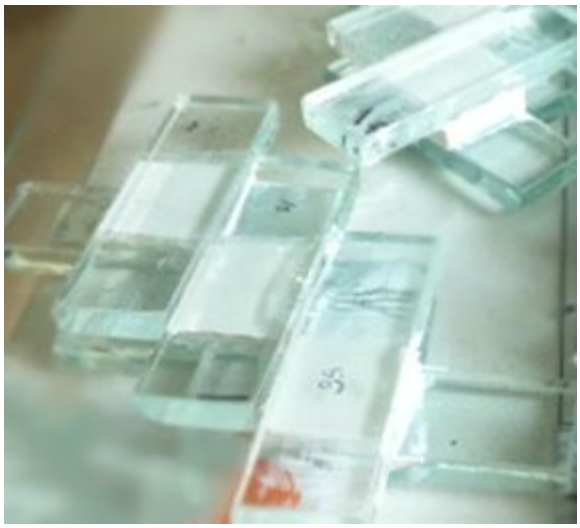

(e) Prepared cross-bonded specimens

Figure 5- 16. Preparation procedures of cross-bonded specimens

4. Cross-bonded specimens can be used to measure both tensile and shear bond strength. Figure 5- 17 shows the setup of specimens on the universal test machine for tensile and shear test.

(a) Tensile test (b) Shear test

Figure 5- 17. Specimen mounting modes in tensile and shear test

5. Apply a loading with a rate 5mm/min to the specimen until it fails. The load-displacement curves are recorded.

Tensile and shear bond strength, elongation rate at break is calculated according to the test results as evaluation indexes.

5.5.3 Influence of pre-loading process

As discussed in section 5.4.3, the irrecoverable deformation in the compression cycling tests results in the softening of loading-strain curves. This permanent change in the curve shape observed from the compressive test raises similar concern in the cross-bonded test, in which the repeated loads may also make appreciable difference in the loading-displacement path. In Wolf and Cleland-Host's work (2004), the pre-straining process is carried out prior to the uniaxial stress relaxation test on the silicone sealants so as to eliminate the softening phenomenon, called as Mullins effect.

Concerning the Mullins effect, it was first discovered and studied by Leonard Mullins (1969), who demonstrates that the stress-strain curves of most of elastomeric materials depend on the ultimate load. When the material undergoes repeated loading-unloading cycles, the stress required to reach the same strain level in the reloading stage is less than that in the initial loading cycle. The phenomenon can be reflected by the irreversible softened stress-strain curve in the reloading stage. If the new load increases beyond previous maximum values, the new softening effect will take place in the subsequently new loading cycle once the new load rises to that maximum value. Mullins effect has been reported in hydrostatic tension (Dorfmann, 2003) and simple shear test (Qi, 2005). The findings suggest that the specimens in the cross-bonded tension and shear test are very likely to experience Mullins effect under cyclic loading.

In order to study the impacts by the pre-loading process on the loading-displacement behaviour of silicone sealant, the specimens are pre-loaded to different strain stages. For sealant type A, 100%, 221% and the ultimate strain level are considered in the pre-loading. The loading-displacement curves of three sealant A specimens are presented in Figure 5- 18.

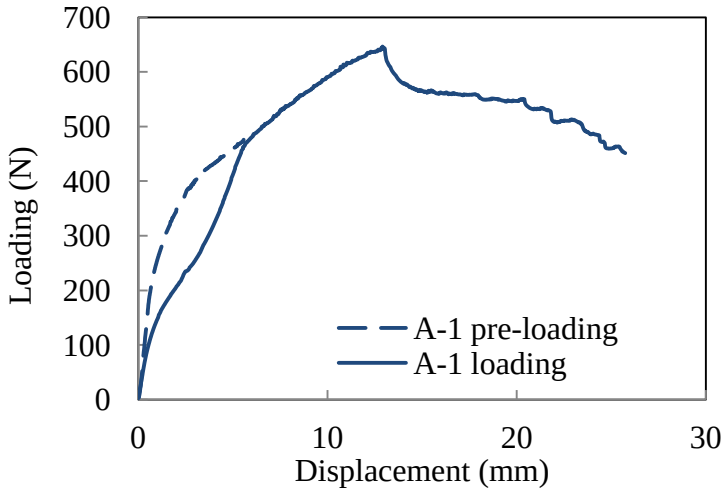

(a). Sealant A-1 Pre-strain to a level of 100%

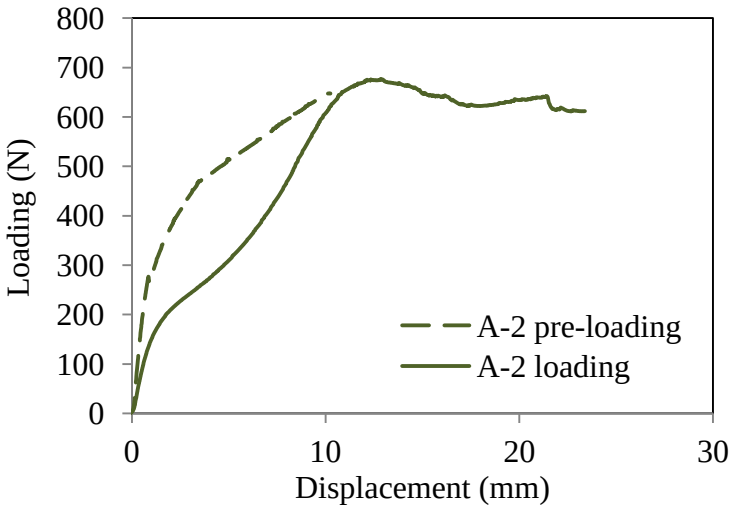

(b). Sealant A-2. Pre-strain to a level of 221%

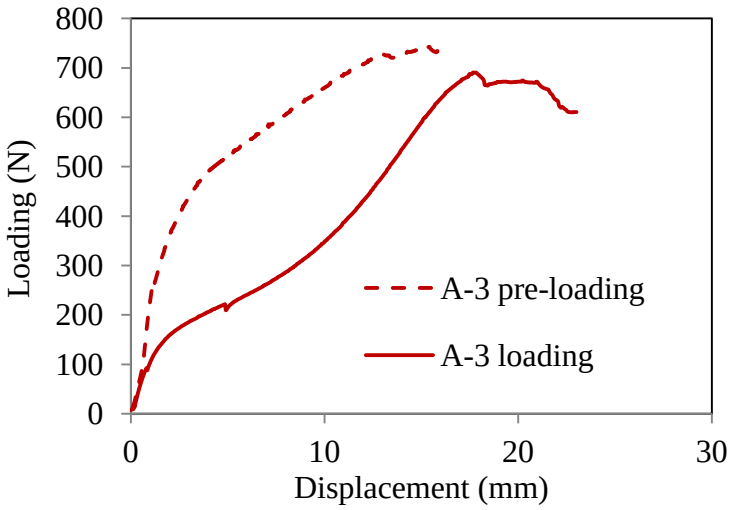

(c). Sealant A-3. Pre-strain to a level of 284%

Figure 5- 18. Sealant A at different strain level in tensile test

As shown in Figure 5- 18 above, it implies that the shape of loading-displacement curve is strongly dependent on the pre-loading process. To better compare the loading-displacement curves under different pre-strain levels, the stress-strain curves of three specimens are plotted together. Both pre-loading and loading curves are presented.

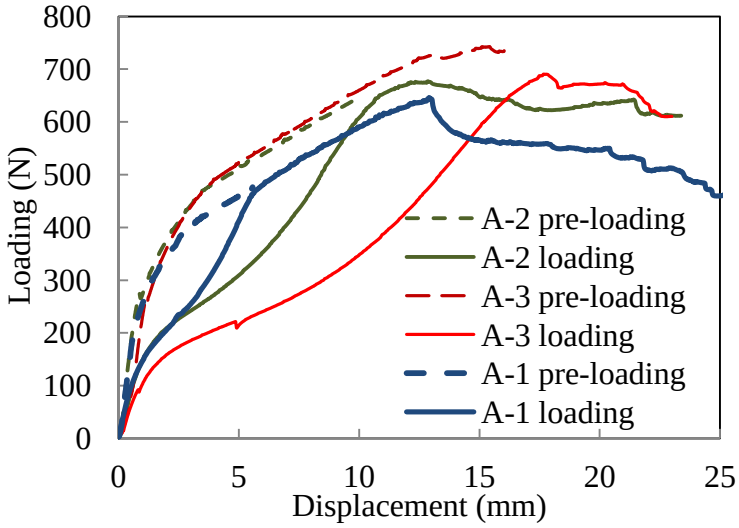

Figure 5- 19. Different level of pre-loading and loading curves of sealant A in tensile test

As shown in Figure 5- 19, the shape of softened loading-displacement curve of each specimen differs significantly due to the different pre-strain levels. On the other hand, it is observed that the maximum nominal stress values, i.e. the applied load at the ultimate level of three different shapes of loading-displacement curves are very close to each other. The maximum nominal stresses and corresponding pre-straining levels are listed in Table 5- 8.

Table 5- 8. Pre-strain level and ultimate stress of Sealant A

Specimen No.	1	2	3	Average value	S.D.
Pre-strain level	100%	221%	284%		
Max. nominal stress (MPa)	1.163	1.172	1.232	1.1890	0.0381

It can be seen that the maximum stresses of the specimen that experienced various pre-strain levels are of little variance. The standard deviation of the maximum stress is only

0.0381. Therefore, different pre-loading level leads to distinct loading-displacement path, however exerts little influence on the maximum stress.

Mullins effect caused by different pre-straining level is also explored in sealant B and C.

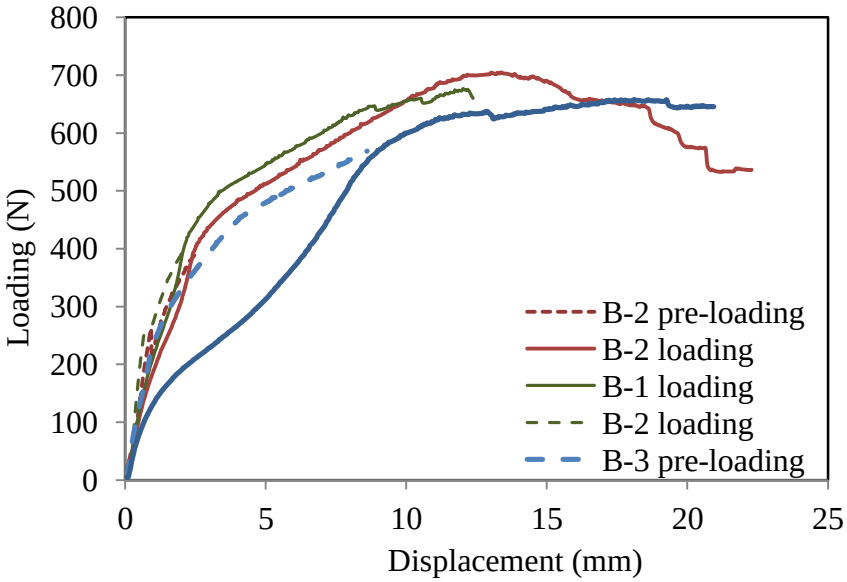

Figure 5- 20. Different level of pre-loading and loading curves of sealant B in tensile test

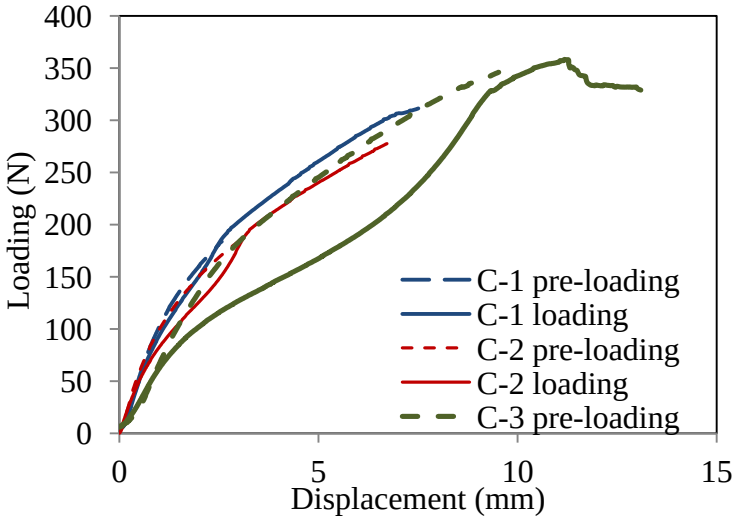

Figure 5- 21. Different level of pre-loading and loading curves of sealant C in tensile test

As observed in Table 5- 9 and Table 5- 10, the variance range of maximum stress is very narrow. It can be further confirmed that the maximum stress is independent on the pre-loading level. Associated with Figure 5- 22 and Figure 5- 23, the softening action in the stress-strain curves of specimen B-1, B-2, C-1 and C-2 is much less obvious compared to other specimens. Small pre-straining level (less than 60%) is not as influential to the loading-displacement curve compared to the higher levels.

Table 5- 9. Pre-strain level and ultimate stress of Sealant B

Specimen No.	1	2	3	Average value	S.D.
Pre-strain level	42%	38%	153%		
Max. nominal stress (MPa)	1.222	1.191	1.208	1.207	0.0155

Table 5- 10. Pre-strain level and ultimate stress of Sealant C

Specimen No.	1	2	3	Average value	S.D.
Pre-strain level	46%	58%	170%		
Max. nominal stress (MPa)	0.690	0.751	0.726	0.721	0.0193

Now the shear bond stress-strain curves are being considered and taken into discussion. It is noted that some specimens failed in the pre-loading step, and there is not corresponding softening curve presented below in Figure 5- 22 and Figure 5- 24:

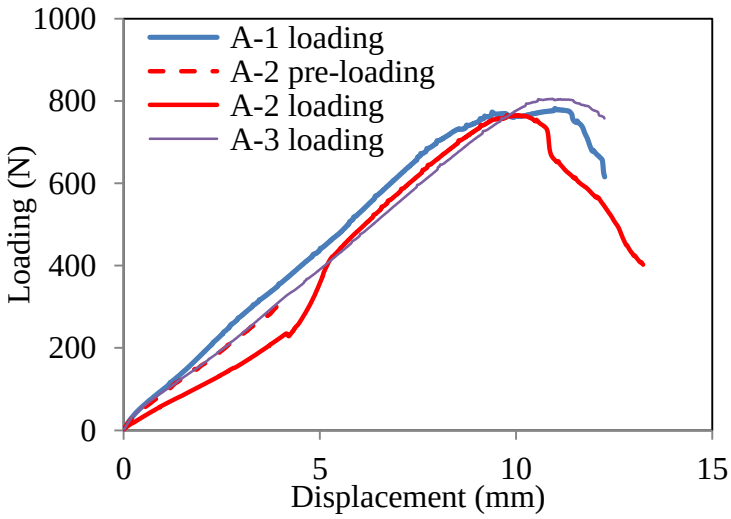

Figure 5- 22. Different level of pre-loading and loading curves of sealant A in shear test

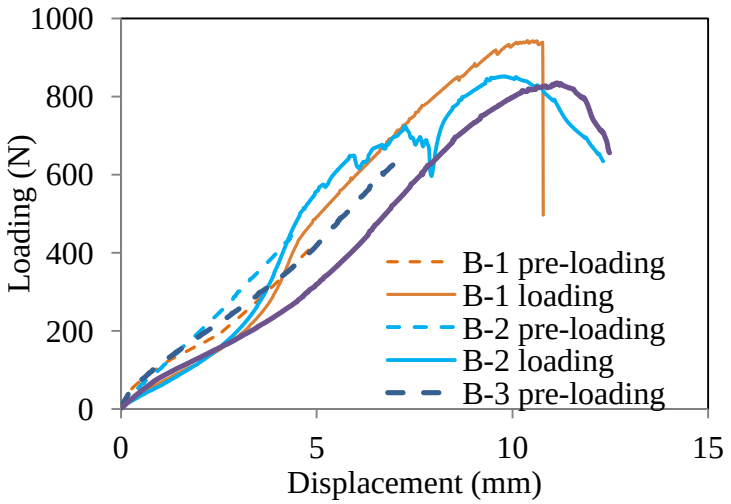

Figure 5- 23. Different level of pre-loading and loading curves of sealant B in shear test

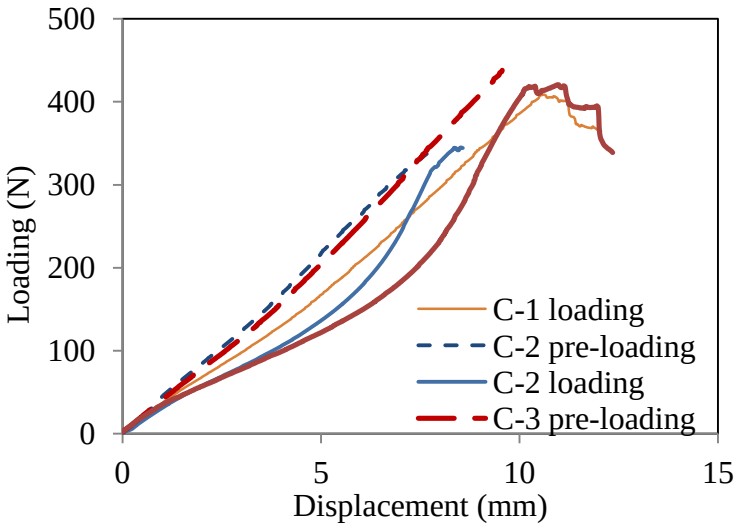

Figure 5- 24. Different level of pre-loading and loading curves of sealant C in shear test

As shown in Figure 5- 22 to Figure 5- 24, Mullins effect is also detected in the shear behaviour of the silicone sealants under different levels of pre-loading. The initial stress-strain relations show almost linearity in the preloading step. In the reloading step, the curves are softened and display obvious nonlinearity. The pre-straining levels loaded in the shear tests, average maximum stress and the standard deviation are listed in Table 5- 11. Similar to the tensile test, the shear strength value remains nearly constant despite the shape of curves are softened under different pre-strain levels.

Table 5- 11. Pre-strain level of each specimen in shear test

Pre-shear strain	Sealant type		
	A	B	C
1	N/A	79%	N/A
2	93%	80%	139%
3	N/A	130%	153%
Average Max.stress(MPa)	1.392	1.541	0.728
S.D.	0.0854	0.0581	0.0193

Regarding the physical mechanism of Mullins effect, a great number of interpretations of Mullins effect in aspect of molecular structures have been proposed (Diani, *et al.*, 2009) , and no unanimously accepted theory prevail to explain the phenomena.

Blanchard and Parkinson (1952) ascribed Mullins effect to the bond cleavage. Low pre-strain breaks the physical bonds at the rubber-particle interface and higher pre-strain breaks chemical bonds. Suzuki *et al.* (2005) observed a great amount of broken polymer chain that contained in stretched silica-filled Styrene Butadiene Rubber (SBR). He also suggested the polymer chain scission might contribute to the Mullins effect. Dannenberg and Brennan (1956) believed that only permanent stress-softening can be attributed to the bond cleavage and they employed chain slipping theory (Houwink 1956) to account for the slow recovery of the Mullins effect. As Houwink proposed, the polymer molecules will slip over the filler surface during the first extension and generate new bonds along the chains. In Kraus's *et al.* (1966) swelling tests of pre-strained filled rubber, he examined only slight change in the cross-linking density, in contrast to a considerable level of stress-softening. It was concluded that the occurrence of bond cleavage is not the main cause to the Mullins effect. On the other hand, the rupture of carbon-black structure, namely the filler-structure cleavage is deemed as a major source of the stress-softening.

It can be concluded that Mullins effect is associated with multiple molecular movements, rather than a consequence of a single type of molecular action. Three main mechanisms suggested are listed as the combined actions of the three factors.

- Backbone bond cleavage
- Molecule slipping
- Filler-structure cleavage

5.5.4 Tensile strength and Shear strength

Average values of the tensile and shear bond strength of three types of sealants are compared in Figure 5- 25.

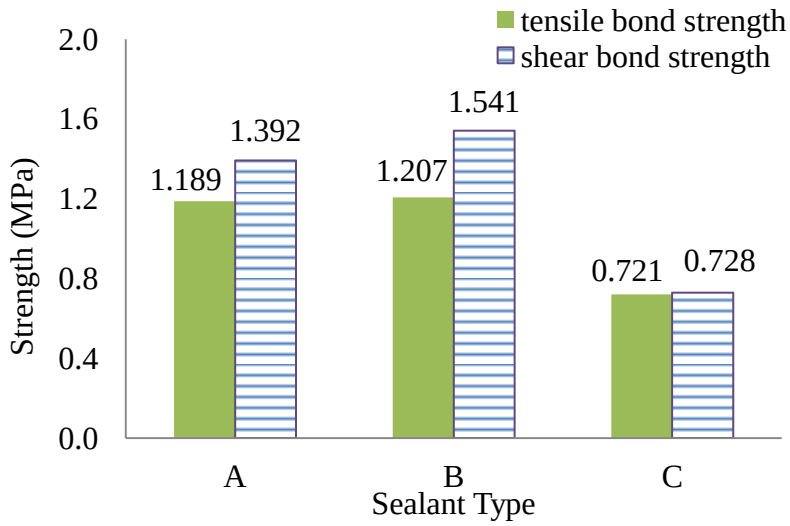

Figure 5- 25. Tensile and shear bond strength comparison between three sealants

By comparing the bond strength amongst the three types of sealant as revealed in Figure 5- 25, it can be seen that sealant B provides the highest tensile bond strength and shear strength, which is 1.68% and 10.7% higher than sealant A, 67.4% and 111.67% higher than sealant C. The two-part sealant again exhibits relatively poor strength compared to the other two types of one-part sealants. For all the three types of sealant, shear bond strength is found to be always higher than the tensile bond strength. For Sealant A and B, the shear strength is 17.07% and 27.6% higher than the tensile strength. The shear strength of sealant C is almost equal to the tensile stress, only 1% higher. This is because both friction and adhesion exist in shear direction and increase the shear strength. Adhesion failure was mainly observed in the shear test, whereas cohesion failure was found in more tensile test.

The elongation rate at break are also listed and compared in Table 5- 12 and Table 5- 13.

Table 5- 12. Tensile elongation rate at break

Cross-bonded tensile test	Sealant type		
	A	B	C
Elongation rate at break	241%	258%	180%
S.D.	0.494	0.853	0.299

Table 5- 13. Shear elongation rate at break

Cross-bonded shear test	Sealant type		
	A	B	C
Elongation rate at break	177%	188%	193%
S.D.	0.109	0.112	0.034

All the specimens showed excellent extensibility. Among the three types of sealant, sealant B has the highest tensile extensibility, and sealant C has the least. However, sealant C has the highest shear extensibility and sealant A has the least.

5.6 Sealants aging test

It is noted that the specimens used in the above mentioned tests are the intact sealant specimens without any aging process. In practical application, sealants are exposed to various natural environmental conditions, such as temperature, humidity and UV exposition variations. The sealants will inevitably suffer the aging problem during the service time. In this section, a series of aging tests are conducted for the secondary silicone sealant aiming to explore the sealant mechanical reactions (e.g. elasticity, strength, elongation rate etc.) under different aging conditions. Cross-bonded specimens are employed in the aging tests. The strength, breakage elongation, loading-displacement curves and hardness of the test specimens are investigated to reveal the aging behaviours. Furthermore, an aging coefficient is proposed to reflect the aging rate within a certain period. The formula is given as:

$$v = \frac{(n_0 - n_t)/n_0}{t} \times 100 \qquad 5\text{- }3$$

where, v is aging rate, in unit of *%/h*, n_0 is the initial property, n_t is the new property after aging, and t is aging period (*h*).

5.6.1 Selection of sealant specimens and the method statement of aging tests

To improve test efficiency, only one type of representative sealant specimen is chosen to carry out following aging tests. Sealant B is a type of commonly used insulating glazing secondary sealant with the physical attributes of representative features. Therefore, the aging responses of sealant B are primarily studied in the following aging tests.

In order to obtain the test results closest to the real scenario, the sealant thickness of the cross-bonded specimen is set to be 12mm (±1mm), which is the same with the thickness of interlayer spacer of conventional IGUs. Considering that the test results of the aged specimens may show a scattered distribution because of complicated intermolecular chemical reactions, at least six specimens are considered as a group for one type of aging condition. Four types of aging tests are considered.

Short-term temperature aging test

The temperature aging test is aimed to simulate different temperature variation in reality. In many regions, the on-site installed IGUs have to endure dramatic temperature change. Apart from ambient temperature, the solar radiation will also heat the sealant joints resulting in a high increase in the sealant temperature, in particular, with dark-colour curtain behind the glass. The temperature at edge areas of tinted or Low-E IGUs can even reach 80 ^{o}C and above during their service lives (Jacob and D'cruz, 1999).

UV-exposure aging test

As mentioned above, installed IGUs are exposed to solar radiation. Solar spectrum consists of ultra-violet, infrared radiations and visible light. The energy of light is inversely proportional to its wave length. The wavelength of ultra-violet radiation is lower than 280 nm, visible light between 380 to 780nm and infrared rays higher than 780nm. The energy of ultra-violet radiations is the highest and therefore imposes greatest threat to the sealant components. Normally the UV-exposure is always combined with high temperature to act upon the IGUs. Therefore the dual environmental impacts should be both considered in the test.

High-temperature and high relative humidity aging test

High-temperature and high relative humidity (RH) environments are common to the IGUs that installed in tropical or sub-tropical regions. The excessive moisture and the oxygen in the air can react with the secondary silicone sealants and thus accelerate their aging rate.

Solution immersion aging test

Water immersion is deemed as a cause to the degradation of mechanical properties of silicone sealants. For the glazing frame without appropriate drain route, the trapped water near the glass edges becomes very common. Acidic or alkaline atmospheres are also very common because of polluted air. NaCl, $CaCl_2$ and $CaCO_3$ solutions are adopted to simulate the neutral, acidic and alkaline environments respectively.

5.6.2 Short-term temperature aging test

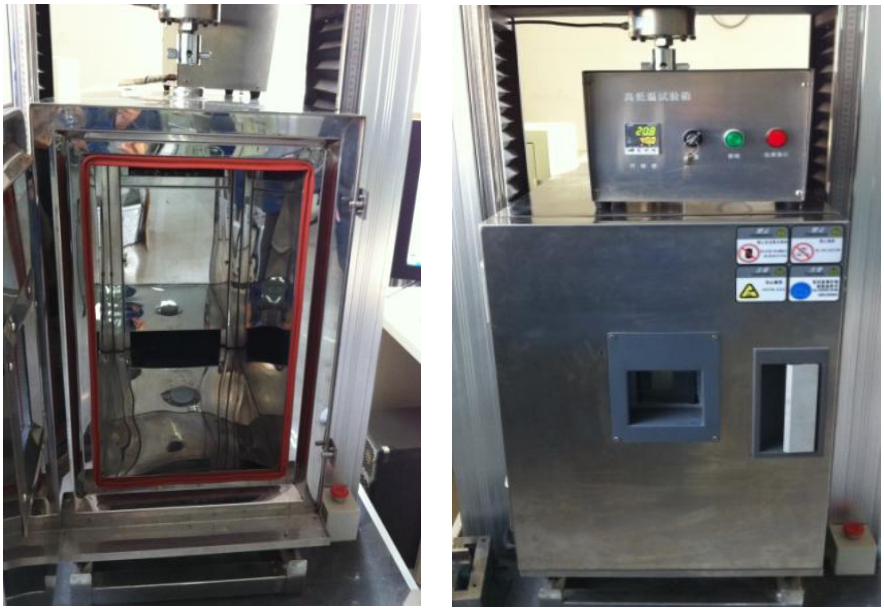

Figure 5- 26. Heating and cooling chamber

A heating and cooling temperature chamber (shown in Figure 5- 26) is employed to subject the specimen to the designated temperature. Four temperatures, i.e. -30, 20, 80, 120^{o} C, are considered to cover the temperature range that most edge seal may experience. Cross-bonded specimens are placed in the chamber under each temperature condition sustaining for 1 hour. This test mainly focuses on the short-term effects induced by drastic temperature rise or drop. The tension and shear tests are then carried out in the chamber with a loading speed is 5mm/min.

The tensile and shear strength are plotted in Figure 5- 27.

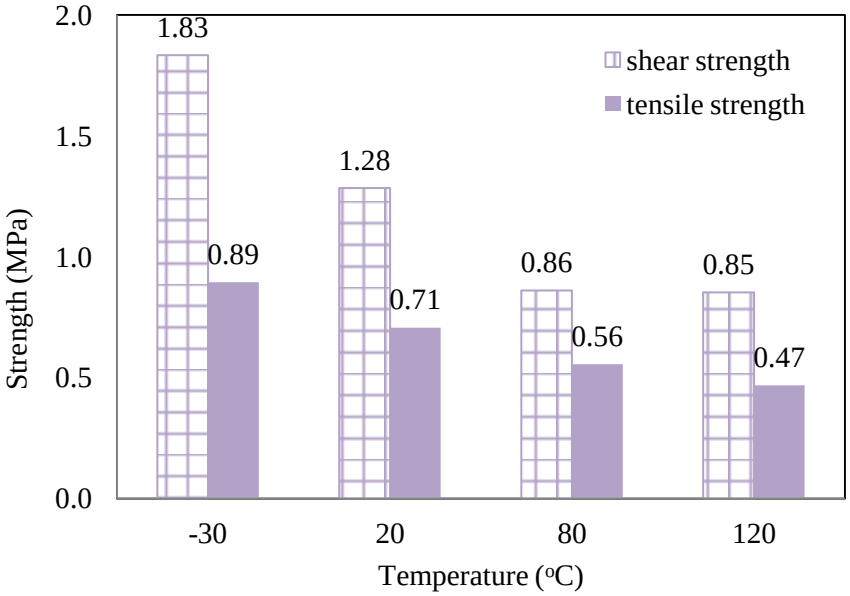

Figure 5- 27. Comparison between tensile and shear strength under different temperature

It can be seen that the tensile strength is reduced by 47.59% from -30°C to 120 °C. The molecular segment movement of siloxane polymer will vary with the temperature. Low temperature impedes the segment movements. The alleviation in the molecular movement is characterised by the loss of elasticity and the increase in strength and hardness. When the temperature rises, the sealant elasticity is gradually recovered and the hardness decreases. The viscous-elastic feature of sealant becomes more obvious in higher temperature.

In terms of the shear test, the shear strength is also decreased by 53.55% from -30°C to 120 °C. Adhesion shear failure occurred in most of specimens in both high and low temperature. The strain distribution of the specimen cross section in the shear test is presented below in Figure 5- 28 to account for the primary failure mode. The contours are processed by the non-contact strain gauge introduced in section 5.3.1.

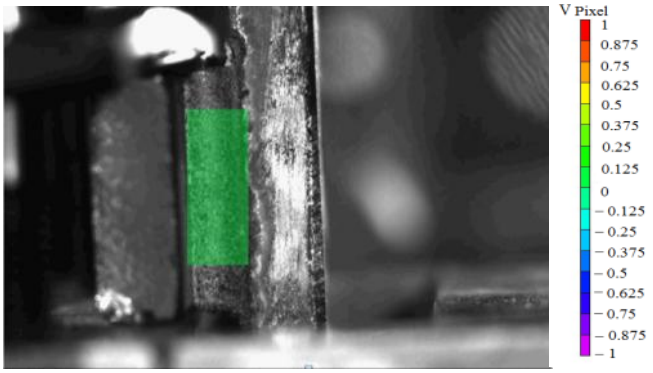

(a) Initial state

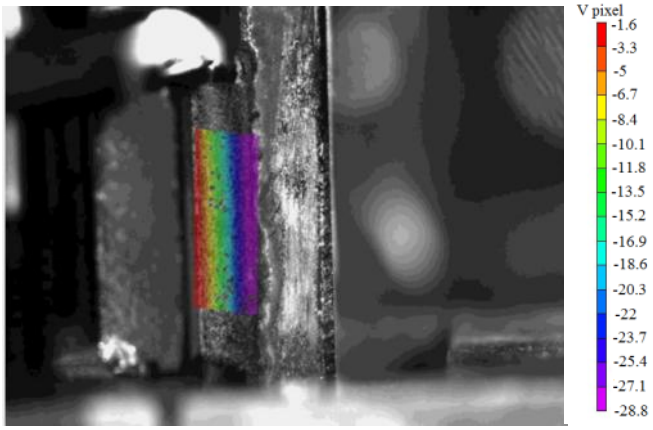

(b) Deformed state

Figure 5- 28. Strain contours during stress bond test

In Figure 5- 28, it is observed that the maximum strain in the shear test is located closest to the adhesion interface, and hence the failure is most likely to take place at the bonded interfaces. If internal defect exists like impurities or voids within the sealant, stress concentration is likely to take place during loading process and hence bring about the cohesion failure.

In order to find the strength sensitivity range to the temperature change, a sensitivity parameter S_T is defined as:

$$S_T = \frac{(n_T - n_O)/n_0}{T} \times 100 \qquad 5\text{- }4$$

where n_T is the property at Temperature T, n_0 is the initial property, and T is the test temperature (^oC). Positive results indicate improved property.

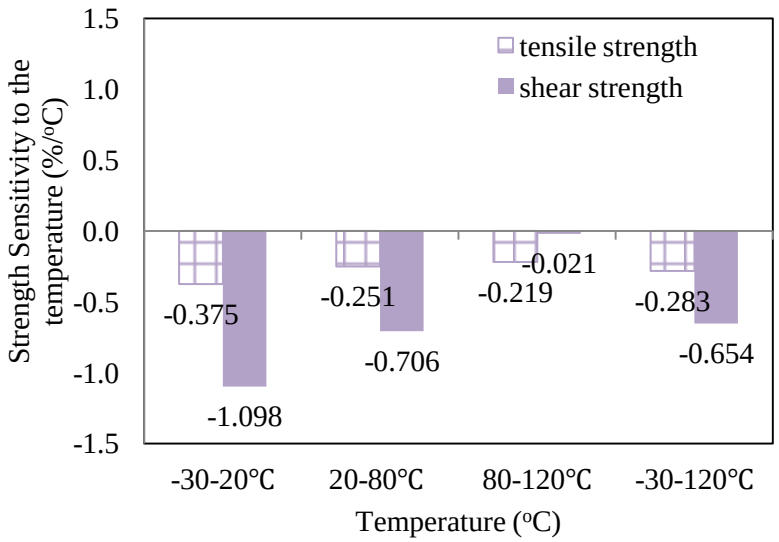

Figure 5- 29. Temperature dependency of tensile strength and shear strength during aging test

As shown in Figure 5- 29, the negative values demonstrate degrading strength along with increasing temperature. The aging rate of strength is declining with increasing temperature change. The rate below 20^{o}C is the highest, 0.375%/ ^{o}C for the tensile strength and 1.098%/^{o}C for the shear strength, which is even higher than the average aging rate. The aging rate of tensile strength remains unchanged above 20^{o}C. When the temperature is between 80 ^{o}C to 120 ^{o}C, the shear strength is almost independent of the temperature change. It can be concluded that the sealant strength is more sensitive to the temperature in cold environments whereas is more stable under high temperature. It is believed that the molecular segment movement within the sealant is to a great extent impeded by the cold temperature field, and therefore result in a significant variation in the bond strengths. On the other hand, the predominant aging mechanism under high temperature is excessive cross-linking reaction, which takes place when the temperature

rises from 20°C to 80°C. Fully cross-linked PDMAs chains will not further affect the strengths, and therefore exert little impact on the strength variation even though the temperature is still increased.

5.6.3 High temperature and RH aging test

High temperature and relative humidity test chamber (shown in Figure 5- 30) is used to generate a temperature cycling environment with high relative humidity (RH).

(a). High temperature and RH cycling test chamber (b). Control panel

Figure 5- 30. Test apparatus for High temperature and RH cycling test

The relative humidity of the test chamber is above 95%. The temperature changes regularly with time and the cycling pattern is given below in Figure 5- 31:

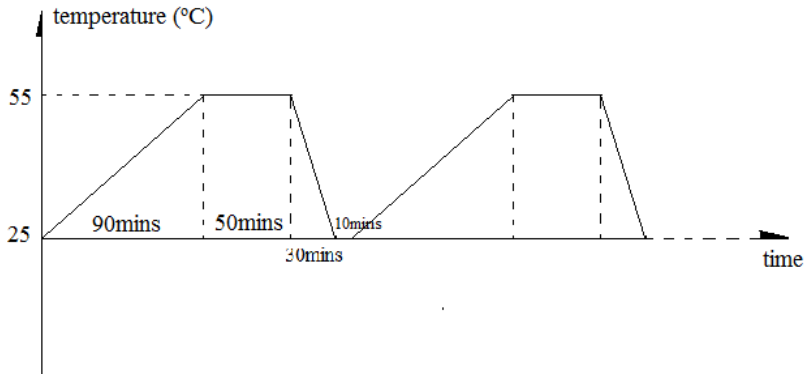

Figure 5- 31. Climatic cycling condition in the test chamber

Aging period is taken into consideration as a parametric study. The specimens are grouped into 20 days, 40days, 60days 80days and 120days. Each group contains six specimens. The aged specimens are applied with identical loading conditions as introduced in the previous tensile and shear tests.

As shown in Figure 5- 32, the tensile and shear bond strength are markedly reduced under high temperature and humidity environments. The tensile strength starts to go down sharply after first 20 days and is reduced by 86.18% in overall 120 days aging period. The sealant is completely de-bonded from the glass substrate in tensile test when the aging period exceeds 80 days. That means the sealant adhesion is totally deprived under the aging condition.

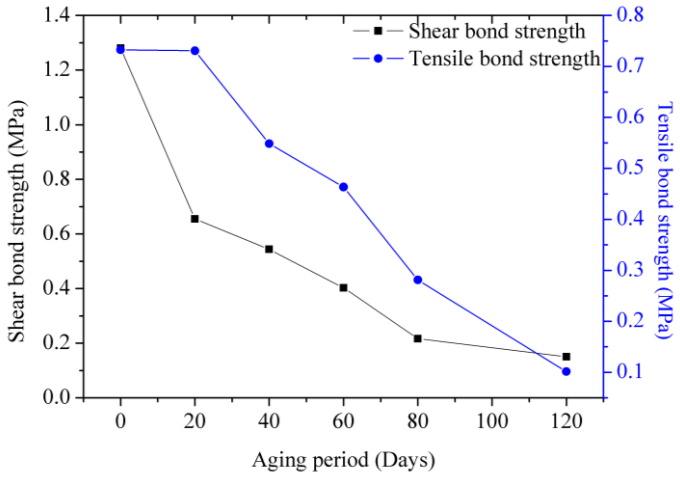

Figure 5- 32. Tensile and shear strength variation with aging time

Combined with the loading-displacement curves plotted in Figure 5- 33, the un-aged curve displays good viscoelasticity by remaining level after yield. However the plateau stage tends to be short with longer aging time and cannot be found above 60 days. This is because the aged specimen has lost most of its viscoelasticity and will directly fracture at the yield point load, as observed in the tests.

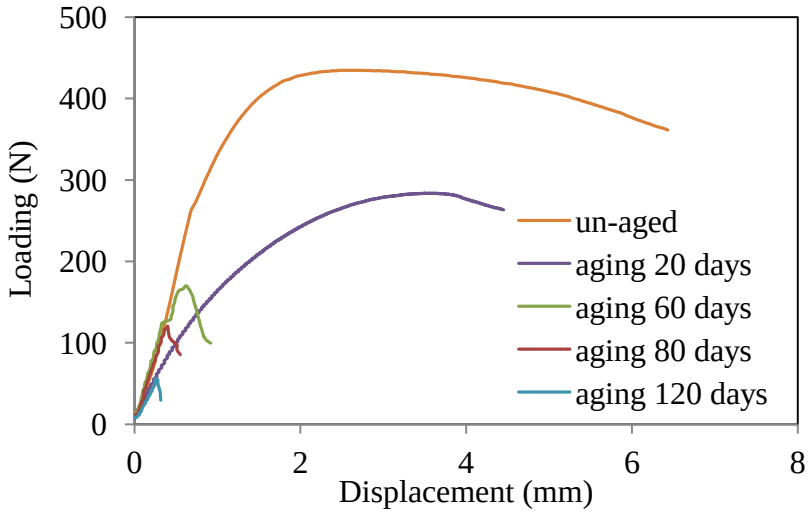

Figure 5- 33. Loading-displacement curves of the specimens of different aging levels

The bonding performance of the silicone sealants depends on two main contributors, i.e., the interfacial adhesive behaviour and the sealant cohesive performance. The adhesion performance is mainly governed by the chemical bonds at the glass-sealant interface, while the cohesive performance relies on the chemical bonds and intermolecular interactions within the sealant. When subjected to a high temperature, the adhesion interface turns to be a high temperature anoxic environment. Since the oxygen is not sufficient to activate the methyl oxidation, the scission of the backbone Si-O bond will be induced by high energy (Wu and Zhong, 2005). PDMAs are degraded into a variety of LMW (low-molecular weight) polymers such as hexmethyl/octamethylcy - cyclotrisiloxane, and other oligomer chains. The Si-O bond scission at the interface due to high temperature is a main reason to the degraded bonding strength.

Within the sealant, high humidity provides abundant moisture to activate the hydrolysis of PDMAs and hence promote the formation of more cross-linking. Meanwhile, high temperature will accelerate the oxidation in PDMA. Since the backbone of PDMA, Si-O bond, possesses the highest bond energy (Buyl, 2001), the oxidation is more likely to occur in the methyl side groups with the lower bond energy and form hydroxyl ended siloxanes and the carboxyl (-COOH) group. The labile carboxyl group then converts into protons and carbon dioxide. The hydroxyl-ended siloxanes will further develop cross-linking. The reaction is shown below Figure 5- 34:

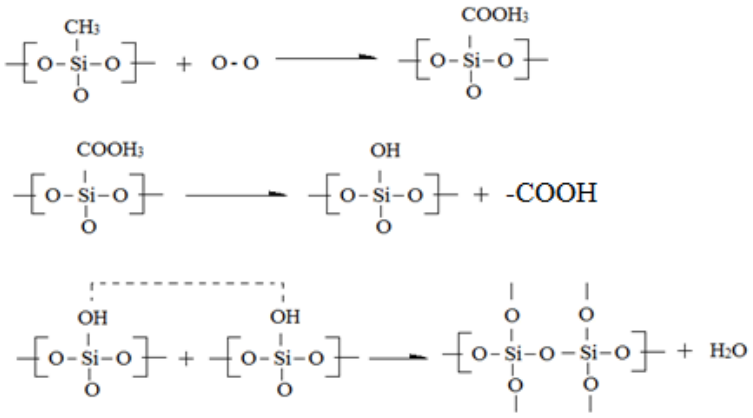

Figure 5- 34. Further cross-linking reaction due to the oxidation in PMDAs

The increase in the three-dimensional PDMA net structure results in a higher molecular weight, hardness, cohesive strength and lower elongation rate at break. The changes in these mechanical properties will also cause the loss of resilience.

The sensitivity analysis to the high temperature and RH is presented below in Figure 5-35. Positive values demonstrates improved property and vice versa.

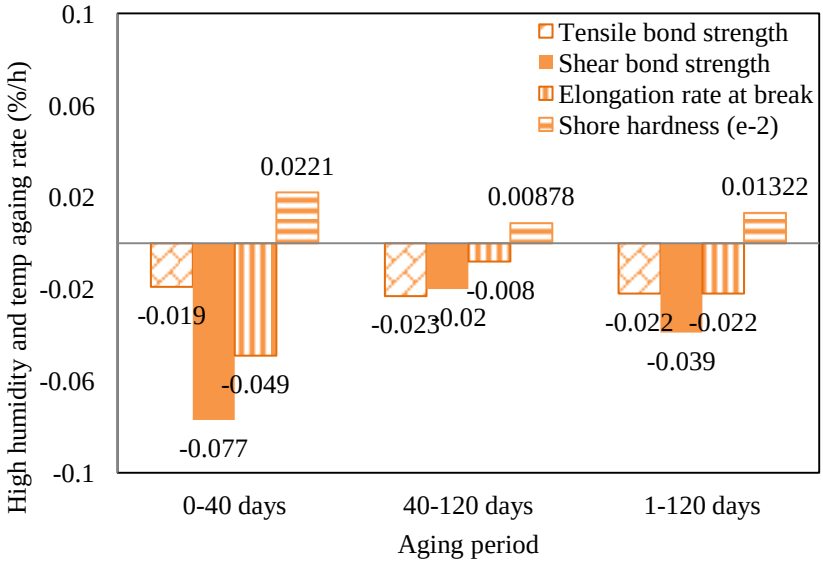

Figure 5- 35. Sensitivity analysis to high temperature and RH aging condition

According to Figure 5- 35, the tensile, shear bond strength and the elongation rate at break rate are degrading under the aging condition whereas the shore hardness is enhanced. Apart from the tensile strength, other properties are more sensitive in the initial aging period, i.e. 0- 40 day, in which the aging rate is higher than that in 40 -120 days. On the contrary, the tensile strength aging rate at a latter aging period is higher than an earlier stage. This is because the further cross-linking formation due to the methyl oxidation at the early stage plays a beneficial role to the tensile bond strength. Such beneficial effect counteracts the bond strength degradation caused by Si-O scission at the interface. In the latter aging periods, the action of Si-O bond cleavage governs the increase of the degradation rate.

5.6.4. UV-exposure aging test

The specimens are placed in the UV chamber (shown in Figure 5- 36) and exposed to a MLU ultraviolet radiator of 300W. The output power is no lower than 40W/m^2. The ambient temperature in the chamber is set to be 50±3^{o}C. Similar to the high temperature and RH aging tests, the specimens are grouped according to different aging period, into 20 days, 40 days, 60 days, 80 days and 120 days. Each group have six specimens. The aged specimens are loaded with speed 5mm/min.

Figure 5- 36. UV exposure chamber

The tensile and shear strengths are plotted and compared. The tensile strength is found to be increasing with the aging time initially and in a later stage (see Figure 5- 37). On the other hand, there is a sharp drop for shear strength in the first forty days, and then undergo a minor recover at the latter stage. The overall rise of tensile strength is 49.04% while the drop of shear strength is 40.64%.

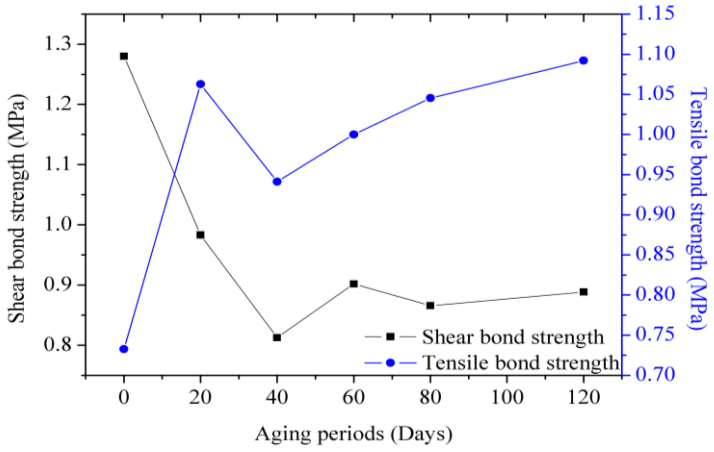

Figure 5- 37. Tensile and shear strength change with different aging period

Opposite aging trends of tensile and shear strengths are attributed to a combined action of strengthened cross-linking reactions and Si-O bond cleavage. The UV exposure and high temperature provide sufficient energy to intensify the chemical reactions within the organic polymer sealant. Two types of reactions will simultaneously take place in different ambient conditions. Further cross-link reactions commences in the aerobic ambient where the methyl side groups are replaced with hydroxyl by oxidation. The cohesive strength is therefore increased. The Si-O scission occurs at the bonding interface, i.e. relatively anoxic ambient, triggered by the high energy of UV radiator and higher temperature. The interfacial adhesive strength will decrease due to the cleavage of the interfacial chemical bonds. The results suggest that the cross-linking reaction is a primary influencing factor to the tensile bond strength, so it can be reinforced by an enhanced level of cross-linking reaction even though the Si-O bonds are weakened at the interface. It is also observed that the bond shear strength is more sensitive to the decomposition reaction of Si-O bond at the interface. When the Si-O bond scission occurs, the shear bond strength is directly affected negatively.

The aging sensitivity analysis is given in Figure 5- 38. The aging rates of strengths at initial stage are much higher than latter stage. So the influence to the sealant strength mainly takes place in the early stage of aging test. The elongation rate at break increases slightly at the beginning and then significantly declines with longer aging time. The increasing rate of the Shore hardness remains stable over the whole aging period.

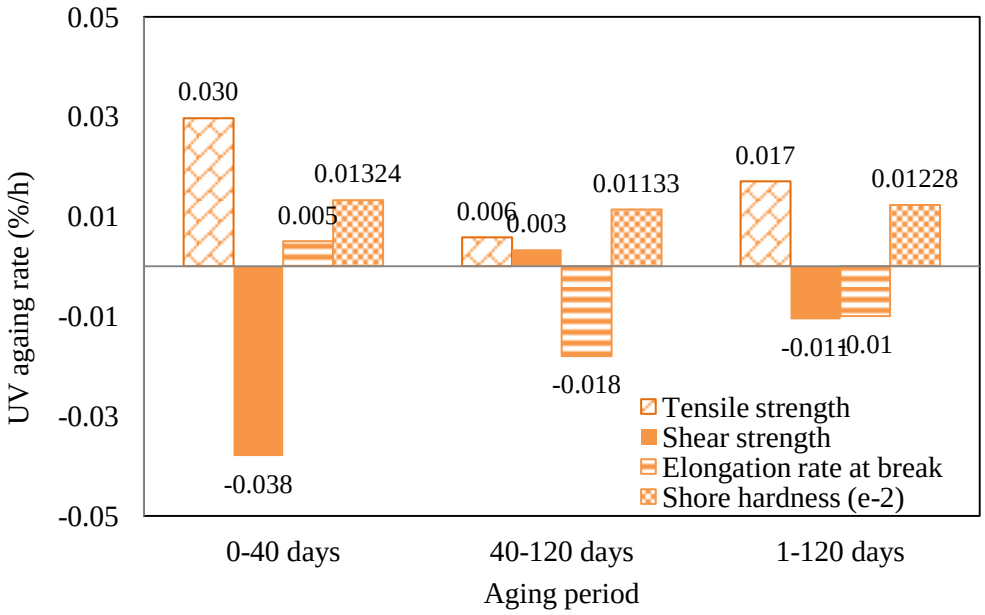

Figure 5- 38. Sensitivity analysis to UV exposure aging condition

5.6.5 Immersion aging test

Four types of solutions are used to conduct immersion aging test: K_2CO_3 provides weak alkaline environment, which is to emulate the effect caused by alkaline cleaning agent. The $CaCl_2$ solution is employed to provide acidic ambient, as $CaCl_2$ is the commonly used desiccant in IGUs. The sealant is inevitable to contact with $CaCl_2$ solution in high humidity environment. Purified water and NaCl solutions are to provide neutral ambient. The concentration is 0.1 mol/L. The total immersion time is 80 days. The specimens are grouped into 20 days, 40 days, 60 days and 80 days, which is to assess the aging performance periodically. The solution temperature remains consistent 70 ± 3 ^{o}C since it is the measured temperature on the sealant surface of installed IGUs when subjected to the solar radiation.

As shown in Figure 5- 39, the tensile strength declines with immersion time. Instead of monotonously decreasing, the curves experience a minor rise after a first sharp drop

within 20 aging days. The total declining rate is K_2CO_3 > $CaCl_2$ > purified water > NaCl, which is reduced by 31.53%, 23.94%, 22.34% and 9.1%. A similar order is observed in Figure 5- 39(b). The shear strength is reduced by 61.72%, 36.82%, 30.16% and 27.77% for K_2CO_3, $CaCl_2$, purified water and NaCl respectively. It is noted in the first 20 days, the hardness and tensile strength are both decreasing whereas the elongation rate at break is increasing. This is the result of the solution permeation into the polymer structure, which increases the volume and thus reduces the cross-linking density. Moreover, the sealant swelling due to moisture infiltration weakens the intermolecular forces between binder (PDMAs) and other fillers in silicone sealants. The elongation rate at break and the Shore hardness change with aging time are presented in Figure 5-40 and Figure 5- 41. With the increasing immersion time, sufficient moisture boosts the hydrolysis and condensation of PDMAs, so that the cross-linking reaction becomes predominant and leads to increasing hardness and decreasing elongation rate at break. The degrading tendency of tensile also goes gently at the latter period.

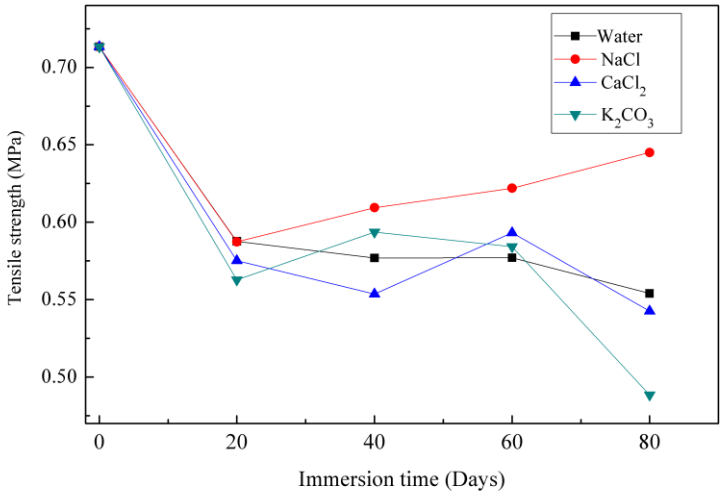

(a). Tensile strength

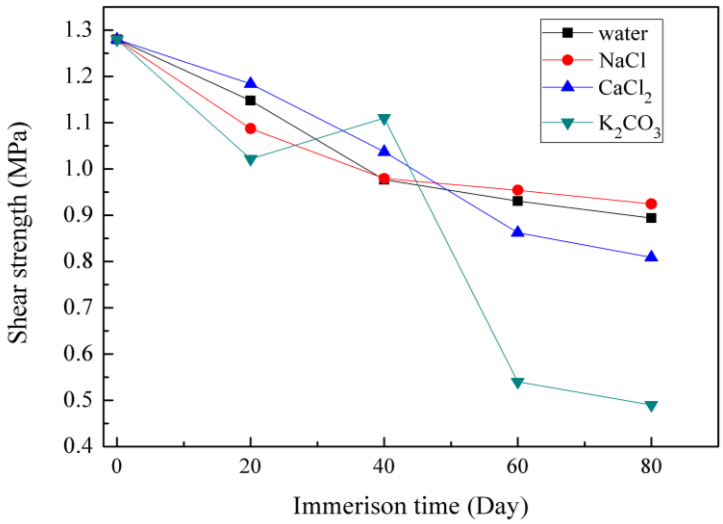

(b) Shear strength

Figure 5- 39. Strength change with increasing aging time

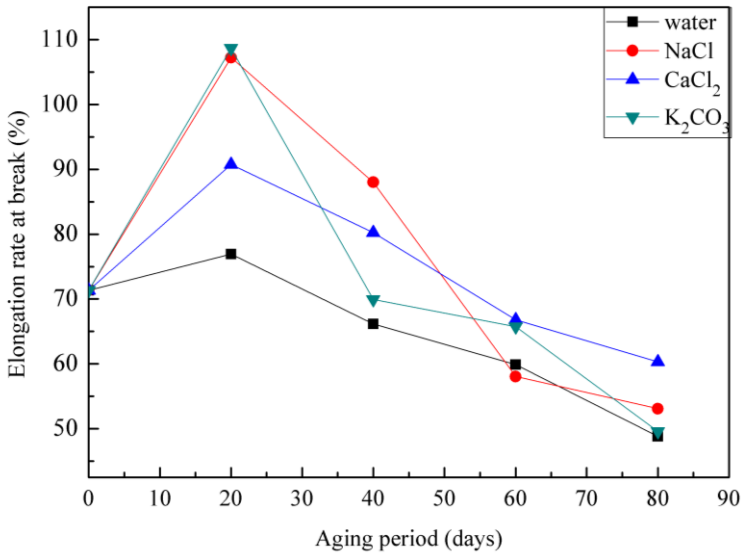

Figure 5- 40. Change of elongation rate at break with increasing aging time

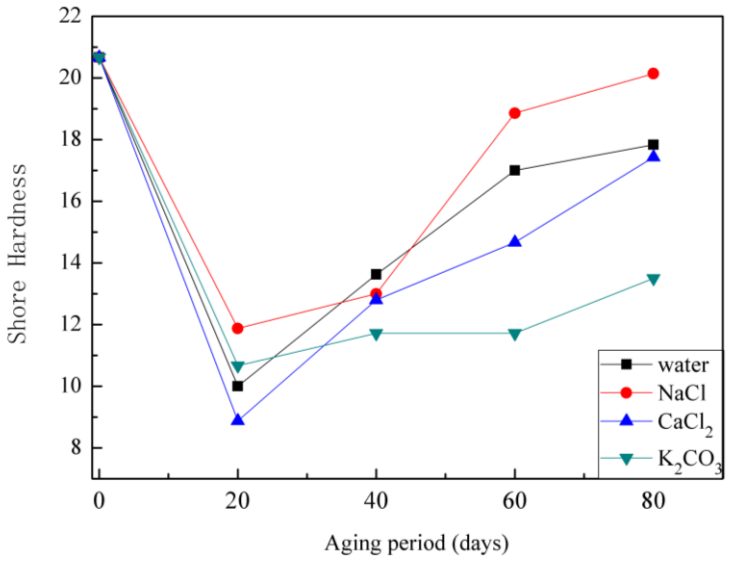

Figure 5- 41. Change of Shore hardness with increasing aging time

It can be concluded that amongst three types of solutions, alkaline environment generates most obvious aging effect to sealant strength; acid ambient is the second most influential and neutral condition is the least. The free hydroxyl radicals contained in alkaline solution will react with the hydrogen ions on the interface so as to decrease the hydrogen bonds. In the acid solution, hydrogen iron can decompose Si-O bond on the interface so as to undermine the adhesion strength. It is observed that both acid and alkaline environment can promote cross-linking reaction despite the swelling phenomenon is in dominant position in the beginning of aging period.

The sensitivity analysis of four solutions is presented below in Figure 5- 42. Apart from K_2CO_3, the tensile and shear strength degradation rate is higher at early aging stage than latter, while the elongation rate at break and the Shore hardness are changing distinctly at latter aging stage.

In terms of K_2CO_3, the decreasing level of shear strength is found to be greater in latter period. It is because that the shear strength is more sensitive to the chemical bonds on

the interface rather than the cross-linking within the sealant. In spite of enhanced cross-linking degree at latter aging stage, the Si-O bond scission and the breakage of hydrogen bonds are also increased, which give rise to the degradation of shear strength.

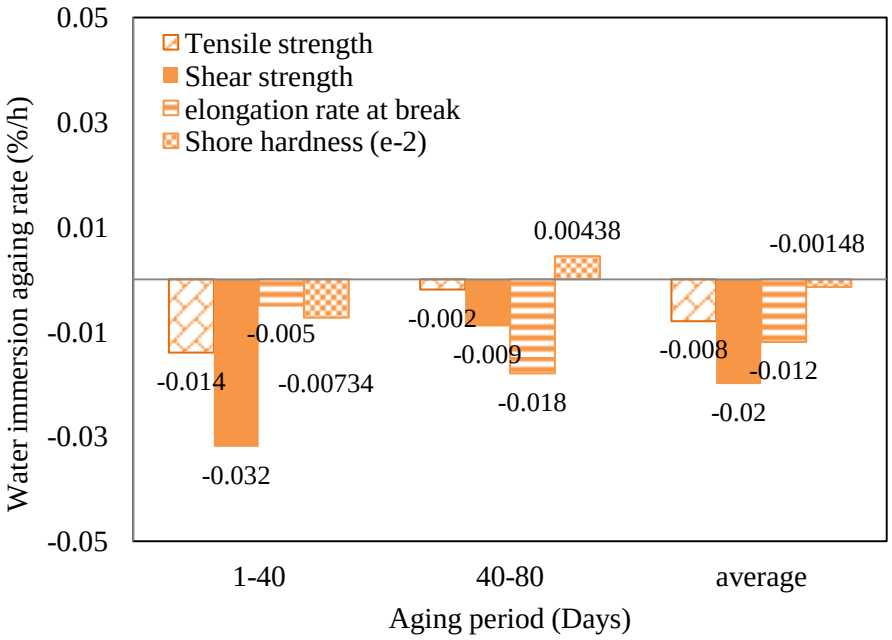

(a) Purified water

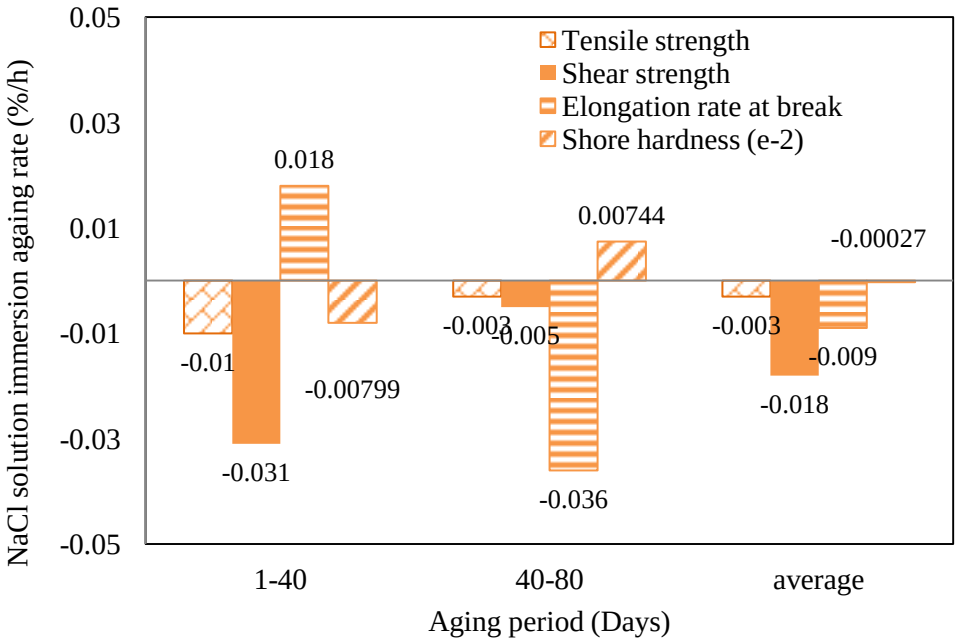

(b). NaCl solution

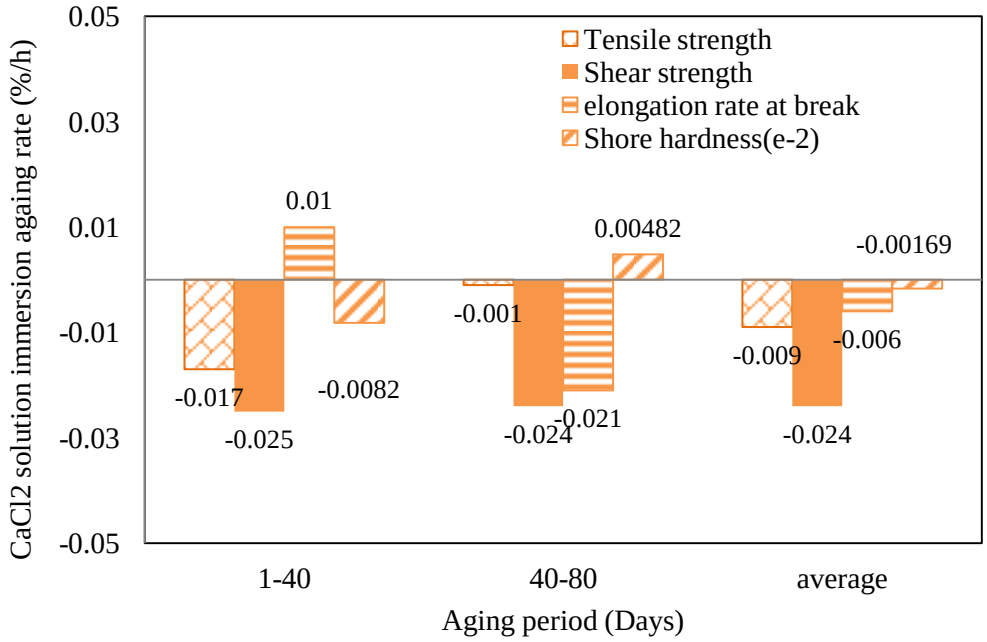

(c). $CaCl_2$ solution

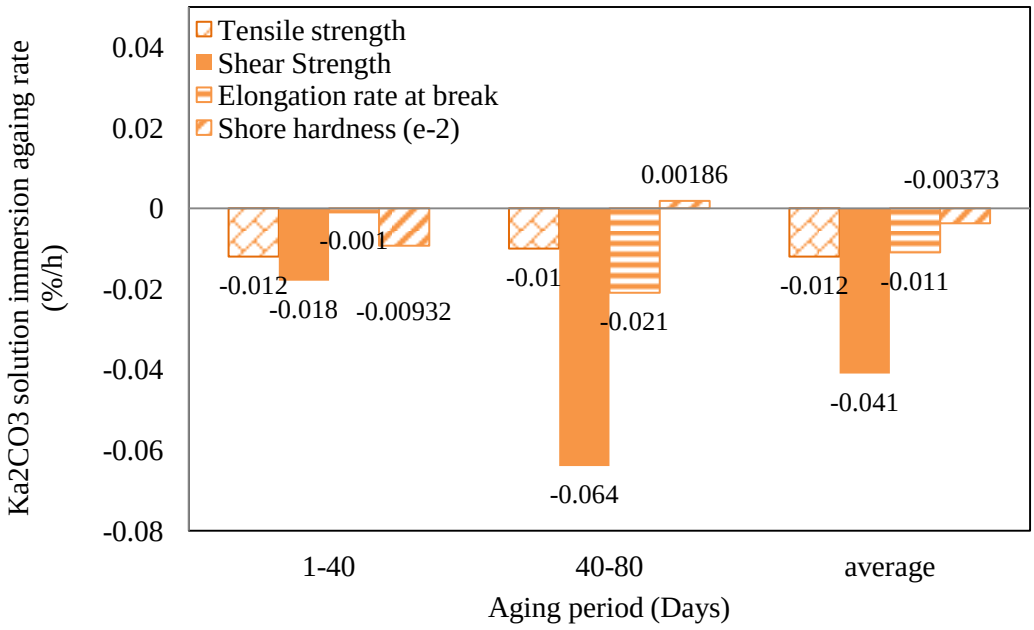

(d). Ka_2CO_3 solution

Figure 5- 42. Sensitivity analysis of solution immersion test

5.7 FEA parametric study on the geometric design of edge seal system

In the above mentioned discussions, the secondary silicone sealants are individually studied. Actual mechanical attack to the geometry-customised edge sealants in the in-service IGUs can be hardly estimated in the experimental work. FEM numerical tool exhibits a number of advantages on this occasion. The hydrostatic fluid model introduced in Chapter 3 will be employed in the numerical analysis. Instead of the simplified edges, the detailed edge seal system will be simulated in hydrostatic fluids models.

5.7.1 FEM model description

Three types of profiles are examined, i.e., Cup-shape, Flex and WE as given in Figure 5- 43.

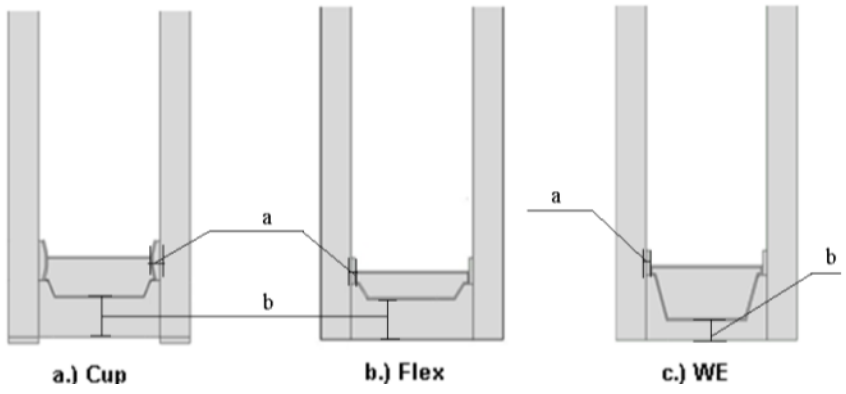

Figure 5- 43. Three designs of the edge seal

Two variables are discussed in the parametric study, *a* is taken as the width of primary sealant, and *b* is the thickness of secondary sealant. *a* and *b* of three mentioned edge seal systems are outlined in Table 5- 14.

Table 5- 14. Parameters *a* and *b* in three edge seal system

	Cup		Flex	WE
a (mm)	centre	side	0.5	0.5
	1	0.7		
b (mm)	4.49		4.49	2.34

Silicone sealant B is adopted as the secondary sealant in the numerical model. The stress-strain curves are characterised of a hyper-elastic feature. ABAQUS allows for either implemented mathematic models or raw experimental data to describe the hyper-elastic material properties of the silicone sealants. Uniaxial tension and compressive test results given in Section 5.3 and 5.4 can be used to depict the stress-strain relation of Sealant B.

The geometric and the material attributes of other components in the IGU have been described by Yang et al. (2004) in detail. The geometric dimension apart from *a* and *b* are identical in the three profiles: the IGU sample is comprised of two pieces of tempered glass panels with a thickness of 4mm and the width of the air cavity is 16mm. The material properties of other components in the IGUs are specified in Table 5- 15**.**

Table 5- 15. Material properties of the components in an IGU

	Glass	Primary sealant (Butyl)	Spacer （Stainless steel）	Desiccant
Young‘s modulus(MPa)	72000	3.9	205000	4.9
Poisson ratio	0.22	0.49	0.3	0.2
Linear thermal expansion(mm/K)	9.00E-06	/	/	/

Assuming the IGU model is in the extreme summer condition, enduring a temperature differential of 60K. A uniform pressure load 1kPa is applied on one side to represent an

average level of wind load in the parametric study. The Von-Mises stresses and the displacement magnitude of the primary sealant and secondary sealant are presented.

5.7.2 FEM Stress analysis

Stress analysis of primary sealant

From Figure 5- 44 (b) and (c), we can find that the maximum stress concentration is at the centre of the rectangular shaped primary sealant, where the joint point of butyl sealant and the metal spacer bar is. But it moves to the right-lower corner of the interface in the curved sealant profile, as shown in Figure 5- 44(a). The results indicate that the thicker bulk can disperse a greater amount of strain energy hence abate the stress/strain concentration on the interface and within the sealant. The primary sealant used in the cup model therefore achieves a favourable performance to reduce the adhesion failure and cohesion failure.

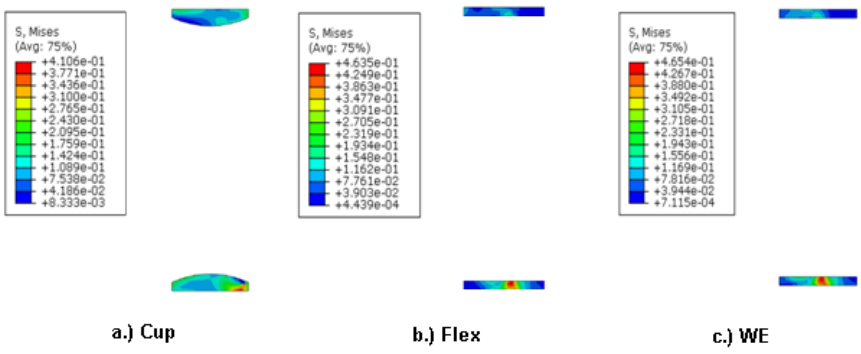

Figure 5- 44 Contour plots of Von-Mises stress in the primary sealants

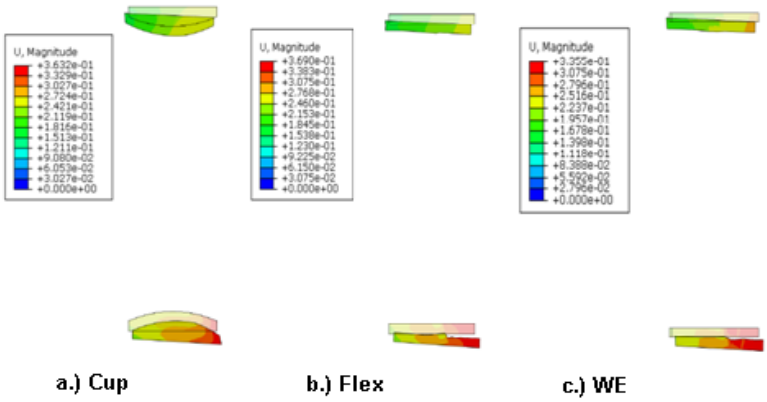

Figure 5- 45 Contour plots of magnitude displacement on the deformed primary sealant

According to the Figure 5- 45, the maximum displacement also occurs at the lower-right corner of the bottom primary sealant. Even though the upper glass experiences higher temperature and the thermal expansion is greater than the lower panel, the applied wind load toward the air cavity can cancel out a certain amount of forces acting on top panel and enhance the bending of the lower panel. As a result, the displacement of primary sealant adhering to the lower side is almost twice as much as that of the upper side. Table 5- 16 lists the comparison of the peak Von-Mises stress for the primary sealants in three models. We can conclude that the cup model offers a reduction of peak stress on the primary sealant by 11.4% for Flex model, and 11.7% for the WE model.

Table 5- 16 Comparison of the peak value for Von-Mises stress of primary sealants

	Cup	Flex	WE
Peak. Von-Mises stress(MPa)	0.4106	0.4635	0.4654
Ratio	1	88.59%	88.23%

Stress analysis of the secondary sealants

As shown in Figure 5- 46, large stresses always occur at the turning point along the interface line between the secondary sealant and the spacer bar. The maximum stress is

found at either the upper concave vertex near the mental spacer or the left-upper corner adjacent to the glass panel. Due to the interactive work of wind load and the thermal expansive movement, the upper sealant will bend inward and large stresses are generated. As presented in Figure 5- 47, the displacements of lower part of sealant are more significant than that of upper part. However, higher stresses do not develop in the lower concave corner. This is because the movement of lower part of sealant is outward bending, which alleviates the abrupt inflexion points, and thus reduce the level of stress concentration.

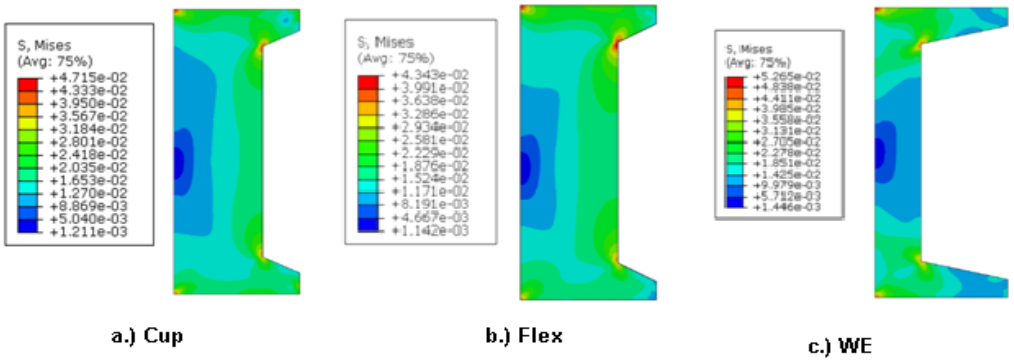

Figure 5- 46. Contour plots of Von-Mises stress on the secondary sealant

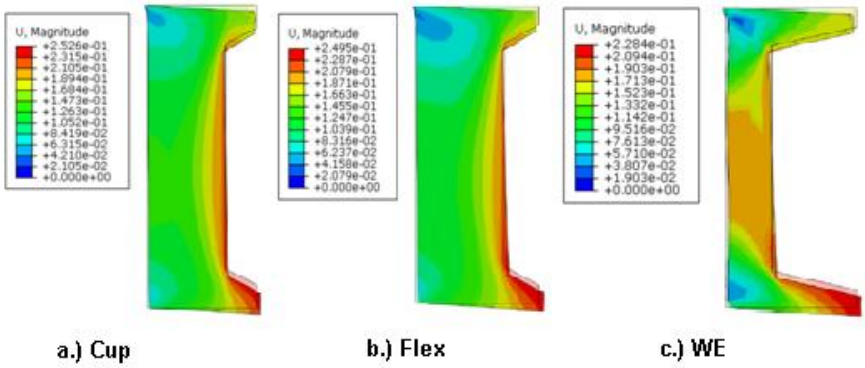

Figure 5- 47. Contour plots of displacement on the deformed secondary sealant

The Flex profile can reduce 17.51% of stress compared to the WE profile and 10.4% to the cup profile. The comparison of peak Von-Mises stresses are shown in the Table 5-17. Compared with the secondary sealants used in WE profile, the sealants used in Flex and cup profile have larger bulk and hence absorb more strain energy resulting from the exerted mechanical actions. The Flex profile plays the most effective role in reducing the maximum stress that occurs on the secondary sealant, and cuts down the possibility of sealant failure.

Table 5- 17 Comparison of the peak value for Von-Mises stress of secondary sealants

	Flex	Cup	WE
Peak. Von-Mises stress(MPa)	0.04343	0.047415	0.05265
Ratio	1	91.16%	82.48%

5.7.3 Results and discussions

In the parametric study, three types of IGU edge seal designs are analysed to investigate the stress distributions influenced by different edge seal designs. With regards to the primary sealants, the curve profile in the cup model can reduce the stress concentration induced at the wedge of different material interface. The value of peak stress is also reduced effectively. The secondary sealant of Flex profile is the best designed in terms of the structural behaviour of edge sealing. The favourable performance is attributed to its dimensional features. The large bulk is able to spread stress/strain energy caused by the mechanical movement. The less abrupt concave angle than that of WE profile can also smoothen the distribution of the stress.

It is noted that all the severe stress concentrations occur near the corners or on the interface where either geometric layout or material phases varies abruptly. The sealant

failure always happened from these vulnerable parts. On this basis, the recommendations for the seal designing in IGUs can be put forward.

1. The concave angles formed by the secondary sealant surfaces should be reduced, or replaced with arch-shaped edges.

2. The conjunction interface between different components should be designated to be smooth without abrupt geometric changes.

3 The thickness of sealant in vulnerable parts should be increased in order to alleviate the severe stress concentration.

4. The improved material properties of sealants can be introduced to ensure the structural integrity of IGU. The sealants with high elastic performance are recommended in order to increase the yield stress/strain.

5.8 Summary

In this chapter, the mechanical properties and behaviours of IGU secondary silicone sealants are examined by performing laboratory tests. The tensile and compressive stress-strain curves of three types of commercially popular sealants are obtained from dumb-bell tensile tests and compression cycling tests. Three types of commercially popular silicone sealants are considered. Sealant A and B are one-part and sealant C is two-part.

In the tensile test, the strength of sealant B is the highest and C is the least. Obvious hardening phenomena are found in sealant A and B. The disparity of curves shape and the strengths of three sealants are explained from the perspective of molecular structures.

The cross-linking density is an important parameter to determine polymer strength. The orientation phenomena of PDMA chains accounts for the hardening section of stress-strain curves occurring in the single-component silicone sealants.

Since the tension behaviour is different from the compression responses in the organic polymer sealants, the compression cycling test is also conducted. Stress relaxation is found in compression cycling test. The stresses are relieved by four-time cycling test and the stress-strain curve in the last loading cycle is accurate enough to depict the sealant behaviour. The compressive secant Young's modulus at 10% and 20% strain levels are calculated and compared between three types of sealants. The compression modulus of sealant B is the highest and is also most sensitive to strain change.

The adhesion behaviour is also discussed by carrying out cross-bonded tests. The tensile strength, shear strength and elongation rate at break of silicone sealants are obtained. Similar to the previous test results, sealant B displays the highest tensile and shear strength and meanwhile the highest elongation rate at break. For all the three sealants, shear strength is always higher than tensile strength.

Pre-loading process in the cross-bonded tests is discussed. Stress-softening loading-displacement curves are observed in the pre-strained specimens. Different pre-loading levels are employed to investigate the impacts to the loading-displacement curve. It is found that pre-loading process can remarkably change the loading-displacement shape, but exert little influence on the peak stress at yield points. The Mullins effect is to account for the stress-softening. The mechanism of the Mullins effect is reviewed. Three major causes: bond cleavage, molecular slipping and fill-structure cleavage are deemed to attribute to the Mullins effect in the silicone sealants.

In the aging test, a variety of aging factors are taken into consideration. The impacts by extreme climatic change, high temperature and high RH condition, UV exposure and solution immersion are adopted to estimate the sealant aging behaviours. The aging mechanisms can be ascribed to two main molecular reactions: excessive cross-linking reaction because of methyl oxidation or hydrolysis leads to the loss of elasticity; the Si-O bond scission on the sealant-glass interface due to high temperature or UV exposure results in the degradation of adhesion strength. It is noted that further cross-linking reaction can reinforce the sealant cohesive strength, and hence increases the tensile bond strength even though the interfacial adhesion is deteriorated. The aging rates of each physical property of silicone sealant are also presented. The sensitive ranges can be found by comparing the aging rates in different aging periods. The aging rates of each physical property of silicone sealant are also presented. The sensitive ranges can be found by comparing the aging rates in different aging periods.

In the last section, the edge seal systems are incorporated in the hydrostatic fluid models. Three commercially available seal profiles are taken in to parametric study. The Von-Mises stress distribution and the deflection distribution of three types of sealant profiles are examined under interactive environmental actions. Recommendations on the geometry design of edge sealants are proposed based on the FEM results.

CHAPTER 6 CONTACT DAMAGE AND OPTIMISATION OF SUPPORTING PILLARS IN VGUS BY XFEM METHOD

6.1 Introduction

Supporting pillars play a significant role in the structural performance of VGUs. They are employed to separate two glass panels under high differential pressure between the external barometric pressure and the internal vacuum space. The pillars are placed in a regular square array between two glass panels, as shown in Figure 6- 1.

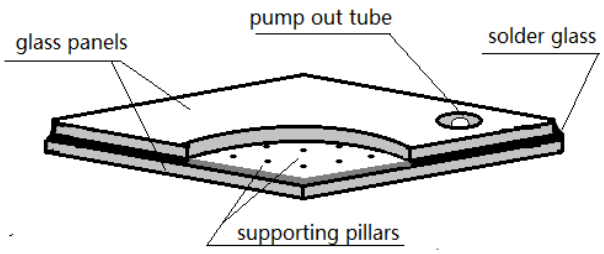

Figure 6- 1. Schematic graph of the supporting pillars in a vacuum glazing unit

Collins and Fischer-Cripps outlined the design procedures of the pillar array two decades ago (Collins and Fischer-Cripps, 1991). Three types of design constraints were presented: the tensile stresses in the vicinity of pillars, the thermal conductance through and the indentation stresses around them. The final design of supporting pillar is as a trade-off result of the combination of these individual constraints. Well established analytical solutions and FEA numerical models for the first two constraints have been introduced in existing studies (Collins and Robison, 1991; Collins and Fischer-Cripps, 1992; Collins and Simko, 1998). Nevertheless, the numerical modelling for the pillar indentation in VGUs is less studied. The indentation behaviour and the resulting cone

cracks cannot be evaluated precisely in the global numerical models because the pillar size is much smaller than the overall VGU dimensions. In this paper, local numerical models are specially developed to investigate the pillar indentation behaviour on glass surfaces to address the third design consideration and hence improve the overall design safety.

6.1.1 Contact damage due to indentation of supporting pillars

The incorporated pillar array results in severe stress concentrations together with a small elastic indentation in the glass near the contact zone of the pillar. The stress concentration of VGUs was observed near pillars by a polariscope, and the concentration intensity diagram is presented in Figure 6- 2(a). The pillar indentation is a long-term action and the stress concentration due to the indentation will pose a number of potential threats to VGUs. When the indentation load reaches a critical value, a ring crack will be triggered on the glass surface (shown in Figure 6- 2b), and then propagate into a cone crack (Figure 6- 2c) if subjected to higher loads. Consequently, these small cracks could result in the breakage under low wind or snow loads.

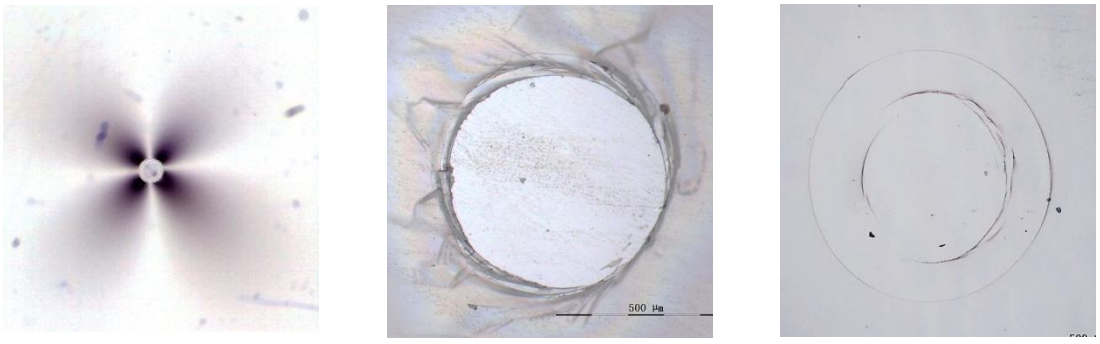

(a) Stress concentration (b) Ring crack (c) Cone crack

Figure 6- 2. Contact damage resulted from supporting pillars in VGUs

Collins and Fischer-Cripps (1991, 1995) discussed the stresses caused by pillar indentation in VGUs. It was found that the pillar indentation can be studied by using Hertzian fracture theory (Hertz, 1896). Auerbach's Law is usually adopted to determine the maximum indentation force that will trigger a Hertzian crack. It is an empirical equation obtained from experiments that dictate a linear relation between the radius of a spherical indenter and the critical applied force (Auerbach, 1891).

$$P_{\mathrm{cr}} = AR \qquad 6\text{-}1$$

where P_{cr} is the critical indentation load; A is the Auerbach constant (N/mm) obtained by experiments, R is the sphere radius (mm).

As recorded in Fischer-Cripps book (2007), a combination of Hertzian tensile stress equation and Griffith Energy Balance Criterion was developed by early researchers to calculate the critical surface tensile stress that forms a cone crack. The theoretical formula implies that the critical indentation force is proportional to the square of the radius of spherical indenter, i.e. $P \propto R^2$. However the conclusion violates the Auerbach empirical linear relation. Satisfactory explanations were not found to account for the contradiction until Frank and Lawn published their paper (Frank and Lawn, 2007). In the paper they made a detailed study of the stress fields acting on a flaw. They found that the contradiction is due to the assumption of uniform stress distribution along the surface flaw path made in Griffith Energy Balance Criterion. In fact, the stresses diminish very fast along the crack depth, and cannot be deemed uniform. Langitan and Lawn (1969) also presented experimental and theoretical analysis to validate two explanations based on flaw statistic model and energy balance concept respectively to explain the Auerbach's Law. Mouginot and Maugis (1985) then further proposed an energy release function $\Phi(c/\bar{a})$ that is related to the pre-existing stress field. The

function curves for different starting radii are depicted in Figure 6- 3, as a function of normalized crack length. The reserachers discovered that Auerbach empirical equation is only valid for a limited range, which is denoted as Auerbach range (Fischer-Cripps and Collins, 1994; Fischer-Cripps, 1997; Langitan and Lawn 1969; Mouginot and Maugis, 1985).

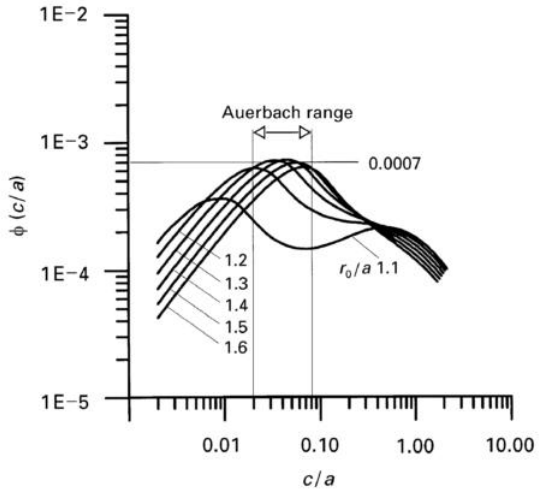

Figure 6- 3. Strain energy release function $\Phi\,(c/\bar{a})$ as a function of normalised crack length, c/a, for different starting radii, r/a for spherical indenters (Fischer-Cripps, 1997)

As given in Figure 6- 4, Auerbach' law is valid for a sphere radius less than roughly 10mm. The supporting pillars employed in the VGUS are normally less than 0.4mm, therefore the Auerbach's law is applicable to depict the pillar indentation behaviour with respect to the design of vacuum glazing (Collins et al., 1995)

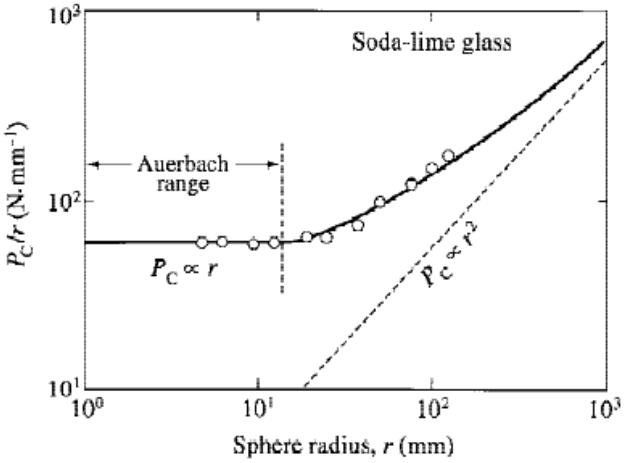

Figure 6- 4. Plot of laboratory results of P_c/R versus $R$for polished soda-lime glass (Lawn, 1998)

Hertz provided a mathematic equation that associate with the radii of contact area $\bar{a}$, critical indentation force P_{cr}, and spherical indenter R (Hertz, 1896):

$$\bar{a}^3 = \frac{3}{4}\frac{P_{cr}R}{E^*} \qquad 6\text{- }2$$

where, E^* is calculated as follows:

$$\frac{1}{E^*} = \frac{(1-\nu^2)}{E} + \frac{(1-\nu'^2)}{E'} \qquad 6\text{- }3$$

where E, E', ν, ν' are Young's modulus and Poisson's ratio for the specimen and the spherical indenter respectively.

In light of cylindrical indenter, the contact radius equals to the indenter radius. It is found that the radial tensile stress pattern along the surface for cylindrical indenter is precisely identical as that for a spherical indenter outside the contact area. So a cylindrical indenter can be deemed as a spherical indenter in terms of the stress distribution outside the contact area. An equivalent R for cylindrical indenter can be substituted in during the calculation.

According to Hertzian contact theory (Hertz, 1896), the maximum tensile stress at the edge of tc

$$\sigma_{max} = (1 - 2\gamma)\frac{P_{cr}}{2\pi\bar{a}^2} \qquad 6\text{- }4$$

It is noted that the maximum tensile stress on the surface is namely the maximum principle stress. In cases of outside the contact ring, it always equals the radial stress in magnitude.

By substituting Eq. (6- 2) to (6- 1), we get

$$P_{cr} = \sqrt{\frac{4E^* A\bar{a}^3}{3}} \qquad 6\text{- }5$$

It can be seen that *P* is in direct linear proportion to 1.5 power of cylindrical radius *a*.

The substitution of Eq. (6- 5) to (6- 4) leads to:

$$\sigma_{max} = \frac{(1-2\gamma)}{\pi}\sqrt{\frac{AE^*}{3\bar{a}}} = \frac{(1-2\gamma)}{\pi}\sqrt{\frac{AE^*}{3}}(\bar{a})^{-0.5} \qquad 6\text{- }6$$

Within the Auerbach's range, the critical indentation force can be expressed in terms of energy release function *Φ(c/a)* (Collins et al., 1995).

$$P_{cr} = \left[\frac{3E}{8E^*}\cdot\frac{\pi^3 v}{(1-v^2)\cdot\varphi\left(\frac{c}{\bar{a}}\right)}\right]\cdot R \qquad 6\text{- }7$$

Therefore, the Auerbach constant *A* in Eq. (6-6) can be replaced with the first term in Eq.(6-7).

$$A = \frac{3E}{8E^*}\cdot\frac{\pi^3 v}{(1-v^2)\cdot\phi\left(\frac{c}{a}\right)} \qquad 6\text{- }8$$

The substitution of Eq. (6- 8) into (6-6) leads to:

$$\sigma_{max} = \frac{(1-2\gamma)}{\pi}\sqrt{\frac{AE^*}{3a}} = \frac{(1-2\gamma)}{\pi}\sqrt{\frac{E^*\pi^3\gamma}{8(1-\nu^2)\phi_{(\frac{c}{a})}}}(\bar{a})^{-0.5} \qquad 6\text{- }9$$

Eq.(6- 9) indicates that the maximum tensile stress in the critical stage cannot be considered as a material constant, but dependent on the contact radius of the indenter and the stress gradient, represented by the function *Φ(c/a)*. However, the calculation process of σ_{max} is of great complexity. Because the energy release function *Φ(c/a)* is different for various initial crack radii, a specific function should be estimated for each radius (Fischer-Cripps, 2007).

In contrast to the energy balance criterion, strength criterion provides a less tedious method to evaluate the critical load. According to conventional strength theory, a crack is generated when the maximum stress reached a critical level. However, a great deal of indentation tests demonstrate that the Hertzian crack does not take place even when the surface maximum radial stress has far exceeded the bulk strength, and the maximum radial stresses at critical state show no consistency. Bao and Jin (1993) proposed a mean strength criterion (MSC) that can be used to predict the pillar indentation for VGUs. Two controversial phenomena detected in the indention tests of brittle materials were explained by the theory. 1, The maximum stress in the critical stage is normally much higher than the bulk strength. 2. Hertzian ring crack always initiates at larger circle than the contact area. The theoretical analysis of MSC showed that the radial stress at the contact circle decays rapidly along the depth and becomes compressive at a certain depth, which coincides with the non-uniform stress fields observed by Frank and Lawn (1995). Bao and Jin suggested that the crack initiation in brittle solids does not rely on the maximum radical stress on the surface in point-wise term, but an average stress over

a certain zone along the depth direction. This conclusion has been validated in his experiments and the criterion has been adopted to evaluate the local strength of glass (Bao et al., 2002; Bao and Gao, 2008; Liu et al., 2010).

The normalized mean stress and the surface radial stress are depicted versus the distance as given in Figure 6- 5.

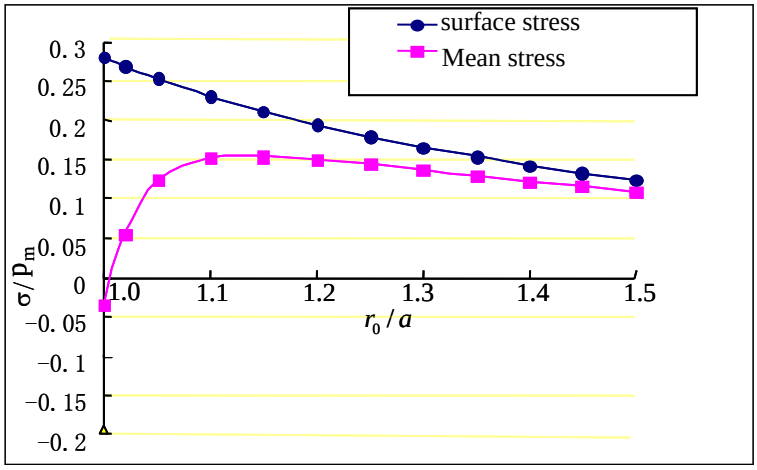

Figure 6- 5. Illustrative diagram of surface stress and average stress distribution outside the contact area (Bao et al., 2002)

As shown in Figure 6- 5, the maximum surface radial stress is exactly on the edge of contact area, but the mean stress is still compressive. The mean stress reaches greatest at roughly 1.1*a*, where the indentation cracks are most likely to occur in this case.

The mean strength (σ_{mean}) at an arbitrary radius r can be calculated by a numerical integration of the radial stress (σ_r) over the integral thickness divided by the thickness Δ (Bao and Jin, 1993)

$$\sigma_{mean} = \frac{1}{\Delta}\int_0^{\Delta} \sigma_r(z,r)dz \qquad 6\text{- }10$$

Where , $\sigma_r\ (z, r)$ is the radical stress near the indenter in cylindrical coordinate.

The integral thickness Δ can be calculated by Eq. (6 - 11).

$$\Delta = 2/\pi * (K_{IC}/\sigma_0)^2 \qquad 6\text{- }11$$

where, σ_0 is the bulk bending strength of glass, K_{IC} is known as the plain strain fracture toughness, and can be readily measured. The integral thickness is a material property, and not affected by the specimen size and geometry.

The analytical expressions of radical stress within the interior of the specimen are given in the book of Fischer-Cripps (2007). The analytical expressions of stress distributions for both spherical and cylindrical indenters are cumbersome to solve at general points, so finite element method is recommended to obtain the stress distribution.

In the present paper, an XFEM numerical method is employed to simulate the crack initiation and propagation due to the indentation load. The local strength introduced in line with MSC will be used in the XFEM modelling as the failure criterion. The contact stresses resulted from pillars are examined and analysed, results of which are used to enhance the overall safety design of VGU by optimising the design of supporting pillars. The relations between the critical loads and the pillar size, the geometry and material attributes are developed on the basis of the verified XFEM models.

6.1.2 XFEM technique

Finite element analysis to explore the Hertzian indentation damage on VGU is rarely documented. It is worthy of further investigation to gain better understanding on vacuum glazing design. To date, a number of fracture criteria based on linear elastic fracture mechanics are available to simulate the crack propagation (Hibbitt, 2010). However, the fracture modelling methods only allow cracks to propagate along the predefined paths. Hence it is not applicable to study on the singular crack growing

behaviour. The arduous re-meshing work will also increase the computation demand if the crack path is of irregular geometry. In this study, a new technique, XFEM included in the ABAQUS package is utilised to simulate the crack initiation and propagation. Different from traditional crack simulations, XFEM allows arbitrary cracks independent of the mesh and the crack path does not need to be prescribed in advance.

The XFEM technique, termed for "extended finite element method", was initially developed by Belytschko (1999). It extends the piecewise polynomial function space of conventional finite element methods with extra enrichment terms. The XFEM enrichments can be illustrated in Figure 6- 6.

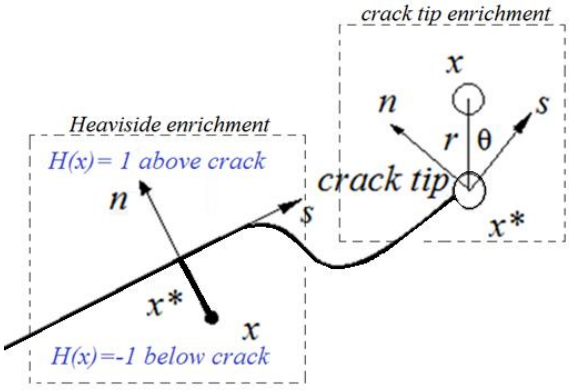

Figure 6- 6. Schematic graph of XFEM enrichments (Hibbitt, 2010)

The displacement interpolation is expressed in the form of (Belytschko, 1999)

$$u^h(x) = \sum_{I \in N} N_I(x)[u_I + H(x)a_I + \sum_{\alpha=1}^{4} F_\alpha(x) b_I^\alpha] \qquad 6\text{- }12$$

where, *uI* is the nodal DOF for conventional shape function NI; aI is nodal DOF of the elements containing the crack tip. $H(x)a_I$ is the Heaviside enrichment term, including *H(x)* as Heaviside distribution accounting for the displacement jump across the crack.

$\sum_{\alpha=1}^{4} F_{\alpha}(x) b_I^{\alpha}$ is the crack tip enrichment term that accounts for the nodes belonging to elements containing crack tip; b_I^{α} is Nodal DOF; $F_a(x)$ is the crack tip asymptotic functions as expressed:

$$[F_{\alpha}(x), \alpha = 1-4] = [\sqrt{r}\sin\frac{\theta}{2}, \sqrt{r}\cos\frac{\theta}{2}, \sqrt{r}\sin\theta\sin\frac{\theta}{2}, \sqrt{r}\sin\theta\cos\frac{\theta}{2}] \quad 6\text{- }13$$

XFEM provides a simple algorithm strategy to simulate the crack initiation and propagation. Several studies have showed that XFEM is competent to simulate various types of cracks. Richardson et al. successfully applied the technique to analyse crack propagation in brittle materials (Richardson et al., 2009). Xu et al. (2010) analysed low-speed head impact on glass by means of XFEM. The impact problem was characterised of quasi-static indentation cracking. A series of influence parameters were considered in the parametric study carried out by XFEM.

In this paper, an XFEM numerical method is employed to simulate the crack initiation and propagation due to indentation load. The local strength introduced in line with MSC will be used in the XFEM modelling as the failure criterion. The stresses induced by pillars are examined and analysed, the results of which are used to enhance the safety design of VGUs by optimising the design of supporting pillars. The relationships between the critical loads and the pillar size, the geometry and material attributes are developed on the basis of the verified XFEM models.

6.2 Contact damage modelling by XFEM technique

6.2.1 Model description

The supporting pillars adopted in the VGUs can be deemed as small cylindrical indenters with the radius from 0.1mm to 0.4mm. The interval spacing of the supporting

pillar array is 30mm to 80mm. In order to obtain a thorough understanding of the indentation damage, the present study will examine the indentation behaviour caused by an individual pillar. A local model is chosen to include only one pillar and a small area of glass plate underneath, as depicted in Figure 6- 7. In this local model, the actual glass length is not taken into consideration as it is much greater than the pillar size. In XFEM analysis, a flat glass disk with thickness 4 mm is established as an asymmetrical model.

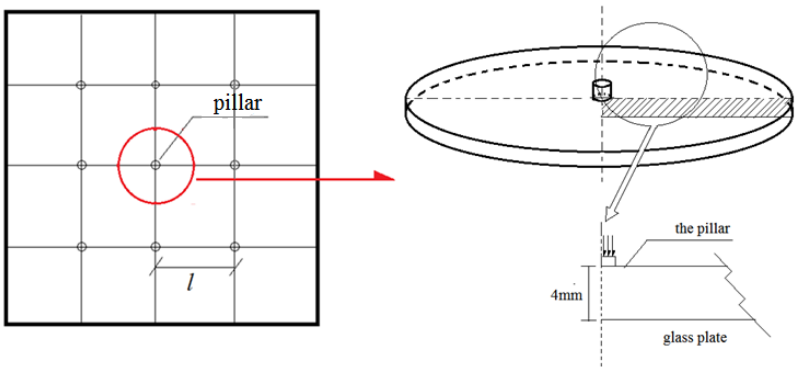

Figure 6- 7. Global and local models of glass and pillars

The linear elastic material properties of soda-lime silicate glass are assigned to the plate, i.e. Young's modulus E = 72000MPa and Poison ratio v = 0.22. The pillar is assumed to be rigid. In the modelling, the element CAX4, a 4-node bilinear axisymmetric quadrilateral element is used to simulate glass plate. The size of indenter is much smaller than that of the glass sample, and the mesh region where indentation crack occurs needs to be refined significantly. An effective indentation zone is specified with density seeds, whereas the outer areas are coarsely meshed. Any potential indentation crack initiation and propagation paths should take place within this effective zone. As shown in Figure 6- 8, the mesh size within the effective indentation zone is 0.009mm and the coarse mesh is 0.243mm. A type of transitive element is employed in the mesh

scheme. This meshing technique increases the number of seeds in power function along a specified direction. Therefore the effective indentation zone can be particularly refined within very small transitive range and all the elements remain in good shape and quality. The transitive elements are achieved by running a python script in ABAQUS CAE.

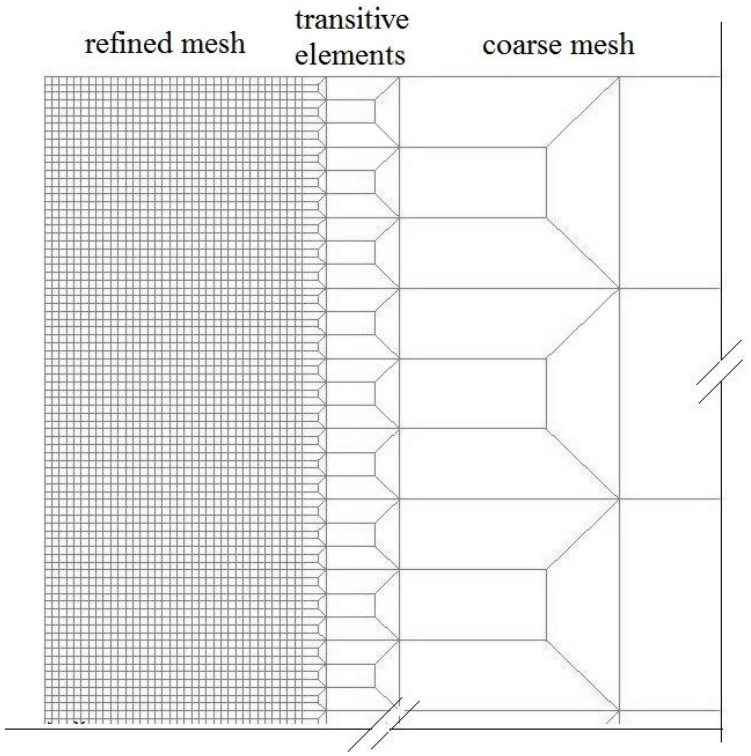

Figure 6- 8. Mesh scheme of pillar indentation model

6.2.2 Failure criterion in XFEM modelling

Two types of failure modes have been specified in studying the glass indentation failure. It is known as “contact damage” when the first indentation conical crack takes place in the vicinity of a supporting pillar. The applied force that leads to the first indentation crack is termed as critical indentation load, measured in kilo-newton (kN). The other one is a time-delayed failure, which refers to the glass fracture due to the growth of pre-existing cracks on the surface. The fracture is characterised of time-delayed occurrence,

as it relies on the further loads induced by the environmental actions. The fracture strength of glass depends on the loading method, velocity and duration etc. Since the fracture test results are of great discrepancies, the failure prediction of glass fracture is always studied by adopting probability models (Fischer-Cripps and Collins, 1994; 1995). In this chapter, the contact damage, i.e. indentation conical crack is primarily studied.

To model the failure of glass, the MSC (Bao and Jin, 1993) is adopted in the model. As mentioned above, the theory demonstrated that the crack initiation in brittle solids does not rely on the maximum radial stress of a point on the surface, but an average value of maximum principle tensile stress over a zone with a specified thickness. In this case, the thickness is chosen as the top layer thickness near the glass surface in the model. This layer is highlighted in Figure 6- 9 and its thickness is defined as the "integral thickness" (Δ) in MSC. It can be calculated with Eq. (6- 11).

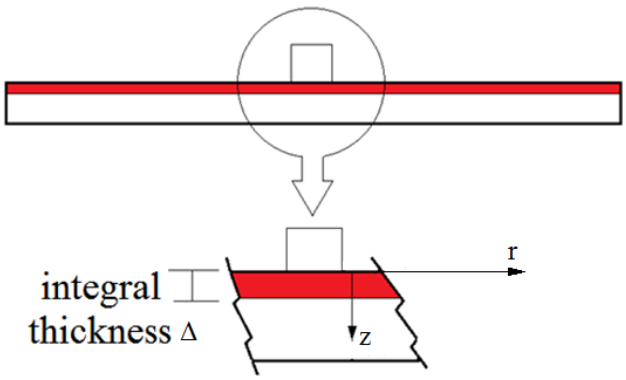

Figure 6- 9 Schematic graph of the average stress over a top layer of glass sample

The mean strength can be calculated by Eq. (6- 10). In engineering practice, the mean strength is also denoted as the local strength, and can be measured by indentation tests (Bao and Gao, 2008). Since the mean stress is not predefined in XFEM simulation

program, an alternative stress quantity should be found. In the typical indentation stress fields, the radial stress σ_r on the surface outside the contact circle equals the maximum tensile principle stress. Once it reaches a critical level, it will lead to an initial cracking (Fischer-Cripps, 2007). Therefore the critical maximum principle stress σ is used in the damage criterion.

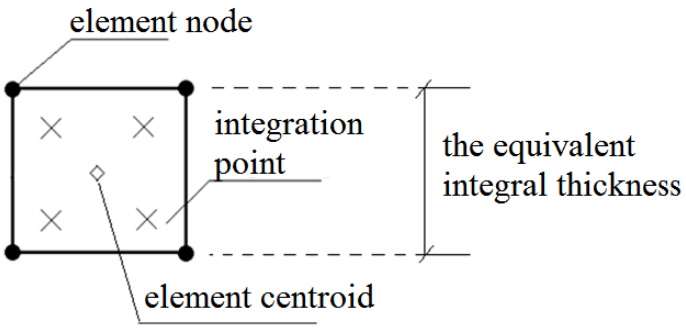

Figure 6- 10. Element type CAX4

As illustrated in Figure 6- 10, the maximum principle tensile stress in an element is obtained by averaging four integration points, and represented on the element centroid. The stress value of an element reflects the numerical integration over this area by means of Gaussian quadrature method (Hibbitt, 2010). Therefore it can be also deemed as the "local strength" according to the concept of MSC, and the mesh height is equivalent to the "integral thickness". The crack will cut through the element where the tensile principle stress reaches critical.

6.2.3 Validation of XFEM modelling

A group of cylindrical indentation tests with different indenter sizes were recorded in Fischer-Cripps (2007). The results are used to validate the numerical modelling in this paper. It is worth noting that the samples surfaces were abraded in two perpendicular

directions prior to experiments, in order to ensure the testing surfaces to have uniform-distributed micro-cracks. The abrading process has effectively avoided the scattering results often caused by the randomly distributed surface flaws (Mouginot and Maugis, 1985).

The XFEM axisymmetric model has a simply supported boundary condition, which agrees with the corresponding experiment. The simulation is divided into two steps. In the first step, the indenter is subjected to a small force and is pushed on to the glass surface. This is to establish a stable and consistent contact relation. In the second step, a constantly growing force is then applied on the rigid indenter.

As the local strength of the test specimen was not given in Fischer Cripps's work, an initial calibration is required to determine the local strength. The sample with the radius equalling 0.21mm is taken to calibrate the numerical model. The local strength value is found to be 220MPa. By adopting this value, the indentation simulations with different indenter radii from 0.1mm to 0.56mm are carried out. The critical indentation load versus the indenter radius to power 3/2 is plotted in Figure 6- 11. The comparison with experimental results is also presented. The plot shows that the numerical modelling fits the experimental data well, and presents a linear relation between the critical indentation load P_{cr} and $a^{3/2}$ as indicated in Eq. (6-5).

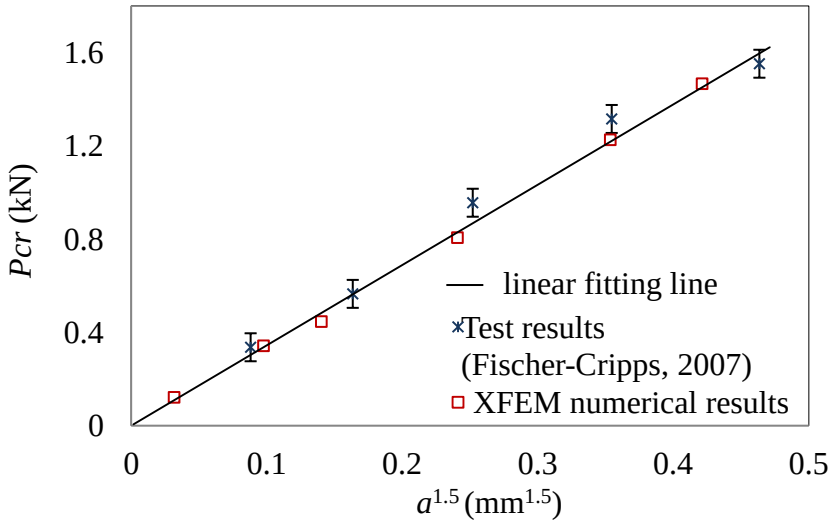

Figure 6- 11. Critical indentation load vs. $a^{1.5}$ relationship

6.3. Results and discussions

6.3.1 Sensitivity study to the pillar geometry

The maximum principle tensile stress distributions over the glass surface layer due to different cylindrical indentations are investigated. A normalised stress is introduced as a dimensionless parameter in order to provide a clear comparison:

$$\sigma_{norm} = \sigma / \sigma_{\text{mean}} \qquad 6\text{- }14$$

where, σ_{norm} is the normalized stress, σ is the maximum principle tensile stress on a distribution path, and σ_{mean} is the local strength, i.e. the value of maximum principle tensile stress when the first conical crack is initiated.

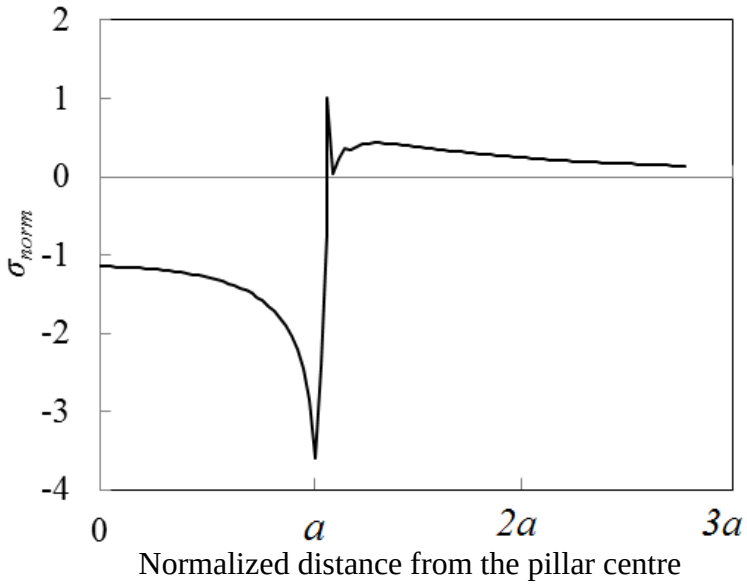

Figure 6- 12. Normalised radial stress distribution under cylindrical pillar indentation

In Figure 6- 12, the normalised radial stress distributions at the critical indentation loading level are presented for different indenter sizes. Tensile stress has a positive sign. As is indicated in the axisymmetric model (see Figure 6- 13), the distribution path starts from the centre of the contact area and points outwards along the radial direction.

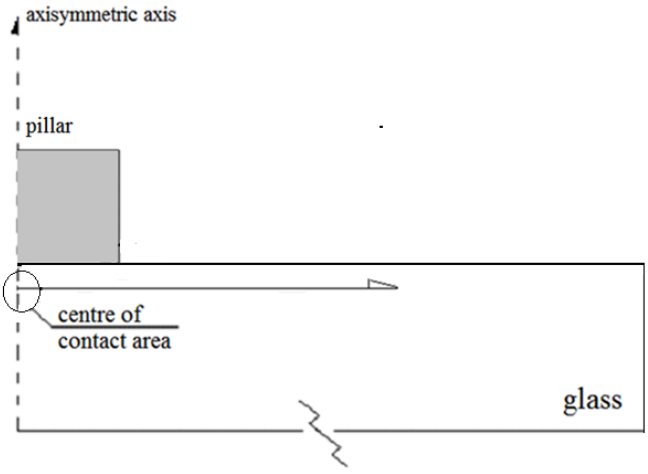

Figure 6- 13 .Distribution path in the axisymmetric model

In Figure 6- 12, it can be observed that the stress concentration in radial direction near the contact edge is considerably significant and it reaches the critical level to trigger the crack while the far-field stresses are much smaller. The results indicate that the crack initiation can be postponed to a higher loading level, as long as the stress concentration near the contact circle is removed.

The formation of stress concentration is further investigated for the case of the cylindrical pillar. Figure 6- 14 illustrates the contact condition between a cylindrical pillar and the glass panel. In the case of indentation, a continuous concave surface is formed on the glass surface. However, the flat base of the rigid cylindrical pillar cannot match the deformed shape that the glass surface has experienced, and thus results in incompatible contact. The indentation stress is not evenly distributed on the contact area but shows concentration on the contact edge. It is also noted that at the contact edge, the stress switches from compression to tension with a presence of spike in the tension zone, as shown in Figure 6- 12. From this observation, one can naturally assume that a round fillet will mitigate the stress concentration and thus the occurrence of indention failure.

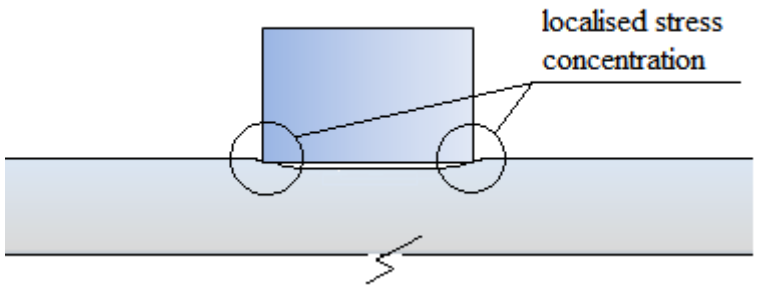

Figure 6- 14. Schematic diagram of contact condition between cylindrical pillar and glass surface

Two types of novel pillar are designed and the resulting stresses are compared. As illustrated in Figure 6- 15, one design is termed “fillet pillar”, referring to the cylindrical pillar with fillets at edges. Although the indentation load will concentrate at the contact edge because of incomplete contact due to the plat surface, the fillet edge provides a smooth transition from compressive stress to tensile stress thus avoids the step rise in tensile stress. The fillet radius is assumed to be 0.05mm here. The parametric study on the fillet radius will be discussed in detail in the next section. The other one design is “spherical pillar,” which is the pillar with spherical surfaces on the top and bottom connected by a short cylindrical section. The design is aimed to guarantee a full contact between the pillar surface and the glass surface so as to eliminate the localised stress concentration near the contact edge. The schematic figures of contact conditions of two novel pillar and the glass surfaces are presented in Figure 6- 16.

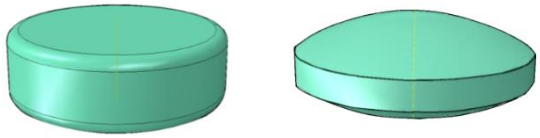

(a) Fillet pillar (b) Spherical pillar

Figure 6- 15. Schematic diagrams of spherical pillar and fillet pillar designs

(a) Fillet pillar (b) Spherical pillar

Figure 6- 16. Schematic diagrams of the contact conditions of spherical pillar and fillet pillar

To assess the mechanical performances, the critical indentation loads versus the contact radii are plotted in Figure 6- 17 for three types of pillars: fillet, spherical, and the traditional cylindrical pillars. In the case of spherical pillar, the contact area varies with the applied load. The contact radius *a* at the critical level can be calculated by the Eq.(6-2) ((Hertz, 1896).

Regarding the effective Young's modulus *E**, this can be given in a simplified form as Eq.(5- 13), since the indenter is deemed to be rigid, i.e,

$$\frac{1}{E^*} = \frac{(1-\nu'^2)}{E'} = \frac{(1-0.22^2)}{72000} = \frac{1}{75662.042} \qquad 6\text{- }15$$

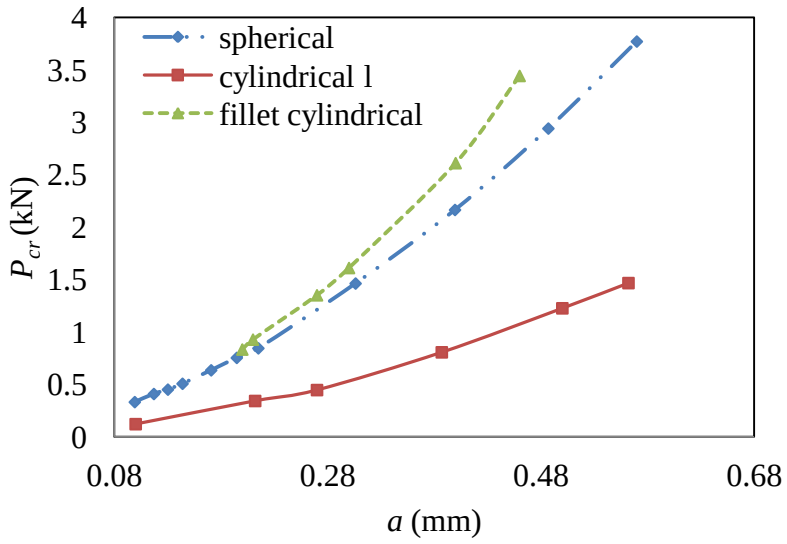

Figure 6- 17. Critical loads vs. contact radii

According to Auerbach's empirical equation, the critical load can be expressed as a function of a1.5, e.g.

for the spherical pillar, $Pcr = 8.67\bar{a}^{1.5}$ 6- 16

for the ordinary cylindrical pillar, $Pcr = 3.44\bar{a}^{1.5}$ 6- 17

The fillet pillar does not follow Auerbach's law because the actual contact area is not exactly the same with profile radius due to the fillet edges. The relation between the critical load and contact radius of fillet pillar can be described by the following polynomial equation.

$$P_{cr} = 11.81\bar{a}^{3} + 4.47\bar{a}^{2} + 2.9\bar{a} \quad 6\text{- }18$$

where, a denotes the profile radius of fillet pillar, instead of actual contact area.

With the same contact radius, it is found that fillet pillar and spherical pillar can both increase the critical load markedly. To understand the increase of critical loads due to the shape of indenter, the normalised maximum principle stress distributions at the critical level for three types of pillars are examined and given in Figure 6- 18.

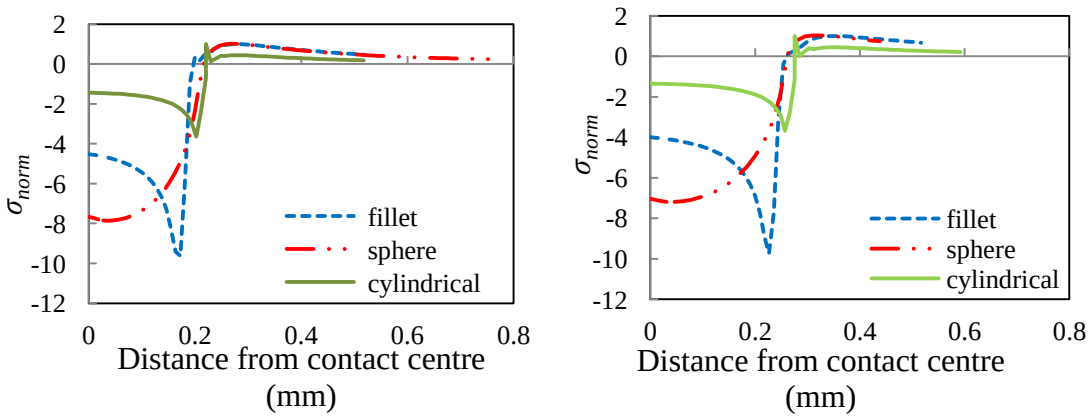

(a) $\bar{a}$ = 0.21mm (b) $\bar{a}$ = 0.27mm

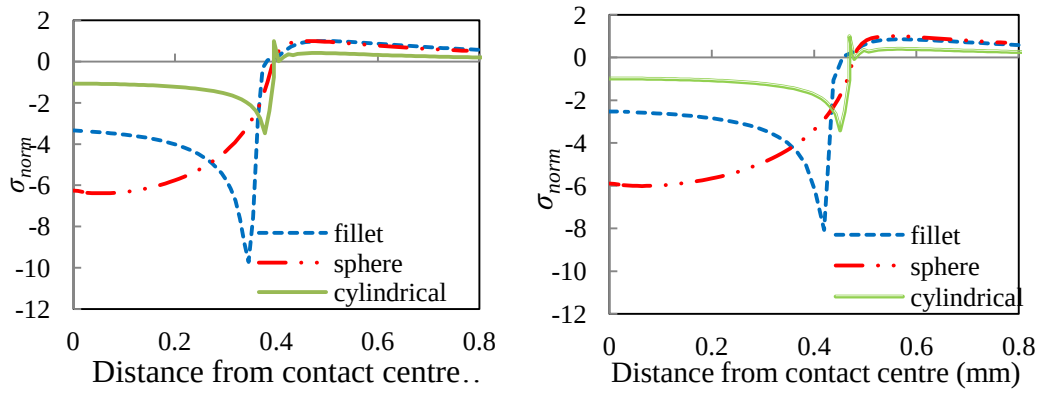

(c) $\bar{a}$ = 0.387mm (d) $\bar{a}$ = 0.46mm

Figure 6- 18. Normalised principle stress distribution at critical loading level

As shown in Figure 6- 18, the normalised principal stress distributions outside the contact area for the fillet and sphere pillars are very similar and the decay rate is relatively small. Both cases exhibit a smooth stress variation, whereas the cylindrical case shows a severe stress concentration near the contact edge.

It is worth noticing that the peak values of the maximum principle tensile stresses of spherical and fillet pillar take place at a larger circle radius *a'*, instead on the contact circle (shown in Figure 6- 19). The numerical results also coincide with the experimental observations in that the crack initiation ring is always larger than the actual contact circle (Bao and Jin, 1993; Bao and Gao, 2002; Fischer-Cripps and Collins, 1994).

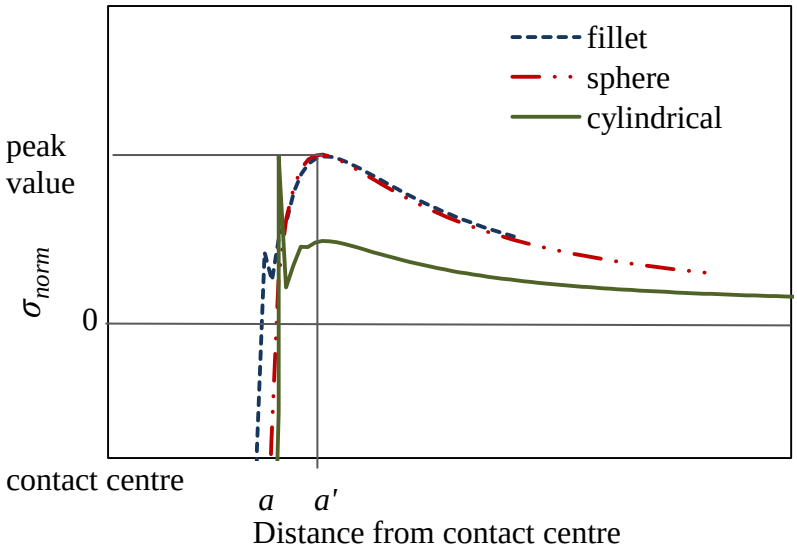

Figure 6- 19. Normalised stress distribution at the position of initial crack

The contradiction can be explained by the MSC theory, which states that the initial crack starts where the mean stress reaches critical value rather than the surface stress. According to the Hertzian equation, the maximum principle tensile stress on the surface occurs on the contact edge. It is found that the stresses on the contact edge decay in depth direction and radial direction. Although the radial stress decays monotonously in both directions, it has a highest decay rate at the contact edge in the depth direction and the decay rate will reduce while increasing the distance from the contact edge. So the peak value of the average radial stresses over a certain thickness may not exactly on the contact edge, but where the stress decay gradient is less severe. The schematic diagram of radial stress distributions in depth direction is given below in Figure 6- 20, σa and σa' refers to the surface radial stresses at contact edge and larger radius *a'* respectively, and $\bar{\sigma}_a$ and $\bar{\sigma}_{a'}$ denote the mean stresses over the top layer of glass surface.

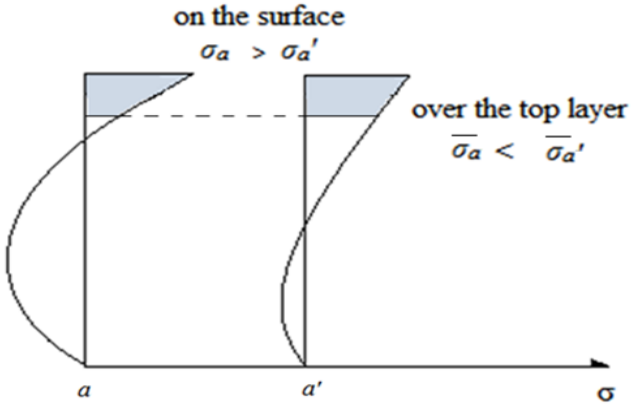

Figure 6- 20. Schematic diagram of radial stress distribution in depth direction

The integration of the vertical stresses over the contact area is equal to the critical indentation load. The vertical stress distribution (σ_z) induced by three types of indenters are plotted with different contact radii in Figure 6- 21. The integration of the critical vertical compressive stress beneath the cylindrical pillar is only one third of that under the spherical pillar and fillet pillar, which explains why the maximum indentation load of the cylindrical pillar is much lower.

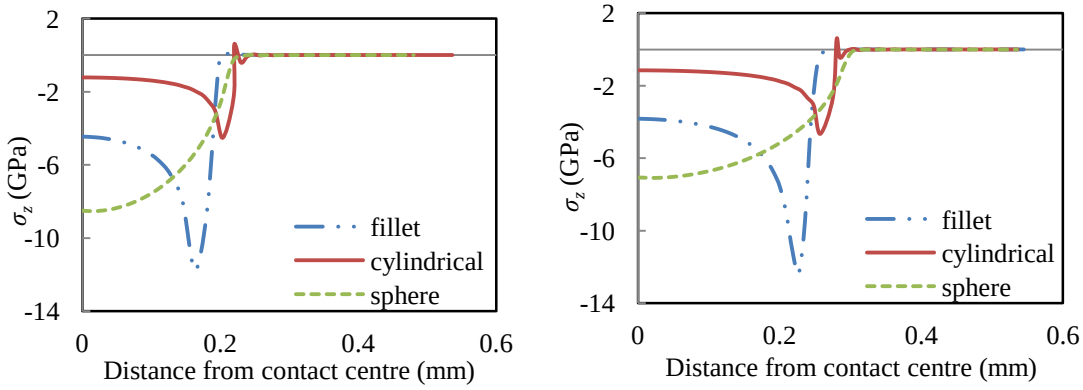

(a) $\bar{a}$ = 0.21mm

(b) $\bar{a}$ = 0.27mm

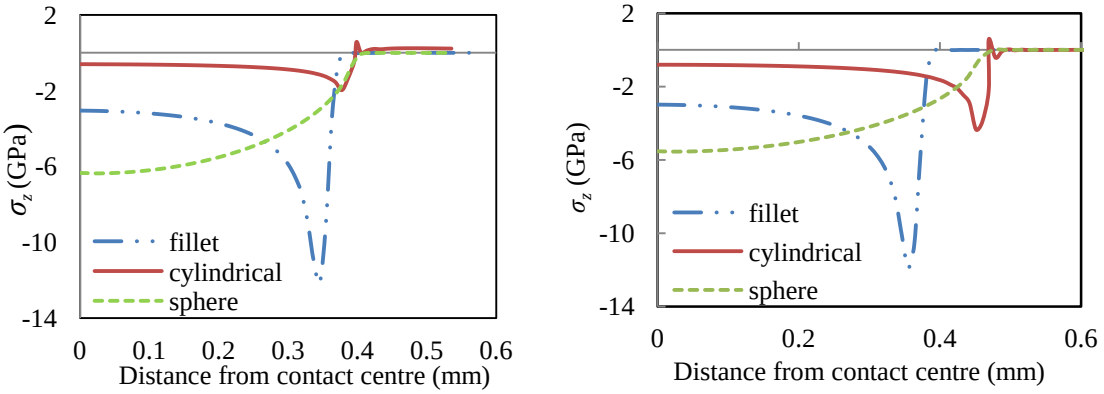

(c) $\bar{a}$ = 0.387mm

(d) $\bar{a}$ = 0.46mm

Figure 6- 21. Vertical stress distribution σ_z with different contact radii at critical loading level

The results suggest that the load bearing capacity of the VGU is greatly affected by the geometry of indenters. The adoption of cylindrical pillars in vacuum glazing gives rise to an earlier occurrence of contact damage due to the more severe stress concentration near the edge of the contact ring. Fillet pillar and spherical pillar are proven to be better alternatives in increasing critical indentation load. A series of parametric studies will be carried out to further investigate the two types of pillars respectively.

6.3.2 Parametric study of fillet size

By observing Figure 6- 22, it is found that both the fillet and the fillet-free cylindrical pillars have small stress concentration zones for the radial compressive stress. This stress concentration occurs in the vicinity of the flat base edge of the indenter. As the round corner of the fillet pillar provides a more compatible contact with the deformed glass, the stress concentration is reduced compared to the cylindrical case.

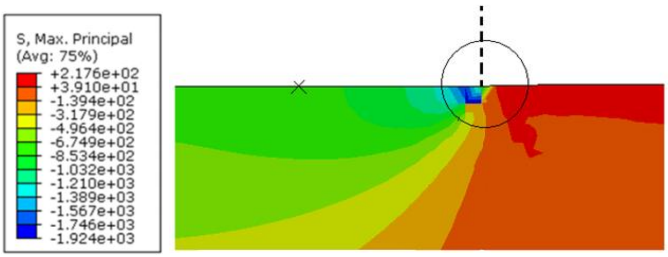

(a) Cylindrical pillar

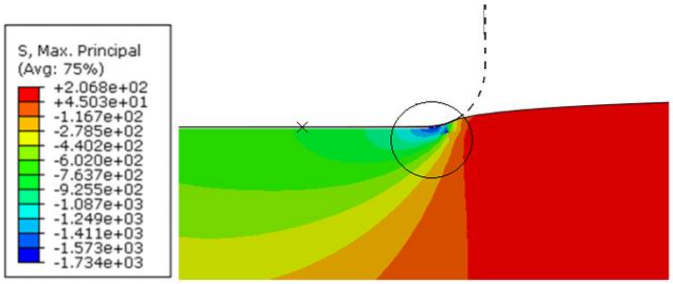

(b) Fillet pillar

Figure 6- 22. Contours of stress distribution under two types of pillars at critical loading level

A group of different fillet radii with four pillar sizes were modelled to discuss the effects caused by the geometry design of fillet pillar. The relationship between the fillet size and P_{cr} are plotted below in Figure 6- 23. The critical loads reach highest value when the fillet size falls into the range 0.03mm-0.04mm.

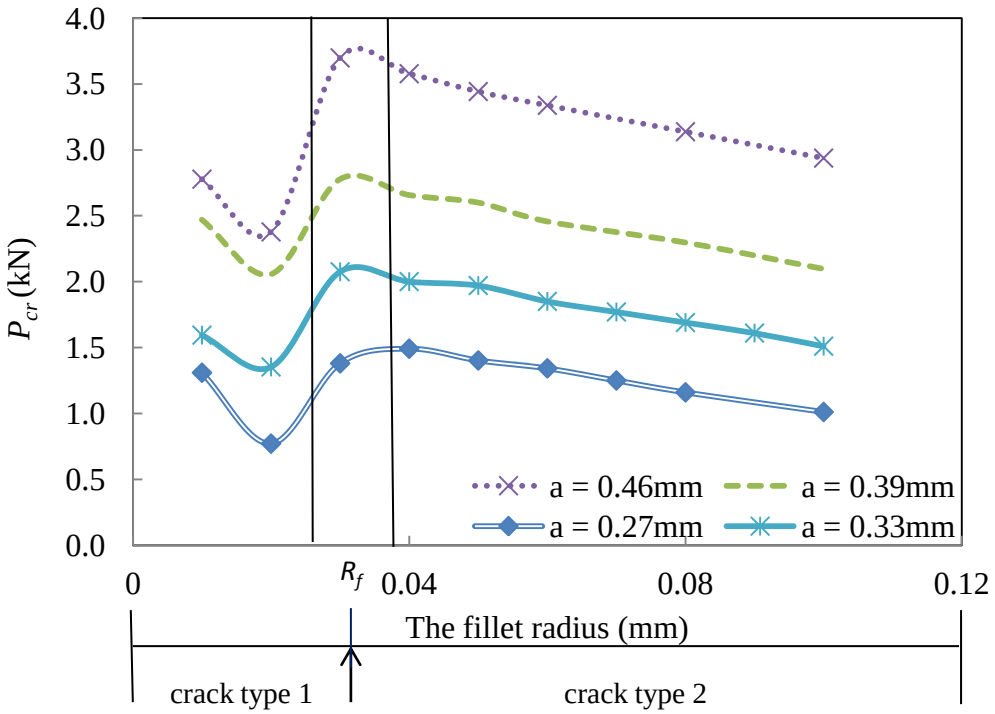

Figure 6- 23. Relations between critical indentation load and the fillet sizes for the pillars of different radii

Figure 6- 24 indicates two types of indentation crack. These two types of cracking mode are observed from the modelling results when varying the fillet size. Crack type 1 shows the crack initiating right at the contact edge (see Figure 6- 24(a)), whereas in crack type 2, the crack initiates outside the contact zone (see Figure 6- 24(b)). A critical fillet size between 0.03mm and 0.04mm is defined as a transition fillet radius between crack type 1 and 2. The stress distributions for these two crack types are compared in Figure 6- 25 to illustrate the cause of cracking, where the locations of the peak stress are coincident with the initiation points of the crack.

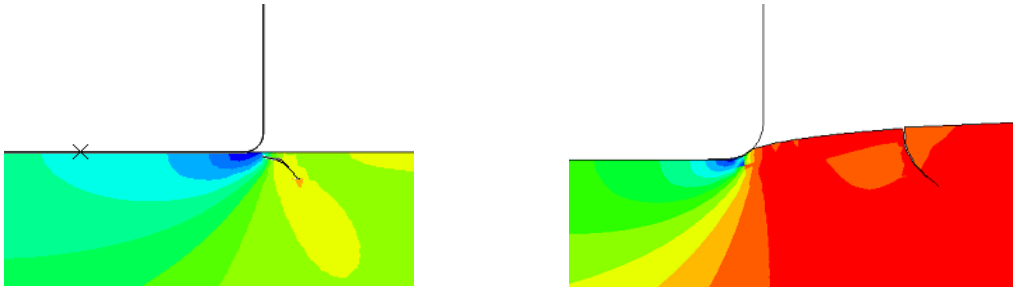

(a) Crack type 1. (b) Crack type 2

Figure 6- 24. Two types of crack pattern

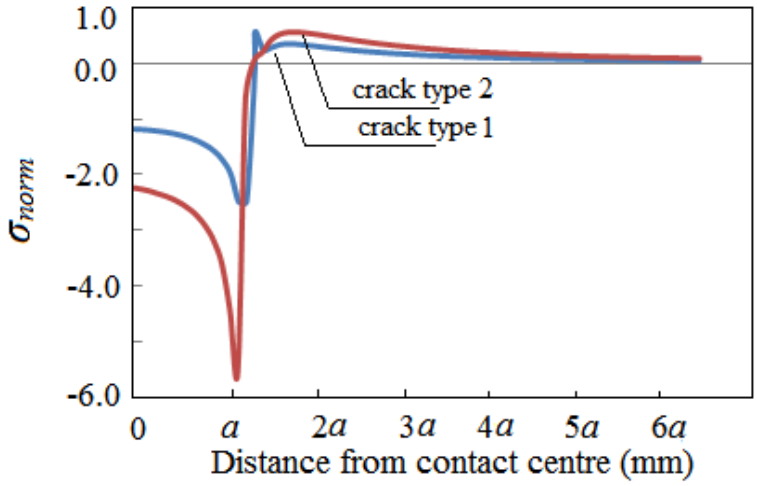

Figure 6- 25. Normalised stress distributions for two types of cracks at critical loading levels

A fillet size for the transition zone between two types of crack mode, R_f, can be deemed as the optimised fillet size, as it renders the highest critical indention loads. When the fillet radius is smaller than R_f, the stress concentration right at the indenter's edge will induce a type 1 crack. With a decreasing radius, the increasing degree of stress concentrating will reduce the critical indentation load. While the fillet radius is greater than R_f, the critical indentation load will decrease due to the increasing fillet radius reducing the contact area.

In Figure 6- 26, each fillet size is applied to several pillar radii and the critical indentation load versus the pillar radius relationship is presented. This is to seek an optimal combination of fillet size and pillar radius that can withstand a maximum critical indentation load. It is found that for pillar radius less than 0.335 mmm, the optimal fillet size is 0.04mm; otherwise, 0.03mm will be the optimal size.

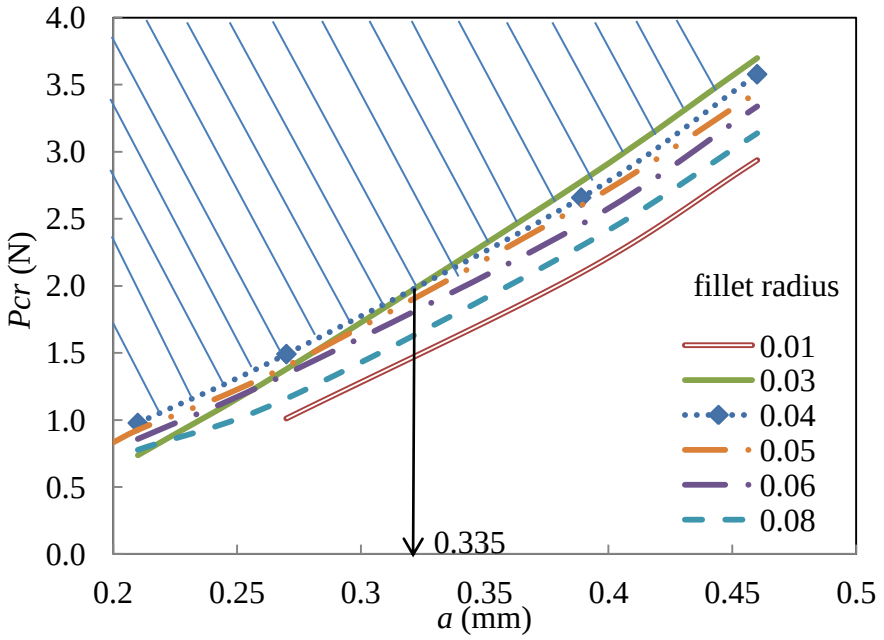

Figure 6- 26. Relation between critical loads and the pillar radius for different fillet size

6.3.3 Dependency study on Young's modulus

The supporting pillars used in VGU are made of high strength material, such as steel or ceramic alloy. In above discussion, the supporting pillars are assumed to be rigid body. However, there is always a certain degree of elastic deformation in the supporting pillars during the indentation. A parametric study is conducted in order to further explore the influence of the Young's modulus (E) of supporting pillars. A comparison between fillet pillar and spherical pillar versus different E are presented in Figure 6- 27.

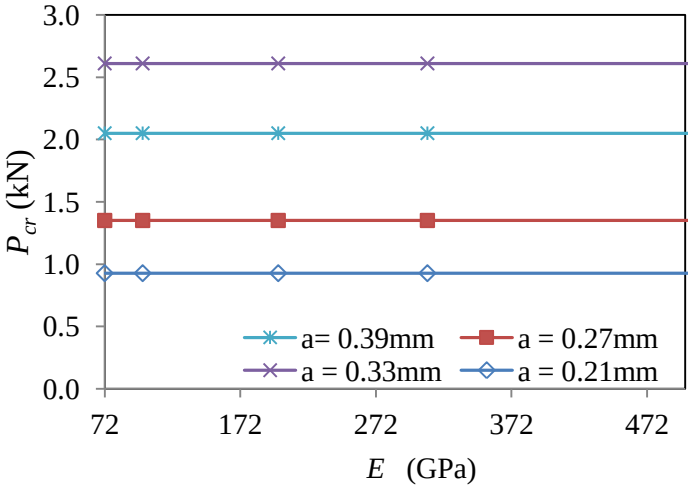

(a) Fillet pillar

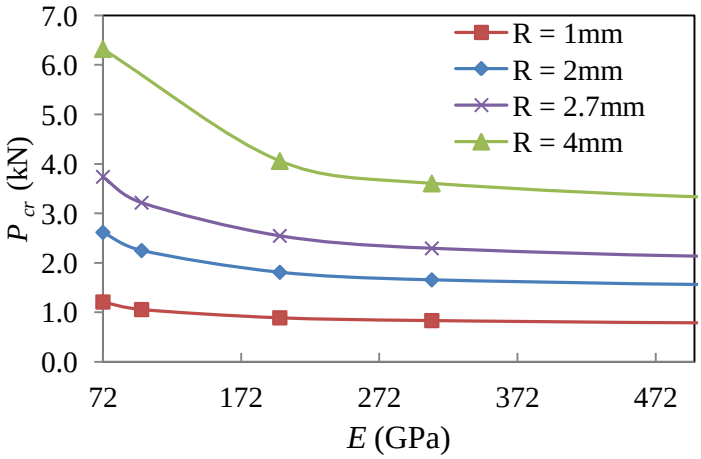

(b) Spherical pillar

Figure 6- 27. Relation between critical indentation load and Young's modulus of two novel types of pillars

It is observed that the critical load of the fillet pillar remains constant with varying Young's moduli. In contrast, the critical load of the spherical pillar depends on the Young's modulus in the low range, and then remains constant when the Young's modulus exceeds 300GPa. The material-dependence of the spherical pillar is due to the contact area being increased in the case of a low Young's modulus value; whereas the

contact area for the fillet pillar mainly containing the flat base does not change considerably with the Young's modulus.

As shown in Figure 6- 28, the vertical normal stress distributions of the spherical pillar with the same radius R = 2mm but different Young's moduli, and subjected to the same loading level (P = 1330N), are compared. The contact radius can be identified at the zero stress points.

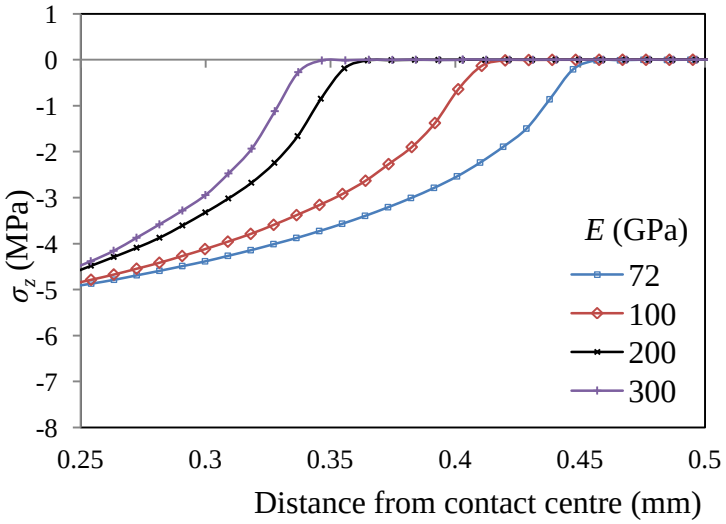

Figure 6- 28.Normal contact stress distributions of spherical pillar

The contact area and the maximum value of contact normal stress change with different Young's moduli as shown in Figure 6- 28. The contact radius of the spherical pillar with a smaller E value is larger. As presented in Figure 6- 27, the critical indentation load tends to be constant only after the Young's modulus reaches 300GPa, which is higher than most materials adopted for the supporting pillars. Therefore, the Young's modulus of the material should be taken into consideration in evaluating the contact stress and the contact area of the spherical pillar.

As suggested in Figure 6- 28, a different Young's modulus will lead to a corresponding differing contact radius, $\bar{a}$, and thus a differing critical indentation load, P_{cr}. Therefore, for a series of spherical pillar sizes, by choosing various values of Young's modulus and recording the corresponding P_{cr} and $\bar{a}$ values, each spherical pillar size can produce a P_{cr} vs. $\bar{a}$ curve section as presented in Figure 6- 29. Also presented in Figure 6- 29 is the P_{cr} vs. $\bar{a}$ curve of a rigid spherical pillar reproduced from Figure 6- 17. Both curves fit well with a deviation of less than 10%.

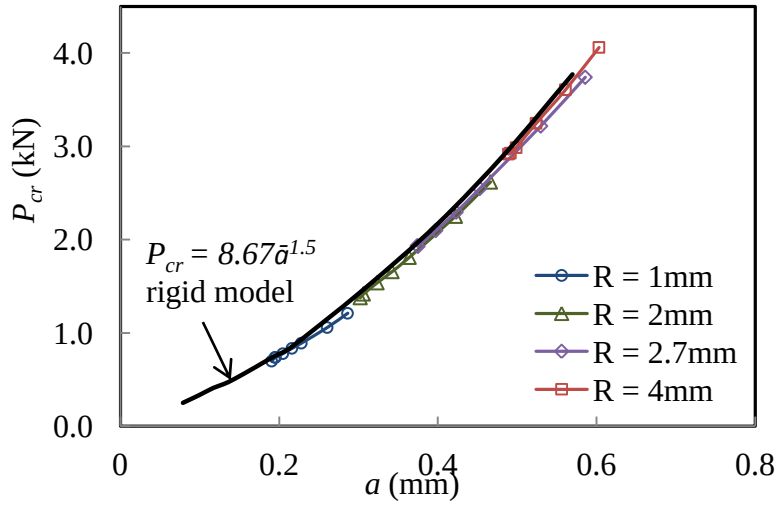

Figure 6- 29. Relations between critical loads and contact radii for the spherical pillars with different radii and Young's modules

The close agreement of the P_{cr} vs. $\bar{a}$ curves between the rigid and elastic spherical pillars actually offers a simple approach to determine the critical indention load of the elastic pillar by using the counterpart rigid model. The P_{cr} vs. $\bar{a}$ curve for the rigid model can be described by the empirical equation given in Eq.(6- 16). With a given contact radius a of an elastic pillar model, P_{cr} can be determined. According to Figure 6- 29, the equation can also be applied to Eq.(6- 16) can be rewritten in terms of the spherical radius (R) and Young's modulus (E), by substituting Eq.(6- 2) and Eq.(6- 3) to Eq.(6- 16) and eliminating $\bar{a}$, i.e.

$$P_{cr} = (0.74 + \frac{50950.8}{E}) \cdot R \qquad 6\text{- }19$$

The above equation provides a solution to predict the critical indentation load P_{cr} by using the indenter's radius, R and Young's modulus, E. This equation is based on the local strength calibrated from the indentation test results (Fischer-Cripps, 2007), which is set to be 220MPa. However, the local strength of the glass depends on the indenter's material properties, glass type and the glass surface condition, and varies in different indentation tests. Another generic equation should be sought to allow for this type of uncertainty.

For a rigid indenter, the substitution of Eq. (6- 1) to Eq. (6- 2) leads to:

$$\bar{a}^3 = \frac{3}{4} \frac{P_{cr}^{\ 2}}{A E_1^{\ *}} \qquad 6\text{- }20$$

where, $E_1^{\ *}$ is the effective Young's modulus of a rigid pillar, expressed as $E^* = E'/(1-\nu'^2)$.

For an elastic indenter, Eq. (6- 2) is expressed as

$$\bar{a}^3 = \frac{3}{4} \frac{P_{cr} R_{elastic}}{E_2^{\ *}} \qquad 6\text{- }21$$

where $R_{elastic}$ is the spherical radius of an elastic indenter and $E_2^{\ *}$ is its effective Young's modulus, as expressed in Eq. (6- 3).

By using the observation from Figure 6- 29 that the critical indentation loads of rigid and elastic models are equal, the substitution of Eq.(6- 19) to Eq. (6- 20) leads to

$$P_{cr} = \frac{E_1^*}{E_2^*} AR_{elastic} \qquad 6\text{- }22$$

Substituting the material properties of the glass into Eq.(6- 22), a general equation is obtained to determine the critical indentation load by the given spherical radius and Young's modulus of the spherical pillar as follows

$$P_{cr} = (1 + \frac{68852}{E}) AR_{elastic} \qquad 6\text{- }23$$

The Poisson's ratios of the prevailing supporting pillars are within the range 0.2 to 0.3, and the minor change in the Poisson's ratio is found not to affect the simulation results. Therefore the Poisson's ratio is deemed to be a constant 0.2 in this case. When using the above equations, the Auerbach's constant, *A*, can be obtained by carrying out indentation tests with two spherical indenter radii or materials.

It is also noticed that high elasticity is important for supporting pillars, as it cannot only improve critical indentation load but also help endure large bending movement of VGU. Meanwhile the high compressive strength is also indispensable especially to the pillars close to the edge seal. It is also stressed in the paper of Collins et al. (1995) that the yield point of supporting pillars should not be too low, otherwise two glass panels will get touched under sufficient loading.

6.4 Conclusions

This chapter has documented the design challenges of VGUs, especially in relation to the supporting pillars. Contact damage, i.e. the Hertzian crack caused by the supporting pillars, has been studied using XFEM modelling. The mean strength criterion was used as the failure criterion. The modelling method has been verified by existing

experimental data, and the results follow the empirical Auerbach's law. The critical indentation load, P_{cr}, is used to represent the load capacity of a VGU. In this paper, the relationship between critical indentation load and different pillar sizes, shapes and material properties are specified.

The critical indentation loads induced by cylindrical, fillet cylindrical and spherical pillars have been compared. It is found that both spherical and fillet pillars can effectively enhance the critical indentation loads. The mechanism of the improvement is to mitigate the stress concentrations in the glass at the contact edges of the pillars. Based on a series of numerical modelling, the critical loads have been found as a function of the contact radii.

In order to optimise the shape of a fillet pillar, the fillet size was analysed. The optimal fillet radius is between 0.03 and 0.04mm. By examining various pillar sizes, a fillet radius of 0.03mm is found to be the best option for the pillar radius larger than 0.335mm; otherwise 0.04mm should be employed.

The Young's modulus, deemed an important material property, has also been considered in the parametric study. The following conclusions have been drawn based on the results: (a) The Young's modulus dependency of the critical indentation load is not obvious for fillet pillars. (b) The lower Young's moduli yield higher critical loads for spherical pillars due to high elastic contact deformation. (c) A simplified equation is derived to calculate the critical indentation load of an elastic pillar, by giving the Young's modulus and the radius of the spherical pillar.

CHAPTER 7. NOVEL HYBRID VACUUM/TRIPLE GLAZING UNITS WITH PRESSURE EQUALISATION DESIGN

7.1 Introduction

As has been introduced in Chapter 5, VGUs exhibit low strength and are more liable to fracture than conventional glazing units. The differential pressure between the outer and inner spaces and the indispensable small size pillar have created a high pre-existing stress state in the constituent glass panels during fabrication of VGUs and hence made the units highly susceptible to breakage even under small applied loads. Therefore, the safety issue becomes a primary hindrance factor for VGUs to be used widely.

In order to overcome this bottleneck problem, two approaches are often considered: 1) to increase the strength of glass panels that VGUs are made of; and 2) to reduce the mechanical loads and impact action on the VGUs in service. To date, most efforts have been placed on the first concept.

A common solution in line with the first concept is to develop a low-melting-point frit sealing technology (Griffiths et al., 1998; Hyde et al., 2000; Wang et al., 2007) and then introduce toughened glass instead of annealed glass. Hyde et al. (2000) have successfully employed a type of edge seal with indium to realize the sealing process at temperature 200^{o}C or less. But the available frit materials that can fulfil the purpose are very expensive hence cannot be widely employed in practical applications. A US patent (Benson 1987) offers a laser sealing technology that keeps the major part of the glass panels cool; however the construction process is of great complexity and unsuitable for mass production. The second concept entails a type of hybrid insulating/vacuum glazing units each fulfilling load bearing and thermal insulation purpose. It involves a VGU and

at least toughened glass panels (Eames, 2008). The VGU is installed as the inner panel enclosed by the toughened glass panes. The environmental load will be primarily applied on the outer panels, which is toughened glass in this design. External loads are mainly shared by both toughened panels with the inner air acting as the transferring medium. The air cavities separated by the inner VGU are linked and thus the VGU will subject to equal air pressure at both surfaces without causing any bending effects.

In this study, a novel hybrid vacuum/triple glazing system with a pressure equalisation design has been devised and reported. In this system, a VGU is enclosed by two glass panels to form a triple glazing unit system. This new design creates an equalised air pressure on both side of the VGU and subject the VGU to no additional external loads apart from the inherent fabrication stress. This results in a hybrid vacuum glazing unit providing high thermal and sound insulation as well as a more durable safety performance. Pressure tests were undertaken on the novel glazing system to confirm the reliability. Results show that, under various loading levels, the stresses and deflections in VGU of this novel glazing system always remain at a marginal level, and hence the likelihood of breakage for this type of glass will be reduced significantly.

7.2 Design concept of hybrid vacuum/triple glazing units (VGUs) with pressure equalisation

The conventional composite vacuum triple glazing units comprised two sheets of toughened monolithic glass panels and a VGU. The VGU is normally placed in the middle, separating the air spaces into two, which can significantly enhance the thermal insulation performance while sharing the loads together with the other two glass panels. The novel hybrid vacuum/triple glazing units have the similar assembly. The key

difference is that this novel design is using a small U-shaped pipe connecting two air spaces. The cross section of both glazing constructions are illustrated in Figure 7- 1.

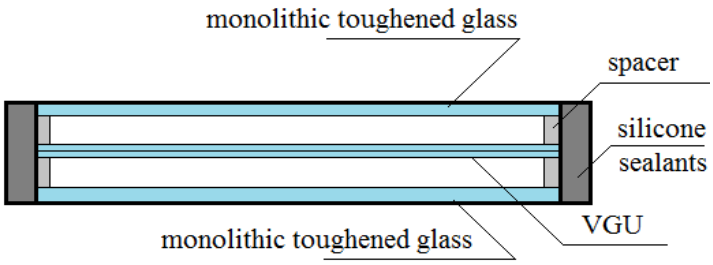

(a) Conventional composite VGU/triple glazing unit (Design I)

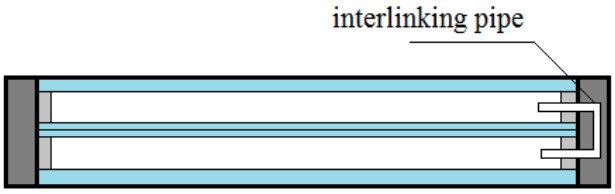

(b) Novel hybrid vacuum/triple glazing unit (Design II)

Figure 7- 1.Schematic diagram of two types of VGUs

In the conventional design case (Design I) as illustrated in Figure 7- 1(a), two air cavities are independently sealed. A uniform load applied to the outer glass panel will result in bending deformation in the receiving glass, which subsequently reduces the volume of the air cavity. According the Boyle's law for gas, the squeezed air will transfer the air pressure to the middle VGU and then to the inner glass panel. VGU is subjected to additional differential pressure from both exposed surfaces and experiences bending stresses, which are added to the inherent stresses caused by the difference in atmospheric pressure and vacuum. A high applied load may render a failure of VGU.

However, in the pressure equalisation design (Design II) shown in Figure 7- 1(b), the U-shape interlinking pipe provides a path to balance the pressure in the two air cavities separated by the VGU. When subjected the environmental actions from wind load, the deformation of the receiving panel will drive air in the first cavity to the second one while retaining the cavity air pressure equalised. Therefore, the loads will be directly transferred to the inner panel, rather than acting upon the VGU in-between.

7.3 Negative pressure experiment

Windows are always subjected to the environmental actions like wind or snow, in a form of uniformly distributed load (UDL). Uniform negative pressure tests were conducted in this study to imitate the equivalent action from such environmental actions. This experimental task is to verify the new system meeting the design expectations, i.e. the vacuum glass experiencing reduced stresses and deformation in service and hence showing a higher safety performance.

The test specimen was assembled with two toughened monolithic glass and a set of VGU with panel size 1000 ×1000mm. The thickness of the toughened monolithic glass panel is 6mm and the adopted VGU is comprised of two glass panels of 5mm the thickness. The panels were separated by 12mm wide aluminium spacers. Silicone structural sealants were employed to glue components together. Before sealing the edge, one set of strain gauge rosette were applied on one surface of VGU. The strain gauge rosettes consist of three gauges measuring the strains at the angles of 0^o, 45^o, and 90^o respectively as shown in Figure 7- 2. Other two sets of strain gauges were applied on the top and bottom surfaces of the toughened glass panels after the specimen was

assembled. Gauges were glued at the centre of each panel, and the connecting pipe was fixed at the edge of the square glass unit.

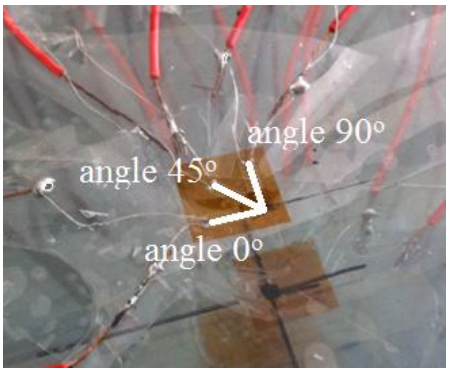

Figure 7- 2. Strain gauge rosette glued on glass surface

In order to compare the stress and strain in both systems as shown in Figure 7- 1(a) and (b), the connecting pipe with a switch valve was fixed in the glazing system in the experiments, as shown in Figure 7- 3.

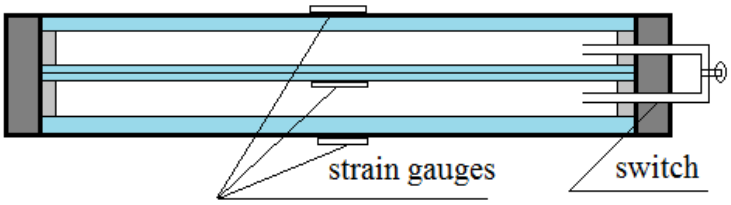

Figure 7- 3. Schematic diagram of the specimen with switchable pressure equalisation valve

The pipe is made of polyvinyl chloride (PVC) and the internal radius is 2mm. When the switch valve is off, the system is equivalent to the conventional composite glazing in Figure 7- 1 (a) (Design I); whereas when the switch valve is on, the structure is in Design II as shown in Figure 7- 1(b). Such design allows the reuse of the test specimens

during the comparison test. In order to have a full curing of the silicone sealant, the sealed glazing units were placed in the laboratory for 14 days before the tests. A negative pressure test device was set up as shown in Figure 7- 4.

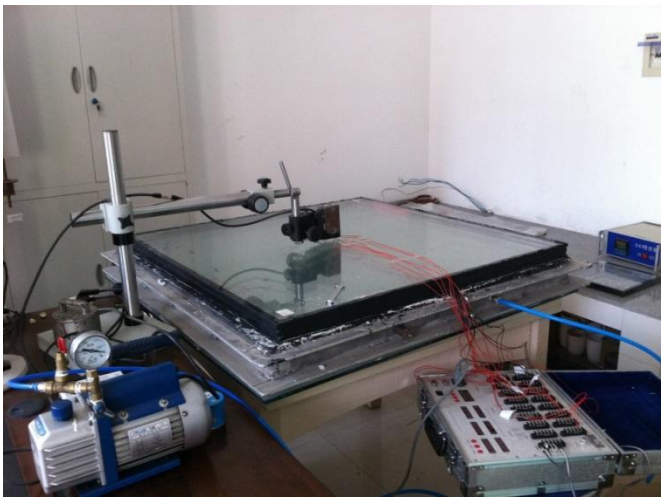

Figure 7- 4. Experimental device for negative pressure test

The test specimen was tightly glued onto a fully sealed chamber by silicone sealants that can provide high air tightness within the chamber. A vacuum pump was connected to the chamber that can evacuate the inner air. A negative pressure dial gauge was installed on the hermetic chamber to indicate the pressure value. A strain gauge data acquisition system that was connected to the strain gauges was employed to record the strain changes on each glass panel and the central deflection of the upper panel was measured by a precision laser displacement meter. The negative pressure tests were carried out three times for each glazing design by turning the switch valve on and off respectively. The strains and the deflections were recorded at a pressure from 0.5kPa to 3kPa with an interval of 0.5kPa.The pressure versus time relation is shown in Figure 7- 5. The pressure tests repeated three times for each type of glazing configuration.

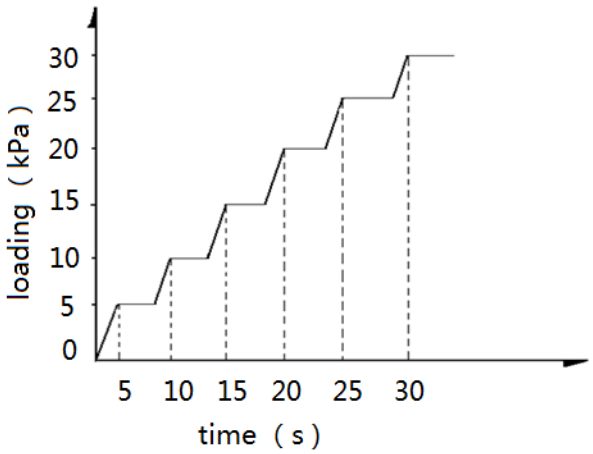

Figure 7- 5. Applied pressure regime

7.4 Results and Discussions

7.4.1 Experimental results

The strains at three directions on the glass surface were measured at different load levels by the strain gauges. At the centre point of the square glass specimen, two in-plane principle strains can be calculated by substituting the strains at 0^o, 45^o, and 90^o to the equation below (Bucciarelli, 2009)

$$\varepsilon_1 = \frac{\varepsilon_0 + \varepsilon_{90}}{2} + \sqrt{\left[\frac{(\varepsilon_0 - \varepsilon_{90})}{2}\right]^2 + \left[\frac{(\varepsilon_0 + \varepsilon_{90}) - 2\varepsilon_{45}}{2}\right]^2} \qquad 7\text{- }1$$

$$\varepsilon_2 = \frac{\varepsilon_0 + \varepsilon_{90}}{2} - \sqrt{\left[\frac{(\varepsilon_0 - \varepsilon_{90})}{2}\right]^2 + \left[\frac{(\varepsilon_0 + \varepsilon_{90}) - 2\varepsilon_{45}}{2}\right]^2} \qquad 7\text{- }2$$

The maximum principal stress can be consequently obtained (Timoshenko and Goodier, 1970)

$$\sigma_{\max} = \frac{E}{1-\nu^2}(\varepsilon_1 + \nu\varepsilon_2) \qquad 7\text{- }3$$

The glass is considered as a type of linear elastic, isotropic and homogeneous material. The maximum in-plane principal stress can be directly determined from the strains in three directions, by substituting Eq. (6-42) and (6-43) into Eq. (6-44):

$$\sigma_{\max} = \frac{E}{2}\left\{\frac{\varepsilon_0 + \varepsilon_{90}}{1-\nu} + \frac{1}{1+\nu}\sqrt{\left(\varepsilon_0 - \varepsilon_{90}\right)^2 + \left(\varepsilon_0 + \varepsilon_{90}\right) - \left[\left(\varepsilon_0 + \varepsilon_{90}\right) - 2\varepsilon_{45}\right]^2}\right\} \quad 7\text{-}4$$

where E is the Young's modulus and is the Poisson's ratio of the glass panel. For glass, the Young's modulus is 72000 MPa and Poisson's ratio is 0.22.

The average values of the maximum stresses on each panel under increasing applied pressure are recorded and presented in Table 7- 1. The stresses are plotted in Figure 7- 6, in order to present a clear comparison. The maximum stresses represented in their absolute values for the upper glass which is in compression on its top surface.

Table 7- 1. Stresses calculated by the measured strains

Pressure（kPa）		**0**	**0.5**	**1**	**1.5**	**2**	**2.5**	**3**
Design I	σ_{upper}(MPa)	0	0.76	1.71	2.75	3.32	3.92	4.41
	σ_{VGU} (MPa)	0	1.27	2.53	3.70	4.79	5.74	6.84
	σ_{lower} (MPa)	0	0.94	2.45	3.51	4.36	5.53	6.59
Design II	σ_{upper}(MPa)	0	1.82	3.37	5.57	6.89	8.49	9.81
	σ_{VGU}(MPa)	0	0.16	0.21	0.35	0.72	0.89	1.02
	σ_{lower}(MPa)	0	1.92	3.83	6.03	7.31	9.26	11.45

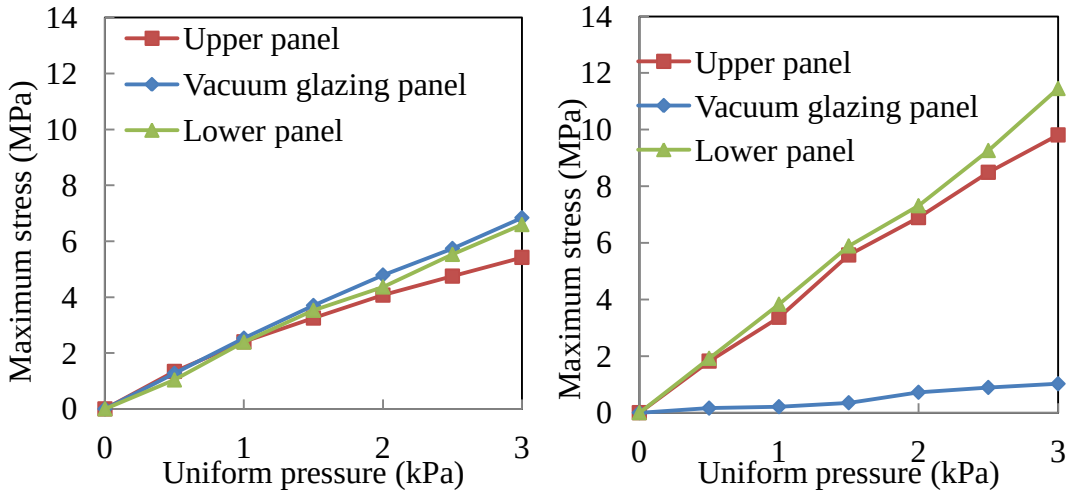

(a) Mode I (b) Mode II

Figure 7- 6. Stresses in each glass panel in Design I and II

The measured results of Design I indicate that when the lower panel is subjected to a uniform negative pressure, it will result in a dishing-type deformation and hence an expansion of the lower air space, which will subsequently lower its pressure and deform the VGU and the upper panel, causing a chain reaction As expected, the stress in the lower panel is greater than the upper one by appropriately 30% to facilitate the load transfer through the air. The stresses developed in the glass panels of VGU are more complicated. Both constituent panels of VGU are supported by a matrix of pillars. Under the test, the top panel is subjected to the increased air pressure while it is supported on equally spaced discrete points. The reaction can then be transferred to the lower one while keep the same cavity width facilitated by the pillars. The developed stresses hence depend on the glass thickness and pillar spacing. In the design practice, the VGU can be treated as a monolithic glass with an effective thickness (Liu, 2009). However, there is yet any well-established model to calculate such effective thickness by allowing for the pillar arrangement.

Figure 7- 6 (b) shows a different stress development in Design II. The stresses in both upper and lower panels have been increased as compared to Design I. The middle VGU panel experiences only a small fraction of stress that is induced in Design I. The results shown in Table 7- 1 affirmed that the stresses in the VGU have been successfully reduced by averagely 87.37% from Design I to Design II. Although the upper and lower panels have to withstand higher stresses in Design II, this can be easily coped by using toughened glass.

The test also suggests that the pressure equilibrium between two air cavities is not fully achieved under the prescribed loading rate. This time lagging effect can be easily altered by changing the size/number of the interlinking pipe. Further research should be conducted to ensure that no high stresses will be induced during the application of the external loads that are of dynamic nature, such as wind.

To further explore the load sharing/transferring behaviours of each glass panel, the maximum deflection of the glass panel is also examined. In the present study, only the deflection of the upper panel was measured. As in the test, the glass panels behave in the linear elastic range, and plate theory is used to calculate the deflections of the unmeasured panels by the strain records. That can be done by using the following equations (Young and Budynas, 2002):

$$\sigma_{max} = \frac{\beta q b^2}{h^2} \qquad 7\text{- }5$$

$$\omega_{max} = \frac{\alpha q b^4}{E h^3} \qquad 7\text{- }6$$

Where, b is the edge length of the plate, t is the thickness, E is the Young's modulus, α and β are the numerical constants that relying on the aspect ratio and material

properties. When the aspect ratio of the plate equals to 1, $\alpha = 0.0463$, and $\beta = 0.2874$ for v = 0.22.

By substituting Eq. (7-5) to (7-6), the maximum deflection can be expressed in Eq. (7-7). The maximum deflection of lower panel can be hence obtained with measured maximum stresses and the thickness.

$$\omega_{\max} = \frac{\alpha \sigma_{\max} b^2}{\beta E t} \qquad 7\text{- }7$$

The experimental bending deflection of the upper panel is used to validate Eq. (7-7) in Figure 7- 7, thus the equation can be applied to the other glass panels.

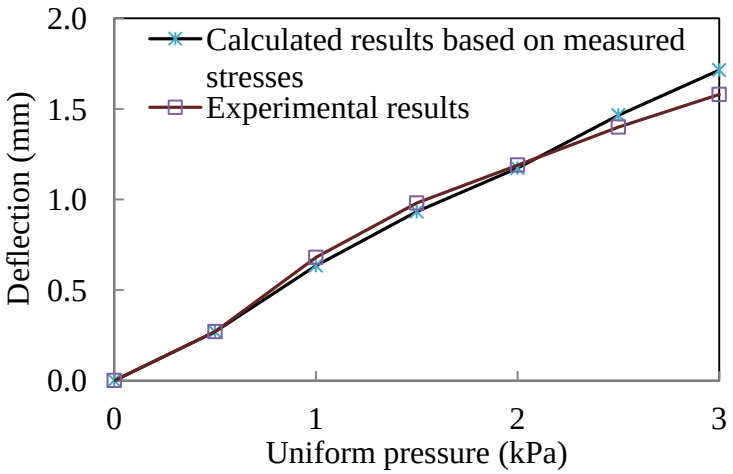

Figure 7- 7. Deflections of the upper glass panel with increasing uniform pressure

It is noted that the bending deflection of the interlayer VGU deserves further discussion because it regards the combined movement of two glass panels. The edges of two glass panels are fused together by solder glass, with the rotation degree of freedom restrained. The support pillars incorporated in the evacuated spacer do not yield interior shear stress or momentum. Hence the two sheets can be deemed to bend on their own neutral

layers. The experiment carried out by Liu (2009) depicted the maximum deflection of inner and outer plates of the vacuum glazing. It was found the deflections of two sheets are almost the same, which indicates the vacuum glazing keeps integrity under the uniform pressure. Nearly no relative displacement was observed in the experiment. Therefore, the unit can be considered as a monolithic glass when calculating the global bending deflection of the vacuum glazing.

A VGU exhibits higher stresses and deflections than a monolithic glass panel with the same thicknesses under equal loading level. An effective thickness instead of the actual thickness should be employed when assuming VGU as a monolithic glass panel in theoretical bending calculation. An approximation method is proposed to give a range of effective thickness.

(I.) Assuming one glass panel simply overlaying the other one without any interaction, the bending of each sheet is independent to the other one. The effective bending stiffness is equal to the sum of stiffness of each glass panel:

$$D_{eff} = D_1 + D_2 \qquad 7\text{- }8$$

where the bending stiffness D can be expressed as:

$$D = \frac{Et^3}{12(1-\nu^2)} \qquad 7\text{- }9$$

The substitution of Eq. (7-9) into Eq. (7-8) leads to

$$t_{eff} = \sqrt[3]{t_1^{\,3} + t_2^{\,3}} \qquad 7\text{- }10$$

In the case of two glass panels of the VGU with the same thickness,

$$t_{eff} = 1.26t \qquad 7\text{- }11$$

(II.) If two glass panels are perfectly bonded together, it can be considered as one monolithic glass panel and the effective thickness is the sum of the thickness of each glass panel.

In terms of actual situation, two glass panels of the VGU are connected by the solder glass seal at edges and the pillar array incorporated between two panels. Therefore the effective thickness of vacuum glazing should fall within this range:

$$1.26t < t_{eff} < 2t \qquad 7\text{- }12$$

Trial and error method in FEM modelling is employed to finally quantify specific value of the effective thickness of VGU. In this case, the effective thickness is found to be 8mm.

The deflection of inter-layer VGU and lower toughened glass panel are calculated and the results are shown in Table 7- 2 and Figure 7- 7.

Table 7- 2. Calculated deflections in two modes

Pressure（kPa）		**0**	**0.5**	**1**	**1.5**	**2**	**2.5**	**3**
Design I	ω_{upper}(mm)	0	0.27	0.68	0.98	1.19	1.4	1.58
	ω_{VGU} (mm)	0	0.34	0.68	0.99	1.28	1.54	1.84
	ω_{lower} (mm)	0	0.34	0.88	1.26	1.56	1.98	2.36
Design II	ω_{upper}(mm)	0	0.68	1.26	2.08	2.57	3.17	3.64
	ω_{VGU} (mm)	0	0.04	0.06	0.10	0.20	0.25	0.29
	ω_{lower} (mm)	0	0.72	1.43	2.20	2.73	3.45	4.27

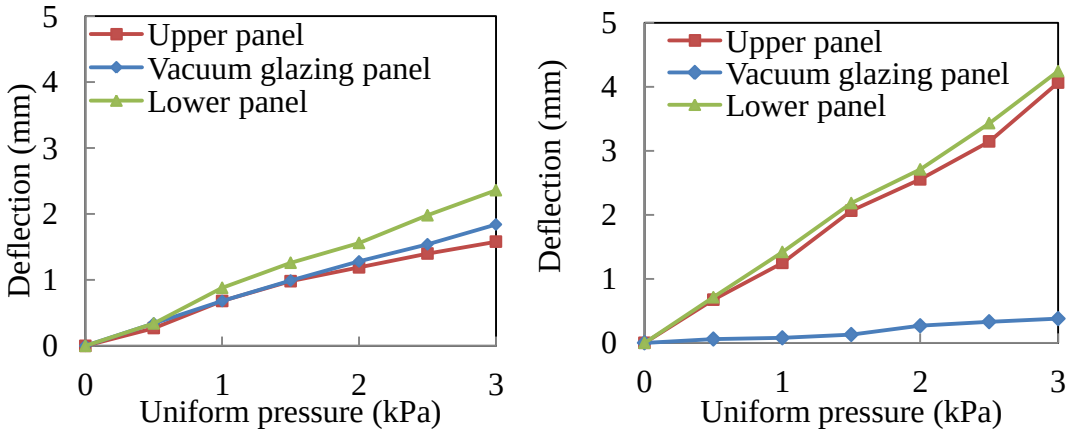

(a) Mode I (b) Mode II

Figure 7- 8. Deflections in each glass panel in Design I and II

As shown in Figure 7- 7(a), the deflection on each glass panel is descending from lower panel to the VGU then to the upper panel. The deflection of the vacuum glazing is very close to that of the upper panel. However, the deflection of VGU in the self-balancing hybrid glazing is almost negligible compared to the other two panels, as presented in Figure 7- 8 (b).

Both the stresses and deflections in the VGU have been found reduced significantly. Therefore the new glazing design is verified to reduce the loads on VGU, which results in a significant reduction in the failure risk in VGU. The hybrid vacuum/triple glazing with pressure equalisation design provides a solution to enhance the safety performance in VGU without having to make it with toughened glass, which is still technically or economically unviable.

7.4.2 Comparison between analytical solutions, numerical modelling and experimental results

In this section, the previously introduced FEM hydrostatic models and the analytical calculation method will be used to compare with the experimental results as cross reference.

The conventional composite glazing unit can be modelled as a piece of 6mm+8mm+6 mm TGU. FEM modelling and the analytical solutions developed in Chapter 4 are employed to compare with the results obtained from negative pressure tests.

Comparison in the conventional composite glazing unit

The maximum stresses and deflections obtained from analytical solutions and FEM modelling are displayed in Table 7- 3 and Table 7 – 4.

Table 7- 3.Stresses and deflections of each panel on composite glazing unit in analytical solution

p (kPa)	σ_{lower} **(MPa)**	ω_{lower}**(mm)**	σ_{VGU}**(MPa)**	ω_{VGU} **(mm)**	σ_{upper}**(MPa)**	ω_{upper}**(mm)**
0.5	1.142	0.407	1.159	0.325	0.790	0.283
1	2.283	0.815	2.317	0.621	1.581	0.565
1.5	3.433	1.225	3.467	0.930	2.379	0.851
2	4.574	1.632	4.625	1.241	3.169	1.133
2.5	5.724	2.042	5.779	1.550	3.960	1.416
3	6.874	2.453	6.939	1.861	4.742	1.696

Table 7- 4. Stresses and deflections of each panel on composite glazing unit in FEM modelling

p (kPa)	σ_{lower} **(MPa)**	ω_{lower}**(mm)**	σ_{VGU}**(MPa)**	ω_{VGU} **(mm)**	σ_{upper}**(MPa)**	ω_{upper}**(mm)**
0.5	1.170	0.380	1.256	0.33	0.700	0.310

1	2.239	0.765	2.360	0.66	1.483	0.630
1.5	3.309	1.148	3.465	0.99	2.275	0.947
2	4.379	1.531	4.568	1.32	3.067	1.263
2.5	5.496	1.860	5.661	1.60	3.870	1.526
3	6.576	2.250	6.760	1.91	4.650	1.820

And the results from experiments, analytical method and FEM numerical modelling are compared in Figure 7- 9.

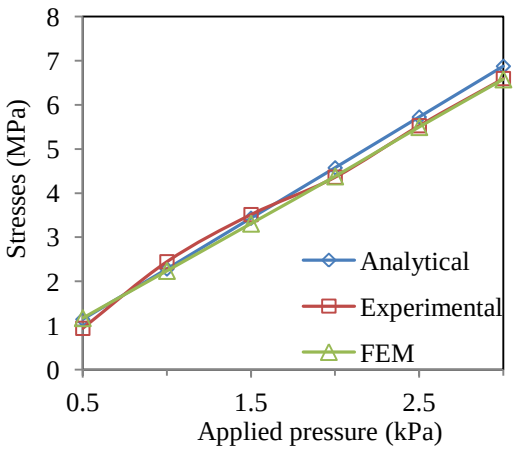

(a) Max. stresses in upper panel

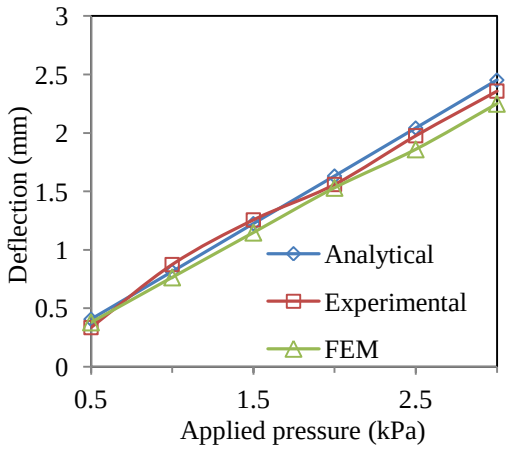

(b) Max. deflections in upper panel

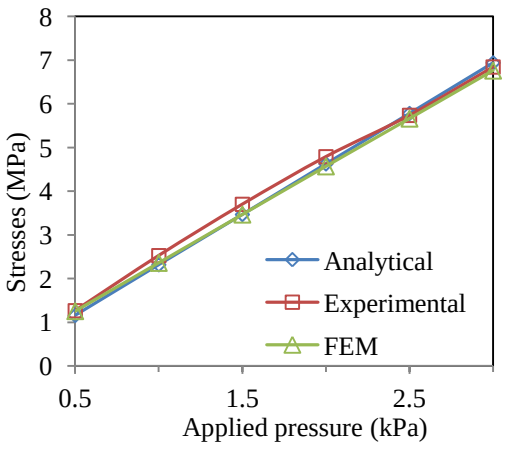

(c) Max. stresses in VGU panel

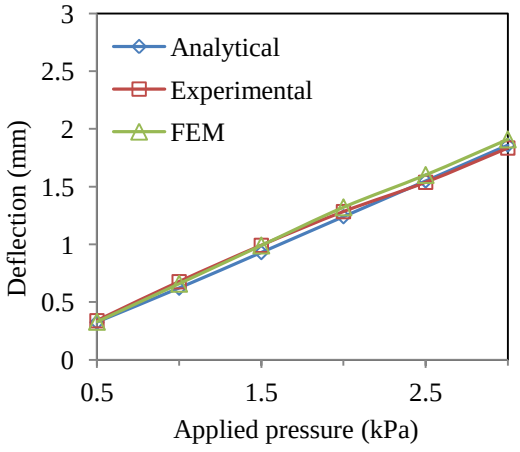

(d) Max. deflections in VGU panel

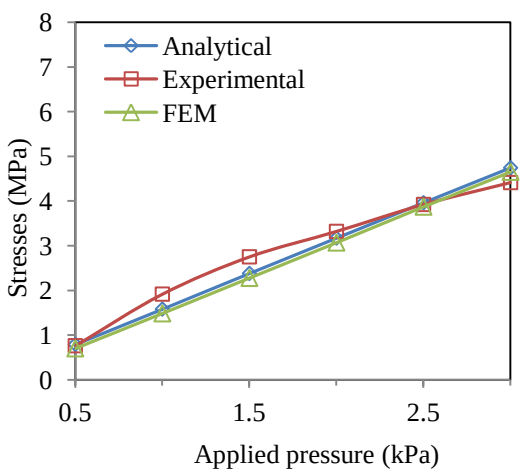

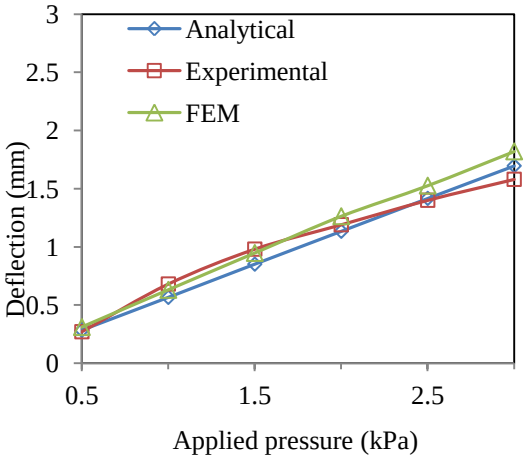

(c) Max. stresses in lower panel (d) Max. deflections in lower panel

Figure 7- 9. Maximum stresses and deflections in the three glass panels of TGUs

As observed in Figure 7- 9, the results obtained from three different methods have reached good agreement. Compared with experimental data, the analytical results are slightly higher meanwhile the numerical results are relatively lower. The average divergence of three approaches is within 5%.

Comparison in the conventional composite glazing unit

In modeling Design II with pressure equalisation, it is assumed that the air movement between two cavities has completed and hence the pressure is equal. To simplify the modeling, an equivalent IGU with vanishing VGU has been assumed. Numerical models resemble the real size of the test specimen. The maximum stresses and deflections of upper and lower panels under increasing pressure loads are compared. The FEM results are listed in Table 7- 5 and compared in Figure 7- 10.

Table 7- 5. Stresses and deflections of each panel on composite glazing unit in FEM modelling

P (kPa)	σ_{lower} (MPa)	ω_{lower}(mm)	σ_{upper}(MPa)	ω_{upper}(mm)
0.5	2.039	0.812	1.717	0.683
1	4.078	1.625	3.434	1.367
1.5	6.116	2.437	5.151	2.05
2	8.154	3.248	6.87	2.734
2.5	10.191	4.06	8.589	3.419
3	12.227	4.871	10.309	4.103

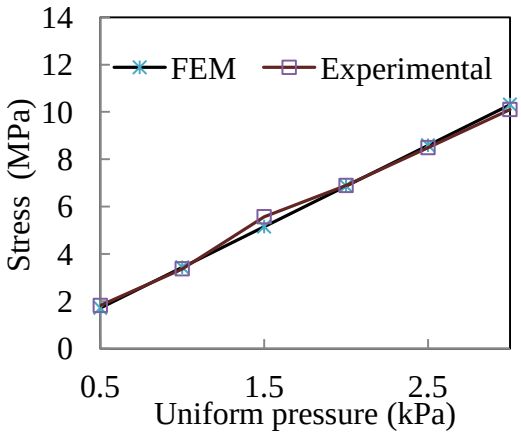

(a) Maximum stresses in upper panel

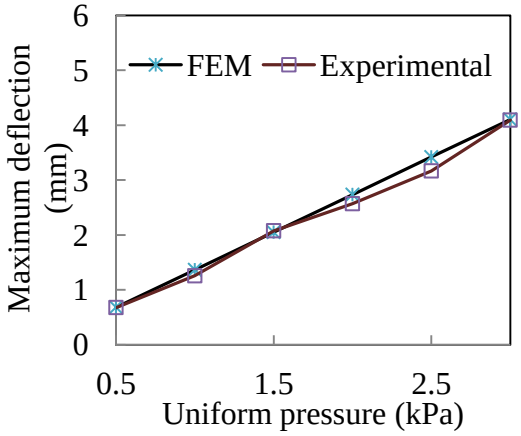

(b) Maximum deflection in upper panel

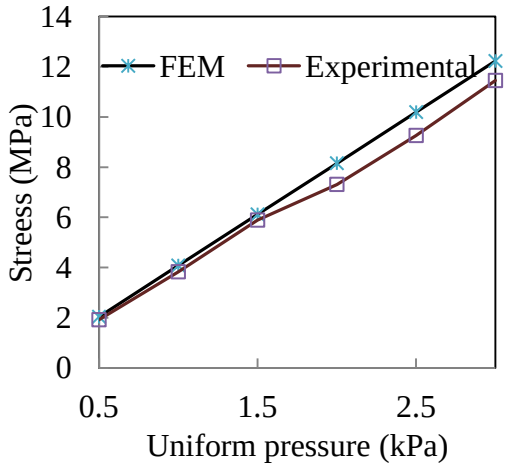

(c) Maximum stresses in lower panel

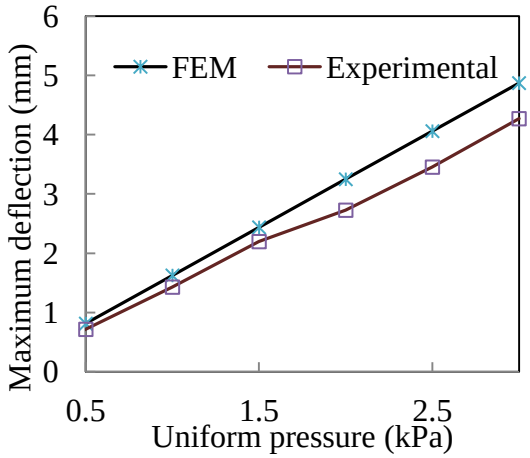

(d) Maximum deflection in lower panel

Figure 7- 10. Comparison of maximum stresses and deflection in hybrid glazing unit

As shown in Figure 7- 10 (a) and (b), the results in the upper panel are in good accordance between experiment and FEM modelling. A somewhat higher discrepancy was observed in the lower panel. The experimental results exhibit lower stresses and deflection than theoretical results. The deviation results from the neglect of VGU inter-panel in the FEM modelling. According to Figure 7- 6 (b), the VGU inter-panel in reality also carried a small portion of load, hence alleviated the pressure loads on the lower panel. This arises from the assumptions used in the numerical modelling that the two interlinked air cavities are fully pressure-equalised. Nevertheless, in the test, the inner VGU experienced a small level of bending action indicating the pressure equalization has yet been fully attained. Changing the size and number of interlinking pipes will adjust the time required for the pressure equalisation. Further research should be performed to identify the optimal interlinking pipe design to accommodate the wind load that is often of dynamic nature.

7.5 Conclusions

An innovative design is proposed to restrict the mechanical loads and the deformation in VGUs to an approximate-zero state. The self-equalisation system for the hybrid glazing has been verified as an effective structural/functional integration component for building windows or curtain wall, in which the high thermal insulation and low load stress are both realized for VGU.

A group of negative pressure tests were carried out. Compared with the conventional composite glazing, the VGU implemented in the self-equalisation hybrid glazing endures very low stresses. So the hybrid glazing is verified to effectively reduce the mechanical forces on the VGU inter-panel. The FEM modelling and analytical methods are also adopted to simulate the experiment as cross reference.

CHAPTER 8. CONCLUSIONS

8.1 General

In this chapter, the main findings and novel contributions achieved by the entire study on the energy-efficient glazing products will be summarised and presented. The study mainly focuses on the structural performances of insulating glass units (IGUs), vacuum glazing units (VGUs) and the proposed hybrid glazing units under the complex environmental factors throughout their service life. The findings that can be used to inform design practice and the recommendations for future work will be outlined.

8.2 Structural performance of IGUs under interactive environmental impacts

In this part of study, the key conclusions are proposed as follows:

- Hydrostatic fluids models implemented in the FEM package ABAQUS have been proven to be a useful tool to analyse the structural behaviours of IGUs subjected to coupled actions from various environmental factors.

- An analysis model has been developed for four-point supported IGUs, aligned with the model from prEN 13474-2 for the edge supported units. The coefficients k_4 and k_5 in the model are determined and presented in the form of design charts.

- It was found that the load partition ratio for each glass panel in IGUs is independent of the loading level or the degree of nonlinearity.

- The load share ratios of IGUs are dependent on the unit size. The load receiving panel will withstand the higher percentage load in the case of small unit size and the load share will tend to be equal with increasing unit size.

- For a given uniform internal load, the increase in the cavity width will result in a linear rise in the maximum deflection of each glass panel. However, the increase in the unit size will leads to a nonlinear increase in the maximum deflection and such deflection will approach an almost constant level once the unit size exceeds 1m.

8.3 Analytical model of triple glazing units

The flexural behaviour of triple glazing units (TGUs) was analysed by using FEM nonlinear hydrostatic TGU models. Novel contributions are summarised as follows:

- The interactive action of the temperature change and the wind load was studied for both winter and summer conditions. It is found that the maximum deflection occurs in the outer panel for the winter season and in the inter-panel for summer.

- A linear analytical method is proposed, which is able to provide an exact solution in the case of small deflection. A nonlinear analytical solution for analysing TGUs is developed for large deflections on the basis of this linear method.

- The changes in the size and the width of the air cavity in a TGUs are found to affect the load share of each glass panel. Increasing the ratio of the glass size and air cavity width tended to equate the load share of each glass panel if their thickness is the same.

- Changing the thickness of the inter-panel from 1mm to 8mm will reduce the global deflection of TGU. The upper panel experiences the highest bending deflection among the three panels, and the deflection proportion of the upper panel ($\omega_{upper}/\omega_{tot}$) becomes greater with higher inter-panel thickness.

8.4 The development of new hybrid pressure equalisation glazing units

- A novel hybrid TGU design was proposed to minimise the loads acting on the middle VGU. The pressure equalisation design for the hybrid glazing has been verified as an effective structural/functional integrative component for building windows or glass wall, in which the thermal and structural performance are both enhanced.

8.5 Experimental studies of mechanical properties and aging performance of secondary silicone sealants

The mechanical properties and structural behaviours of three types of commercial sealants used for IGU's edge seal are analysed in this section. The following are the main findings in this study:

- From the tensile test, the strength of the single component Sealant B is the highest and the double-component is the lowest and such differences are related to the cross-linking density. The hardening phenomena is found in the stress-strain curves of the single-component silicone sealants, but not observed in the two-component sealant. The orientation of PDMA chains accounts for these hardening behaviours observed from the stress-strain curves.

- The compressive modulus at the 10% and 20% strain levels were calculated and compared between various sealants. The compression modulus of the one-component sealant is the highest and is also most sensitive to the strain change.

- The shear interfacial strength is always higher than the interfacial tensile strength. The one-component sealant displays the highest interfacial tensile and shear strength as well as the highest elongation rate at breakage.

- It was found that pre-loading in the cross-bonded tests can remarkably change the loading-displacement behaviour of the silicone sealants, but impose little influence on the peak stress. Stress-softening type of loading-displacement curves are observed in the pre-strained specimens.

- The aging mechanisms in the silicone sealant are attributed to two main molecular reactions: excessive cross-linking reaction because of methyl oxidation or hydrolysis, and the Si-O bond scission on the sealant-glass interface due to high temperature or UV exposure.

- In the immersion test, the interfacial tensile and shear bond strength and the Shore hardness of the sealant specimens are most affected by the K_2CO_3 solution, which provided a weak alkaline environment.

- Three commercially available edge seal profiles were examined in the parametric study. Von-Mises stress distribution and the deformation distribution of three types of sealant profiles were examined when IGUs were under interactive environmental actions. It was found that all the severe stress concentrations occur near the corners or on the interface, where either geometric

configurations or material properties varies abruptly. The sealant failure always initiates from these vulnerable spots.

8.6 Contact damage and optimisation of supporting pillars in VGUs by XFEM method

Listed as follows are the key conclusions from this part of the study:

- The extended Finite element method, known as XFEM, was successfully employed to simulate the Hertzian crack, caused by the supporting pillars in VGUs. The mean strength criterion is proposed as the failure criterion. The novel modelling method is verified by existing experimental data, and the results follow the empirical Auerbach's law well.

- It is found that both spherical and fillet pillars can effectively enhance the critical indentation loads. Such improvement is attained by mitigating the stress concentrations in the glass at the contact edges of the pillars.

- In order to optimise the shape of a fillet pillar, the fillet size was analysed. The optimal fillet radius is between 0.03 and 0.04mm. By examining various pillar sizes, a fillet radius of 0.03mm is found to be the best option for the pillar radius larger than 0.335mm; otherwise 0.04mm should be employed.

- The Young's modulus dependency of the critical indentation load is not obvious for fillet pillars. The lower Young's moduli yield higher critical loads for spherical pillars due to high elastic contact deformation. A simplified equation is derived to calculate the critical indentation load of an elastic pillar, by providing the Young's modulus and the radius of the spherical pillar.

8.7 Recommendations on future work

This doctoral research highlights a number of issues which require further investigation, which would be undertaken in the following areas:

- Hydrostatic fluid models are capable of simulating the non-uniform temperature field of the glass panels and other solid materials. However, the temperature field of the sealed air in the cavity can only be considered to be uniformly distributed. The differential temperature in the cavity air will be potentially severe, in particular once the thermal performance has been improved. Few publications can be found in this field.

- In this thesis, the point supported conditions were assumed in the numerical modelling for IGUs. The details of the connections, including the articulated bolts and isolation materials were not established in this simulation. A detailed investigation would entail the real distribution and intensity of the local stresses induced around the bolt holes.

- The negative pressure tests in the novel hybrid glazing component were carried out only for 1000×1000mm specimens with an interlinking pipe of 2mm in radius. More geometric configurations are recommended to study the lag effect of the pressure equalisation of hybrid glazing units.

- Although well-planned experimental investigations on the edge seal of IGUs have been carried out, more information on the long-term aging behaviours would help to have a better understanding of the durability of IGUs, which are subjected to the field exposure.

- A correlation between the experimental ageing results and the field data are not yet established, thus the aging behaviours of sealants from accelerated laboratory work can be translated to the real service behaviour.

- Different structural behaviours arising from various energy-efficient glazing edge designs have been studied by considering static loadings only. Dynamic loading conditions should also be considered, e.g. under the impact loads, in future work.

REFERENCE

Adhesive and sealant Council (2013): **Adhesion and Cohesion**, last access date: 18th Dec 2013 http://www.adhesives.org/adhesives-sealants/science-of-adhesion

Ahagon, A., Gent, A. G., (1975). **Effect of interfacial bonding on the strength of adhesion**, Journal of Polymer Science: Polymer Physics Edition, 13, 1285-1300.

Amstock, J.S., (1997) **Chapter 12: Sealants,** Glass in construction, US, McGraw-Hill

ASTM, (2002(a)). **E 2188-2 Standard Test Method for Insulating Glass Unit Performance1**, ASTM International, PA, US

ASTM, (2002(b)). **E 2189–2 Standard Test Method for Testing Resistance to Fogging in Insulating Glass Units**, ASTM International PA, US

ASTM, (2002(c)). **E 2190-8 Standard Specification for Insulating Glass Unit Performance and Evaluation**, ASTM International, PA, US

ASTM, (2006). **E546-8: Standard Test Method for Frost/Dew Point of Sealed Insulating Glass Units1**, ASTM International, PA, US

Auerbach, F., (1891). **Measurement of Hardness**, the Journal of Physical Chemistry, 43-61.

Bao, Y., Gao, S. J., (2008). **Local strength evaluation and proof test of glass components via spherical indentation**, Journal of Non-Crystalline Solids, 1278-1381.

Bao, Y., Jin, Z., (1993). **Size effects and a mean-strength criterion for ceramics**, Engineering Structure and Materials 8, 829-935.

Bao, Y., Su, S., Yang, J., (2002). **Non-destructively determining local strength and residual stress of glass by Hertzian indentation,** Acta Materialia 50, 4659-4666.

Belytschko, T., (1999). **A finite element method for crack growth without remeshing**, International Journal for Numerical Methods in Engineering, 46, 131–150.

Benson, D. K., (1987), Laser sealed vacuum insulation windows, The United States of America as represented by the United States Department of Energy, United Stated

Bergha, S., *et al.*, (2013) **spacers and edge seals in insulating glass units: A state -of-the-art review and future perspectives,** Energy and Buildings, Vol. 58, 263–280

BIS, (2010). **Estimating the amount of CO2 emissions that the construction industry can influence**,Department for Business, Innovation and Skills,London, UK

Blanchard, A.F., Parkinson, D., (1952) **Breakage of carbon-rubber networks by applied stress**. Journal of industrial and Engineering Chemistry, Vol 44, 799-812

BSI, (2002), **Glass in building — Insulating glass units, Part 4: Methods of test for the physical attributes of edge seals,** BS EN1279-4:2002

BSI, (2002). **prEN13474-2 Glass in Building - Design of glass panes- Part 2: Design for uniformly distributed loads**, BSI, London, UK

BSI, (2005). **BS 6262-3:2005 Glazing for buildings Code of practice for fire, security and wind loading**, BSI, London, UK

BSI. (2010) **Rubber — General procedures for preparing and conditioning test pieces for physical test methods**, BS ISO 23529:2010

BSI, (2011), **Rubber, vulcanized or thermoplastic — Determination of compression stress-strain properties,** BS ISO 7743:2011

BSI, (2011). **BS EN 410:2011 Glass in building —Determination of luminous and solar characteristics of glazing**,BSI, London, UK

BSI, (2011). **BS EN 673:2011 Glass in building —Determination of thermal transmittance (U value)— Calculation method**, BSI, London, UK

BSI (2011) Rubber, vulcanized or thermoplastic — Determination of tensile stress-strain properties, BS ISO 37:2011

BSI, (2013). **Draft BS EN 16612 Glass in building - Determination of the load resistance of glass panes by calculation and testing**, London, UK

Bucciarelli, L, (2009).Engineering Mechanics for Structures, Dover Publications.

Burgess, J., C, (1999). **The history, scientific basis and application of international IGU durability tests**, Building and Environment, 34, 363-368.

Buyl, F.D, (2001) **Silicone sealants and structural adhesives,** International Journal of Adhesion & Adhesives Vol. 21, 411–422

CGSB, (1997). **CAN/CGSB-12.8-97 Insulating glass units**, Canadian General Standards Board, Cananda

Chen. Y.B. *et al.* (2013) **A study on silixone cross-linker and coupling agent for the improvement of slilicone sealant (Chinese),** Development guide to building materials, No. 8, 55-57

Chien, W-Z, (1947) **Large deflection of a circular clamped plate under uniform pressure**, Chinese, Journal of Physics, 7, 102- 113.

Chien, W-Z., and Yeh, K-Y, (1957) **Large deflection of a rectangular plate under uniform pressure**, Proceedings of the International Congress of Mathematicians., Brussels, 6, 403-409.

Clarson, S.J, Semlyen J.A. (1993) **Siloxane polymers**. (**Ellis Horwood and Prentice-Hall, Polymer Science and Technology Series)**, UK, Prentice Hall

Collins, R. E. and Fischer-Cripps, A. C., (1991) **Design of Support Pillar Arrays in Flat Evacuated Windows**, Australian Journal of Physics vol.44(5) 545-564.

Collins, R. E., Robinson, S. J., (1991). **Evacuated Glazing**, Solar Energy, 47, 27-38..

Col Collins R. E., Fischer-Cripps A. C and Tang J.Z., (1992), **Transparent evacuated insulation**, Solar Energy Vol.49 No. 5 333-350.

Collins, R. E., Turner, G. M., Fischer-Cripps, A., Tang, J., Simko, T. M., Dey, C. J., Clugston, D. A., Zhang, Q. C., Garrison, J. D., (1995). **Vacuum Glazing - A New Component for Insulating Windows**, Building and Environments 30, 459-492.

Collins, R. E., Simko, T. M., (1998). **Current status of the science and technology of vacuum glazing**, Solar Energy, 62, 189-213.

Collins, R.E. Asano, O. Misonou M., et al., (1999) **Vacuum glazing: design options and performance capability**, Proceedings of Glass in Buildings Conference Bath UK 221–226.

Committee on climate change, (2008) **Climate Change Act**, Her Majesty's Stationery Office and Queen's Printer of Acts of Parliament, UK

Crank, J. (1975) **The Mathematics of Diffusion**, 2nd ed. Oxford, Clarendon Press

Dannenberg E.M., Brennan, J.J., (1965) **Strain –energy as a criterion for stress softening in carbon-black-filled vulcanizates**. Rubber Chemistry and Technology, Vol 39, 597-608

Diani, J., Fayolle., B., Gilormini, P., (2009), **A review on the Mullins effect**, European Polymer Journal, Vol 45, 601–612

Doll, L.M., Hendrickson, G., Lagos, G. et al. (2005) **An Insulating Glass Knowledge Base Phase II Final Report**, USA: Aspen Research Corporation.

Dorfmann, A., (2003) **Stress softening of elastomers in hydrostatic tension**, Acta Mechanica Vol 165, 117-137

Dow Corning (1993) **Silicone Structural Glazing Manual, Germany,** Dow Corning Corporation

Dow Corning, (2013) **Insulating Glass Technical Manual: The use of Silicone Sealants in Dual-Sealed Insulating Glass Units**, USA: Dow Corning Inc.

Eames, P. C., (2008). **Vacuum glazing: Current performance and future prospects**, Vacuum, 82, 717-722.

Elmahdy, A. H., (1993). **Heat transfer at the edge of sealed insulating glass untis: comparison of hot box measurements with finite-difference modeling**, ASHRAE Transactions: Symposia 99, 915-922.

Ernst, R.L.,. (1997) **Chapter 16 Inert Gases**, In: Amstock J.S. (ed.) Handbook of glass in construction. New York: McGraw-Hill. 323-338.

Fang, Y. P., Eames, P. C., (2006). **Thermal performance of an electrochromic vacuum glazing**, Energy Conversion and Management, 47, 3602-3610.

Fang, Y. P., Eames, P. C., Norton, B., Hyde, T. J., (2006). **Experimental validation of a numerical model for heat transfer in vacuum glazing**, Solar Energy, 80, 564-577.

Fang, Y. P., Hyde, T. J., Eames, P. C., Hewitt, N., (2009). **Theoretical and experimental analysis of the vacuum pressure in a vacuum glazing after extreme thermal cycling**, Solar Energy, 83, 1723-1730.

Fang, Y. P., Hyde, T. J., Hewitt, N. J., (2011). **The Influence of Isolation on the Thermal Performance of Triple Vacuum Glazing,**, In: Proceedings of Glass Performance Days

Fang, Y., Hyde, T., Hewitt, N., Eames, P. C., Norton, B., (2009). **Comparison of vacuum glazing thermal performance predicted using two- and three-dimensional models and their experimental validation**, Solar Energy Materials and Solar Cells, 93, 1492-1498.

Fares, M. E., Zenkour, A. M., El-Marghany, M, Kh, (2000) **Non-linear thermal effects on the bending response of cross-ply laminated plates using refined first-order theory**, Composite Structure, 49, 257-267.

Feldmeier, F., Heinrich, R., Hepp, B. Schimid, J. and Stiell, W., (1984) **The aging behaviour of insulating glass**, Institut fur Fenstertechnik, Rosenheim, Germany, October, 1984.

Feldmeier, F., (2003). **Insulating Units Exposed to Wind and Weather– Load Sharing and Internal Loads**, In: Glass Processing Days, Finland

Fischer-Cripps, A. D., (1997). **Prediction Hertzian fracture**, Journal of Materials Science, 32, 1277 — 1285

Fischer-Cripps, A., Collins, R., (1994). **The probability of Hertzian fracture**, Journal of Material Science 29, 2216-2230.

Fischer-Cripps, A., Collins, R. E., Turner, B. M., Bezzel, E., (1995). **Stress and fracture probabilit in evacuated glazing**, Building and Environment, 30, 41-59.

Fischer-Cripps, A., (2007). **Hertzian Fracture**, In: Fischer-Cripps, A. (Ed.) Introduction of Contact Mechanics, Springer Science + Business Media, New York, US, 116-135.

Frank, F., Lawn, B., (1967). **On the theory of Hertzian fracture**, In: Proceedings of the Royal Society London, UK

Gan, G., (2001). **Thermal Transmittance of Multiple Glazing: Computational Fluids Dynamics Prediction**, Applied Thermal Engineering, 21, 1583-1592.

Garrison J. D. and R. E. Collins, (1998) **Manufacture and cost of vacuum glazing**, Solar Energy Vol. 62, No. 3, 189–213.

Garvin, S.L. and Marshall, W.J. (1995) **Double -glazing units: A BRE guide to improved durability**, London: Construction Research Communications Ltd.

Garvin, S. L., (1998). **Insulating glazing units**, Building Research Establishment Centre,London, UK

Garvin, S. L., Wilson, J. U., (1998). **Environmental conditions in window frames with double glazing units**, Construction and Building Materials, 12, 289-302.

Garvin, S. L., (2000). **Durability of double glazing units**,Building Research Establishment,London, UK

Garvin, S.L. (2000) **Insulating glazing units**, London: Construction Research Communications Ltd.

Garvin, S., (2001). **Durability of double glazing units** In Whole Life Performance of Facades. Bath, 2001. Bath: Centre for Window and Cladding Technology. 107-118.

Gedde, U.W..(1995), **Chapter 9: Chain Orientation**; Polymer Physics, 1st Edition, Netherlands, Springer Netherlands. 199-216

Griffiths, P. W., Leo, M. D., Cartwright, P., Eames, P. C., Yianoulis, P., leftheriotis, G., Norton, B., (1998). fabrication of evacuated glazing at low temperature, Solar Energy, 63, 243-249.

Guardian (2009) **Guardian Gearing Up to Bring Vacuum Glazing to Market**, Available at: http://www.windowanddoor.com/news-item/companies/guardian-gearing-up-bring-vacuum-glazing-market (Accessed: 22nd Jan of 2013).

Gustavsen, A., Uvslokk, S., Jelle, B. P., (2005). **Numerical and experimental studies of the effect of various glazing spacers on the window U-value and the glazing temperature**, In: Nordic Building Physics Symposium (NBPS), Iceland

Hertz, H. (1896) **Hertz's Miscellaneous Papers,** Nature 55, 6-9.

Hess, R. (1986). **Glass thickness measurement. Design of single and insulating glass using the membrane effect in rectangular plates large deflection.** Institute of Building Technology, Swiss Federal Institute of Technology Zurich.

Hibbitt, Karlsson, Sorensen, (2010). **Abaqus/CAE User's Manual**,Pennsylvania State, USA

Hinnells, M. (2005) **The cost of a 60% cut in CO2 emissions from homes: what do experience curves tell us**, Proceedings of BIEE Conference, 16-19.

Houwink, R.,(1956) **Slipping of molecules during the deformation of reinforced rubber.** Rubber Chemistry and Technology, Vol 29, 888-893

Hyde, T. J., Griffiths, P. W., Eames, P. C., Norton, B., (2000). **Developement of a novel low temperature edge seal for evacuated glazing,** In: World Renewable Energy Congress VI, University of Ulster, Newtonabbey, Northern Island, UK

IGMA and IGCC, (2003). **Certification & testing insulating glass units ASTM E 2190**,Insulating Glass Manufacturing Alliance and Insulating Glass Certificate Council, US

ISO/TC 206, (2011), **Fine ceramics (advanced ceramics, advanced technical ceramics) — Test method for interfacial bond strength of ceramic materials,** ISO 13124:2011(E)

Jacob, D. J., (1999). **Introduction to Atmospheric Chemistry**, Princeton University Press, US.

Jacob, L., D'Cruz, J., (1999). **Fundamental Concepts for the Design, Manufacture and Testing of IG Units for Warm Climate**, In: Glass Processing Days Tampere, Finland

Jos, G., Oliver, G., Janssens-Maenhout, Peters, J., (2012). **Trends in global CO2 Emissions 2012 Report**, PBL Netherlands Environmental Assessment Agency, Bilthoven

Klosowski, J M., (1989). **Sealants in Construction**, New York and Basel, Marcel Dekker, Inc.

Koebel, M. M., Manz, H., Emanuel Mayerhofer, K., Keller, B., (2010). **Service-life limitations in vacuum glazing: A transient pressure balance model,** Solar Energy Materials and Solar Cells, 94, 1015-1024.

Koiter, W.T., (1966) **On the nonlinear theory of thin elastic shells,** Proceedings of the Koninklijke Nederlande Akademie van Wetenschappen B69, 1-54.

Kraus, G., Childers, C.W., and Rollman K.W., (1966) **Stress softening in carbon black reinforced vulcanizates: Strain rate and temperature effects.** Journal of Applied Polymer Science, Vol 10, 229-240

Kulshreshtha, A. K., Vasile, C., (2002). **Handbook of Polymer Blends and Composites, Volume 1**, Rapra Technology Limited.

Kumins, C. A., (1978). **Measurement of water vapor transmission through insulating glass sealants**, Thermalchimica, Acta, 22, 163-173.

Langitan, F. B., Lawn, B. R., (1969). **Hertzian Fracture experiments on abraded glass surfaces as definitive evidence for an energy balance explanation of Auerbach's Law**, Journal of Applied Physics, 40, 4009-4017.

Lawrence, D. (2007) **A review of the durability and of performance silicone structural glazing systems,** Glass processing days, Tampere, Finland,190-193

Lenzen, M., Collins, R. E., (1997). **Long term field tests of vacuum glazing**, Solar Energy, 61, 11-15.

Lenzen, M., Turner, G.M., Collins, R. E., (1999). **Thermal outgassing of vacuum glazing**. Journal of Vacuum Science Technology, A 17, 1002- 1017

Liu, X. G., (2009). **Safety evaluation and failure detection of glass curtain wall**, China Building Materials Academy, Ph.D.

Liu, X. G., Bao, Y., Xu, H., (2010). **Propagation mechanism and control criterion of fracture indentation in vacuum glazing** Materials Science and Technology, 6, 878-882.

Ma, C., Yang, S., Shi, M., (2009). **Thermal analysis of IGUs**, China Construction Metal Materials, 05, 27-32.

Ma, J., (2004). **Failure mechanisms and solutions of IGUs**, Glass, 177, 49-52.

Manz, H., (2008). **On minimizing heat transport in architectural glazing**, Renewable Energy 33, 119-128.

Manz, H., Brunner, S., Wullschleger, L., (2006). **Triple vacuum glazing: Heat transfer and basic mechanical design constraints**, Solar Energy, 80, 1632-1642.

Miguel, L. D., (2005). **Predicting Time to Fogging of Insulated Glass Units**, Technical Series, 05, 1-6.

Minaai, T. Kumagai, M., Nara, A., Tanemura, S., (2005). **Study of the outgassing behaviour of SnO_2 : F films on glass in vacuum glazing under external energy excitation.** Materials Science & Engineering Building 119, 252-257

Mingotti, N., Chenvidyakarn, T., Woods, A. W., (2013). **Combined impacts of climate and wall insulation on the energy benefit of an extra layer of glazing in the facade**, Energy and Buildings, 58, 237-249.

Mognato, E., Stevanato, A., Luca De, R., (2007). **Insulating glass unit comparison of laboratory according to prEN 1279**, In: Glass Performance Days 2007, Finland

Mouginot, R., Maugis, D., (1985). **Fracture indentation beneath flat and spherical punches**, Journal of Materials Science, 20, 4354-4376.

Mullins, L. (1969) **Softening of rubber by deformation**. Rubber Chemistry and Technology Vol 42:339–362.

Nadel S.J. and Amstock J.S.. (1997). **Chapter 18 Low-Emissivity Coatings.** In:. Amstock, J.S. (ed.) Handbok of glass in construction. New York: McGraw-Hill. 363-390.

Ng, N., Collins, R. E., So, L., (2006). **Thermal conductance measurement on vacuum glazing**, International Journal of Heat and Mass Transfer, 49, 4877-4885.

Noll, W.(1968) **Chemistry and technology of silicones,** USA**,** Academic Press Inc.

NSG Ltd. (2010) **Nippon Sheet Glass Spacia,** Available at: http://www.nsg-spacia.co.jp/ (Accessed: 22nd Jan of 2013).

Olivier G.J., Janssens-Maenhout G. and Peters J., (2012). **Trends in global CO2 Emissions 2012 Report**, PBL Netherlands Environmental Assessment Agency, Bilthoven,

Pai, P. F., Palazotto, A. N., (1996) **Large-deformation analysis of flexible beams**, International journal of Solids and Structures, 33, 1335- 1353

Palmerio, A. F., Reddy, J. N., Schmidt, R., (1990) **On a moderate rotation theory of elastic anisotropic shells- Part 1 Theory**, International Journal of Non-linear Mechanics, 25, 687 – 700.

Papaefthimiou, S., Leftheriotis, G., Yianoulis, P., Hyde, T. J., Eames, P. C., Fang, Y., Pennarun, P. Y., Jannasch, P., (2006). **Development of electrochromic evacuated advanced glazing**, Energy and Buildings, 38, 1455-1467.

Pietraszkiewicz, W., (1989) **Geometrically nonlinear theories of thin elastic shells**, Advances in Mechanics, 12, 51- 130

Powell, F. J., Hahn, M. H., (1978). **Measurement of the frost point of air in sealed insulating glass**, International Journal of Refrigeration, 1, 87-91.

PPG, (2010). Center of glass U-value for double and triple glazed Insulating glass units with Solarban 60 Low-e glass with 100% air, argon or krypton, or mixtures of these gases,

Qi, H.J. and Boyce, M.C., (2005) **Stress-strain behaviour of thermoplastic polyurethanes**, Mechanics of Materials, Vol 37, 817-839

Ratcliffe, L., (1994). **Consumers' Guide to Double Glazing: A Guide to Understanding and Selecting Double Glazing and Windows for the Home** LGR Design & Services, West Yorkshire.

Reddy, J.N., (1982) **Analysis of layered composite plates accounting for large deflections and transverse shear strains**, Recent Advances in Nonlinear Computational Mechanics, Pineridge Press Ltd, Swansea, 155- 202.

Reddy, J.N., Chandrashekhara, K., (1985) **Nonlinear analysis of laminated shells including transverse shear strains**, AIAA Journal, 23, 440- 441.

Reddy, J.N. (1990) **A general non-linear third-order theory of plates with moderate thickness,** International journal of Non-linear Mechanics, 25, 677-686

Reed, J., (2012). Evaluation of Triple Glazed Insulating Glass Strength, In, Architectural Testing, US.

Richardson, L., Hegemann, J., Sifakis, E., (2009). **An XFEM method for modelling geometrically elaborate crack propagation in brittle materials**, Internation Journal for Numerical Methods in Engineering 1, 1-41.

Rowland, G.A., (1998) **Adhesives and adhesion, Chemistry in New Zealand Journal,** No.71, 17-27

Sandberg, L.B. (1991) **Comparsions of silicone and urethane sealant durabilities**, Journal of Materials in Civil Engineering Vol 3: 278-291

Schmidt, G., (1997) **Sealants for IG units' performance parameters and requirements**, Glass processing days, Tempere, Finland; 247-251

Schmidt, R. and Reddy, J. N., (1988) **A refined small strain and moderate rotation theory of elastic anisotropic shells**, Journal of Applied Mechanics, Trans. ASME, 55, 611-617

Simko, T. M., Fischer-Cripps, A. C., Collins, R. E., (1998). **Temperature-induced stresses in vacuum glazing: modelling and experimental validation**, Solar Energy, 6, 1-21.

Sing, G., Venkateswara Rao, G., Iyengar, N., (1994), **Geometrically nonlinear flexural response characteristics of shear deformable unsymmetrically laminated plates**, Computers and Structures, 53, 69- 81

Song, H., Sun, H., Zhang, J., Zhang, Y., (2008). **FEM thermal analysis of IGUs**, Doors and Windows, 6, 37-40.

Song, S.-Y., Jo, J.-H., Yeo, M.-S., Kim, Y.-D., Song, K.-D., (2007). **Evaluation of inside surface condensation in double glazing window system with insulation spacer: A case study of residential complex**, Building and Environment, 42, 940-950.

Stetson, T.D., (1865) **Improvement in window glass**, United States Patent Office, NewYork: No.49 167

Suzuki, N. Ito, M. and Yatsuyanagi, F., (2005) **Effects of rubber/filler interactions on deformation behaviour of silica filled SBR systems**. Polymer, Vol 46, 193-201

Tang, J. (2011) **Introduction of development and technique of vacuum glazing**, Symposiums of Beijing Synergy Vacuum Glazing Technology Co LTD 1-6.

Timoshenko S. and Goodier J. N., (1970) **Theory of elasticity**, McGraw-Hill. New York

Timoshenko, S., (1940). **Theory of plates and shells**, McGraw-Hill, New York and London.

Torol, P. G., Lichtenberger, W., Major, A., (2002). **In-Situ Dew-point Measurement to Assess Life Span of Insulating Glass Units**, In: The Use of Glass in Buildings, PA, US

United Nations, (1998) **Kyoto protocol of the United Nations Framework Convention on Climate Change,** Kyoto, Japan

Van-Den-Bergh, S., Hart, R., Jelle, B. P., Gustavsen, A., (2013). **Window spacers and edge seals in insulating glass units: A state-of-the-art review and future perspectives**, Energy and Buildings, 58, 263-280.

Ventsel, E., Krauthammer, T., (2001). **Thin Plates and Shells Theory, Analysis, and Applications**, Marcel Dekker, Inc., New York, Basel.

Von Kármán, T. (1910), **Festigkeitsproblem im Maschinenbau,** Encyklo-pädie der Mathematischen Wissenchaften. Volume IV, 311–385

Voyutski, S.S. (1963), **Autoadhesion and adhesion of high polymer,** Wiley, New York.

Vuolio, A., (2003). **Structural behaviour of glass structure in facades**, Technology Laboratory of Steel Structures, PhD.

Wang, J., Eames, P. C., Zhao, J. F., Fang, T., (2007). **Stresses in vacuum glazing fabricated at low temperature**, Solar Energy Materials and Solar Cells, 91, 290-303.

Wilberforce, P., (1999) **The link between glazing and climate change**, Proceedings of Glazing in Building Bath UK 159-164.

Wolf, A. (1988). **New Development in the Field of Insulating Glass Units**, Construction and Building Materials 2(3): 134-144.

Wolf, A. T. (1992a). **Studies into the Life-Expectancy of Insulating Glass Units**, Building and Environment 27(3): 305-319.

Wolf, A. T. and Waters L. J. (1992b) **Factors Governing the Life-Expectancy of Dual-Sealed Insulating Glass Units**, Science and Technology of Building Seals, Sealants, Glazing, and Waterproofing, Second Volume 1200: 222-237, 323.

Wolf, A.T. and Waters, L.J., (1993), **Factors governing the life expectancy of dual-sealed insulating glass units,** Construction and Building Materials, Vol 7, No. 2, 101-107

Wolf, A. T. (1998) **Silicone Sealed Insulating Glass Units. Wiesbaden**, Dow Corning co. Ltd.

Wolf, A. T. (2003). **Edge-Seal Effects on Service-life and Utility value of Dual-Sealed Insulating Glass Units.** Glass Processing Days 15-18 June, Tampere, Finland

Wolf, A.T. and Clehand-Host, L.(2004) **Material properties for use in FEA Modelling: Sealant behaviour with ambient laboratory climate Aging,** Journal of ASTM international, Vol 1, No. 7, 1-13a

Wu, Q., Zhong, Z.H. (2012) **Discussion on the aging performance of silicone sealants for double glazing units,** China Academic Journal, No.22, 19-24

Wuethrich, W., (2005), **Heat transmission reducing closure element,**, Patent, E., No. 1529921, Switzerland

Wullschleger, L., Manz, H., Wakili, K. C., (2009). **Finite element analysis of temperature-induced deflection of vacuum glazing,** , Construction and Building Materials 23, 1378-2388.

Xu, J., Li, Y., Chen, X., (2010). **Characteristics of windshield cracking upon low-speed impact: Numerical simulation based on the extended finite element method**, Computation al Materials Science 48, 528-588.

Yang, J., and Ledbetter. S..(2004). **Stress analysis of the insulated glazing units under the thermal loading using finite element method**, Velux A/P Panels (SC-P) Discovery & Development, UK

Young, W. C., Budynas, R. G., (2002). Roark's formula for stress and strain, McGraw-Hill, New York.

Yuan, C., Zhou, K, Wu, L, and An, D. (2009) **Finite Element Method to Analyse Vehicle Air Spring**, Journal of mechanical engineering, 45(6), 42-46.

Zoller, A., (1924), **Hollow pane of glass** patent, G., No.387655, Germany

Zuege, K., Srinivasan, R. and Amstock, J.S (1997) **'Chapter 13 Warm edge-seal technology'**, in Amstock, J.S. (ed.) Handbook of glass in construction. New York: McGraw-Hill,. 219-269.